Utilization of nanostructured surfaces for sensing applications and the use of nanoentities for the fabrication of new materials

by

Christopher A. E. Hamlett

A Thesis Submitted to
The University of Birmingham
for the degree of
Doctor of Philosophy

School of Chemistry,
The University of Birmingham,
September 2008.

UNIVERSITY^{OF}
BIRMINGHAM

University of Birmingham Research Archive

e-theses repository

This thesis is dedicated to the memory of my late grandfather Prof. H. S. Ferns former Professor Emeritus of Political Science, University of Birmingham.

ABSTRACT

The application of nanoscience in various scientific fields is introduced in **Chapter 1** by outlining some of the major drivers of this rapidly evolving field. Methods of nanoscale fabrication, utilizing both 'top-down' and 'bottom-up' approaches, are also introduced in this chapter. Nanoscale characterization techniques that allow the visualization of the 'nanoworld' are introduced in **Chapter 2**.

Chapter 3 is concerned with the modification of Si_3N_4 substrates with self-assembled monolayers (SAMs) of 3-aminopropyltrimethoxysilane (APTMS) *via* a vapour deposition method. This investigation was carried out by forming APTMS SAMs, from the solution phase, on both SiO_2 and Si_3N_4 substrates and comparing them to provide a model with which to compare SAMs formed by a novel vapour phase methodology.

Chapter 4 further develops the work from **Chapter 3** by chemically modifying Si_3N_4 resonators with APTMS SAMs *via* vapour deposition. The chemically modified resonators were then used for the mass detection of citrate passivated Au nanoparticles and the results were compared to AFM and XPS studies of the same system but on planar substrates.

Chapter 5 is concerned with the fabrication of a bioarray for the patterned immobilization of human spermatozoa cells. Such arrays would allow for the

investigation of specific individual sperm cells. This could have a use in the field of artificial insemination.

Chapter 6 utilizes citrate passivated Au nanoparticles to prepare composite PEO/Au nanoparticle solutions for the formation of sub-micron diameter electrospinning. Such fibres are electrospun from solutions of 4 different concentrations of PEO and then subsequently characterized by optical microscopy, AFM, TEM and DSC.

Acknowledgements

There are many people who I would like to thank for their help and support during both the research for and writing up of this thesis.

CONTENTS

CHAPTER 3: Formation of amino terminated self-assembled monolayers on silicon nitride from the vapour phase 54

CHAPTER 6: *Formation of sub-micron fibres from aqueous PEO/Au*

nanoparticle composite solutions via electrospinning 160

ON CD-ROM

+ PDF copies of my publications

FIGURES

CHAPTER 1: Nanotechnology: the appliance of nanoscience

Figure 1. The predicted outlook for nanotechnology compared to other major technological evolutions by Norman Poire (Economist, Merrill Lynch)

Figure 2. A graph depicting the number of transistors per computer chip increasing with a trend described by Moore's law

Figure 3. Example of a MEMS clutch system

Figure 4. A schematic representation of a photolithography process

Figure 5. The use of a FIB for a) milling and b) metal deposition

Figure 6. A cartoon representation of a surfactant molecule

Figure 7. Cartoon representation of the formation of a self-assembled monolayer (SAM) of alkanethiols on metal substrates showing a) physisorption of surfactants onto a substrate, b) the formation of islands of chemisorbed surfactants, c) full surface coverage of substrate by surfactants and d) the tilt of surfactants

Figure 8. Cartoon representation of the formation of silane SAMs on hydroxylated surfaces (where X = Cl or OR)

Figure 9. A cartoon depiction of post pattern processing of a chemically-patterned substrate by a) preferential adsorption, b) backfilling and c) preferential etching

Figure 10. AFM image of citrate-passivated Au nanoparticles preferentially adsorbed to binary SAMs patterned by e-beam irradiation

Figure 11. An outline of the microcontact printing process showing a) patterned stamp, b) inked stamp, c) the inked stamp is placed on the substrate and d) the stamp is removed leaving a patterned SAM on the substrate

Figure 12. Images showing both biological and materials science applications of microcontact printing applications: a) tethering of bacteria on a bioarray and b) controlled cell growth c) array of silica dots and d) controlled, patterned growth of carbon nanotubes (inset: cross section of a carbon nanotube)

Figure 13. An outline of the DPN process showing a) an AFM tip inked with surfactant molecules, b) the application of an inked tip to a substrate, the formation of dot structures, c) and d). e) represents a lateral force microscopy (LFM) image of a dot structure showing well ordered, densely packed surfactant molecules in the centre of the dot (dark areas) and surfactant molecules lying prone on the surface at the periphery of the dot (lighter areas) and the formation of line structures, f) and g)

CHAPTER 4: **Mass sensing using a chemically-modified microresonator: SAMs meets MEMS**

CHAPTER 5: Sticky SAMs for sperm arrays

CHAPTER 6: Formation of sub-micron fibres from aqueous PEO/Au nanoparticle composite solutions via electrospinning

ABBREVIATIONS

AET	Aminoethanethiol
AFM	Atomic Force Microscopy
APTMS	3-Aminopropyltrimethoxysilane
DDT	Dodecanethiol
DNA	Deoxyribonucleic acid
DPN	Dip Pen Nanolithography
DSC	Differential Scanning Calorimetry
EBSS	Earle's Balanced Salt Solution
EDX	Energy Dispersive X-ray analysis
FIB	Focused Ion Beam
LFM	Lateral Force Microscopy
MEMS	Microelectromechanical Systems
PDMS	Polydimethylsiloxane
PEO	Polyethylene oxide
PLL	Poly-l-lysine
RCA solution	Radio Corporation of America solution
RMS	Root Mean Square
SAMs	Self Assembled Monolayers
SEM	Scanning Electron Microscopy
STM	Scanning Tunnelling Microscopy
sµcp	Submerged Microcontact Printing

TEM	Transmission Electron Microscopy
UHQ	Ultra High Quality
UHV	Ultra High Vacuum
XPS	X-ray Photoelectron Spectroscopy
μcp	Microcontact Printing

CHAPTER 1

Nanotechnology: the appliance of nanoscience

CHAPTER 1

Nanotechnology: the appliance of nanoscience

The microcontact printing and DPN sections of **Chapter 1** has been published as part of a book chapter entitled *'Integrating nanolithography with nanoassembly using soft lithographic methods'* in the book entitled *'Bottom-up nanofabrication: Supramolecules, Self-Assemblies and Organized Films'* (2007) edited by K. Ariga and H. S. Nalwa[1] and has also been published as part of the review: Diegoli et al *Proc. IMechE.* **221** 589-629 (2007)[2]

ABSTRACT: *Nanotechnology is the commercialisation of nanoscience, which is the study of systems in the sub 100 nm size regime. Nanotechnology is already beginning to revolutionise many aspects of our daily lives and this chapter introduces some of the main drivers of nanotechnology and some of the approaches which have been investigated to achieve this goal. The fabrication of nanoscale structures and devices can be achieved using two different approaches, namely the top-down and bottom-up methodologies, which will be introduced in this chapter.*

1.1. What is nanotechnology?

Nanotechnology is the application and commercialisation of knowledge gleaned from nanoscientific research, which is the study of systems which have at least one dimension in the sub 100 nm regime. Nanoscience is highly interdisciplinary and represents the overlap of knowledge from many

(bio)scientific and engineering disciplines. In 1959 Richard Feynman delivered his famous speech, entitled 'There's plenty of room at the bottom',[3] in which he envisaged the entirety of the Encyclopaedia Britannica being written on a pin head using atomic manipulation. It is Feynman's speech that is widely regarded as providing the impetus and early insights into the possibility of nanoscale fabrication.

The potential importance of nanotechnology is massive and, as predicted by Merrill Lynch economist Norman Poire,[4] will impact our daily lives to the same extent as the motor car or personal computer, a prediction illustrated in **Figure 1**.
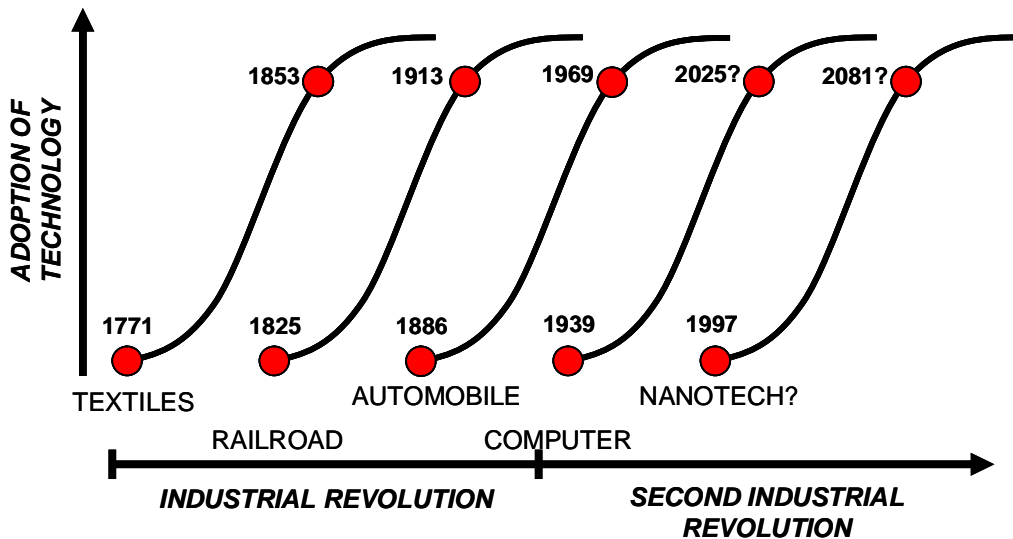
Figure 1. The predicted outlook for nanotechnology compared to other major technological evolutions by Norman Poire (Economist, Merrill Lynch)[5]

1.2. Driving forces of nanotechnology

1.2.1. Moore's Law

The introduction and widespread use of the personal computer has revolutionized modern day life. The constant requirements of computers to perform ever more complex operations demands computer chips with increasingly better performance. To date, the rate of increase of the processing power of computer chips has followed 'Moore's Law' which is named after Gordon Moore (a chemist) who, in 1965,[6] predicted the number of transistors present on a computer chip to double every 18 to 24 months. **Figure 2** shows that the rate of growth of the number of transistors per computer chip has indeed followed the trend described by Moore's Law up to the present day. However, in order for computer chips to continue to follow Moore's Law, transistors must be made smaller and smaller. Therefore, fabrication methodologies must continually improve in order to allow the manufacture of increasingly smaller transistors. This need for the continuation of Moore's Law is a huge driving force behind the development of both nanofabrication techniques and nanostructured materials. Currently the smallest transistors have a gate length of 45 nm[7] using Intel's 45 nm logic technology.
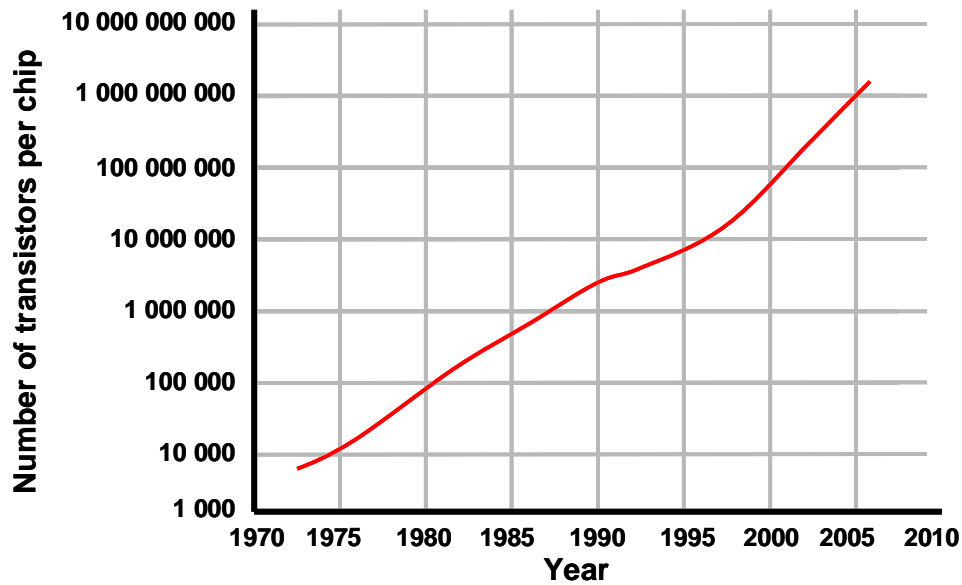
Figure 2. A graph depicting the number of transistors per computer chip increasing with a trend described by Moore's law (redrawn from[8])

1.2.2. Nanomedicine

Medical science is another area in which nanotechnology is being extensively researched. For example, it is hoped that nanotechnology may provide improved diagnostic techniques, such as bioarrays.[9] Bioarrays can be used for the detection of biological species, such as proteins, which will improve the early detection of diseases, such as cancers.[10] Drug delivery[11-13] is another area of medicine that may be revolutionised by nanotechnology. Gene therapy is one example of a site specific drug delivery method that is the subject of intense research and relies upon nanoparticulate carriers.[14, 15] It involves the delivery of genetic information to specific cells and transferring genetic information directly to the nucleus of cells. Research into the remote guidance of drugs to specific

5

sites in the body includes the use of magnetic fields to control a magnetic nanoparticle constituent of the drug delivery device.[16, 17]

1.2.3. Nanomaterials

The frontiers of materials science can be pushed forward by careful structural control on the nanoscale in a wide variety of ways. For example, the mechanical properties of materials can be tailored by control of atomic arrangement on the nanoscale. An example being that the reduction of the grain size of a given metal can result in the hardness of a material increasing.[18-20] Similarly, the nanostructuring of materials, for example, by the control of surface morphology, can allow the manipulation of, for example, the optical[21, 22] or wetting[23-25] properties of a material.

1.3. Fabrication on the nanoscale

Nanoscale fabrication processes can be divided into two distinct methodologies, these being 'top-down' and 'bottom-up' approaches. Top-down techniques involve the removal of material in order to form nanoscale architectures, whilst bottom-up approaches utilizing molecular and nanoscale 'building blocks' to build up nanostructures. Such nanoscale building blocks include particles[26, 27] and biological entities, such as DNA[28, 29] and proteins.[30]

This section introduces an example of both types of nanoscale approach by discussing

(i) Microelectromechanical systems (MEMS), and

(ii) Self-assembled monolayers (SAMs)

1.3.1. Top-down approaches

Top-down approaches, as mentioned above, are nanofabrication methods that involve the removal of material in order to form structures and devices. This section will introduce the field of microelectromechanical systems (MEMS) and two of the top-down fabrication techniques used in this field.

The field of microelectromechanical systems (MEMS) is concerned with the integration of mechanical components, in the micrometre regime, and microelectronic components with a view to the fabrication of functional devices on both the micron and sub-micron scale.[31] The main material used in MEMS is monocrystalline Si due to its excellent mechanical and conductive properties[32] and, hence, many fabrication techniques used in the microelectronic industry are exploited in the manufacture of MEMS devices.[33] The favourable properties of monocrystalline Si as a material for MEMS fabrication are that it is flexible with good fatigue strength. Thus, it can be used as a material for moving parts and can perform such tasks over many cycles without significant degradation, whilst its semiconductive properties allows it's use in integrated circuits.[34]

Much of the research into MEMS devices is directed towards the fabrication and integration of micron, and sub micron, scale functional devices[35-38], such as actuators and switches, and sensors[39-46], for both chemical and physical detection. **Figure 3** shows a MEMS clutch system and is an example of the complex MEMS devices that have been fabricated.
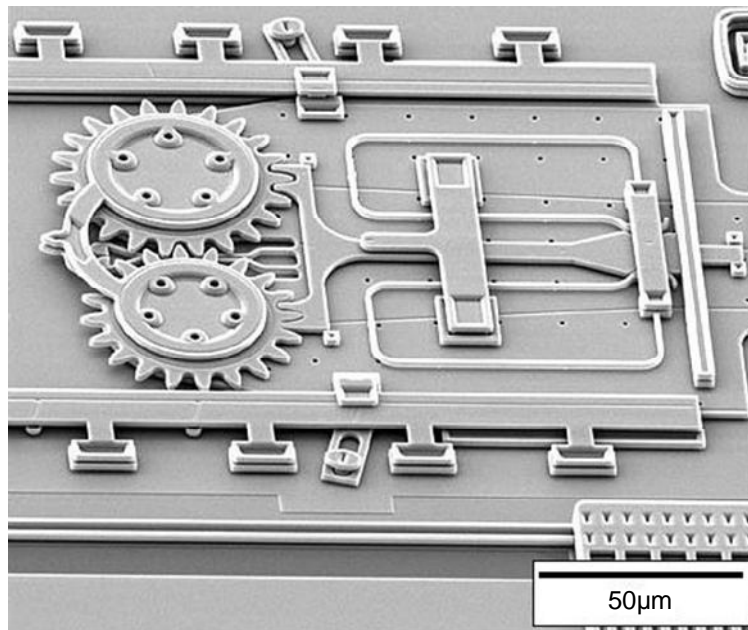
Figure 3. Example of a MEMS clutch system[47] (Scale bar added to [47])

MEMS devices are typically fabricated using 'top-down' processing techniques with two methods used to manufacture MEMS devices being photolithography and focused ion beam (FIB) milling.

1.3.1.1. Photolithography

Photolithography, as depicted in **Figure 4**, is a well-established fabrication technique in the microelectronics industry and is also used for the fabrication of MEMS devices.[48] This process involves the application of a photoresist to the substrate (**Figure 4a**). The photoresist is a radiation-sensitive polymer whose solubility changes upon exposure to the light source used in the photolithographic process.[49] In the presence of a photomask (**Figure 4b**) the resist-covered substrate is irradiated with light (**Figure 4c**). The resist can respond in one of two ways to the incident irradiation:

(i) Positive tone resist

In this case the resist becomes more soluble upon photo irradiation, *via* fragmentation, to an organic developer (**Figure 4e**) and is removed leaving the un-irradiated areas of resist on the substrate. Application of a Si etchant then etches the exposed Si from where the resist was removed (**Figure 4f**).

(ii) Negative tone resist

In this case the resist becomes less soluble upon photo irradiation, *via* cross linking, to an organic developer (**Figure 4g**) and is not removed. Instead

the un-irradiated areas of resist are removed by the developer and subsequent application of a Si etchant removes the exposed Si (**Figure 4h**).

a) Photoresist applied to substrate

b) Photomask placed in close proximity to resist

c) Substrate / photomask irradiated

d) Solubility of exposed resist changes

e) Areas of exposed resist removed by etching

g) Areas of unexposed resist removed by etching

f) Remaining resist removed

h) Remaining resist removed

POSITIVE RESIST

NEGATIVE RESIST
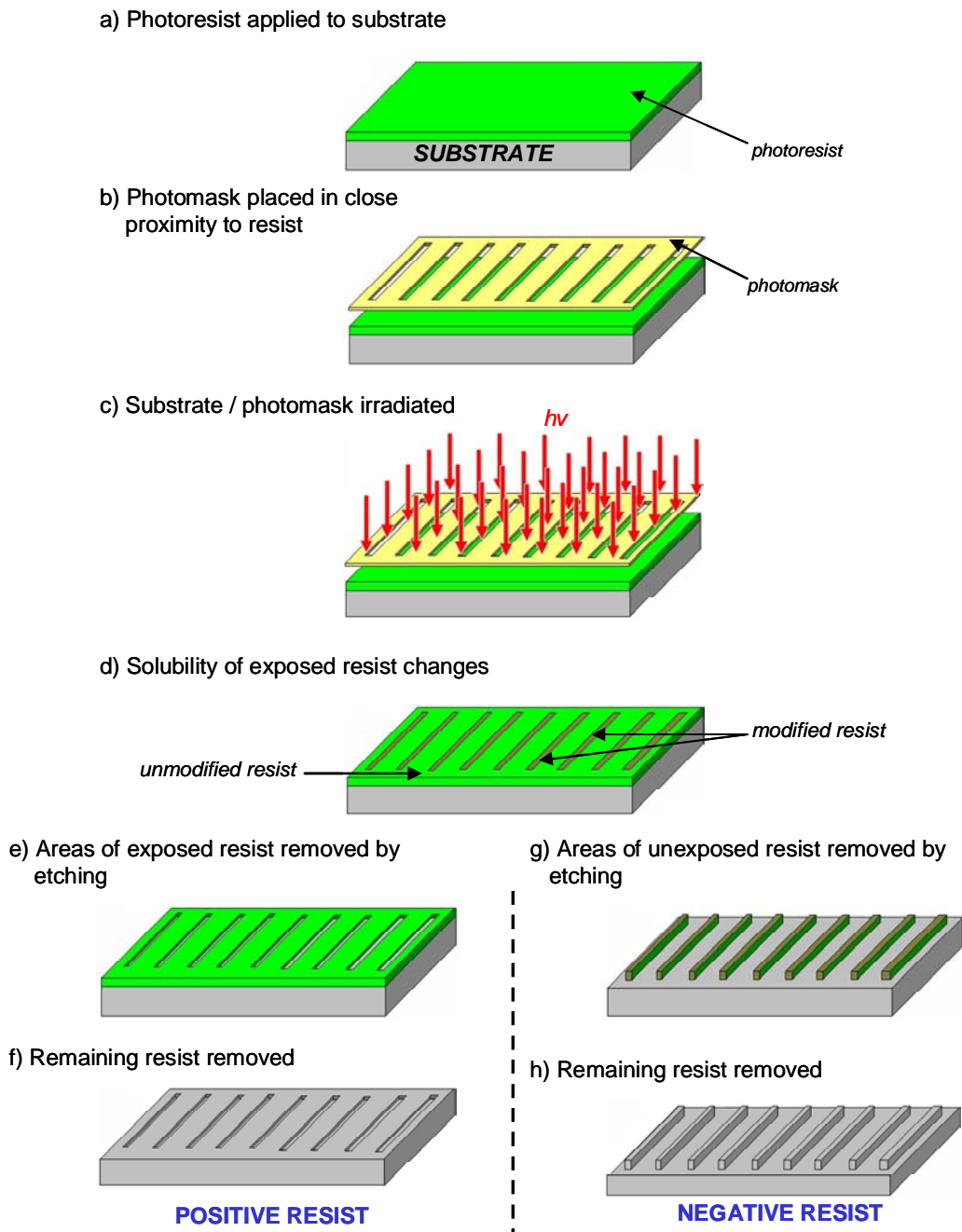
Figure 4. A schematic representation of a photolithography process

1.3.1.2. Focused Ion Beam (FIB)

Another fabrication technique used in MEMS is focused ion beam (FIB). The FIB uses a beam of Ga^+ ions, which is focused to less than 10 nm in diameter, which can be used for precision milling under UHV conditions (**Figure 5a**) to create features with lateral resolutions of the order of 10 nm.[50]
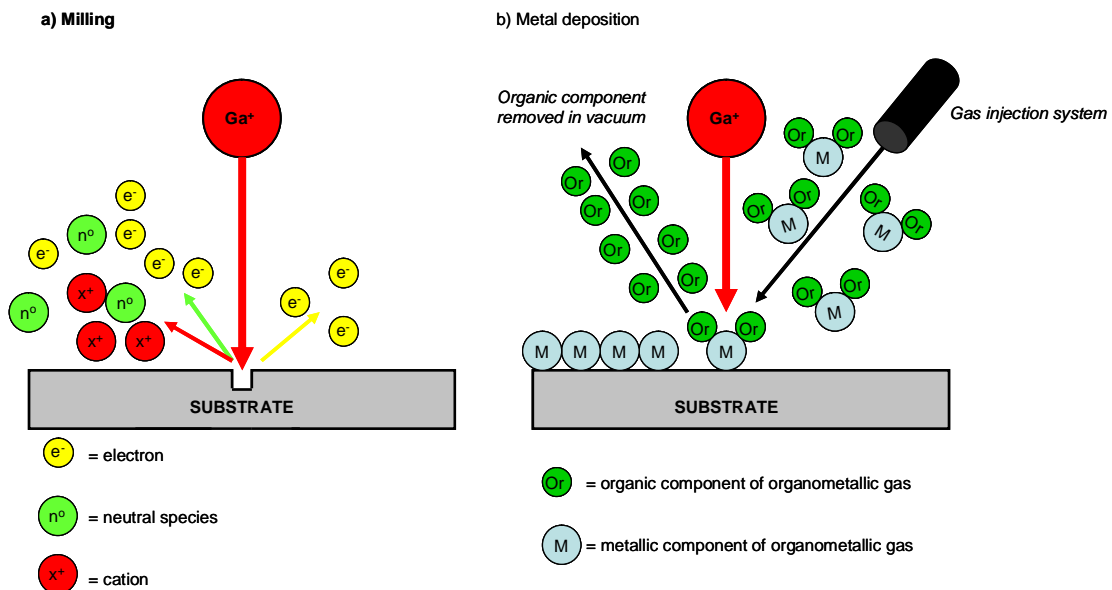
Figure 5. The use of a FIB for a) milling and b) metal deposition (figure redrawn from [51])

FIB can also be used for the deposition of metals (**Figure 5b**) and insulators by the injection of organometallic precursor molecules near the substrate surface to create features of the order of 10 nm in size.[52] The precursor molecules adsorb to the substrate and decompose upon exposure to the gallium ion beam. The decomposition of the precursor molecules results in the volatile fragments of the molecule being removed by the UHV, leaving the desired

species, which are the non-volatile fragments, on the surface of the substrate. The deposited material is not pure due to the presence of organic contaminants that are present as a result of residual carbonaceous material from the precursor molecules.[53] Ga^+ ions from the ion beam are also present in the deposited material.[53] Examples of species that are deposited using FIB include platinum, using (methylcyclopentadientyl)trimethyl platinum as the precursor molecule[54], and tungsten, the precursor molecule being $W(CO)_6$.[55] SiO_2 can also be deposited by the decomposition of 1,3,5,7-tetramethylcyclotetrasiloxane (TMCTS) in the presence of either O_2 or H_2O.[53]

1.3.2. Bottom up approaches

The bottom-up approach to nanofabrication involves the assembly of nanoscale 'building blocks', which include nanoparticles and individual molecules, to form nanostructures. Self-assembled monolayers (SAMs) represent an example of a bottom-up approach to the chemical functionalization of surfaces. This section will discuss the formation of SAMs on both metallic and Si surfaces and techniques used to create patterned SAMs will be introduced.

Self-assembled monolayers (SAMs) are ultra-thin, quasi-crystalline layers of surfactant molecules that form when surfactant molecules (**Figure 6**) spontaneously adsorb to the surface of a substrate. The first report in the literature for SAMs was by Bigelow *et al.* in 1946[56] when it was found that polar

organic molecules form monolayers on clean metal surfaces. However, it was not until 1983 when Nuzzo *et al.*[57] showed that monolayers of disulfides readily form on Au substrates, that research in this area of surface science gathered pace.

The head group of the surfactant molecules (**Figure 6**) must be of a specific chemical functionality to facilitate binding to the substrate. Such substrate, surfactant systems include surfactants with -SH head groups on metallic substrates, such as Au,[57-67] Ag,[59, 61, 68-71] and molecules with silane headgroups forming SAMs on SiO_2 surfaces.[62, 72-84]
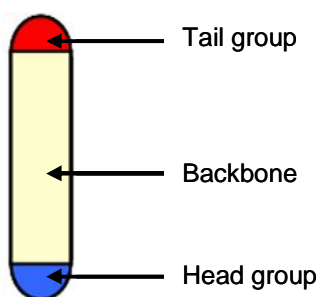
Figure 6. A cartoon representation of a surfactant molecule

The tail group of the adsorbed surfactants governs the chemical nature of the surface after the SAM is formed as it represents the chemical functionality that the surface presents to the surrounding environment. The fact that SAMs can be used to alter the chemistry of a surface represents a route to tailor the behaviour of surfaces. For example, a hydrophilic surface (e.g. silica) can be made to be hydrophobic upon the formation of a SAM that presents a hydrophobic surface (e.g. $-CH_3$ groups) to the surrounding environment. The backbone of the surfactant molecule can help to promote long range order of the

SAM *via* van der Waals interactions between adjacent surfactant molecules within the SAM.[85]

As previously mentioned SAMs can be formed from various surfactants on a range of substrates with two commonly utilised systems being surfactants with S containing head groups on metal substrates and alkyl silanes on hydroxylated surfaces. The mechanisms by which SAMs are formed on these different substrates are significantly different and therefore, will be discussed separately.

i) SAMs on metallic substrates

Surfactants possessing a S-based head group, for example thiol (R-SH) and disulfide (R-S-S-R) groups, readily form SAMs on Au[57-67], Ag[59, 61, 68-71] and other metal surfaces.[59, 61, 86-93] The driving force of the adsorption of the alkanethiols to Au surfaces is the formation of the highly stable (~167 kJ.mol^{-1} [62]) S-Au bond between the surfactant and the Au substrate.

The mechanism by which alkanethiolates form SAMs on Au is shown in **Figure 7**. The substrate is immersed in a solution of alkanethiolates which weakly physisorb onto the substrate[94] (**Figure 7a**) allowing the S-containing head group to chemisorb on the substrate surface forming the Au-S bond (represented by the molecules standing perpendicular to the surface in **Figure 7b**). As more alkanethiolate molecules adsorb on the surface, islands of surfactant molecules

14

form as a result of attractive intermolecular van der Waals forces[95] (**Figure 7b**). These surfactant islands continue to grow until the substrate surface is covered by a layer of surfactants of monomolecular thickness (**Figure 7c**). In order to minimise the free energy of the system, and to maximise intramolecular van der Waal forces, the surfactant molecules tilt at an angle which is commonly ~30 ° to the surface of the substrate[96] (**Figure 7d**).

The initial adsorption steps, both physisorption and chemisorption of the surfactants to the substrate occur relatively quickly, of the order of minutes.[64] Conversely, the ordering of the chains and reorientation of the chains, in order to maximise intermolecular van der Waals forces, can take several hours.[97] The chemistry of the backbone influences the rate of SAM formation[63] which is highlighted by the fact that alkanethiols with a long chain alkyl backbone form SAMs at a faster rate than those consisting of a shorter alkyl backbone.[98] This difference in the rate of SAM formation is due to the attractive van der Waals forces between adjacent molecules increasing as a function of chain length.[97]
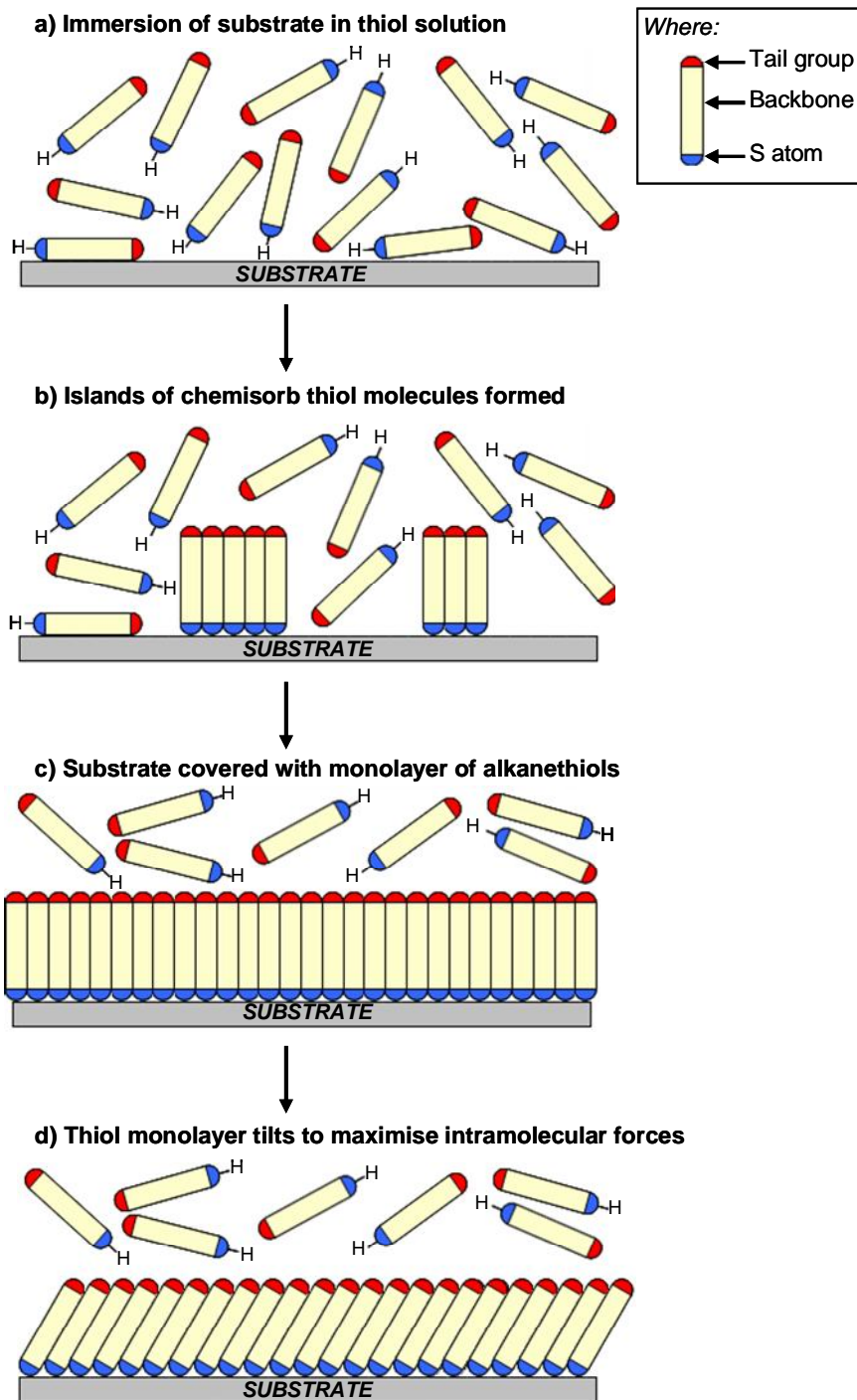
Figure 7. Cartoon representation of the formation of a self-assembled monolayer (SAM) of alkanethiols on metal substrates showing a) physisorption of surfactants onto a substrate, b) the formation of islands of chemisorbed surfactants, c) full surface coverage of substrate by surfactants and d) the tilt of surfactants

ii) SAMs formed on hydroxylated Si substrates

SAMs of organosilane derivatives, surfactants possessing -SiX$_3$ headgroups (where X = Cl or OR), can be formed on SiO$_2$ surfaces[62, 72-84] with the driving force being the formation of the Si-O covalent bond (~360 kJ.mol^{-1} [99]). Substrates such as glass and silica can be hydroxylated by wet chemical methods, such as immersion in piranha solution[100, 101] (7:3 solution of concentrated sulphuric acid and hydrogen peroxide) and an RCA solution[100] (1:1:5 solution of ammonium hydroxide, hydrogen peroxide and water), or dry methods, such as exposure of the substrate to UV light in the presence of an O$_3$ plasma.[102]

The mechanism of SAM formation from silane derivatives (**Figure 8**) proceeds when the surfactant molecules physisorb to the hydrophilic substrate in the presence of a physisorbed water layer[103], which is of the order of a few molecules thick (**Figure 8a**). This water layer provides a reaction medium for the hydrolysis of the headgroup (**Figure 8b**) which then covalently cross links to the exposed -OH groups on the surface *via* condensation reactions[104, 105] (**Figure 8c**). The headgroups of adjacent surfactant molecules can also cross-link, *via* condensation reactions, (**Figure 8c**) resulting in a highly stable monolayer.[105]

a) Surfactant molecules physisorb on the surface of the substrate
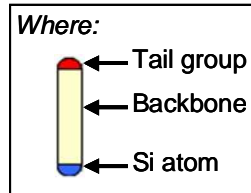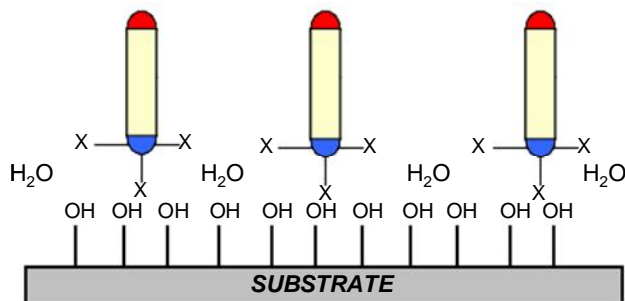
b) Reactive headgroups hydroxylated by physisorbed water molecules
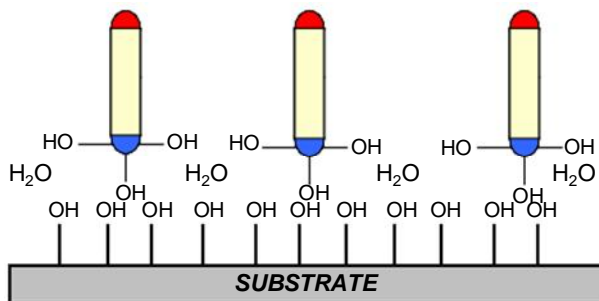
c) Hydroxylated headgroups chemisorb to substrate and crosslink via dehydration reactions
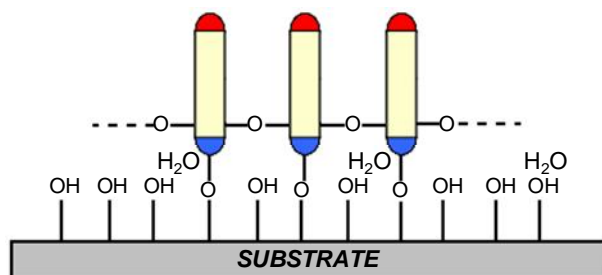
Figure 8. Cartoon representation of the formation of silane SAMs on hydroxylated surfaces (where X = Cl or OR)

One of the most important issues in producing high quality alkylsilane SAMs is the amount of water present in the system. It has been shown that the presence of some water is critical for SAM formation with the absence of water

18

resulting in incomplete monolayers.[106] However, if there is excess water in the system the silane groups of separate surfactant molecules have been shown to cross-link in solution, which leads to the formation of polysiloxane particles in solution, which then deposit on the surface.[107] Other factors such as temperature[83] and the concentration of the surfactant solution[108, 109] have been shown to influence the quality of the SAMs.

1.3.2.1. Patterned SAMs

Patterned SAMs can be employed as chemically selective templates on a substrate to allow further modification of the substrate at specific locations by several post-patterning processes (**Figure 9**). Such post-patterning techniques include the selective adsorption of particles,[27, 110] or other nanoscale 'building blocks' (**Figure 9a**),[111-113] backfilling with a second surfactant, which presents a different chemical functionality to that of the original patterned SAM (**Figure 9b**), or by selective etching of the exposed substrate[114-116] (**Figure 9c**).
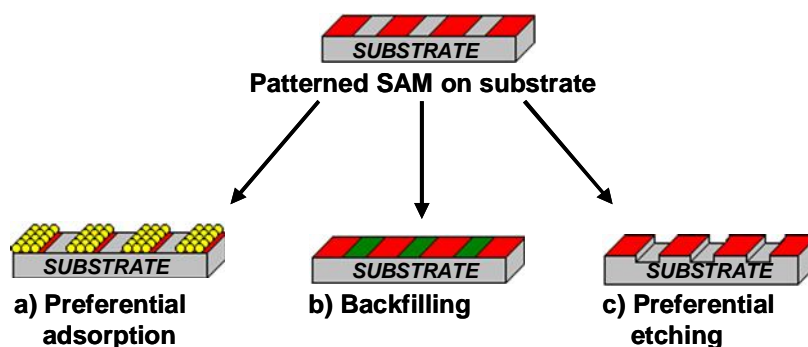
Figure 9. A cartoon depiction of post pattern processing of a chemically-patterned substrate by a) preferential adsorption, b) backfilling and c) preferential etching

This section will introduce the formation of patterned SAMs by i) energetic irradiation, ii) soft lithography and iii) mechanical methods.

i) Energetic irradiation

The exposure to energetic irradiation, such as UV irradiation, X-ray photons and electron beams, can induce specific chemical reaction[117, 118] or degradation of the SAM.[117, 119] For example, it has been shown that SAMs presenting nitro (-NO$_2$) groups, formed on either Au[118] or SiO$_2$[120, 121] surfaces, have had their terminal group converted to an amino (-NH$_2$) functionality upon irradiation of electrons[121] and X-rays.[120] Mendes *et al.*[121] utilised this conversion chemistry, termed 'precision chemical engineering',[119] by using e-beam irradiation to fabricate patterned areas of -NH$_2$ terminal groups on -NO$_2$ terminated SAMs in order to selectively adsorb Au nanoparticles to the surface as shown in **Figure 10**.
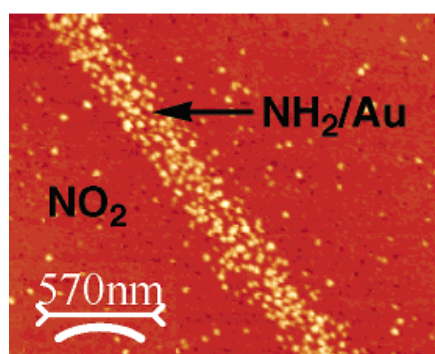
Figure 10. AFM image of citrate-passivated Au nanoparticles preferentially adsorbed to binary SAMs patterned by e-beam irradiation (image edited from[121])

Sun *et al.*[122-124] utilized scanning near field microscopy (SNOM), using light with a wavelength of 244 nm, to oxidise Au-S bonds in SAMs attached to Au surfaces. Areas of the SAM in which the Au-S bond was cleaved were then removed and feature sizes of 20 nm[124] have been achieved using this method, which is significantly less than the diffraction limit, that is limiting to the minimum feature size attainable using other, more conventional, optical patterning methods.

ii) Soft lithographies

As opposed to the modification of self-assembled monolayers with energetic irradiation, soft lithographies rely on diffusion of surfactants from a surfactant source to a substrate to form a chemical pattern. This section introduces two such soft lithographical techniques.

Microcontact printing (µcp)

Microcontact printing[125-128] utilizes an elastomeric stamp that is prepared by casting a pre-polymer against a patterned master, commonly prepared by conventional photolithographic techniques[129]. This pre-polymer is subsequently cured allowing it to be peeled from the master[130] as an elastomeric polymer with the 'negative' features of the master.

The stamp (**Figure 11a**) is then inked (**Figure 11b**) with a solution of a given surfactant and applied to a substrate of choice (**Figure 11c**). The surface of the inked stamp features deforms slightly to conform to the roughness of the substrate giving so-called 'conformal contact'.[131, 132] Whilst in conformal contact with the substrate the ink molecules diffuse from the stamp to the substrate. It has been shown that the inked stamp can be used for multiple printing runs without the need for re-inking.[133] After a given printing time the stamp is removed from the substrate resulting in a chemically patterned SAM on the substrate (**Figure 11d**).
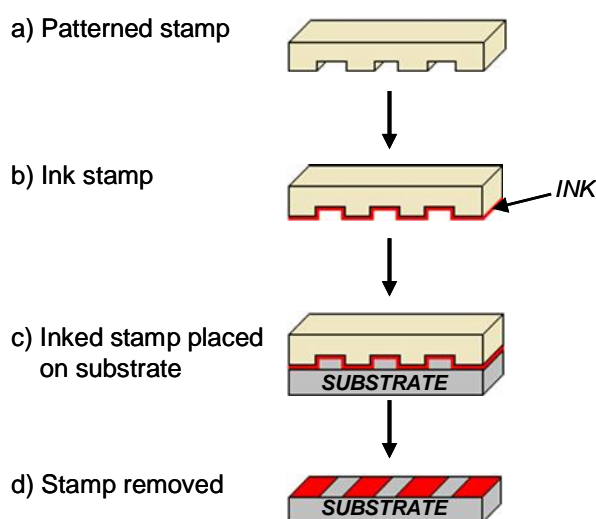
a) Patterned stamp

b) Ink stamp — *INK*

c) Inked stamp placed on substrate — *SUBSTRATE*

d) Stamp removed — *SUBSTRATE*

Figure 11. An outline of the microcontact printing process showing a) patterned stamp, b) inked stamp, c) the inked stamp is placed on the substrate and d) the stamp is removed leaving a patterned SAM on the substrate

Microcontact printing has been investigated for use in many applications. In the biological sciences, microcontact printing has been used for the formation of bioarrays[134-136] (**Figure 12a**) and the controlled patterning of cells[137-139]

(**Figure 12b**). In the field of materials science, arrays of silica dots[27] have been created (**Figure 12c**) which can be used for optical applications, whilst patterns of carbon nanotubes[140], that exhibit unique electrical properties, have been grown on templates defined by microcontact printing (**Figure 12d**).

**BIOLOGICAL
APPLICATIONS**
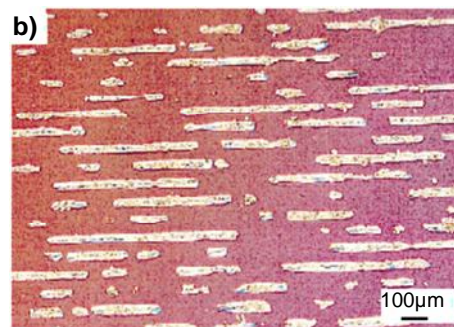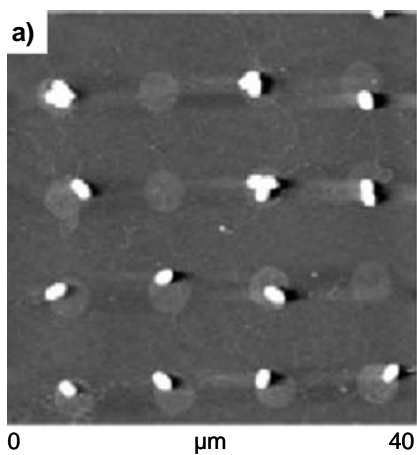
**MATERIALS SCIENCE
APPLICATIONS**
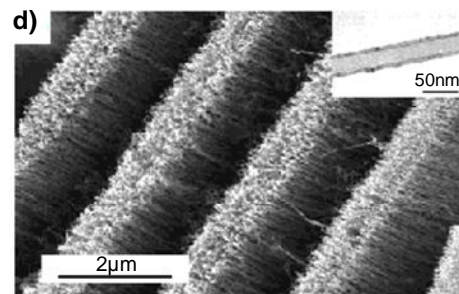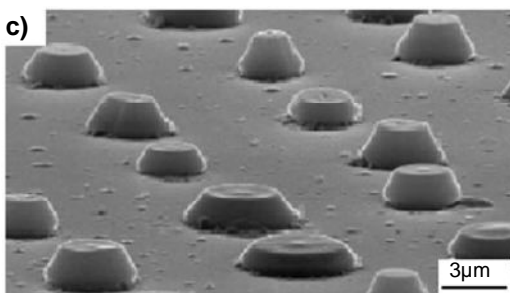
Figure 12. Images showing both biological and materials science applications of microcontact printing applications: a) tethering of bacteria on a bioarray [141] and b) controlled cell growth[142] c) array of silica dots[27, 143] and d) controlled, patterned growth of carbon nanotubes[140] (inset: cross section of a carbon nanotube)

A more in depth description of microcontact printing will be presented in **Chapter 5**.

Dip-Pen Nanolithography (DPN)

Dip-Pen Nanolithography (DPN)[144, 145] involves the inking of an AFM tip (**Figure 13a**), either by immersing the AFM cantilever in the ink or by bringing the AFM tip in contact with an inkpad impregnated with the desired ink. The inked AFM tip is then brought into contact with the substrate where, in most cases, a water meniscus spontaneously forms (**Figure 13b**) due to atmospheric water. The water meniscus presents a diffusion pathway from the tip to the substrate (**Figure 13c**). Upon contact with the substrate the AFM can either dwell on the surface before being removed, to form dots of ink on the substrate surface (**Figure 13d**), or scanned across the surface (**Figure 13f**) before being removed, to form line patterns of ink on the surface of the substrate (**Figure 13g**). The inked AFM tip is most commonly scanned across the substrate in contact mode[144], although there have been reports of the AFM tip being scanned in tapping mode[146] to form chemical patterns.
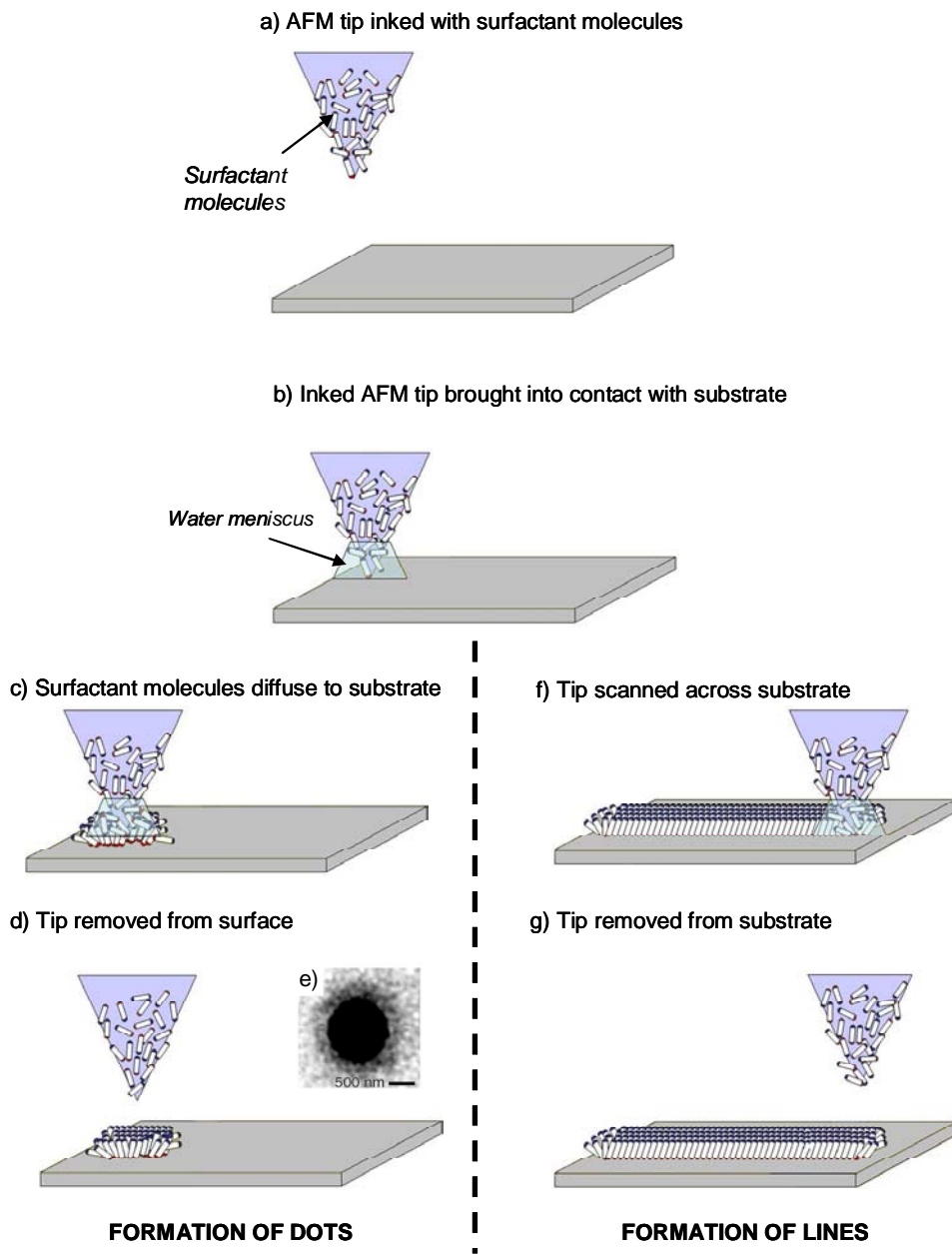
a) AFM tip inked with surfactant molecules

Surfactant molecules

b) Inked AFM tip brought into contact with substrate

Water meniscus

c) Surfactant molecules diffuse to substrate

f) Tip scanned across substrate

d) Tip removed from surface

e)

500 nm

g) Tip removed from substrate

FORMATION OF DOTS

FORMATION OF LINES

Figure 13. An outline of the DPN process showing a) an AFM tip inked with surfactant molecules, b) the application of an inked tip to a substrate, the formation of dot structures, c) and d). e) represents a lateral force microscopy (LFM) image of a dot structure showing well ordered, densely packed surfactant molecules in the centre of the dot (dark areas) and surfactant molecules lying prone on the surface at the periphery of the dot (lighter areas)[147] and the formation of line structures, f) and g)

The chemical pattern formed by DPN can then be developed by either etching or particle adsorption, while the exposed surface of the underlying substrate can be backfilled by immersion in a different surfactant to that of the pattern as shown in **Figure 9**. The use of a single AFM tip makes DPN an inherently serial technique, but arrays of AFM tips have been used to transform it into a highly parallel technique capable of producing nanostructures over areas on the square centimetre scale in a matter of minutes.[148]

DPN is a very versatile technique because not only can it be used to form complex chemical patterns on surfaces (**Figure 14a and b**) it can also be used to deposit material in precise locations, such as at specific points along a single strand of DNA[149] (**Figure 14c**). **Figure 14d** is an image of two electrodes connected by an indium wire deposited by using a DPN based technique called thermal DPN[150, 151] in which the AFM tip is heated in order to melt a solid 'ink' which wets the AFM tip. The AFM tip then deposits the indium at a desired location which solidifies upon cooling, thus using the AFM tip is used as a 'nano-soldering iron'.[151]

COMPLEX PATTERNS

310nm

a)

0   μm   15

b)

8μm

PRECISION DEPOSITION

c)

1.00
0.75
0.50
0.25
0

0   0.25   0.50   0.75   1.00
μm

d)

electrodes

indium oxide deposit

600nm
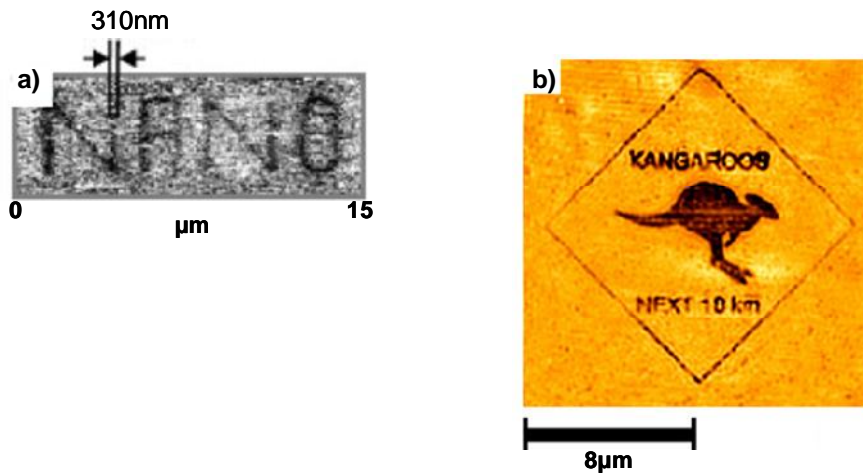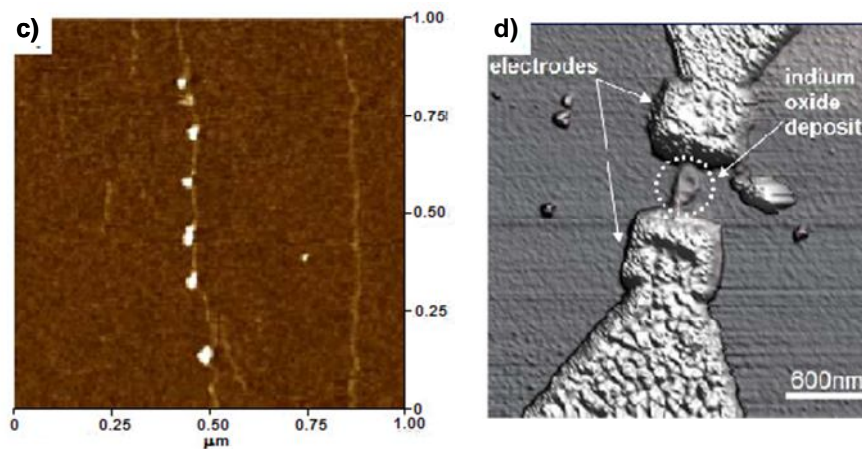
Figure 14. Images showing both the complex patterns which can be formed by DPN the precision deposition of material achievable DPN. The images are a) polypyrolle drawn on Si wafers,[152] b) a kangaroo drawn using MHA on Au,[153] c) dots of Cy3-antibody deposited on a stretched strand of DNA[149] and d) Two Au electrodes connected by indium oxide deposited by thermal DPN. [151]

iii) Mechanical methods

DPN is not the only instance where AFM tips can be used to create patterned SAMs. The AFM tip has been shown to alter SAMs using mechanical forces.[154] An example of such a technique is nanoshaving,[155, 156] in which shear forces, exerted by the AFM tip, displace the surfactant molecules from the SAM. Nanografting,[157, 158] another mechanical method of patterning SAMs, involves performing a nanoshaving operation in the presence of a solution containing secondary surfactants which functionalise the bare substrate exposed by the nanoshaving process.

1.4. Conclusions

This chapter has introduced some of the main drivers of nanotechnology and the two main approaches to nanoscale fabrication, namely the top down and bottom up approaches. Top down approaches are employed in this thesis in the form of FIB, to fabricate the microresonators used in **Chapter 4**, and photolithography, to fabricate the master used for the microcontact printing process in **Chapter 5**. Bottom up approaches are employed in the form of SAMs on both Si (**Chapters 3** and **4**) and Au (**Chapter 5**) surfaces for the attachment of nanoparticulate and biological species respectively. **Chapter 5** also employs microcontact printing to fabricate pattered SAMs on Au and glass for use as bioarrays.

1.5. References

1.   Hamlett, C. A. E.; Preece, J. A., Book chapter entitled 'Integrating nanolithography with nanoassembly using soft lithographic methods' published in Ariga, K.; Nalwa, H. S., (Eds) Bottom-up nanofabrication (Supramolecules, Self-   Assemblies and Organized Films), American Scientific Publishers, California   (2007)

2   Diegoli, S.; Hamlett, C. A. E.; Leigh, S. J.; Mendes, P. M.; Preece, J. A., Engineering nanostructures at surfaces using nanolithography. *J. Aerospace Eng.* **2007,** 221, 589-629

3.   Feynman R., There's plenty of room at the bottom. In California Institute of Technology (CALTECH), 1959.

4.   Milunovic S., Big prospects for nanotech. *Red Herring* May 2002.

5.   Davis M.; Walter M., Next-wave publishing technology: revolutions in process and content. *The Seybold Report* **2003,** 3, 3-15.

6.   Moore G. E., Cramming more components onto integrated circuits. *Electronics* **1965,** 38, 114-117.

7.   Press   release   from   Intel   website. *http://www.intel.com/pressroom/archive/releases/20060125comp.htm (Cited 20/02/2007)* **Jan 25th 2006**.

8.   Press   release   from   Intel   Website *http:www.intel.com/technology/mooreslaw/index.htm.* (Cited 01/02/2007).

9.   Christensen C. B. V., Arrays on biological and chemical analysis. *Talanta* **2002,** 56, 289-299.

10.   Rosi N. L.; Mirkin C. A., Nanostructures in biodiagnostics. *Chem. Rev.* **2005,** 105, 1547-1562.

11.   Sahoo S. K.; Labhasetwar V., Nanotech approaches to drug delivery and imaging. *Drug Discov. Today.* **2003,** 8, 1112-1120.

12.   Orive G.; Hernández R. M.; Gascón A. R.; Dominguez-Gil A.; Pedraz J. L., Drug delivery in biotechnology: present and future. *Curr. Opin. Biotech.* **2003,** 14, 659-664.

13.   Shawgo R. S.; Richards Grayson A. C.; Li Y.; Cima M. J., BioMEMS for drug delivery. *Curr. Opin. Solid State Mater. Sci.* **2002,** 6, 329-334.

14. Read M. L.; Singh S.; Ahmed Z.; Stevenson M.; Briggs S. S.; Oupicky D.; Barrett L. B.; Spice R.; Kendall M.; Berry M.; Preece J. A.; Logan A.; Seymour L. W., A versatile reducible polycation-based system for efficient delivery of a broad range of nucleic acids. *Nucleic Acids Res.* **2005,** 33, e86 (16pp).

15. Carlisle R. C.; Etrych T.; Briggs S. S.; Preece J. A.; Ulbrich K.; Seymour L. W., Polymer-coated polyethyleneimine/DNA complexes designed for triggered activation by intracellular reduction. *J. Gen. Med.* **2004,** 6, 337-344.

16. Caruthers S. D.; Wickline S. A.; Lanza G. M., Nanotechnological applications in medicine. *Curr. Opin. Biotech.* **2007,** 18, 26-30.

17. Jurgons R.; Seliger C.; Hilpert A.; Trahms L.; Odenbach S.; Alexiou C., Drug loaded magnetic nanoparticles for cancer therapy. *J. Phys. - Condens. Mat.* **2006,** 18, S2893-S2902.

18. Jia K.; Fischer T. E.; Gallois B., Microstructure, hardness and toughness of nanostructured and coventional WC-Co composites. *Nanostruct. Mater.* **1998,** 10, 875-891.

19. Sherman D.; Brandon D., Mechanical properties of hard materials and their relation to microstructure. *Adv. Eng. Mater.* **1999,** 1, 161-181.

20. Zhang S.; Sun D.; Fu Y.; Du H., Toughening of hard nanostructural thin films: a critical review. *Surf. Coat. Tech.* **2005,** 198, 2-8.

21. Sánchez-Iglesias A.; Pastoriza-Santos I.; Pérez-Juste J.; Rodríguez-González B.; Garcia de Abajo F. J.; Liz-Marzán L. M., Synthesis and optical properties of gold nanodecahedra with size control. *Adv. Mater.* **2006,** 18, 2529-2534.

22. Torrison L.; Tolle J.; Smith D. S.; Poweleit C.; Menendez J.; Kouvetakis J., Morphological and optical properties of Si nanostructures imbedded in SiO_2 and Si_3N_4 films grown by single source chemical vapor deposition. *J. Appl. Phys.* **2002,** 92, 7475-7480.

23. Shang H. M.; Wang Y.; Takahashi K.; Cao G. Z.; Li D.; Xia Y. N., Nanostructured superhydrophobic surfaces. *J. Mater. Sci.* **2005,** 40, 3587-3591.

24. Cao L. L.; Hu H. H.; Gao D., Design and fabrication of micro-textures for inducing a superhydrophobic behavior on hydrophilic materials. *Langmuir* **2007,** 23, 4310-4314.

25. Nosonovsky M., Multiscale roughness and stability of superhydrophobic biomimetic interfaces. *Langmuir* **2007,** 23, 3157-3161.

26. Geissler M.; Wolf H.; Stutz R.; Delamarche E.; Grummt U.-W.; Michel B.; Bietsch A., Fabrication of metal nanowires using microcontact printing. *Langmuir* **2003,** 19, 6301-6311.

27. Khalil A. S. G.; Konjhodzic D.; Marlow F., Hierarchy selection, position control, and orientation of growing mesostructures by patterned surfaces. *Adv. Mater.* **2006,** 18, 1055-1058.

28. Xu C.; Taylor P.; Ersoz M.; Fletcher P. D. I.; Paunov V. N., Microcontact printing of DNA-surfactant arrays on solid substrates. *J. Mater. Chem.* **2003,** 13, 3044-3048.

29. Zhang G.; Yan X.; Hou X.; Lu G.; Yang B.; Wu L.; Shen J., Binary DNA arrays on heterogeneous patterned surfaces. *Langmuir* **2003,** 19, 9850-9854.

30. Zhou D.; Bruckbaur A.; Ying L.; Abell C.; Klenerman D., Building three-dimensional surface biological assemblies on the nanometer scale. *Nano. Lett.* **2003,** 3, 1517-1520.

31. Maboudian R., Surface processes in MEMS technology. *Surf. Sci. Rep.* **1998,** 30, 207-269.

32. Lang W., Silicon microstructuring technology. *Mater. Sci. Tech.* **1996,** R17, 1-55.

33. Romig Jr A. D.; Dugger M. T.; McWhorter P. J., Materials issues in microelectromechanical devices: science, engineering, manufacturability and reiability. *Acta Mater.* **2003,** 51, 5837-5866.

34. ISSYS Integrated Sensing Systems website. *http://www.mems-issys.com/html/durability.html (Cited 05/03/07)*

35. Akiyama T.; Collard D.; Fujita H., Scratch drive actuator with mechanical links for self-assembly of three-dimensional MEMS. *Journal of Microelectromechanical Systems* **1997,** 6, 10-17.

36. Saif M. T. A., On a tunable bistable MEMS - Theory and experiment. *J. Microelectromech. S.* **2000,** 9, 157-170.

37. Sallese J. M.; Bouvet D., Principles of space-charge based bi-stable MEMS: The junction-MEMS. *Sensor. Actuat. A-Phys* **2007,** 133, 173-179.

38. Zhang Y. H.; Ding G. F.; Shun X. F.; Gu D. H.; Cai B. C.; Lai Z. S., Preparing of a high speed bistable electromagnetic RF MEMS switch. *Sensor. Actuat. A-Phys* **2007,** 134, 532-537.

39. Choi N. J.; Lee Y. S.; Kwak J. H.; Park J. S.; Park K. B.; Shin K. S.; Park H. D.; Kim J. C.; Huh J. S.; Lee D. D., Chemical warfare agent sensor using MEMS structure and thick film fabrication method. *Sensor. Actuat. B-Chem.* **2005,** 108, 177-183.

40. Gong J. W.; Chen Q. F.; Fei W. F.; Seal S., Micromachined nanocrystalline SnO_2 chemical gas sensors for electronic nose. *Sensor. Actuat. B-Chem.* **2004,** 102, 117-125.

41. Lavrik N. V.; Sepaniak M. J.; Datskos P. G., Cantilever transducers as a platform for chemical and biological sensors. *Rev. Sci. Instrum.* **2004,** 75, 2229-2253.

42. Meier D. C.; Taylor C. J.; Cavicchi R. E.; White V. E.; Ellzy M. W.; Sumpter K. B.; Semancik S., Chemical warfare agent detection using MEMS-compatible microsensor arrays. *IEEE Sens. J.* **2005,** 5, 712-725.

43. Mlsna T. E.; Cemalovic S.; Warburton M.; Hobson S. T.; Mlsna D. A.; Patel S. V., Chemicapacitive microsensors for chemical warfare agent and toxic industrial chemical detection. *Sensor. Actuat. B-Chem.* **2006,** 116, 192-201.

44. Varadan V. K.; Varadan V. V., Microsensors, microelectromechanical systems (MEMS), and electronics for smart structures and systems. *Smart Mater. Struct.* **2000,** 9, 953-972.

45. Zee F.; Judy J. W., Micromachined polymer-based chemical gas sensor array. *Sensor. Actuat. B-Chem.* **2001,** 72, 120-128.

46. Zhou W.; Khaliq A.; Tang Y. J.; Ji H. F.; Selmic R. R., Simulation and design of piezoelectric microcantilever chemical sensors. *Sensor. Actuat. A-Phys* **2005,** 125, 69-75.

47. http://www.memx.com/image_gallery.htm (Cited 11/07/07).

48. Hierlemann A.; Brand O.; Hagleitner C.; Baltes H., Microfabrication techniques for chemical/biosensors. *P. IEEE* **2003,** 91, 839-863.

49. Wallraff G. M.; Hinsberg W. D., Lithographic imaging techniques for the formation of nanoscopic features. *Chem. Rev.* **1999,** 99, 1801-1821.

50. Tseng A. A., Recent developments in micromilling using focused ion beam technology. *J. Micromech. Microeng.* **2004,** 14, R15-R34.

51. http://www.fibics.com/FIBBasics.html (Cited 21/7/07).

52. Morita M.; Kometani R.; Watanabe K.; Kanda K.; Haruyama Y.; Hoshino T.; Kondo K.; Kaito T.; Ichihashi T.; Fujita J.; Ishida.; Ochiai Y.; Tajima T.;

Matsui S., Free-space-wiring fabrication in nano-space by focused-ion-beam chemical vapor deposition. *J. Vac. Sci. Technol. B* **2003,** 21, 2737-2741.

53.   Puers R.; Reyntjens S., Fabrication and testing of custom vacuum encapsulations deposited by focused ion beam direct-write CVD. *Sensor. Actuat. A-Phys* **2001,** 92, 249-256.

54.   Smith S.; Walton A. J.; Bond S.; Ross A. W. S.; Stevenson J. T. M.; Gundlach A. M., Electrical characterization of platinum deposited by focused ion beam. *IEEE Trans. Semiconduct. M.* **2003,** 16, 199-206.

55.   Reyntjens S.; Puers R., A review of focused ion beam applications in microsystem technology. *J. Micromech. Microeng.* **2001,** 11, 287-300.

56.   Bigelow W. C.; Pickett D. L.; Zisman W. A., Oleophobic monolayers .1. Films adsorbed from solution in non-polar liquids. *J. Coll. Sci.* **1946,** 1, 513-538.

57.   Nuzzo R. G.; Allara D. L., Adsorption of bifunctional organic disulfides on gold surfaces. *J. Am. Chem. Soc.* **1983,** 105, 4481-4483.

58.   Prime K. L.; Whitesides G. M., Self-assembled organic monolayers - Model systems for studying adsorption of proteins at surfaces. *Science* **1991,** 252, 1164-1167.

59.   Laibinis P. E.; D., B. C.; Whitesides G. M., Attenuation of photoelectrons in monolayers of normal-alkanethiols adsorbed on copper, silver, and gold. *J. Phys. Chem.* **1991,** 95, 7017-7021.

60.   Laibinis P. E.; Nuzzo R. G.; Whitesides G. M., Structure of monolayers formed by coadsorption of 2 normal-alkanethiols of different chain lengths on gold and Its relation to wetting. *J. Phys. Chem.* **1992,** 96, 5097-5105.

61.   Laibinis P. E.; Whitesides G. M., Omega-terminated alkanethiolate monolayers on surfaces of copper, silver, and gold have similar wettabilities. *J. Am. Chem. Soc.* **1992,** 114, 1990-1995.

62.   Ulman A., Formation and structure of self-assembled monolayers. *Chem. Rev.* **1996**, 1533-1554.

63.   Schreiber F., Structure and growth of self-assembling monolayers. *Prog. Surf. Sci.* **2000,** 65, 151-256.

64.   Love J. C.; Estroff L. A.; Kriebel J. K.; Nuzzo R. G.; Whitesides G. M., Self-assembled monolayers of thiolates on metals as a form of nanotechnology. *Chem. Rev.* **2005,** 105, 1103-1169.

65. Holzl M.; Tinazli A.; Leitner C.; Hahn C. D.; Lackner B.; Tampe R.; Gruber H. J., Protein-resistant self-assembled monolayers on gold with latent aldehyde functions. *Langmuir* **2007,** 23, 5571-5577.

66. Laredo T.; Leitch J.; Chen M. H.; Burgess I. J.; Dutcher J. R.; Lipkowski J., Measurement of the charge number per adsorbed molecule and packing densities of self-assembled long-chain monolayers of thiols. *Langmuir* **2007,** 23, 6205-6211.

67. Zhang S.; Chandra K. L.; Gorman C. B., Self-assembled monolayers of terminal alkynes on gold. *J. Am. Chem. Soc.* **2007,** 129, 4876-4877.

68. Schoenfisch M. H.; Pemberton J. E., Air stability of alkanethiol self-assembled monolayers on silver and gold surfaces. *J. Am. Chem. Soc.* **1998,** 120, 4502-4513.

69. Hung M. C.; Wu K. Y.; Tao Y. T.; Huang H. W., Highly efficient top-emitting organic light-emitting diodes with self-assembed monolayer-modified Ag as anodes. *Appl. Phys. Lett.* **2006,** 89, 203106 (3pp).

70. Wang Y. H.; Song W.; Jie Z.; Ning G.; Wesche K. D., Preparation and study of complex self-assembled film as a super-thin barrier on silver. *Appl. Surf. Sci.* **2006,** 252, 8264-8269.

71. Weiss E. A.; Chiechi R. C.; Kaufman G. K.; Kriebel J. K.; Li Z. F.; Duati M.; Rampi M. A.; Whitesides G. M., Influence of defects on the electrical characteristics of mercury-drop junctions: Self-assembled monolayers of n-alkanethiolates on rough and smooth silver. *J. Am. Chem. Soc.* **2007,** 129, 4336-4349.

72. Stevens M. J., Thoughts on the structure of alkylsilane monolayers. *Langmuir* **1999,** 15, 2773-2778.

73. Vallant T.; Kattner J.; Brunner H.; Mayer U.; Hoffmann H., Investigation of the formation and structure of self-assembled alkylsiloxane monolayers on silicon using in situ attenuated total reflection infrared spectroscopy. *Langmuir* **1999,** 15, 5339-5346.

74. Hooper A. E.; Werho D.; Hopson T.; Palmer O., Evaluation of amine- and amide-terminated self-assembled monolayers as 'Molecular glues' for Au and SiO_2 substrates. *Surf. Interface Anal.* **2001,** 31, 809-814.

75. Hozumi A.; Sugimura H.; Yokogawa Y.; Kameyama T.; Takai O., Zeta-potentials of planar silicon plates covered with alkyl- and fluoroalkylsilane self-assembled monolayers. *Colloid. Surface. A* **2001,** 182, 257-261.

76. Sugimura H.; Hozumi A.; Kameyama T.; Takai O., Organosilane self-assembled monolayers formed at the vapour/solid interface. *Surf. Interface Anal.* **2002,** 34, 550-554.

77. Qian L. M.; Tian F.; Xiao X. D., Tribological properties of self-assembled monolayers and their substrates under various humid environments. *Tribol. Lett.* **2003,** 15, 169-176.

78. Rozlosnik N.; Gerstenberg M. C.; Larsen N. B., Effect of solvents and concentration on the formation of a self-assembled monolayer of octadecylsiloxane on silicon (001). *Langmuir* **2003,** 19, 1182-1188.

79. Wang Y. L.; Lieberman M., Growth of ultrasmooth octadecyltrichlorosilane self-assembled monolayers on SiO_2. *Langmuir* **2003,** 19, 1159-1167.

80. Duwez A. S., Exploiting electron spectroscopies to probe the structure and organization of self-assembled monolayers: a review. *J. Electron. Spectrosc.* **2004,** 134, 97-138.

81. Onclin S.; Ravoo B. J.; Reinhoudt D. N., Engineering silicon oxide surfaces using self-assembled monolayers. *Angew. Chem. Int. Ed.* **2005,** 44, 6282-6304.

82. Toworfe G. K.; Composto R. J.; Shapiro I. M.; Ducheyne P., Nucleation and growth of calcium phosphate on amine-, carboxyl- and hydroxyl-silane self-assembled monolayers. *Biomaterials* **2006,** 27, 631-642.

83. Barriga J.; Coto B.; Fernandez B., Molecular dynamics study of optimal packing structure of OTS self-assembled monolayers on SiO_2 surfaces. *Tribol. Int.* **2007,** 40, 960-966.

84. Kumaki D.; Ando S.; Shimono S.; Yamashita Y.; Umeda T.; Tokito S., Significant improvement of electron mobility in organic thin-film transistors based on thiazolothiazole derivative by employing self-assembled monolayer. *Appl. Phys. Lett.* **2007,** 90, 053506 (3pp).

85. Bareman J. P.; Klein M. L., Collective tilt behaviour in dense, substrate-supported monolayers of long-chain molecules: A molecular dynamics study. *J. Phys. Chem.* **1990,** 94, 5202-5205.

86. Laibinis P. E.; Whitesides G. M., Self-assembled monolayers of n-alkanethiolates on copper are barrier films that protect the metal against oxidation by air. *J. Am. Chem. Soc.* **1992,** 114, 9022-9028.

87. Lee S.; Park J.; Ragan R.; Kim S.; Lee Z.; Lim D. K.; Ohlberg D. A. A.; Williams R. S., Self-assembled monolayers on Pt(111): Molecular packing structure and strain effects observed by scanning tunneling microscopy. *J. Am. Chem. Soc.* **2006,** 128, 5745-5750.

88. Li D. G.; Yu X. J.; Dong Y. H., The different self-assembled way of n- and t-dodecyl mercaptan on the surface of copper. *Appl. Surf. Sci.* **2007,** 253, 4182-4187.

89. Liakos I. L.; Newman R. C.; McAlpine E.; Alexander M. R., Study of the resistance of SAMs on aluminium to acidic and basic solutions using dynamic contact angle measurement. *Langmuir* **2007,** 23, 995-999.

90. Stapleton J. J.; Daniel T. A.; Uppili S.; Cabarcos O. M.; Naciri J.; Shashidhar R.; Allara D. L., Self-assembly, characterization, and chemical stability of isocyanide-bound molecular wire monolayers on gold and palladium surfaces. *Langmuir* **2005,** 21, 11061-11070.

91. Tambe N. S.; Bhushan B., Nanotribological characterization of self-assembled monolayers deposited on silicon and aluminium substrates. *Nanotechnology* **2005,** 16, 1549-1558.

92. Tan Y. S.; Srinivasan M.; Pehkonen S. O.; Chooi S. Y. M., Effects of ring substituents on the protective properties of self-assembled benzenethiols on copper. *Corros. Sci.* **2006,** 48, 840-862.

93. Williams J. A.; Gorman C. B., Scanning tunneling microscopy-based replacement lithography on self-assembled monolayers: Comparison of gold, palladium, and platinum substrates. *Langmuir* **2007,** 23, 3103-3105.

94. Xu S.; Cruchon-Dupeyrat, S. J. N.; Garno J. C.; Liu G. Y.; Jenning G. K.; Yong T.-H.; Laibinis P. E., In situ studies of thiol self-assembly on gold from solution using atomic force microscopy. *J. Chem. Phys.* **1998,** 108, 5002-5012.

95. Barrena E.; Ocal C.; Salmeron M., Evolution of the structure and mechanical stability of self-assembled alkanethiol islands on Au(111) due to diffusion and ripening. *J. Chem. Phys.* **1999,** 111, 9797-9802.

96. Nuzzo R. G.; Dubois L. H.; Allara D. L., Fundamental studies of microscopic wetting on organic surfaces. 1. Formation and structural characterization of a self-consistent series of polyfunctional organic monolayers. *J. Am. Chem. Soc.* **1990,** 112, 558-569.

97. Ulman A., *An Introduction to Ultrathin Organic Films from Langmuir-Blodgett to Self-Assembly*. Adademic Press Limited: London, 1991.

98. Bain C. D.; Troughton E. B.; Tao Y. T.; Evall J.; Whitesides G. M.; Nuzzo R. G., Formation of monolayer films by the spontaneous assembly of organic thiols from solution onto gold. *J. Am. Chem. Soc.* **1989,** 111, 321-335.

99. Dabrowski J.; Müssig H.-J., *Silicon surface and formation of interfaces*. London, 2000.

100. Kern W., *Handbook of semiconductor wafer cleaning technology*. Noyes Publications: New Jersey, 1993.

101. Petitdidier S.; Bertagna V.; Rochat N.; Rouchon D.; Besson P.; Erre R.; Chemla M., Growth mechanism and characterization of chemical oxide films produced in peroxide mixtures on Si(100) surfaces. *Thin Solid Films* **2005,** 476, 51-58.

102. Choi K.; Eom T.-C.; Lee C., Comparison of the removal efficiency for organic contaminants on silicon wafers stored in plastic boxes between UV/O_3 and ECR oxygen plasma cleaning methods. *Thin Solid Films* **2003,** 435, 227-231.

103. Sagiv J., Organized monolayers by adsorption. 1. Formation and structure of olephobic monolayers on solid surfaces. *J. Am. Chem. Soc.* **1980,** 102, 92-98.

104. Wasserman S. R.; Tao Y. T.; Whitesides G. M., Structure and reactivity of alkylsiloxane monolayers formed by reaction of alkyltrichlorosilanes on silicon substrates. *Langmuir* **1989,** 5, 1074-1087.

105. Aswal D. K.; Lenfant S.; Guerin D.; Yakhmi J. V.; Vuillaume D., Self assembled monolayers on silicon for molecular electronics. *Anal. Chim. Acta* **2006,** 568, 84-108.

106. Le Grange J. D.; Markham J. L.; Kurkjian C. R., Effects of surface hydration on the deposition of silane monolayers on silica. *Langmuir* **1993,** 9, 1749-1753.

107. Bunker B. C.; Carpick R. W.; Assink R. A.; Thomas M. L.; Hankins M. G.; Voigt J. A.; Sipola D.; de Boer M. P.; Gulley G. L., The impact of solution agglomeration on the deposition of self-assembled monolayers. *Langmuir* **2000**, 7742-7751.

108. Kulkarni S. A.; Mirji S. A.; Mandale A. B.; Gupta R. P.; Vijayamohanan K. P., Growth kinetics and thermodynamic stability of octadecyltrichlorosilane self-assembled monolayer on Si (100) substrate. *Mater. Lett.* **2005,** 59, 3890-3895.

109. Lee B. H.; Sung M. M., Effect of island size on the packing density in the early stages of alkylsilane-based monolayer self assembly. *B. Kor. Chem. Soc.* **2005,** 26, 127-130.

110. Geissler, M.; Wolf, H.; Stutz, R.; Delamarche, E.; Grummt, U. W.; Michel, B.; Bietsch, A., Fabrication of metal nanowires using microcontact printing. *Langmuir* **2003,** 19, 6301-6311.

111. Xu C.; Taylor P.; Ersoz M.; Fletcher P. D. I.; Paunov V. N., Microcontact printing of DNA-surfactant arrays on solid substrates. *J. Mater. Chem.* **2003,** 13, 3044-3048.

112. Zhang G.; Yan X.; Hou X. L.; Lu G.; Yang B.; Wu L. X.; Shen J. C., Binary DNA arrays on heterogeneous patterned surfaces. *Langmuir* **2003,** 19, 9850-9854.

113. Zhou D.; Bruckbauer A.; Ying L. M.; Abell C.; Klenerman D., Building three-dimensional surface biological assemblies on the nanometer scale. *Nano. Lett.* **2003,** 3, 1517-1520.

114. Kumar A.; Whitesides G. M., Features of gold having micrometer to centimeter dimensions can be formed through a combination of stamping with an elastomeric stamp and an alkanethiol ink followed by chemical etching. *Appl. Phys. Lett.* **1993,** 63, 2002-2004.

115. Xia Y. N.; Zhao X. M.; Kim E.; Whitesides G. M., A selective etching solution for use with patterned self-assembled monolayers of alkanethiolates on gold. *Chem. Mater.* **1995,** 7, 2332-2337.

116. Xia Y. N.; Tien J.; Qin D.; Whitesides G. M., Non-photolithographic methods for fabrication of elastomeric stamps for use in microcontact printing. *Langmuir* **1996,** 12, 4033-4038.

117. Zharnikov M.; Grunze M., Modification of thiol-derived self-assembling monolayers by electron and x-ray irradiation: Scientific and lithographic aspects. *J. Vac. Sci. Technol. B* **2002,** 20, 1793-1807.

118. Eck W.; Stadler V.; Geyer W.; Zharnikov M.; Gölzhäuser A.; Grunze M., Generation of surface amino groups on aromatic self-assembled monolayers by low energy electron beams - A first step towards chemical lithography. *Adv. Mater.* **2000,** 12, 805-808.

119. Mendes P. M.; Preece J. A., Precision chemical engineering: Integrating nanolithography and nanoassembly. *Curr. Opin. Colloid In.* **2004,** 9, 236-248.

120. Mendes P. M.; Belloni M.; Ashworth M.; Hardy C.; Nikitin K.; Fitzmaurice D.; Critchley K.; Evans S. D.; A., P. J., A novel example of X-ray-radiation induced chemical reduction of an aromatic nitro-group-containing thin film on SiO_2 to an aromatic amine film. *ChemPhysChem* **2003,** 4, 884-889.

121. Mendes P. M.; Jacke S.; Critchley K.; Plaza J.; Chen Y.; Nikitin K.; Palmer R. E.; Preece J. A.; Evans S. D.; Fitzmaurice D., Gold nanoparticle patterning of silicon wafers using chemical e-beam lithography. *Langmuir* **2004,** 20, 3766-3768.

122. Sun S.; Chong K. S. L.; Leggett G. J., Photopatterning of self-assembled monolayers at 244nm and applications to the fabrication of functional microstructures and nanostructures. *Nanotechnology* **2005,** 16, 1798-1808.

123. Sun S.; Chong K. S. L.; Leggett G. J., Nanoscale molecular patterns fabricated by using scanning near-field optical lithography. *J. Am. Chem. Soc.* **2002,** 124, 2414-2415.

124. Sun S.; Leggett G. J., Matching the resolution of electron beam lithography by scanning near field photolithography. *Nano. Lett.* **2004,** 4, 1381-1384.

125. Xia Y.; Whitesides G. M., Soft lithography. *Angew. Chem. Int. Ed.* **1998,** 37, 550-575.

126. Smith R. K.; Lewis P. A.; Weiss P. S., Patterning self-assembled monolayers. *Prog. Surf. Sci.* **2004,** 75, 1-68.

127. Quist A. P.; Pavlovic E.; Oscarsson S., Recent advances in microcontact printing. *Anal. Bioanal. Chem.* **2005,** 381, 591-600.

128. Rogers J. A.; Nuzzo R. G., Recent progress in soft lithography. *Mater. Today* **2005,** 8, 50-56.

129. Xia Y.; Zhao X.-M.; Kim E.; Whitesides G. M., A selective etching solution for use with patterned self-assembled monolayers of alkanethiolates on gold. *Chem. Mater.* **1995,** 7, 2332-2337.

130. Wilbur J. L.; Kumar A.; Kim E.; Whitesides G. M., Microfabrication by microcontact printing of self-assembled monolayers. *Adv. Mater.* **1994,** 6, 600-604.

131. Michel B.; Bernard A.; Bietsch A.; Delamarche E.; Geissler M.; Juncker D.; Kind H.; Renault J.-P.; Rothuizen H.; Schmid H.; Schmidt-Winkel P.; Stutz R.; Wolf H., Printing meets lithography: Soft approaches to high-resolution patterning. *IBM J. Res. Dev.* **2001,** 45, 697-719.

132. Bietsch A.; Michel B., Conformal contact and pattern stability of stamps used for soft lithography. *J. Appl. Phys.* **2000,** 88, 4310-4318.

133. Balmer T. E.; Schmid H.; Stutz R.; Delamarche E.; Michel B.; Spencer N. D.; Wolf H., Diffusion of alkanethiols in PDMS and its implications on microcontact printing (μcp). *Langmuir* **2005,** 21, 622-632.

134. Bernard A.; Renault J. P.; Michel B.; Bosshard H. R.; Delamarche E., Microcontact printing of proteins. *Adv. Mater.* **2000,** 12, 1067-1070.

135. Inerowicz H. D.; Howell S.; Regnier F. E.; Reifenberger R., Multiprotein immunoassay arrays fabricated by microcontact printing. *Langmuir* **2002,** 18, 5263-5268.

136. Lebed K.; Pyka-Fosciak G.; Raczkowska J.; Lekka M.; Styczen J., Binding activity of patterned concanavalin A studied by atomic force microscopy. *J. Phys. - Condens. Mat.* **2005,** 17, S1447-S1458.

137. Singhvi R.; Kumar A.; Lopez G. P.; Stephanopoulos G. N.; Wang D. I. C.; Whitesides G. M.; Ingber D. E., Engineering cell-shape and function. *Science* **1994,** 264, 696-698.

138. James C. D.; Davis R.; Meyer M.; Turner A.; Turner S.; Withers G.; Kam L.; Banker G.; Craighead H.; Isaacson M.; Turner J.; Shain W., Aligned microcontact printing of micrometer-scale poly-L-lysine structures for controlled growth of cultured neurons on planar microelectrode arrays. *IEEE T. Bio.-Med. Eng.* **2000,** 47, 17-21.

139. Vogt A. K.; Stefani F. D.; Best A.; Nelles G.; Yasuda A.; Knoll W.; Offenhausser A., Impact of micropatterned surfaces on neuronal polarity. *J. Neurosci. Meth.* **2004,** 134, 191-198.

140. Huang S.; Mau A. W. H., Selective growth of aligned carbon nanotubes on a silver-patterned substrate by the silver mirror reaction. *J. Phys. Chem. B* **2003,** 107, 3455-3458.

141. Rozhok S.; Shen C. K.-F.; Littler P.-L. H.; Fan Z.; Liu C.; Mirkin C. A.; Holz R. C., Methods for fabricating microarrays of motile bacteria. *Small* **2005,** 1, 445-451.

142. Zhang S.; Yan L.; Altman M.; Lässle M.; Nugent H.; Frankel F.; Lauffenburger D. A.; Whiesides G. M.; Rich A., Biological surface engineering: A simple system for cell pattern formation. *Biomaterials* **1999,** 20, 1213-1220.

143. Khalil A. S. G.; Konjhodzic D.; Marlow F., Hierarchy selection, position control and orientation of growing mesostructures by patterned surfaces. *Adv. Mater.* **2006,** 18, 1055-1058.

144. Piner R. D.; Zhu J.; Xu F.; Hong S. H.; Mirkin C. A., "Dip-pen" nanolithography. *Science* **1999,** 283, (5402), 661-663.

145. Ginger D. S.; Zhang H.; Mirkin C. A., The evolution of dip-pen nanolithography. *Angew. Chem. Int. Ed.* **2004,** 43, 30-45.

146. Agarwal G.; Sowards L. A.; Naik R. R.; Stone M. O., Dip-pen nanolithography in tapping mode. *J. Am. Chem. Soc.* **2003,** 125, 580-583.

147. Sheehan P. E.; Whitman L. J., Thiol diffusion and the role of humidity in "Dip-Pen Nanolithography". *Phys. Rev. Lett.* **2002,** 88, 156104 (4pp).

148. Salaita K.; Lee S. W.; Wang X. F.; Huang L.; Dellinger T. M.; Liu C.; Mirkin C. A., Sub-100 nm, centimeter-scale, parallel dip-pen nanolithography. *Small* **2005,** 1, 940-945.

149. Li B.; Zhang Y.; Hu J.; Li M. Q., Fabricating protein nanopatterns on a single DNA molecule with dip-pen nanolithography. *Ultramicroscopy* **2005,** 105, 312-315.

150. Sheehan P. E.; Whitman L. J.; King W. P.; Nelson B. A., Nanoscale deposition of solid inks *via* thermal dip pen nanolithography. *Appl. Phys. Lett.* **2004,** 85, 1589-1591.

151. Nelson B. A.; King W. P.; Laracuente A. R.; Sheehan P. E.; Whitman L. J., Direct deposition of continuous metal nanostructures by thermal dip-pen nanolithography. *Appl. Phys. Lett.* **2006,** 88, 033104 (3pp).

152. Lim J. H.; Mirkin C. A., Electrostatically driven dip-pen nanolithography of conducting polymers. *Adv. Mater.* **2002,** 14, 1474-1477.

153. Rosner B.; Duenas T.; Banerjee D.; Shile R.; Amro N.; Rendlen J., Functional extensions of dip pen nanolithography (TM): active probes and microfluidic ink delivery. *Smart Mater. Struct.* **2006,** 15, S124-S130.

154. Samori P., Scanning probe microscopies beyond imaging. *J. Mater. Chem.* **2004,** 14, 1353-1366.

155. Wendel M.; Kuhn S.; Lorenz H.; Kotthaus J. P.; Holland M., Nanolithography with an atomic-force microscope for integrated fabrication of quantum electronic devices. *Appl. Phys. Lett.* **1994,** 65, 1775-1777.

156. Headrick J. E.; Armstrong M.; Cratty J.; Hammond S.; Sheriff B. A.; Berrie C. L., Nanoscale patterning of alkyl monolayers on silicon using the atomic force microscope. *Langmuir* **2005,** 21, 4117-4122.

157. Xu S.; Liu G. Y., Nanometer-scale fabrication by simultaneous nanoshaving and molecular self-assembly. *Langmuir* **1997,** 13, 127-129.

158. Ryu S.; Schatz G. C., Nanografting: Modeling and simulation. *Journal of the American Chemical Society* **2006,** 128, 11563-11573.

CHAPTER 2

Nanoscale characterisation techniques:

seeing the small

CHAPTER 2

Nanoscale characterisation techniques: seeing the small

ABSTRACT: *There are many characterisation techniques that are employed in nanoscience to visualise the nanoworld by investigating various properties of a nanostructure. This chapter the various microscopies, spectroscopies and other characterization techniques used in this thesis will be introduced.*

2.1. Nanoscale characterization techniques

This chapter gives a brief overview of atomic force microscopy (AFM), scanning electron microscopy (SEM), transmission electron microscopy (TEM) which have been used, in this thesis, to visualise the micron and sub-micron regimes. The spectroscopic methods used in this thesis, namely UV-*vis* spectroscopy, X-ray photoelectron spectroscopy (XPS) and spectroscopic ellipsometry, are outlined. The other techniques used, namely contact angle analysis and differential scanning calorimetry (DSC), were used to investigate the wettability and structure of samples respectively and are also outlined in this chapter.

2.2. Microscopies

2.2.1. Atomic Force Microscopy

The Atomic Force Microscope (AFM), introduced by Binnig *et al.*[1] in 1986, measures the attractive and repulsive forces between a sharp tip, mounted on a Si_3N_4 cantilever, and the surface of a sample. Unlike STM, the AFM can be used to study the surface of insulating materials[2] in addition to conductive samples as it is not reliant on electrical conduction between the tip and sample surface. An AFM (**Figure 15**) uses a photodiode to detect the position of a reflected laser beam from the top side of the cantilever. The position of the laser on the photodiode is recorded by the controller electronics, *via* a feedback loop, which can then be converted into a map of interactions between the tip and the substrate surface.
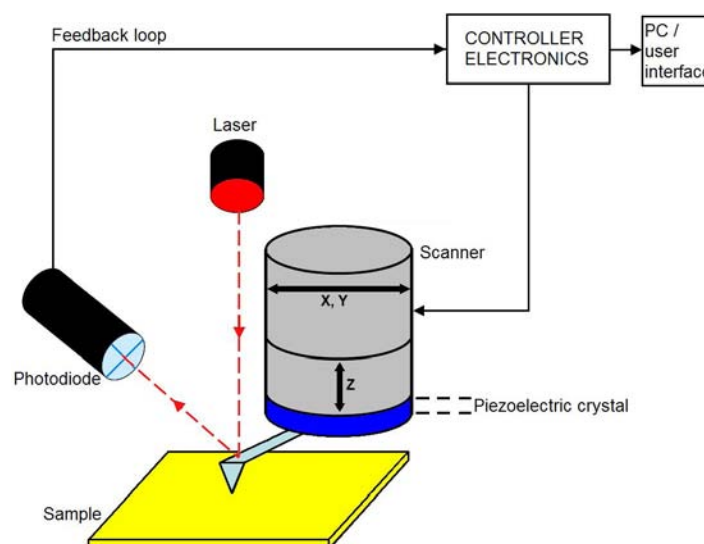
Figure 15. Schematic diagram of the layout of an Atomic Force Microscope (based on a diagram from[3])

AFM measurements can be performed in two different modes and these are contact and or tapping mode. Contact mode involves the tip and the substrate being kept in constant contact and the tip being rastered across the surface with the resultant deflection of the cantilever monitored by the position of the laser on the photodiode. During tapping mode AFM the cantilever is vibrated close to its resonant frequency and the change of oscillation of the cantilever is detected upon interaction between the tip and surface.[1]

2.2.2. Electron microscopies

Electron microscopies rely on the interaction of electron beams with a sample. Two common electron microscopies, scanning electron microscopy (SEM) and transmission electron microscopy (TEM), will be outlined in this section.

2.2.2.1. Scanning Electron Microscopy

Scanning electron microscopy (SEM) involves the irradiating a surface with electrons in a raster pattern.[2] These incident electrons result in the backscattering of electrons from the surface of the sample or induce secondary electrons to be emitted from the sample surface.[4] The detection of backscattered or secondary electrons allows the topography of the surface to be mapped. The

SEM can also be used for chemical analysis of the sample by analysis of the energy of characteristic X-rays emitted from the sample.[4]

2.2.2.2. Transmission Electron Microscopy

Transmission electron microscopy (TEM) involves a beam of electrons being passed through a sample (less than ~30 nm thick[5]) onto a fluorescent screen.[6] The scattering of the electron beam as it passes through the sample, due to the interaction with inhomogeneities such as defect or structural changes, produces contrasts in the acquired image.[6]

2.3. Spectroscopies

Spectroscopies measure the interaction of a sample with a range of radiation. Spectroscopic methods used in this thesis are introduced in this section and other spectroscopies used for nanoscale characterisation are outlined.

2.3.1. UV-vis spectroscopy

UV-visible spectroscopy is a method of measuring the absorbance of electromagnetic radiation by visible and long wavelength UV light being passed through a solution of interest and measuring the extent to which the radiation is

absorbed at each wavelength. UV-vis spectroscopy can be used to give rapid assessment of the concentration and particle size of metallic nanoparticles.[7] Metallic nanoparticles absorb the UV-vis radiation at specific energies due to the oscillations of the electron cloud of the nanoparticle at the surface of the particle, which is known as the Plasmon absorbance.[8]

2.3.2. X-ray photoelectron spectroscopy

X-ray photoelectron spectroscopy (XPS) is a method for determining the chemical composition of a materials' surface and involves the irradiation of the sample with X-rays. The X-rays, with energy hv, interact with the surface atoms by exciting core electrons within the atoms.[9] If the electrons are excited enough, to overcome the electron binding energy within their atomic orbital (E_B), they are ejected from the atom in the form of a photoelectron with energy (E_K) as shown in (**Figure 16**). The energy of the photoelectrons are measured and a spectrum of photoelectron energies is recorded.
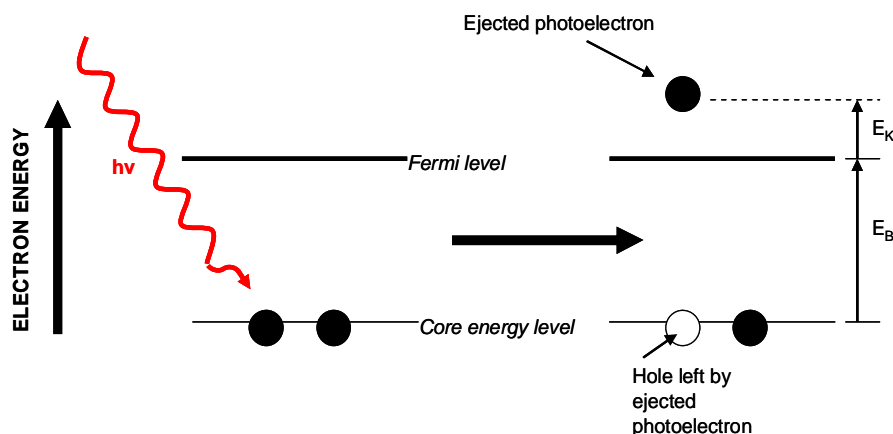
Figure 16. A cartoon representation of photoelectron emission

The electron binding energy is dependant on the chemical environment of the electron, thus the electron binding energy is characteristic of the electronic orbital and element in which it exists.[9] Knowledge of the kinetic energy of the ejected photoelectron and the energy of the incident X-ray radiation upon the sample allows the electron binding energy to be determined by use of **Equation 1**.[10]

$$E_K = h\nu - E_B \hspace{3cm} \textbf{(Equation 1)}$$

2.3.3. Ellipsometry

Ellipsometry is a method of measuring the optical properties of thin films by measuring changes of an elliptically polarised light beam due to interaction with the sample. Elliptically polarised light occurs as a result of the combination of two or more polarised light beams (represented as linearly polarised light beams 1 and 2 in **Figure 17a**) having the same frequency and amplitude, as shown in **Figure 17a.**[11] Upon transmission through a thin film, and subsequent reflection from the underlying substrate as shown in **Figure 17b**, the amplitudes of both the electric and magnetic vectors of the elliptical polarisation of the light are altered due to refraction through the thin film and this information can be used to calculate the thickness of the thin film.[12]

a) Elliptically polarised light

= Resultant polarised light
= Linearly polarised light beam 1
= Linearly polarised light beam 2
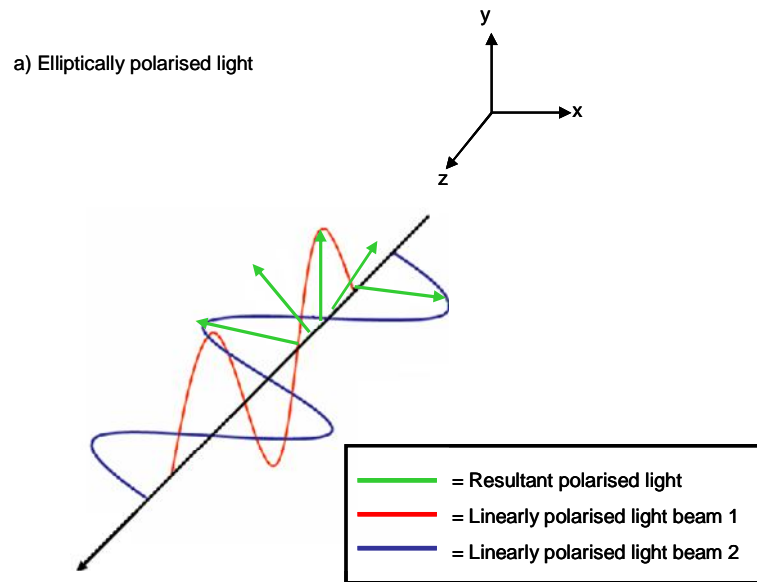
b) Setup of an ellipsometric experiment

Light source and polariser

Detector and analyser

Thin film

Underlying substrate

= Incident light

= Reflected light
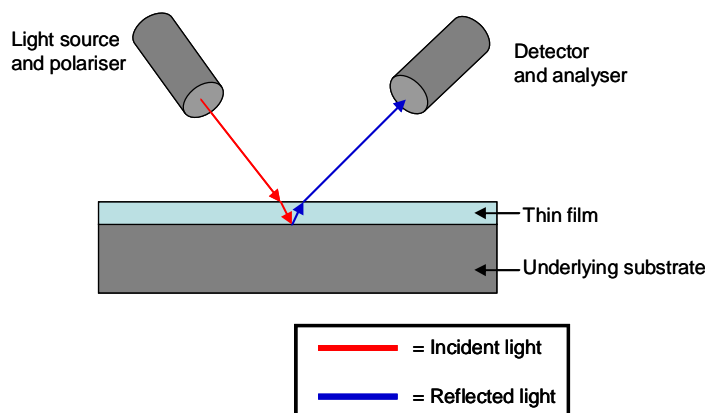
Figure 17. a) Elliptically polarised light as a result of magnetic and electrical components being out of phase (redrawn from [12]) and b) a cartoon representation of the configuration of an ellipsometric experiment

Ellipsometry measures the phase shift (Δ) and the ratio of the magnitudes of the total reflection coefficients (tan Ψ) of the reflected light, as a result of interaction with the thin film.[11] The experimental data is then compared to a computer model, which incorporates the refraction index and extinction

coefficient of the thin film, and a 'best fit' thickness of the film can be elucidated.[11] The spectroscopic element of ellipsometry is introduced by the use of a spectroscopic ellipsometer that measure the film thickness using light over a range of wavelengths.

2.4. Other characterisation techniques

2.4.1. Contact angle analysis

Contact angle analysis measures the wettability of a surface[5, 13] by the application of a liquid drop and measuring the angle of the drop to the surface at the boundary of the surface, substrate and surrounding atmosphere (the three-phase point) as shown in **Figure 18**. This angle can be measured either by simply placing a liquid drop on the sample surface and measuring the angle (sessile drop method) or by measuring the angle by increasing and decreasing the volume of the drop to determine the advancing and receding contact angles, respectively.[5] The difference between the advancing and receding angles (contact angle hysteresis) gives an indication of the smoothness and quality of the self-assembled monolayer. Rough surfaces yield higher hysteresis than smooth surfaces. The chemical composition of the surface is critical to the value of the contact angle. For example, the water contact angle of hydrophobic surfaces is much higher than that of hydrophilic surfaces.

a) Increasing drop volume
(advancing angle, θ_a)

b) Decreasing drop volume
(receding angle, θ_r)

Syringe

Direction of
liquid flow

θ_a

SUBSTRATE

θ_r

SUBSTRATE
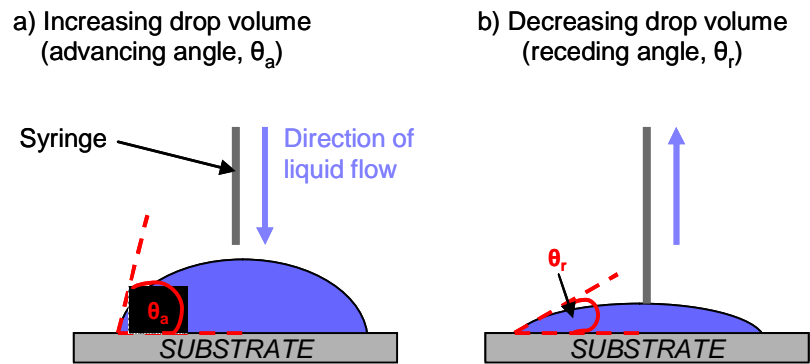
Figure 18. Dynamic contact angle analysis which measures a) advancing contact angle (θ_a) and

b) receding contact angle (θ_r)

2.4.2. Differential Scanning Calorimetry (DSC)

Differential scanning calorimetry (DSC) is a method of measuring temperature dependant events, such as phase changes, and is achieved by increasing the temperature of both the sample and a reference in such a manner as to keep them both at the same temperature as each other. The reference sample is fabricated from a material which undergoes no thermal events in the temperature range over which the experiment will be conducted. The difference in energy required to heat the sample, compared to the reference, compensates for thermal events with extra heat required for endothermic events and less heat required for exothermic events.[14]

2.5. References

1. Binnig G.; Quate C. F.; Gerber Ch., Atomic force microscopy. *Phys. Rev. Lett.***1986,** 56, 930-933.

2. Skoog D. A.; Holler F. J.; Nieman T. A., *Principles of instrumental analysis (5th Edition)*. Saunders College Publishing: Orlando, 1998.

3. Scanning Probe Microscopy Training Notebook (Version 3.0). *Digital Instruments. Veeco Metrology Group* **2000**.

4. Goodhew P. J., *Electron Microscopy and Analysis*. Wykeham Publications: London, 1975.

5. Ulman A., *An Introduction to Ultrathin Organic Films from Langmuir-Blodgett to Self-Assembly*. Adademic Press Limited: London, 1991.

6. Callister Jr W. D., *Materials science and engineering. An introduction (5th Edition)*. John Wiley & Sons: New York, 2000.

7. Haiss W.; Thanh N. T. K.; Aveyard J.; Fernig D. G., Determination of size and concentration of gold nanoparticles from UV-Vis spectra. *Anal. Chem.* **2007,** 79, 4215-4221.

8. Shipway A. N.; Katz E.; Wilner I., Nanoparticle arrays on surfaces for electronic, optical and sensor applications. *ChemPhysChem* **2000,** 1, 18-52.

9. Briggs D.; Seah M. P., *Practical surface analysis Volume 1- Auger and X-ray photoeletron spectroscopy*. John Wiley & Sons: Chichester (UK), 1996.

10. Zangwill A., *Physics at surfaces*. Cambridge University Press: Cambridge, 1996.

11. Tompkins H. G.; McGahan W. A., *Spectroscopic ellipsometry and reflectometry a user's guide*. Wiley-Interscience: New York, 1999.

12. Gonçalves D.; Irene E. A., Fundamentals and applications of spectroscopic ellipsometry. *Quim. Nova* **2002,** 25, 794-800.

13. Chaudhury M. K., Interfacial interaction between low-energy surfaces. *Mat. Sci. Eng. R* **1996,** 16, 97-159.

14. Elias H.-G., *An Introduction to Polymer Science*. VCH: Weinheim, 1997.

CHAPTER 3

Formation of amino terminated self-assembled monolayers on silicon nitride from the vapour phase

CHAPTER 3

Formation of amino terminated self-assembled monolayers on silicon nitride from the vapour phase

The work presented in **Chapter 3** has been published in the following research article: Hamlett et al. *Surface Science* **602** 2724-2733 (2008).[1]

ABSTRACT: *Self-assembled monolayer (SAM) formation of silanes on SiO$_2$ surfaces is well known. However, SAMs formed on silicon nitride (Si$_3$N$_4$) surfaces are less well-known, but are of technological interest with a view to the chemical modification of microelectromechanical systems (MEMS) devices formed from this material. Therefore, this chapter presents the formation and characterisation of 3-aminopropyltrimethoxy silane (APTMS) SAMs on Si$_3$N$_4$ substrates from both the solution and vapour phase. As a comparison the well characterised APTMS SAM is formed on SiO$_2$ surfaces.*

3.1. Introduction

SAMs, as introduced in **Chapter 1** (**section 1.3.2.**), are ordered, quasi-crystalline structures which are formed when surfactant molecules, with specifically functionalised headgroups, adsorb onto substrates.[2] The use of SAMs provides a facile method of chemically-modifying surfaces, and they are

commonly formed on a solid substrate *via* adsorption of surfactant molecules from the solution phase.

The formation of SAMs of surfactants containing silane headgroups on Si containing substrates has been widely studied[3-8] and is presented in **Chapter 1** (**section 1.3.2.ii.**). SiO_2 is the most widely researched Si based substrate for SAM formation.[3-5, 7, 9-13] However, there are relatively fewer investigations into using SAMs to chemically modify Si_3N_4 substrates.[6, 14-16] Microelectromechanical systems (MEMS) devices are commonly fabricated from Si_3N_4, thus the ability to form SAMs on MEMS devices allows control of the surface chemical properties of MEMS devices. SAMs have been studied as coatings for MEMS devices for both their anti-stiction[16, 17] and chemical immobilization[5] properties.

Formation from the solution phase is by far the most common method of preparing SAMs.[4, 5, 7] However, there have been studies in which vapour phase methods have been employed to form SAMs on both Au[18, 19] and SiO_2 surfaces.[3, 20, 21] The formation of SAMs from the vapour phase has been studied with a view to using a solvent free system[20] which has environmental benefits due to a reduction of waste solvents. SAM formation from the vapour phase has also been studied in an attempt to reduce the formation of polymeric aggregates which can be problematic when forming SAMs from solution.[22] The problem of aggregation occurs due to condensation reactions between organosilane

molecules in solution that can form inverse micelle structures,[22] which then subsequently adsorb on the substrate.

3.2. Aims and objectives

The work in this chapter describes a technique to chemically modify Si_3N_4 substrates with a view to using the technique to chemically modify Si_3N_4 MEMS microresonators in order to create a mass sensitive detector for the adsorption of specific species. It was found that the MEMS devices were so delicate that the use of a sonic bath for the formation of SAMs from the solution phase destroyed the devices. Therefore, the objective of this chapter is to investigate a methodology, for the chemical modification of Si_3N_4 substrates that does not involve a sonic bath. The approach will be to initially form APTMS SAMs on SiO_2 (a well studied system) and Si_3N_4 substrates (a less well studied system) in order to establish a model system for the chemical modification of Si_3N_4 substrates. A vapour phase methodology will then be used to chemically modify Si_3N_4 substrates with APTMS, the morphology of which will then be compared to that of the model system.

3.3. Results and discussion

This section investigates the modification of SiO_2 and Si_3N_4 surfaces with APTMS from the solution phase. These results will subsequently be used as a

reference for the characterisation of Si_3N_4 surface modified by APTMS *via* a vapour deposition method. The surface of the Si_3N_4 substrates is hydroxylated prior to SAM formation as described by Wei *et al.*[23] thus a -OH functionalised surface is formed on the Si_3N_4 substrates allowing similar surface reactions to that of the SiO_2 substrates. The hydroxylated surface of the Si_3N_4 substrates is made possible by the formation of a SiO_2 layer on the surface of the Si_3N_4 substrates during cleaning which can be seen in **Figure 19**. The Si_3N_4 substrates, prior to the cleaning procedure, exhibit a single Si2p peak (**Figure 19b**) however, upon cleaning using the method described by Wei *et al.*[23] , this peak broadens (**Figure 19d**). This broadening is due to splitting of the Si2p peak (**Figure 19e**) upon cleaning of the substrate and the peaks are assigned as the Si2p peaks for Si present in Si_3N_4 (~103.0 eV[24]) and SiO_2 (~104.5 eV[24]) thus the hydroxylation of the Si_3N_4 surface is confirmed. Further evidence for the formation of a SiO_2 layer on the Si_3N_4 surface is due to an increase in the ratio of O1s to N1s peaks upon cleaning (**Figure 19a** and **Figure 19c**). The SiO_2 layer was estimated to be of the order of 2 nm thick as this value provided a good model with which to fit the ellipsometric data of the bare substrate.

Along with the Si2s, Si2p, O1s and N1s peaks, which are due to the elements which constitute both the Si_3N_4 substrate and the SiO_2 formed by the cleaning method, a C1s peak can be seen in the survey spectra of Si_3N_4 before (**Figure 19a**) and after (**Figure 19c**) cleaning. This C1s peak is due to the

adsorption of volatile organic species which rapidly adsorb on the substrate upon exposure to air.
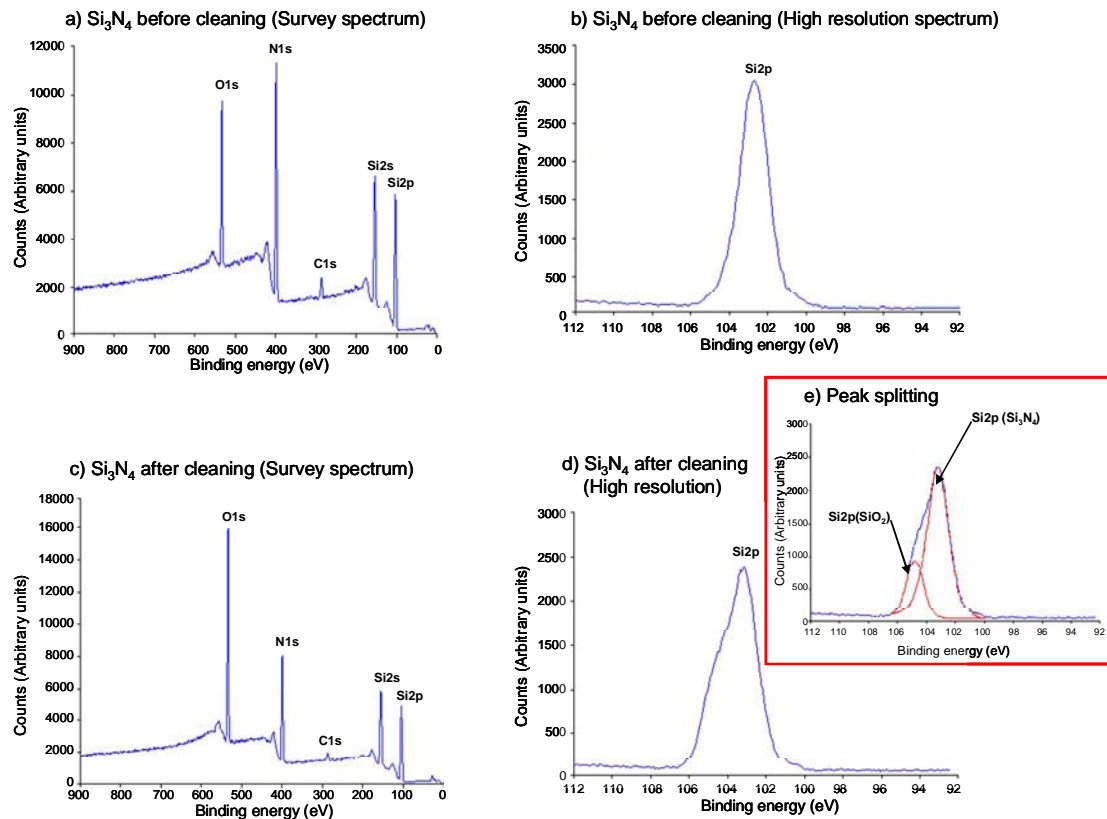
Figure 19. XPS spectra of Si_3N_4 substrates a) before and c) after the cleaning process. b) and d) are high resolution spectra of the Si2p peaks of the Si_3N_4 substrates before and after cleaning respectively and e) shows the Si2p peak splitting as a result of the cleaning process

3.3.1. Comparison of APTMS SAMs formed from solution phase on SiO_2 and Si_3N_4 surfaces

This section presents the characterisation of both SiO_2 and Si_3N_4 surfaces modified by the immersion of substrates in APTMS solution (0.5 mM in EtOH) for three different immersion times (30, 60 and 120 min).

3.3.1.1. Contact angle

A dynamic contact angle analysis method was used to measure the water contact angle of both SiO_2 and Si_3N_4 surfaces before and after immersion in ethanolic APTMS solution and the results are shown in **Figure 20**.
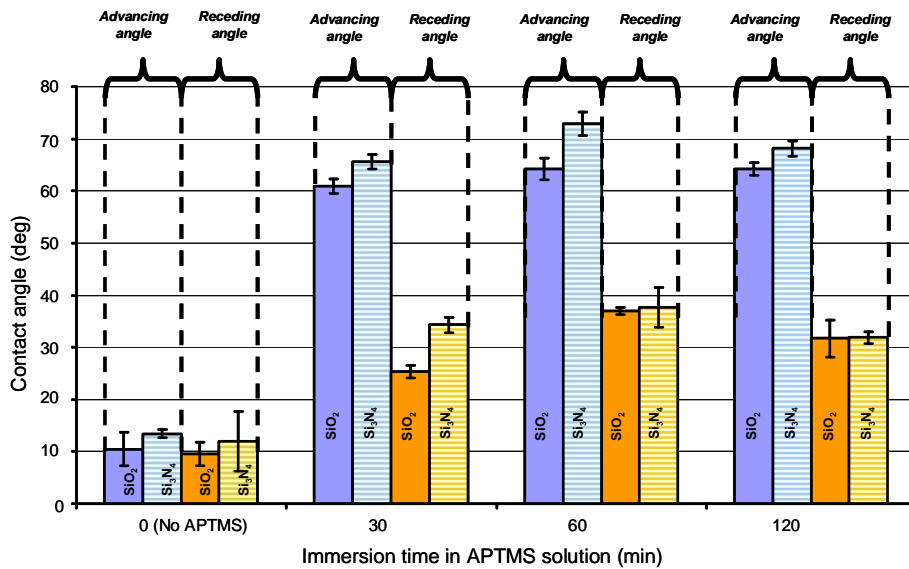
Figure 20. Contact angle data of Si/SiO_2 and Si/Si_3N_4 substrates immersed in APTMS solution (0.5mM in EtOH) for various times

The bare hydroxylated SiO_2 and Si_3N_4 substrates are both hydrophilic (θ_a and θ_r ~10 °), whereas, after immersion in APTMS solution, the surface becomes significantly less hydrophilic (θ_a and θ_r <60 °). The literature value for APTMS SAMs on SiO_2 is ~68 °.[9, 10] Therefore, the contact angle data (**Figure 20**) suggests that APTMS SAMs are formed on both substrates. However, the degree of formation and structure of the SAMs needs to be probed, see **sections 3.3.1.2.** and **3.3.1.3.**

3.3.1.2. AFM

AFM images of SiO_2 **(Figure 21)** and Si_3N_4 **(Figure 22)**, surfaces modified by solution phase APTMS at different immersion times are presented in this section along with a comparison of roughness data of these systems **(Figure 23)**.
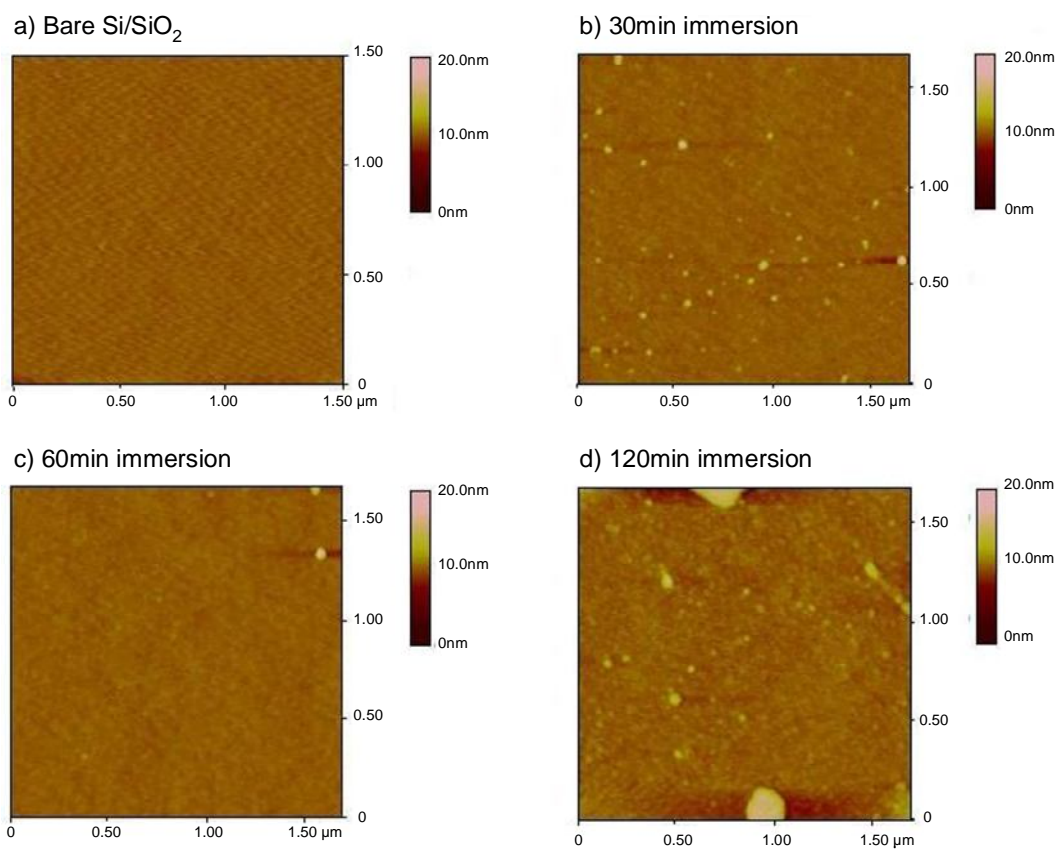
Figure 21. AFM images of a) bare Si/SiO_2 substrate and b-d) Si/SiO_2 substrates immersed in APTMS solution (0.5 mM in EtOH)
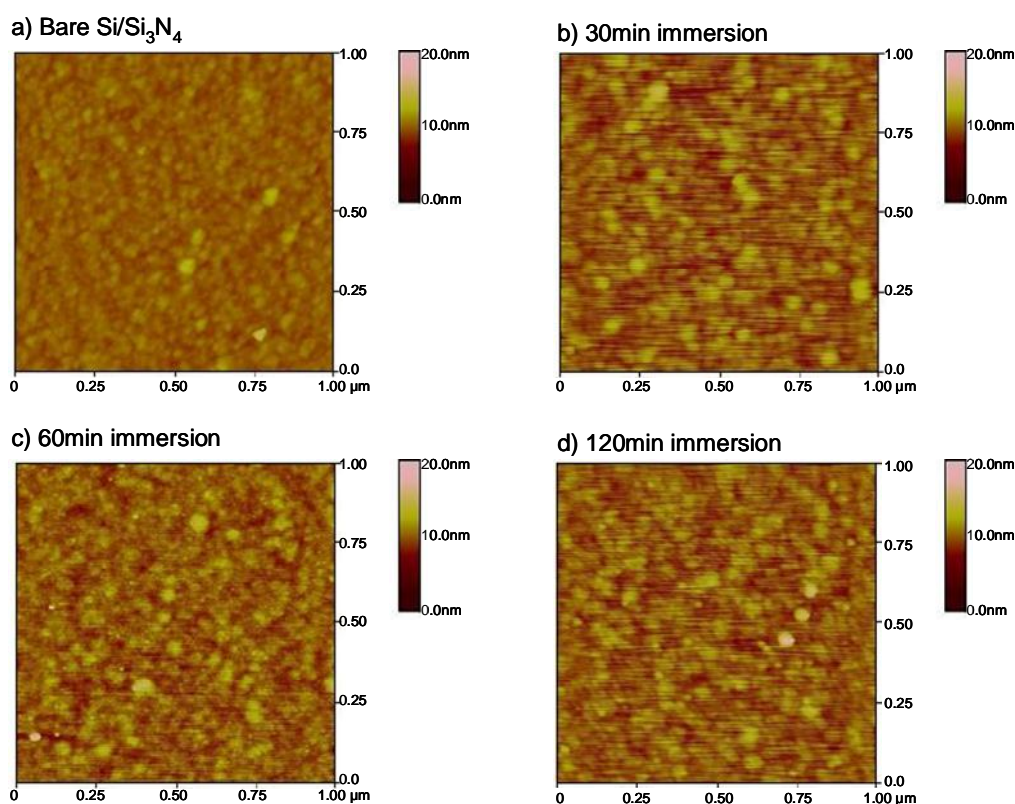
Figure 22. AFM images of a) bare Si_3N_4 substrate and b-d) Si_3N_4 substrates immersed in APTMS solution (0.5 mM in EtOH)

Visual inspection of **Figure 21** and **Figure 22** shows that the SAMs formed on SiO_2 substrates are smoother than those formed on Si_3N_4, which is quantitatively born out by the RMS data recorded in **Table 1** and represented by the graph in **Figure 23**. However, it should be noted that the bare Si_3N_4 substrate is rougher (RMS roughness = 0.770 nm) than the SiO_2 substrate (RMS roughness = 0.430 nm). The RMS roughness (whole image) roughly doubles after immersion of both substrates for 30 min, and after 60 min immersion the RMS roughness reduces and subsequently increases again after an immersion time of 120 min. It can be seen that the RMS roughness of the SAM on SiO_2 after

62

60 min immersion in APTMS solution is smoother than the original bare substrate. Such smoothing has been previously observed[25], and is rationalised in terms of a "carpet effect". This "carpet effect" is due to the SAM being bound to the substrate at relatively few points, and thus masks the roughness of the underlying substrate.[25] At longer immersion times (120 min), in both cases, the roughness increases as polysiloxane particulates, formed in solution, are deposited.

Table 1. RMS roughness data of Si/SiO_2 and Si/Si_3N_4 substrates immersed in APTMS solution at various immersion times

Immersion time (min)	SUBSTRATE			
	Si/SiO$_2$		*Si/Si$_3$N$_4$*	
	RMS roughness (nm)	**Error (nm)**	**RMS roughness (nm)**	**Error (nm)**
0	0.430	±0.056	0.770	±0.329
30	0.916	±0.329	1.405	±0.404
60	0.297	±0.022	1.270	±0.223
120	0.598	±0.298	1.312	±0.250
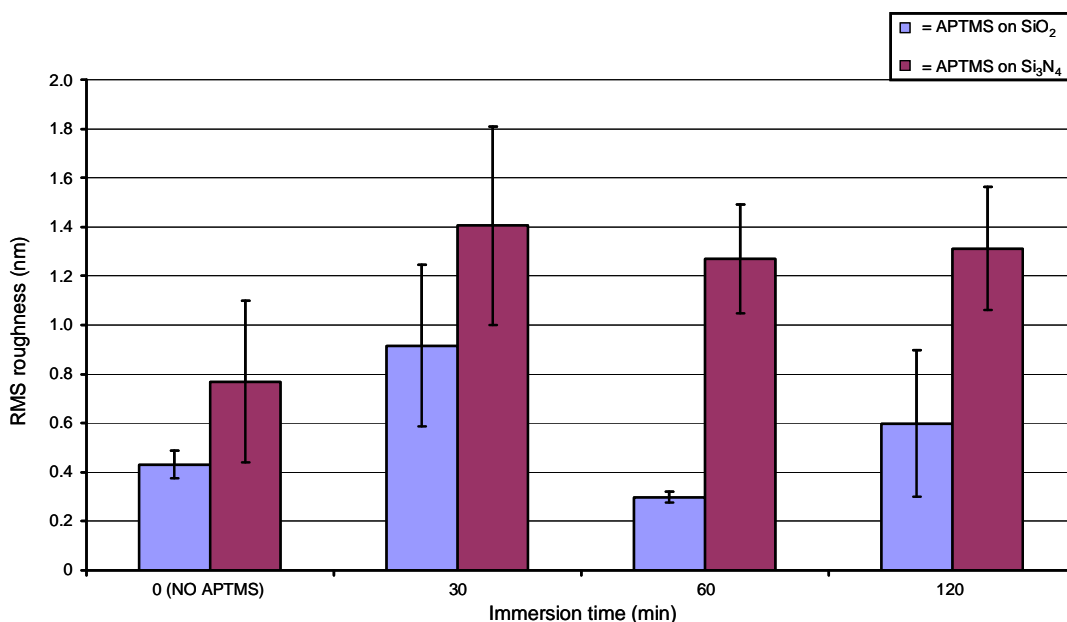
Figure 23. RMS roughness data of Si/SiO$_2$ and Si/Si$_3$N$_4$ substrates immersed in APTMS solution (0.5 mM in EtOH) for various times

In summary, an immersion time of 60 min results in the minimum roughness of both Si/SiO$_2$ and Si/Si$_3$N$_4$ substrates immersed in APTMS solution (**Figure 23**). The occurrence of a minimum roughness at 60 min immersion can be explained by the presence of fewer aggregates on the surface, when compared to immersion times of 30 min and 120 min of both types of substrate, which results in smoother surfaces.

3.3.1.3. Ellipsometry

Modelling the molecular structure of APTMS (**Figure 24**) reveals that the distance between the N atom, from the -NH$_2$ group, and the methoxy O atoms is

64

~0.56 nm. Thus, it is expected that a well-formed SAM would have a thickness of the order of 0.5 - 0.6 nm.
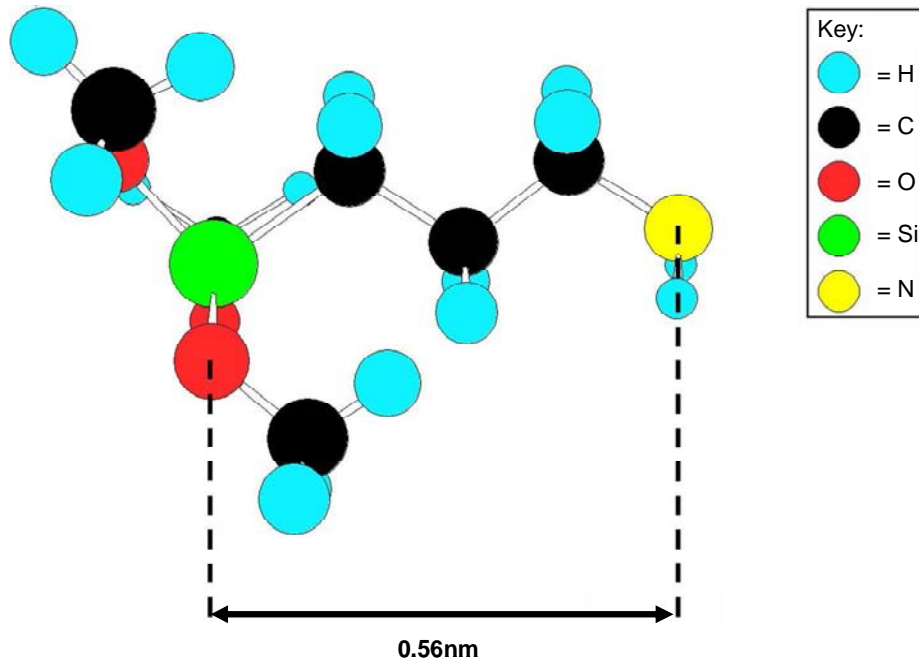
Figure 24. The structure of APTMS with the O-N distance being shown. (This distance was calculated using Chem3D Ultra 7.0 software.)

The ellipsometric thickness of both Si/SiO_2 and Si_3N_4 substrates after immersion in APTMS solution is shown in **Table 2** and **Figure 25**. Satisfyingly the ellipsometric thickness data for 60 min immersion time of both Si/SiO_2 and Si/Si_3N_4 substrates in APTMS solution are 0.546 nm and 0.557 nm, **Table 2 and Figure 25** respectively, whilst at shorter and longer immersion times the thickness is greater. This increase of thickness at shorter and larger immersion times is in agreement with RMS roughness data (**Table 1, Figure 23** and **Figure 28**).

Table 2. Ellipsometric thickness data of Si/SiO$_2$ and Si$_3$N$_4$ surfaces immersed in APTMS solution for various immersion times

Immersion time (min)	Substrate			
	Si/SiO$_2$		Si/Si$_3$N$_4$	
	Thickness (nm)	Error (nm)	Thickness (nm)	Error (nm)
30	1.242	± 0.288	0.933	± 0.523
60	0.546	± 0.132	0.557	± 0.312
120	1.769	± 0.383	0.993	± 0.476
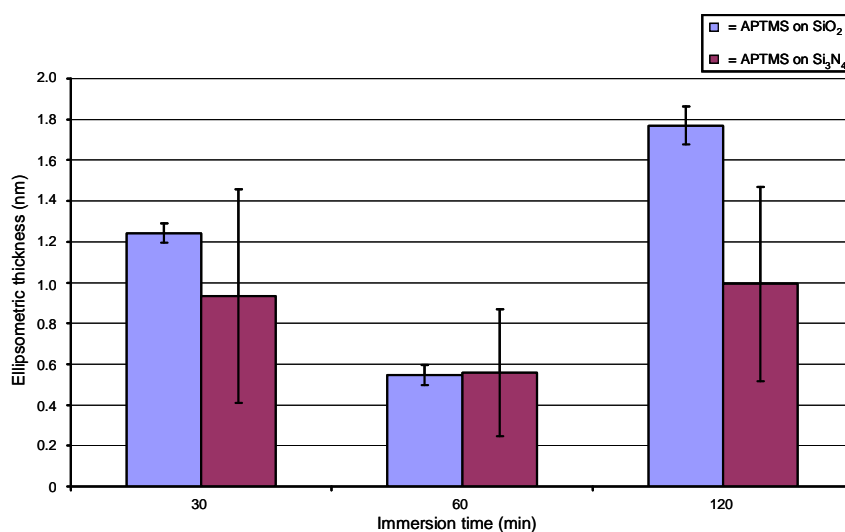
Figure 25. Ellipsometric SAM thicknesses of Si/SiO$_2$ and Si/Si$_3$N$_4$ substrates after immersion in APTMS solution (0.5 mM in EtOH)

3.3.1.4. XPS

XPS spectra were recorded for bare Si/SiO$_2$ before and after immersion in APTMS solution for 60 min (**Figure 26**) and for Si/Si$_3$N$_4$ substrates before and after immersion in APTMS solution for 60 min (**Figure 27**). XPS spectra were obtained for 60 min immersion because the AFM data showed this immersion time resulted in the smoothest surfaces of the immersion times studied and

ellipsometric measurements suggested that at 60 min immersion time monolayer coverage of APTMS was achieved.
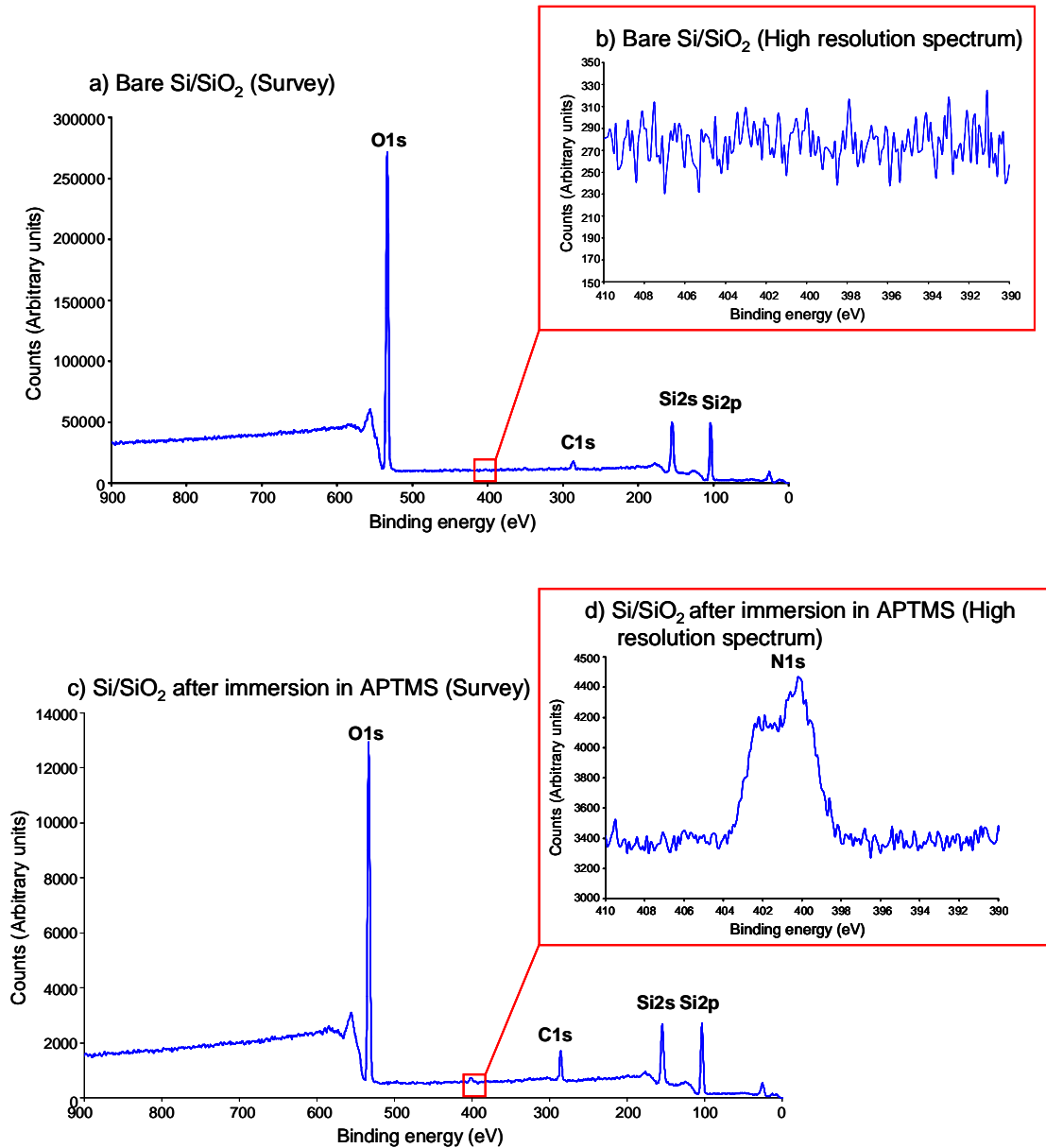
Figure 26. XPS spectra of Si/SiO$_2$ substrates before and after immersion in APTMS solution. a) Survey spectrum of bare Si/SiO$_2$ substrate with inset b) being a high resolution spectrum of the energy range where N1s peak would be found. c) survey spectrum of Si/SiO$_2$ after 60 min immersion in APTMS solution for 60 min with inset d) being a high resolution spectrum of N1s peak
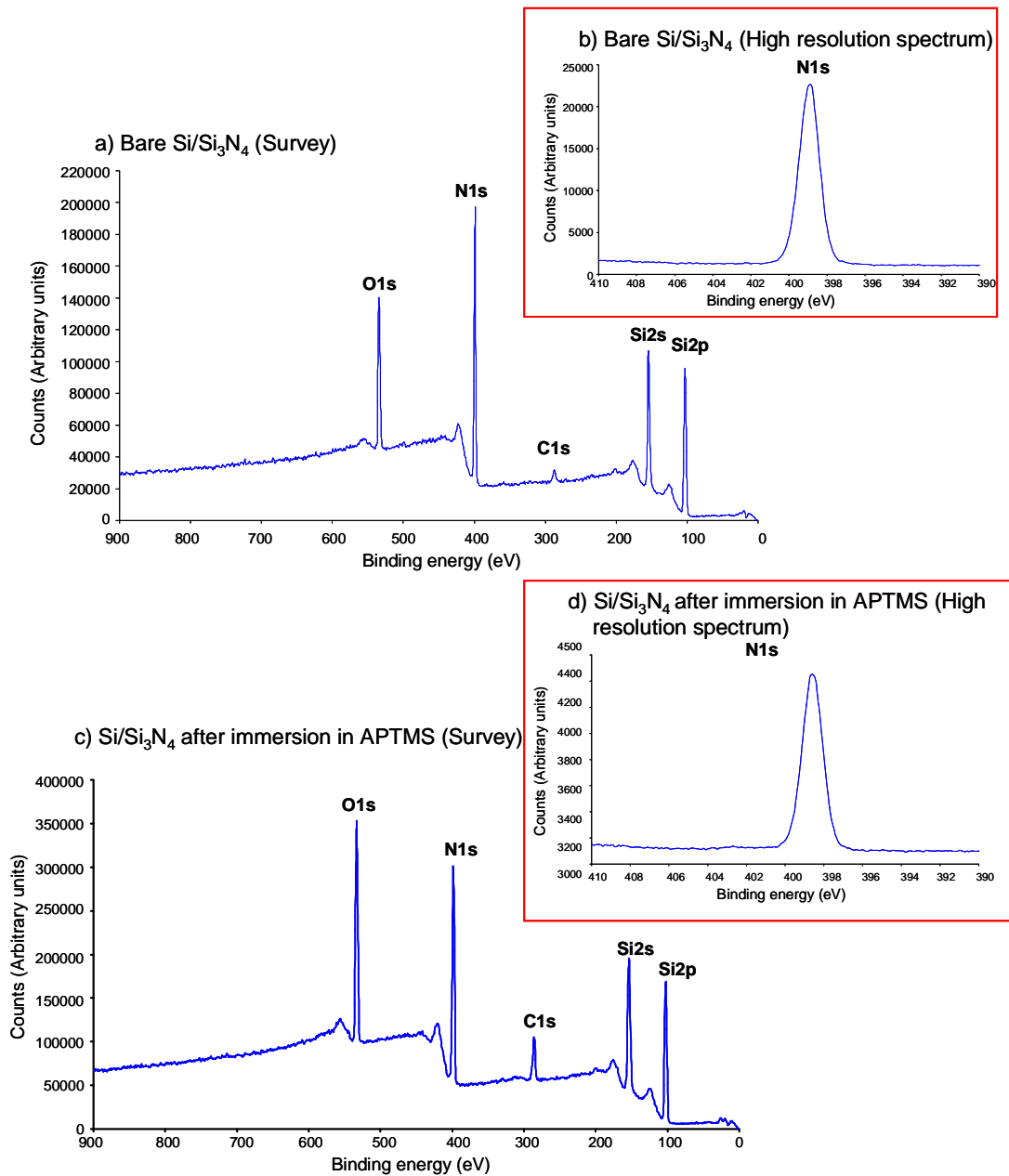
Figure 27. XPS spectra of a) bare Si/Si₃N₄ with inset b) being a high resolution spectrum of the N1s peak and c) Si/Si₃N₄ after immersion in APTMS solution for 60 min with inset d) being a high resolution spectrum of the N1s peak

The XPS survey spectrum of bare SiO_2 (**Figure 26a**) reveals the presence of Si2p, Si2s and O1s peaks, which are due to the elemental composition of the SiO_2 substrate. A C1s peak occurs due to the presence of carbon on the surface of the clean substrate due to the adsorption of volatile organic compounds on the

surface upon exposure of the substrate to air. Immersion of the Si/SiO_2 substrate in APTMS solution results in the appearance of a N1s peak (**Figure 26c** and **d**). This peak represents the N1s photoelectron, thus confirming the presence of nitrogen which correspond to the adsorption of APTMS.[11]

Bare Si/Si_3N_4 substrates, as discussed in **section 3.3.**, display Si2p, Si2s, C1s, N1s and O1s peaks (**Figure 27**). These peaks correspond to the presence of Si and N in Si_3N_4 (Si2p, Si2s and N1s peaks), the formation of a ~2 nm layer of SiO_2 during the cleaning procedure (O1s peak) and the adsorption of volatile organic compounds upon exposure to air (C1s peak). The Si2p, Si2s, C1s, N1s and O1s peaks, present in the XPS spectra of the bare substrate, are also the peaks that correspond to the adsorption of APTMS molecules. Therefore, XPS cannot be used to verify the formation of APTMS SAMs on Si_3N_4 substrates because the peaks expected for APTMS SAMs are already present in the XPS spectra of the bare substrate.

3.3.1.5. Comparison of APTMS SAMs formed from solution phase on both SiO_2 and Si_3N_4 surfaces

The results presented so far show that, upon exposure to APTMS solution, both Si/SiO_2 and Si/Si_3N_4 substrates exhibit contact angles similar to that found in the literature for fully formed APTMS SAMs. The AFM and ellipsometric data support the formation of fully formed APTMS SAMs at 60 min

immersion times (**Figure 28b**) due to a decrease in RMS roughness (carpet effect) and the thickness is consistent with that of a fully formed APTMS SAM. However, at 30 min and 120 min immersion times the formation of smooth APTMS SAMs does not occur due to both RMS roughness values and ellipsometric thicknesses being significantly different than those expected for a fully formed SAM. At 30 min immersion (**Figure 28a**) the APTMS molecules may form physisorbed bilayers due to the RMS roughness being greater than that of the bare substrate and the thickness being approximately twice the length of an APTMS molecule. At 120 min (**Figure 28c**) the RMS roughness is greater than that of both a fully formed SAM and the bare substrate due to the presence of polysiloxane aggregates adsorbed on the surface (**Figure 21** and **Figure 22**). The presence of such aggregates also leads to a greater ellipsometric thickness than that of a fully formed APTMS SAM. XPS data (**Figure 26** and **Figure 27**) confirm the adsorption of APTMS on SiO_2 substrates due to the appearance of the N1s peak upon immersion of the substrate in APTMS solution. However, a similar observation cannot made for the adsorption of APTMS on the Si_3N_4 substrates because the XPS spectrum of bare Si_3N_4 substrates shows the same peaks that correspond to the constituent atoms of an APTMS molecule.
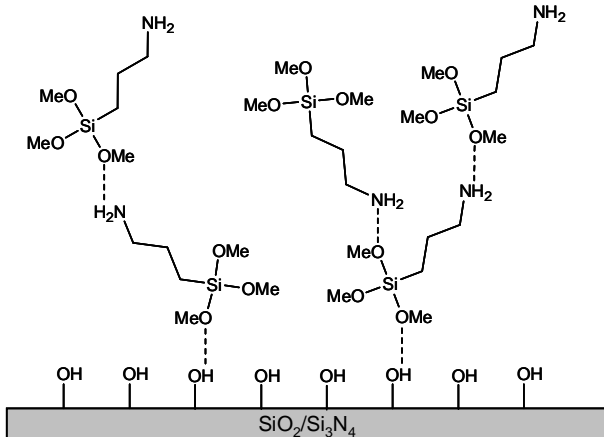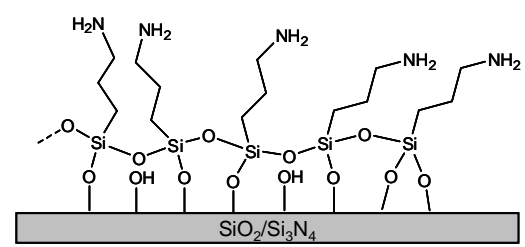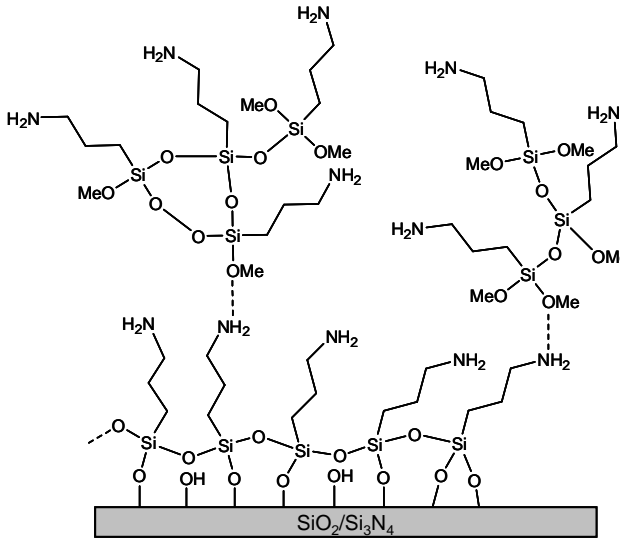
	AFM: RMS roughness (nm)		ELLIPSOMETRY: Thickness (nm)	
	SiO_2	Si_3N_4	SiO_2	Si_3N_4
a) 30min immersion	0.916 ±0.329	1.405 ±0.404	1.242 ±0.288	0.933 ±0.523
b) 60min immersion	0.297 ±0.022	1.270 ±0.223	0.546 ±0.132	0.557 ±0.312
c) 120min immersion	0.598 ±0.298	1.312 ±0.250	1.769 ±0.383	0.993 ±0.476

Figure 28. Models of APTMS formation on surface of Si/SiO$_2$ and Si/Si$_3$N$_4$ substrates at three different immersion times. (The RMS roughness and ellipsometric thickness are included for comparison to the models)

3.3.2. APTMS SAMs on Si_3N_4 from vapour phase

Vapour phase modification of Si_3N_4 substrates is studied here with a view to using such a system for the surface modification of MEMS device. The vapour deposition process used for Si_3N_4 modification (**Figure 29a-g**) involves the use of a glass vapour chamber (**Figure 29h**). The vapour chamber consists of two parts (**Figure 29a**) with the top section consisting of a gas tap. The bottom section of the chamber consists of an Al gauze, on which the substrates are placed, and an inlet, in which a Subaseal^{TM} stopper is placed allowing for the injection of APTMS. After the substrates have been placed in the chamber, and the top section attached, the chamber is purged with $N_{2(g)}$ (**Figure 29b**) to displace atmospheric water from within the chamber. The chamber is then heated under vacuum, using a heat gun, to encourage desorption of water adsorbed from the inside of the chamber which is subsequently removed by the vacuum (**Figure 29c**). After the chamber has cooled to room temperature APTMS liquid (2 ml) is injected through the Subaseal^{TM} (**Figure 29d**) whilst the chamber is continuously evacuated for a further 30 min (**Figure 29e**). The choice of vacuum pump used determines the pressure at which the deposition takes place and is referred to as the deposition pressure (P_{dep}). The gas tap is then closed leaving the substrates in an atmosphere of APTMS vapour (**Figure 29f**) and after a further 30 min the vacuum is released (**Figure 29g**) and the substrates removed from the chamber.
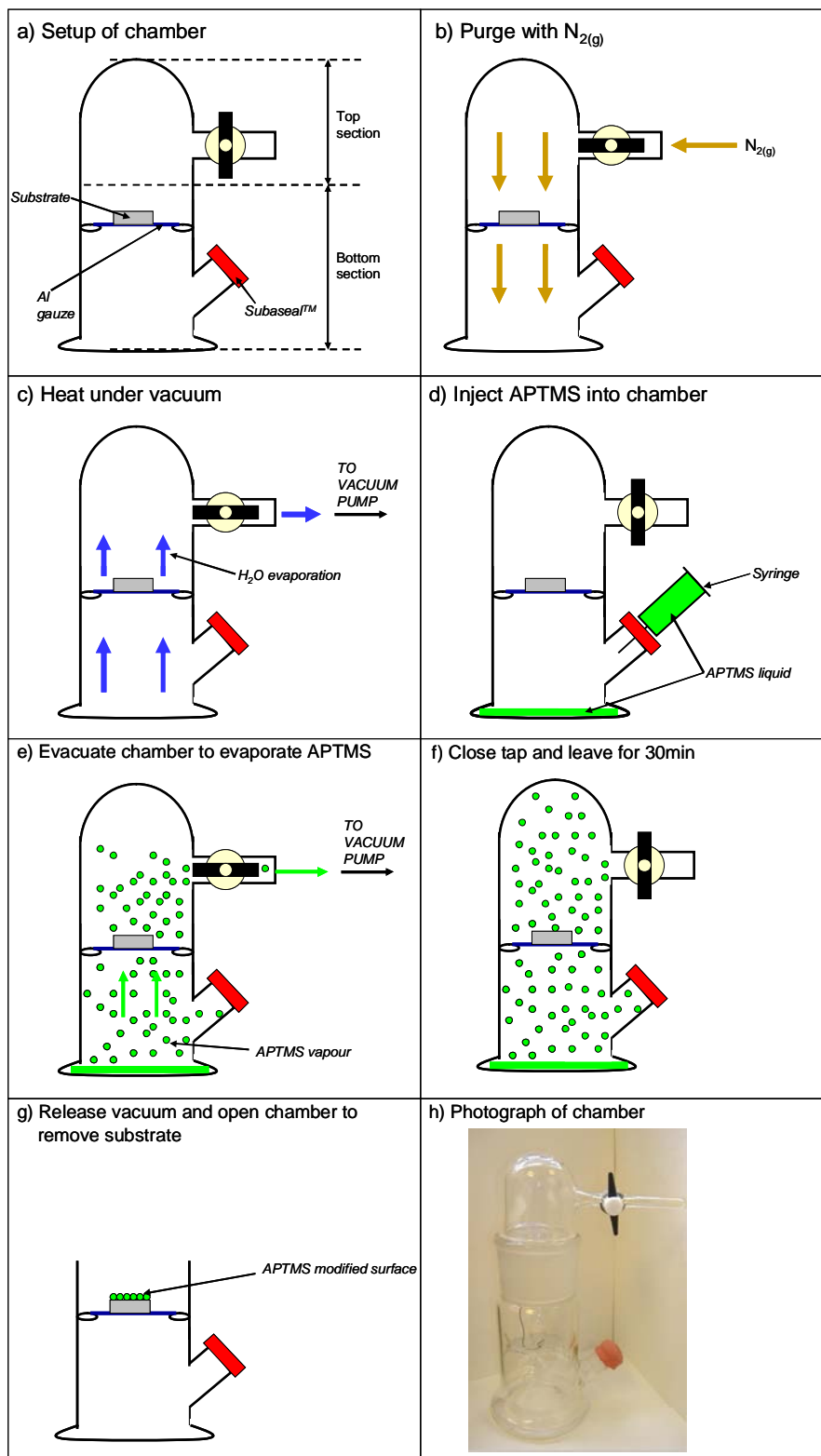
Figure 29. a-g) Cartoon representations of the vapour deposition process and h) a photograph of the vapour chamber

The following sections show the characterisation of Si_3N_4 substrate modified by the method described using four different deposition pressures (P_{dep}) which are 0.1 mbar, 1.15 mbar, 30 mbar and 168 mbar.

3.3.2.1. Contact angle

Figure 30 shows that the surfaces are significantly more hydrophobic than the bare, clean Si_3N_4 surfaces. At P_{dep} = 0.1 mbar and 1.15 mbar the contact angles are larger than those obtained by solution deposition which could be due to the presence of a rough surface (see **section 2.3.2.2.**) as this can increase the contact angle.[26, 27] At P_{dep} = 30 mbar the contact angles are significantly less than those obtained from the solution phase suggesting that the hydrophilic substrate is not completely covered by APTMS molecules. At P_{dep} = 168 mbar the resultant surface exhibits contact angles comparable to that of fully formed APTMS SAMs on Si_3N_4 substrates modified by immersion in APTMS solution for 60 min (**Figure 20**) thus indicates $-NH_2$ functionality of the surface (**section 3.3.1**).
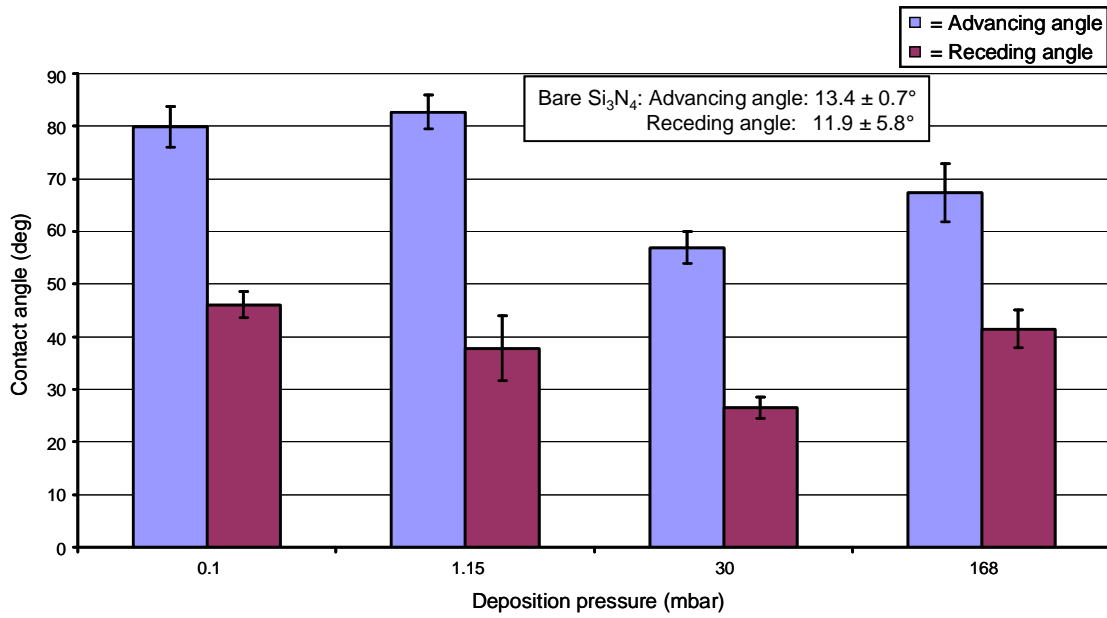
Figure 30. Contact angle data of Si/Si$_3$N$_4$ substrates exposed to APTMS vapour for 60 min at four different pressures

3.3.2.2. AFM

AFM images were taken for Si$_3$N$_4$ surfaces which were modified with APTMS at four different pressures (P_{dep} = 0.1 mbar, 1.15 mbar, 30 mbar and 168 mbar), as shown in **Figure 31**.
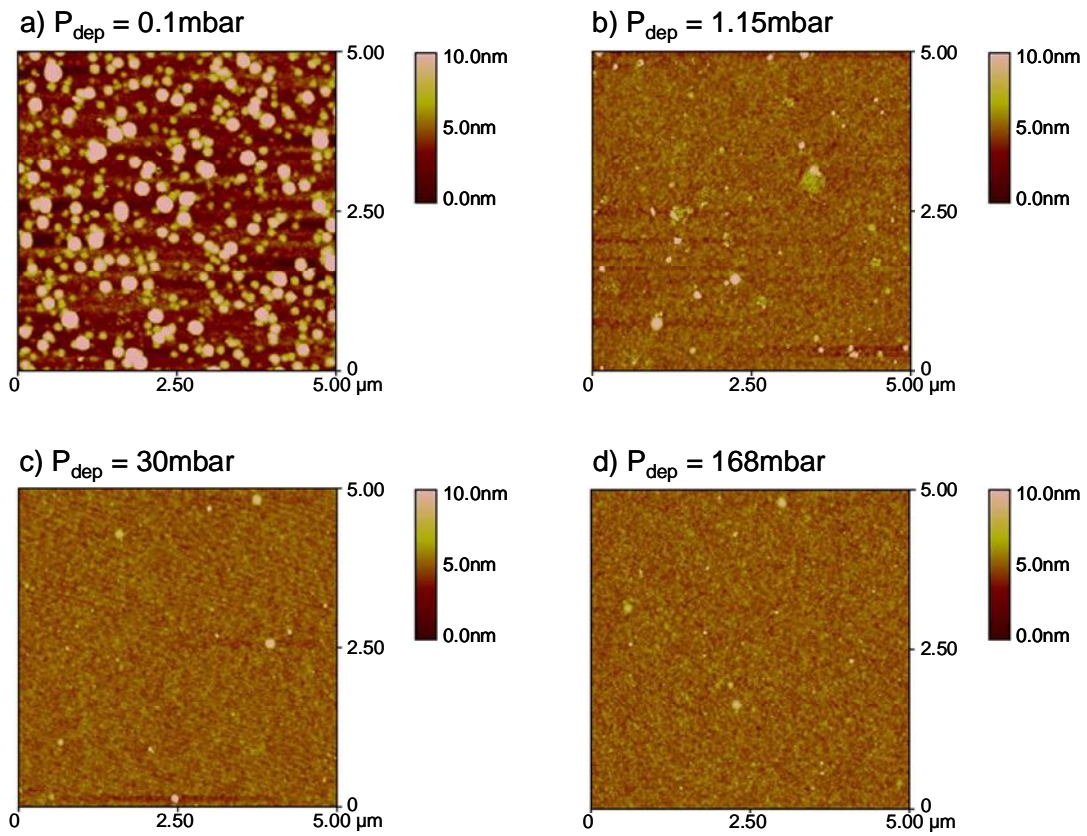
Figure 31. AFM images of Si/Si$_3$N$_4$ substrates exposed to APTMS vapour for 60 min at various deposition pressures (P$_{dep}$)

Figure 31 shows Si$_3$N$_4$ substrates modified at P$_{dep}$ = 0.1 mbar exhibit a greater amount of adsorbed aggregates than those modified at 1.15 mbar, 30 mbar and 168 mbar.
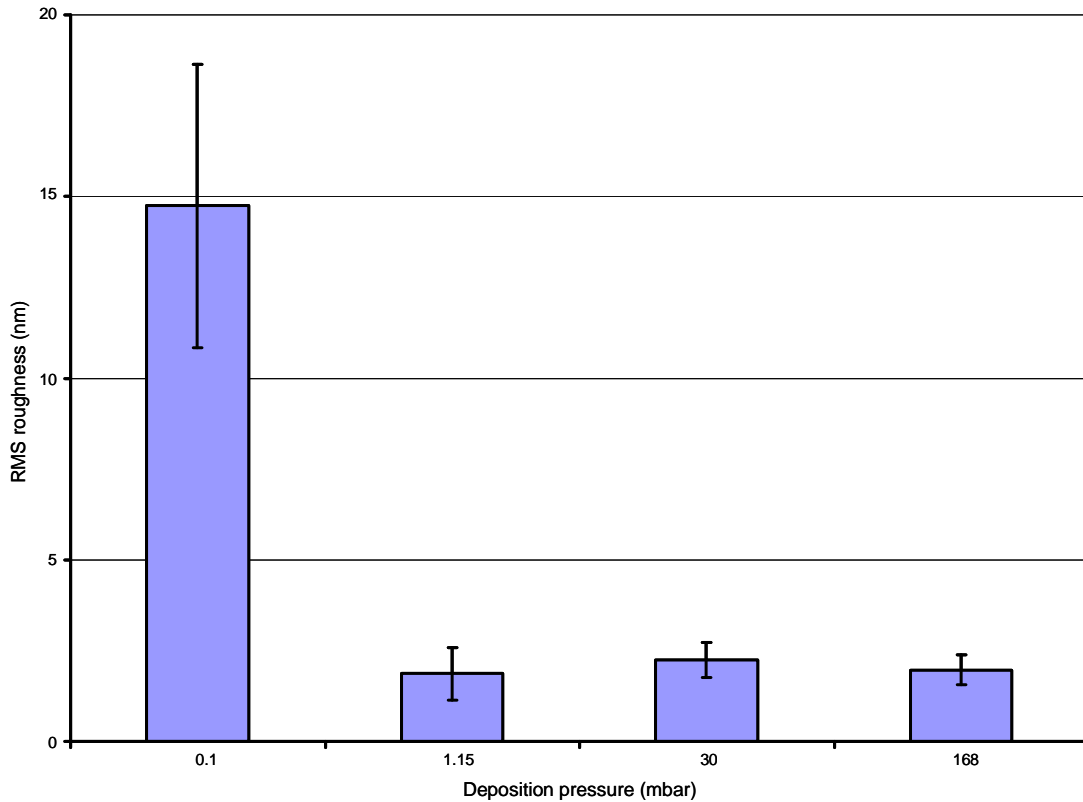
Figure 32. RMS roughness values of Si/Si$_3$N$_4$ exposed to APTMS vapour for 60 min at four different pressures

At 0.1 mbar the boiling point of APTMS is ~25 °C thus, at room temperature, the vapour will be saturated with APTMS leading to a high deposition rate of the molecules on the substrate, which is born out in its high RMS roughness (**Figure 32**).

3.3.2.3. Ellipsometry

Ellipsometric data obtained for Si$_3$N$_4$ substrates modified with APTMS vapour at different pressures is presented in **Figure 33**, ellipsometric data is not presented for surfaces modified at P$_{dep}$ = 0.1 mbar due to the large RMS

roughness (**Figure 32**) of the surfaces obtained by AFM leading to ellipsometric data yielding unreliable thickness measurements. In the case of ellipsometry unreliable thicknesses implies that the error obtained by the modelling is greater than the actual thickness value obtained.
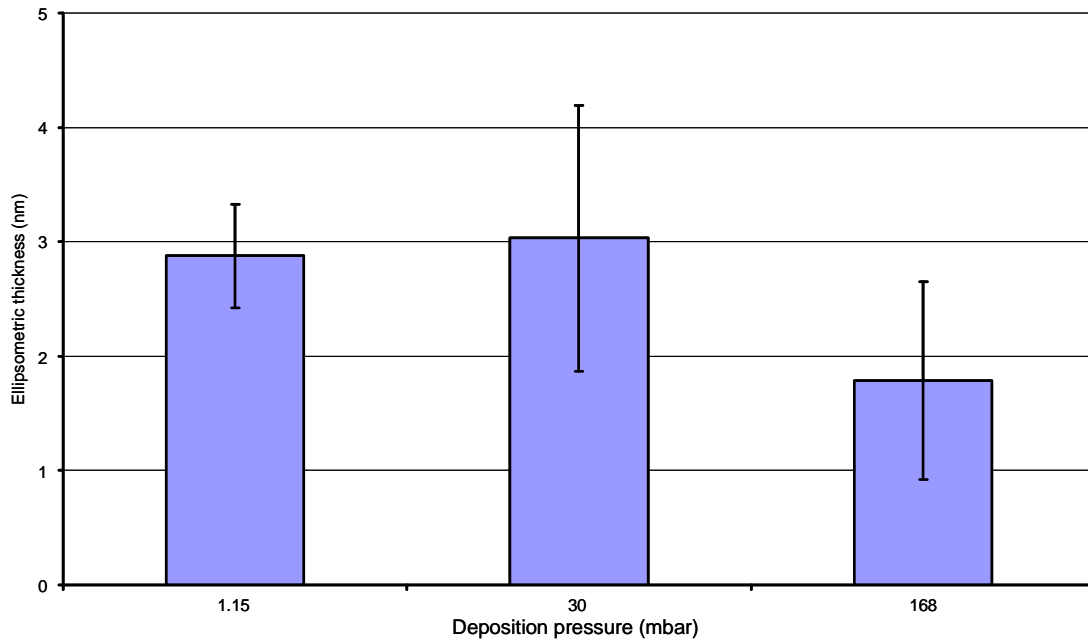
Figure 33. Ellipsometric thickness of Si/Si$_3$N$_4$ substrates exposed to APTMS vapour for 60 min at three different pressures

The ellipsometric thickness of Si$_3$N$_4$ substrates exposed to APTMS vapour at P$_{dep}$ = 1.15 mbar, 30 mbar and 168 mbar is approximately twice that of monomolecular thickness. This increase of thickness (comparing **Figure 33** to **Figure 25**) is probably due to the presence of aggregates on the surface (**Figure 31**) and the formation of multilayers (**Figure 34b**).
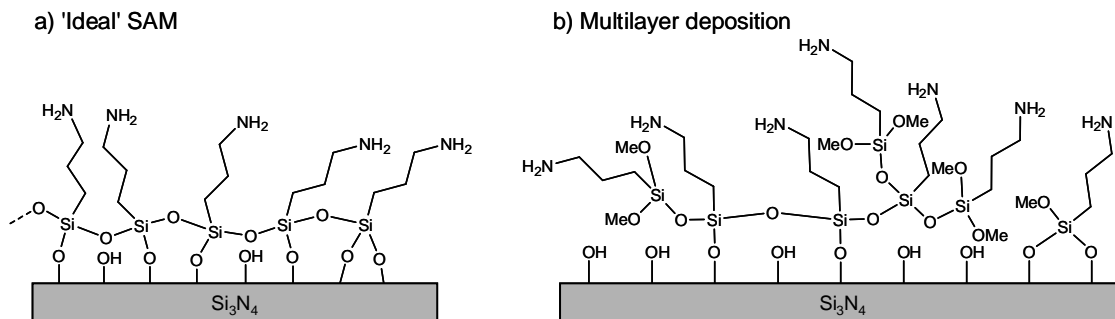
Figure 34. Schematic diagrams depicting a) an ideal APTMS SAM and b) a multilayer of APTMS

3.3.2.4. XPS

Si_3N_4 substrates exposed to APTMS vapour (**Figure 35b**) show the presence of the constituent atomic species of an APTMS molecule, however, these peaks also appear in the spectrum for bare Si/Si_3N_4 (**Figure 35a**) due to reasons discussed in **section 2.3.1.3**.
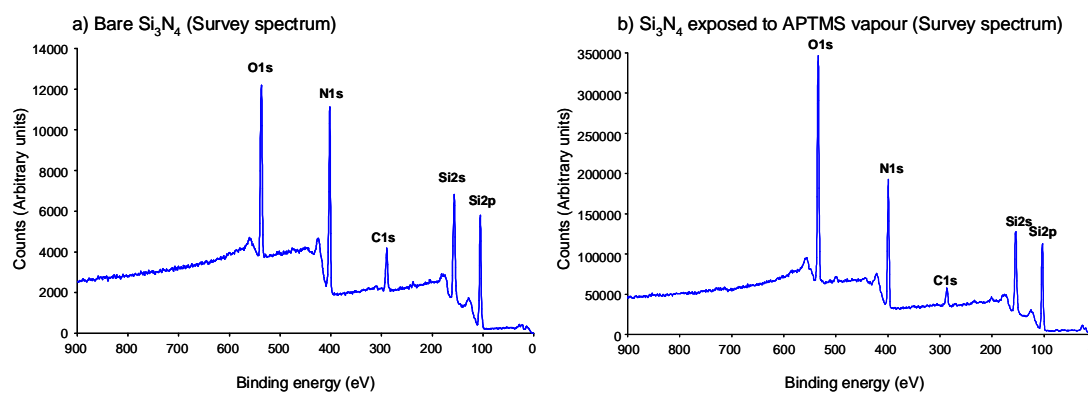
Figure 35. XPS survey spectra of Si/Si_3N_4 substrates a) before and b) after exposure to APTMS vapour for 60 min. XPS spectrum 17b) is of a sample prepared at P_{dep} = 168 mbar and is representative of survey spectra of Si/Si_3N_4 substrates exposed to APTMS vapour at all pressures studied

3.4. Conclusions

The formation of APTMS SAMs on SiO_2 and Si_3N_4 substrates from both the solution (SiO_2 and Si_3N_4) and vapour (Si_3N_4) phases have been studied. Contact angle data of SiO_2 and Si_3N_4 immersed in APTMS solution is consistent with that of a fully formed APTMS SAM found in the literature. However, upon investigation with AFM and ellipsometry immersion times of 30 min and 120 min for both substrates yielded surfaces of greater roughness and thickness than that expected of a fully formed SAM. The AFM and ellipsometric results for immersion times of 30 min and 120 min are consistent with either physisorbed bilayer structures (30 min immersion, **Figure 28a**) or surfaces on which polysiloxane aggregates adsorb (120 min immersion, **Figure 28c**). AFM and ellipsometric data do support the formation of fully formed APTMS SAMs on both SiO_2 and Si_3N_4 substrates after 60 min immersion in APTMS solution (**Figure 28b**). XPS data confirmed the adsorption of APTMS on the SiO_2 substrates but could not be used to confirm the presence of APTMS on the Si_3N_4 substrates. Therefore, APTMS structures form on SiO_2 and Si_3N_4 substrates but only 60 min immersion times result in the formation of fully formed SAMs.

The characterisation of Si_3N_4 substrates exposed to APTMS vapour show that the contact angle of substrates modified at 0.1 mbar and 1.15 mbar are significantly greater than that of a fully formed SAM formed in the solution phase due to an increase of surface roughness. The lower than expected contact angle

observed at a deposition pressure of 30 mbar is due to incomplete coverage of the underlying hydrophilic substrate by APTMS. After modification at 168 mbar the contact angle is comparable to that of a fully formed SAM thus confirming -NH$_2$ functionality of the surface. AFM data shows that deposition of APTMS at 0.1 mbar yields significantly rougher surfaces than at the other pressures studied. The greater roughness at P$_{dep}$ = 0.1 mbar is due to the adsorption of a greater number of aggregates to the surface at 0.1 mbar compared to other deposition pressure due to the reduced boiling point of APTMS at 0.1 mbar being comparable to room temperature. Therefore, the boiling of APTMS at 0.1 mbar leads to a saturated atmosphere of APTMS molecules within the chamber increasing the chance of cross linking of APTMS molecules hence a greater chance of polysiloxane aggregate formation. The ellipsometric data for 1.15 mbar, 30 mbar and 168 mbar deposition pressure is greater than that of a fully formed SAM which suggests the formation of multilayered structures.

This work has shown that fully formed SAMs can be formed from solution on both SiO$_2$ and Si$_3$N$_4$ substrates after 60 min immersion and that the vapour phase technique described in this chapter yields multilayer structures on Si$_3$N$_4$ substrates which present -NH$_2$ functionality.

The work presented in this chapter confirms that the vapour phase deposition technique described in this chapter can be used to successfully modify Si$_3$N$_4$ substrates with APTMS. The increase of contact angle data upon

exposure to APTMS vapour confirms that chemical modification of Si_3N_4 substrates is successful. AFM images show that the modified substrates are much rougher at P_{dep} = 0.1 mbar than at greater pressures (P_{dep} = 1.15 mbar, 30 mbar and 168 mbar). Ellipsometric measurements suggest monolayer formation after exposure of Si_3N_4 to APTMS solution for 60 min but, upon exposure to APTMS vapour, the formation of multilayers of APTMS may occur.

3.5. Future work

This objective of this work was to chemically modify Si_3N_4 substrates with a view to the modification of MEMS devices. Thus, the next step of this work is to modify MEMS devices using this method and this will be described in **Chapter 4**.

3.6. Experimental

All chemicals were obtained from Aldrich unless stated.

3.6.1. Cleaning of substrates

3.6.1.1. Cleaning of SiO_2

SiO_2 coated Si substrates (Compart Technology LTD) were immersed in piranha solution (70% H_2SO_4 (98%, Fisher Scientific):30% H_2O_2 (30%, Fisher

Scientific) at 90 - 100 °C for 60 min, rinsed with UHQ water (resistivity = 18 MΩcm) and immersed in RCA solution (UHQ H_2O : H_2O_2 (30%) : NH_4OH in a ratio of 5:1:1) in a sonic bath for 60 min at room temperature. The substrates were rinsed and stored in UHQ water until use.

3.6.1.2. Cleaning of Si_3N_4

Si/Si_3N_4 (500 nm thick Si_3N_4, Silson Ltd, Northampton, UK) were cleaned and hydroxylated using a method described by Wei *et al.*[23] The substrates were rinsed well in EtOH then ultra high quality (UHQ) water (resistivity = 18MΩcm). The substrates were then immersed in Piranha solution (7 parts H_2SO_4 (98%): 3 parts H_2O_2 (30%)) at 90 - 100 °C for 30 min and then rinsed thoroughly with UHQ water.

The substrates were then immersed in NaOH (0.5 M) for 20 min, HCl (0.1 M) for 10 min and NaOH (0.5 M) for 10 min and rinsed with UHQ water between each immersion. The substrates were then rinsed with HCl (0.1 M), water and then purged with $N_{2(g)}$ for 30 min.

3.6.2. Formation of SAMs

3.6.2.1. Formation of SAMs from solution phase

The first step in preparing SAMs on SiO_2 and Si_3N_4 substrates from the solution phase involved the exchange of surface water on the substrate with

anhydrous EtOH. This exchange process involves the immersion of the substrate in vials containing various ratios of EtOH and UHQ H_2O. Initially the substrate was immersed in pure UHQ water, then in water/EtOH ratios of 3:1, 1:1, 1:3, pure solvent and, finally, anhydrous EtOH.

The substrate is then immersed in a glass vial containing a 0.5 mM solution of APTMS in anhydrous EtOH under a N_2 atmosphere and placed in a water cooled sonic bath. After immersion for a given time the substrate was immediately rinsed in EtOH and then rinsed in toluene, EtOH, then placed in a clean vial containing fresh EtOH and placed in a sonic bath for 5 min. This rinsing and sonication process was repeated and then the substrate was rinsed sequentially in EtOH, chloroform and EtOH and cured in a vacuum oven at 120 °C for 30 min.

3.6.2.2. Formation of SAMs from vapour phase

The vapour deposition steps used for the formation of APTMS SAMs on Si_3N_4 is described in **section 3.2.2.** After the vapour deposition the substrates were removed from the chamber and rinsed sequentially in EtOH, chloroform and EtOH then cured in a vacuum oven at 120 °C for 30 min.

3.6.3. Characterisation of SAMs

3.6.3.1. Contact angle analysis

Contact angle measurements were carried out using a home built contact angle goniometer and the images processed using Camtel FTA200 software. UHQ water was applied to the surface using a 25 μl syringe. The volume of the drop was increased and decreased in order to obtain information about the advancing (θ_a) and receding (θ_r) contact angles, respectively.

3.6.3.2. AFM

AFM images were obtained using a Dimension D3100 Scanning Probe Microscope (Veeco) and the images analysed using Nanoscope III v5.12r software. All AFM images were obtained by operating the AFM in tapping mode with the use of RTESP – Tap300 Metrology Probes (Veeco) (nominal spring constant = 20 - 80 Nm^{-1}, nominal resonant frequency = 288 - 328 kHz).

3.6.3.3. Ellipsometry

Ellipsometry measurements were taken using a Jobin-Yvon UVISEL ellipsometer with a He-Ne laser light source at an angle of incidence of 70 °C

using a wavelength range of 450 – 800 nm. SAMs were formed. DeltaPsi software was used to record and model the ellipsometric parameters Δ and ψ, for bare and modified substrates.

3.6.3.4. XPS

XPS measurements were performed using a VG ESCALab 250 equipped with an Al K_{α} x-ray source (1486.68 eV) which was operated at 15 kV. Peak fitting and analysis of the data was carried out using Avantage software.

3.7. References

1. Hamlett, C. A. E.; Critchley, K.; Gorzny, M.; Evans, S. D.; Prewett, P. D.; Preece, J. A., Vapour phase formation of amino functionalised Si_3N_4 surfaces, *Surf. Sci.* **2008**, 602, 2724-2733.

2. Ulman A., *An Introduction to Ultrathin Organic Films from Langmuir-Blodgett to Self-Assembly*. Adademic Press Limited: London, 1991.

3. C. Chu-jiang; S. Zhi-gang; X. Yu-shan; M. Shu-lin, Surface topography and character of γ-aminopropyltrimethoxysilane and dodecyltrimethoxysilane films adsorbed on the silicon oxide substrate *via* vapour phase deposition. *J. Phys. D* **2006,** 39, 4829-4837.

4. Carraro C.; Yauw O. W.; Sung M. M.; Maboudian R., Observation of three growth mechanisms in self-assembled monolayers. *J. Phys. Chem. B* **1998,** 102, 4441-4445.

5. Hooper A. E.; Werho D.; Hopson T.; Palmer O., Evaluation of amine- and amide-terminated self-assembled monolayers as 'molecular glues' for Au and SiO$_2$ substrates. *Surf. Interface Anal.* **2001,** 31, 809-814.

6. Sung M. M.; Kluth G. J.; Maboudian R., Formation of alkylsiloxane self-assembled monolayers on Si$_3$N$_4$. *J. Vac. Sci. Technol. A* **1999,** 17, 540-544.

7. Wang Y. L.; Lieberman M., Growth of ultrasmooth octadecyltrichlorosilane self-assembled monolayers on SiO$_2$. *Langmuir* **2003,** 19, 1159-1167.

8. Zhang F.; Srinivasan M. P., Self-assembled molecular films of aminosilanes and their immobilization capacities. *Langmuir* **2004,** 20, 2309-2314.

9. Petri D. F. S.; Wenz G.; Schunk P.; Schimmel T., An improved method for the assembly of amino-terminated monolayers on SiO$_2$ and the vapour deposition of gold layers. *Langmuir* **1999,** 15, 4520-4523.

10. Flink S.; van Veggel F. C. J. M.; Reinhoudt D. N., Functionalization of self-assembled monolayers on glass and oxidized silicon wafers by surface reactions. *J. Phys. Org. Chem.* **2001,** 14, 407-415.

11. Mendes P. M.; Belloni M.; Ashworth M.; Hardy C.; Nikitin K.; Fitzmaurice D.; Critchley K.; Evans S. D.; Preece J. A., A novel example of X-ray-radiation induced chemical reduction of an aromatic nitro-group-containing thin film on SiO$_2$ to an aromatic amine film. *ChemPhysChem* **2003,** 4, 884-889.

12. Barriga J.; Coto B.; Fernandez B., Molecular dynamics study of optimal packing structure of OTS self-assembled monolayers on SiO$_2$ surfaces. *Tribol. Int.* **2007,** 40, (6), 960-966.

13. Mendes P. M.; Jacke S.; Critchley K.; Plaza J.; Chen Y.; Nikitin K.; Palmer R. E.; Preece J. A.; Evans S. D.; Fitzmaurice D., Gold nanoparticle patterning of silicon wafers using chemical e-beam lithography. *Langmuir* **2004,** 20, 3766-3768.

14. Ito T.; Namba M.; Bühlmann P.; Umezawa Y., Modification of silicon nitride tips with trichlorosilane self-assembled monolayers (SAMs) for chemical force microscopy. *Langmuir* **1997,** 13, 4324-4332.

15. Tsukruk V. V.; Bliznyuk V. N., Adhesive and friction forces between chemically modified silicon and silicon nitride surfaces. *Langmuir* **1998,** 14, 446-455.

16. Kim J.-M.; Baek C.-W.; Park J.-H.; Shin D.-S.; Lee Y.-S.; Kim Y.-K., Continuous anti-stiction coatings using self-assembled monolayers for gold microstructures. *J. Micromech. Microeng.* **2002,** 12, 688-695.

17. Zhuang Y. X.; Hansen O.; Knieling T.; Wang C.; Rombach P.; Lang W.; Benecke W.; Kehlenbeck M.; Koblitz J., Thermal stability of vapour phase deposited self-assembled monolayers for MEMS anti-stiction. *J. Micromech. Microeng.* **2006,** 16, 2259-2264.

18. McLellan J. M.; Geissler M.; Xia Y., Self-assembly of hexadecanethiol molecules on gold from the vapour phase as directed by a two-dimensional array of silica beads. *Chem. Phys. Lett.* **2005,** 408, 80-83.

19. Owens T. M.; Süzer S.; Banaszak Holl M. M., Variable energy X-ray photoemission studies of alkylsilane based monolayers on gold. *J. Phys. Chem. B* **2003,** 107, 3177-3182.

20.   Sugimura H.; Hozumi A.; Kameyama T.; Takai O., Organosilane self-assembled monolayers formed at the vapour/solid interface. *Surf. Interface Anal.* **2002,** 34, 550-554.

21.   Fadeev A. Y.; McCarthy T. J., Self-assemble is not the only reaction possible between alkyltrichlorosilanes and surfaces: Monomolecular and oligomeric covalently attached layers of dichloro- and trichloroalkylsilanes on silicon. *Langmuir* **2000,** 16, 7268-7274.

22.   Bunker B. C.; Carpick R. W.; Assink R. A.; Thomas M. L.; Hankins M. G.; Voigt J. A.; Sipola D.; de Boer M. P.; Gulley G. L., The impact of solution agglomeration on the deposition of self-assembled monolayers. *Langmuir* **2000**, 16, 7742-7751.

23.   Wei. Z. Q.; Wang C.; Bai C. L., Surface imaging of fragile materials with hydrophilic atomic force microscope tips. *Surf. Sci.* **2000,** 467, 185-190.

24.   NIST X-ray photoelectron spectroscopy database. *http://srdata.nist.gov/xps/*.

25.   Banga R.; Yarwood J.; Morgan A. M.; Evans B.; Kells J., FTIR and AFM studies of the kinetics and self-assembly of alkyltrichlorosilanes and (perfluoroalkyl)trichlorosilanes onto glass and silicon. *Langmuir* **1995,** 11, 4393-4399.

26.   Hoque E.; DeRose J. A.; Hoffman P.; Bhushan B.; Mathieu H. J., Chemical stability of nonwetting, low adhesion self-assembled monolayer films formed by perfluoroalkylsilinization of copper. *J. Chem. Phys.* **2007,** 126, 114706 (8pp).

27.   Müller B.; Riedel M.; Michel R.; DePaul S. M.; Hofer R.; Heger D.; Grützmacher D., Impact of nanometer-scale roughness on contact-angle

hysteresis and globulin adsorption. *J. Vac. Sci. Technol. B* **2001,** 19, 1715-1720.

3.8. Acknowledgments

CHAPTER 4

Mass sensing using a chemically modified microresonator: SAMs meets MEMS

CHAPTER 4

Mass sensing using a chemically-modified microresonator:

SAMs meets MEMS

ABSTRACT: Micro-Electromechanical Systems (MEMS) are devices whereby mechanical and electrical components in the micrometre regime have been integrated. Such devices show promise in a wide variety of sensing applications. Self-assembled monolayers (SAMs) can be used to functionalise the surface of MEMS devices in order to fabricate chemically specific mass sensing devices.

This work investigates the pH-dependent adsorption of citrate passivated Au nanoparticles on silicon nitride surfaces modified with 3-aminopropyltrimethoxysilane (APTMS) SAMs using both atomic force microscopy (AFM) and X-ray photoelectron spectroscopy (XPS) analysis. The AFM and XPS results are used as a comparison for mass adsorption data of the citrate passivated Au nanoparticles adsorbed on MEMS resonators modified using SAMs.

4.1. Introduction

Microelectromechanical systems (MEMS), as introduced in **Chapter 1 (section 1.3.1.)**, are formed by the integration of electrical and mechanical components for production of functional micron-scale devices.[1] Examples of the use of MEMS devices include actuators[2, 3] and sensors.[4-16]

MEMS devices can be used as chemical sensors using two different approaches. One approach is by mass detection,[7, 13, 17, 18] whereby the resonant frequency of a MEMS resonator is altered upon the adsorption of chemical species. The resultant change of resonant frequency is directly proportional to the mass adsorbed on its surface, hence the mass of the adsorbed species can be calculated using knowledge of the mass sensitivity of the device. Such devices operate on a similar principle to both quartz crystal microbalances (QCM)[19, 20] and surface acoustic wave (SAW) devices.[21, 22] The species adsorbed on the surface of MEMS mass detection devices is dictated by the surface chemistry of the resonators. SAMs have been used in an attempt to immobilize specific species to the surface of MEMS sensors.[5, 9, 11, 12, 14]

Another approach to chemical detection, using MEMS devices, exploits the change of the electrical properties of the device upon adsorption of specific chemical species.[8, 9, 11, 12, 16] Electronic properties, for example the electrical resistance, can be altered by the adsorption of analytes. Therefore, this allows MEMS sensors to be integrated into electrical circuits in order to monitor the change of electronic properties of the device over a period of time.

4.2. Aims and objectives

The aim of the research described in this chapter is to demonstrate that the vapour phase methodology described in **chapter 3** can be used to modify

microresonators for their application as mass-sensing devices. Chemical functionalization of microresonators could have applications in determining the abundance of specific species in local environments, for example in local urban environments. Citrate passivated Au nanoparticles have been shown to exhibit pH dependent adsorption to -NH_2 terminated SAMs.[23] Therefore, the work presented in this chapter is aimed at showing how the adsorption of citrate passivated Au nanoparticles on 3-aminopropyltrimethoxysilane (APTMS) modified Si_3N_4 resonators changes as a function of the pH of the nanoparticle solution. Upon immersion in an acidic solution of citrate passivated Au nanoparticles the -NH_2 terminus of the monolayer becomes protonated. Therefore, a positive surface is presented to the local environment allowing the electrostatic attraction of the negatively charged Au nanoparticles (**Figure 36**).
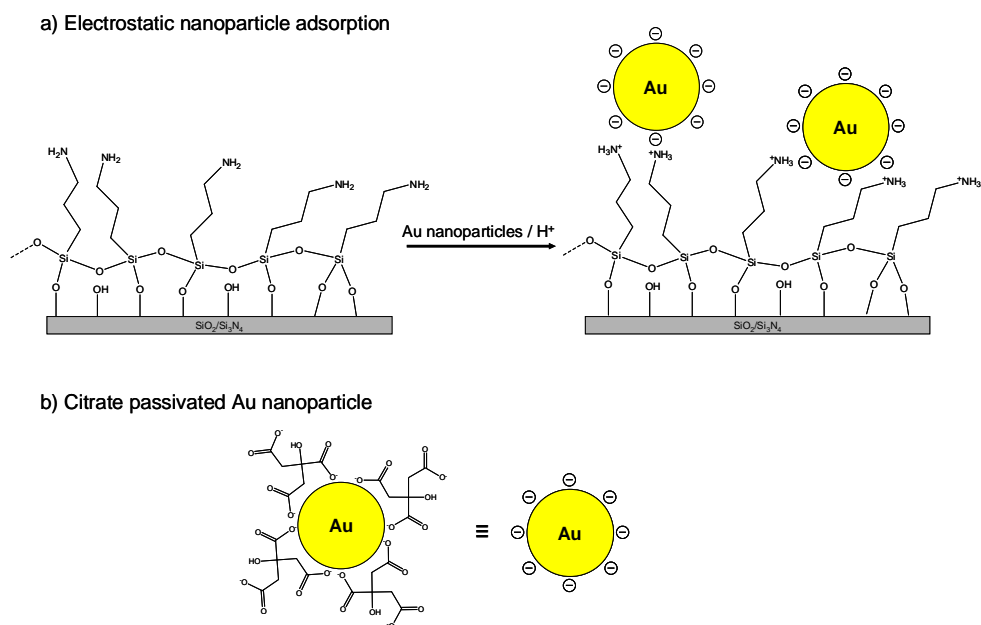
Figure 36. Cartoon representations of a) the electrostatic adsorption of citrate passivated Au nanoparticles to a protonated APTMS SAM, and b) the negatively charged citrate passivated nanoparticle

By using both AFM and XPS analysis to study the adsorption of citrate passivated Au nanoparticles to APTMS modified Si_3N_4 substrates over a range of pH values, the trend of nanoparticle adsorption for this particular system can be evaluated. Thus, providing both a reference of the pH dependent adsorption of citrate passivated Au nanoparticles to Si_3N_4 resonators modified with APTMS SAMs and a proof-of-principle experiment that modified microresonators can be used as mass sensors for nanoparticles.

4.3. Results and discussion

This section presents data on the adsorption of citrate passivated Au nanoparticles from solution to chemically modified Si_3N_4 substrates investigated by both AFM and XPS analysis. Resonance experiments were also performed in order to investigate the adsorption of citrate passivated Au nanoparticles on APTMS modified Si_3N_4 resonators with a view to using such a system as a mass sensitive detector.

4.3.1. Au nanoparticle adsorption studies

4.3.1.1. AFM

AFM images were obtained of Si_3N_4 substrates, modified with APTMS SAMs, after immersion for 2 hr in aqueous solutions of citrate passivated Au

nanoparticles at five different values (3, 4, 5, 6, and 7) of pH (**Figure 37a-e**) and a graph of nanoparticle density vs the pH is shown in **Figure 38**.

After immersion of APTMS modified Si_3N_4 substrates in citrate passivated Au nanoparticles at pH values of 3 and 4 (**Figure 37a and b**) it can be seen that the occurrence of Au nanoparticle aggregates adsorbed on the surface is more pronounced than at higher values of pH (**Figure 37c-e**). Presumably the occurrence of a higher degree of nanoparticulate aggregates at pH values of 3 and 4, compared to pH values 5 - 7, is due to a higher degree of protonation of the passivating citrate anions thus, a lower degree of electrostatic repulsion between the particles. The maximum adsorption of citrate passivated Au nanoparticles occurs at pH 5 (**Figure 37c and Figure 38**) which is consistent with previous work in optimal adsorption of citrate passivated Au nanoparticles occurs at pH 4.5.[23]
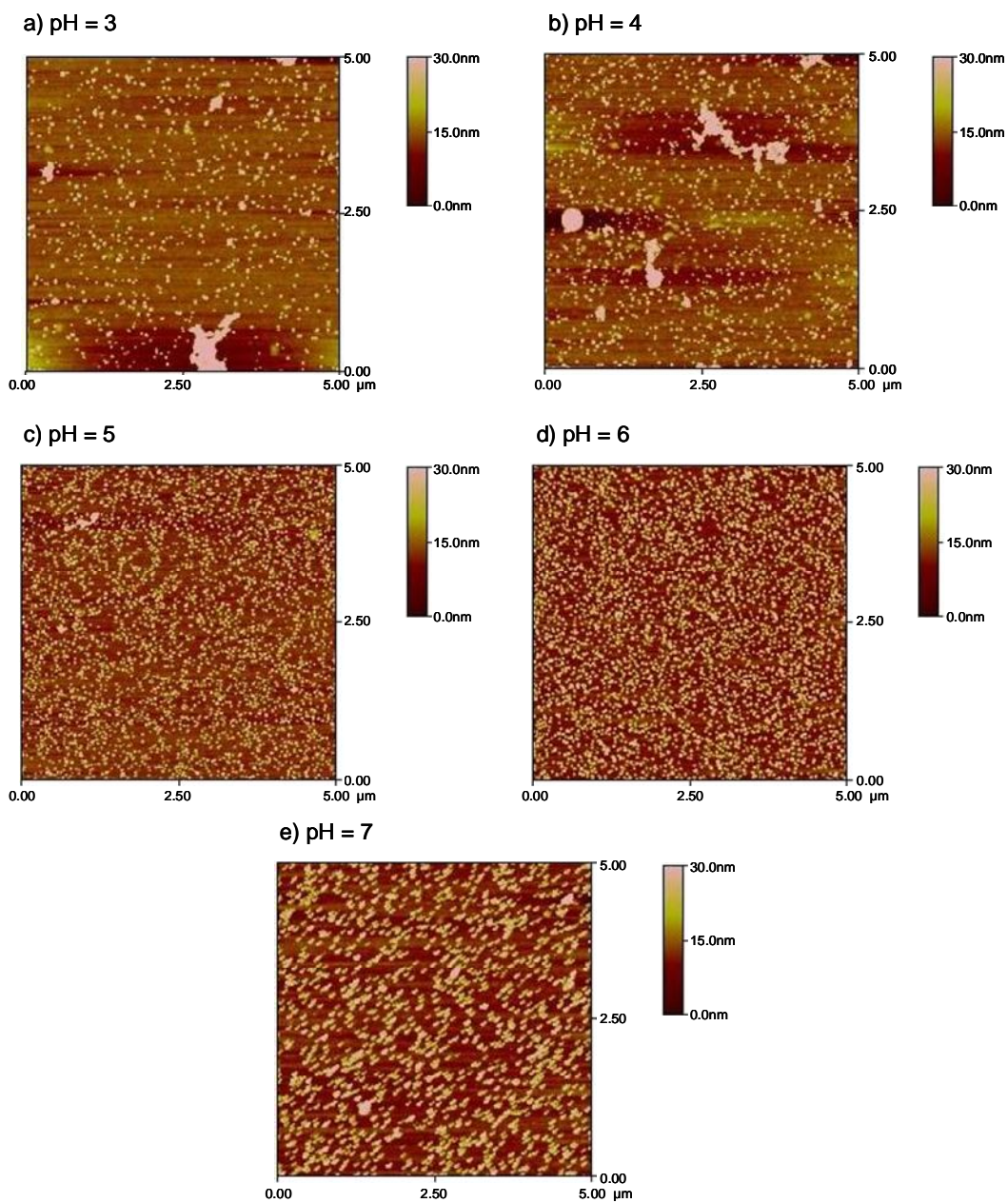
Figure 37. AFM images of pH dependent adsorption of citrate passivated nanoparticles on APTMS modified Si_3N_4 substrates at five different values of pH
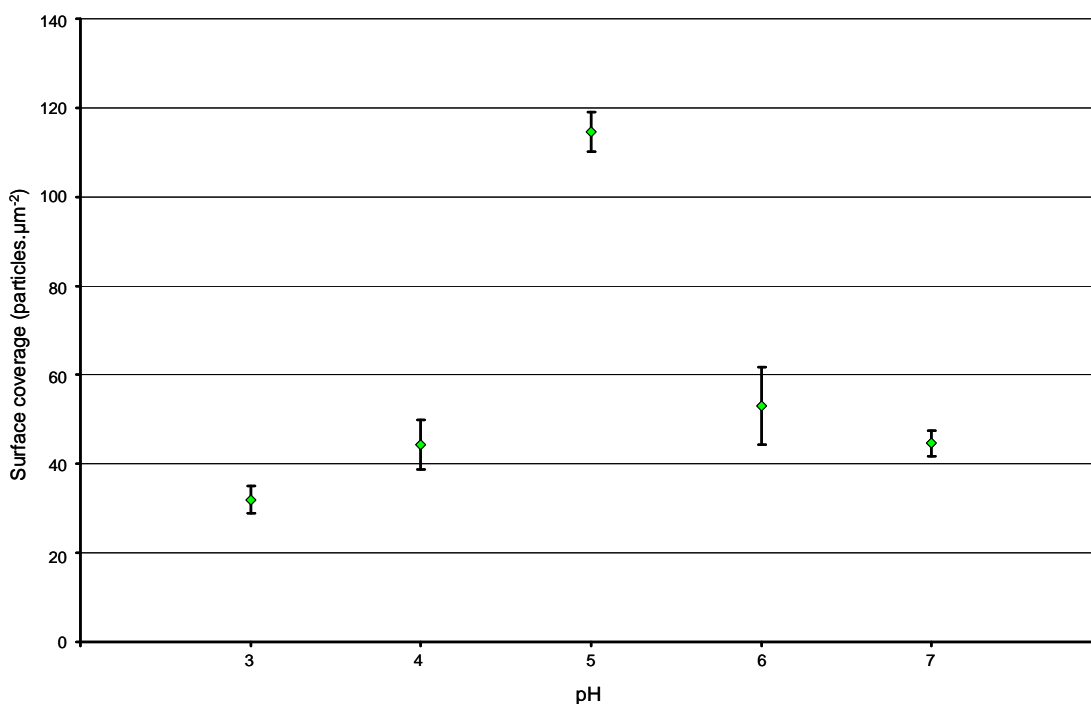
Figure 38. Graph showing particle density vs pH of citrate passivated Au nanoparticles adsorbed onto APTMS modified Si_3N_4 substrates

It was observed that the maximum adsorption of citrate passivated Au nanoparticle occurs at pH 5 (**Figure 37** and **Figure 38**). The pK_a of aliphatic amine groups is 8 - 11 in free solution,[24] however when attached to a surface the pK_a decreases to 6 - 8.[25] The pK_a of COOH groups in free solution is ~4.8.[26] Therefore, over the range of pH values studied (pH 3 - 7) the APTMS SAM will be fully protonated in the pH range of 3 - 6 and partially protonated at pH 7. The citrate passivated Au nanoparticles display COOH moieties on their surfaces and therefore the majority of the particles will be deprotonated in the pH range of 5 - 7. At pH values of 3 and 4 the COOH groups will not be fully deprotonated hence, the repulsive electrostatic forces no longer exist between the particles, leading to aggregation of the nanoparticles as observed by AFM (**Figure 37**).

The protonated Au nanoparticles do not lend themselves to electrostatic attachment to the protonated APTMS SAMs, although hydrogen bonding will occur, and hence there is low nanoparticle adsorption at pH values of 3 and 4. The maximum adsorption of Au nanoparticles occurs at pH 5, which is due to the citrate passivated nanoparticles being negatively charged at this pH and therefore binding to the protonated $-^+NH_3$ surface. However, at pH 6 and 7 nanoparticle adsorption is not as high as that observed at pH 5. This observation is due to the Au nanoparticle becoming increasingly deprotonated as the pH increases, so nanoparticles adsorbed to the APTMS SAM could hinder other negatively charged particles from adsorbing to the surface due to electrostatic repulsion.

4.3.2.2. XPS

In this chapter the AFM is used to probe an area of 5 µm x 5 µm. XPS spectroscopy analyses a spot size of approximately 0.5 mm in size and hence, is a much more accurate method of determining the structure of a surface. However, AFM analysis yields images of the surface. Therefore, the XPS analysis presented in this chapter is used to corroborate the AFM data.

XPS spectra were recorded of APTMS modified Si_3N_4 substrates after immersion in solutions of citrate passivated Au nanoparticles over the pH range 3 - 7. The Au4f spectra (**Figure 39**) and Si2p spectra, shown in **Appendix B2**,

were used to calculate the Au/Si ratio in order to determine the relative change of nanoparticle adsorption. The Au/Si ratios were used to study the adsorption of Au nanoparticles using the Si substrate as an internal standard, assuming that this is constant.
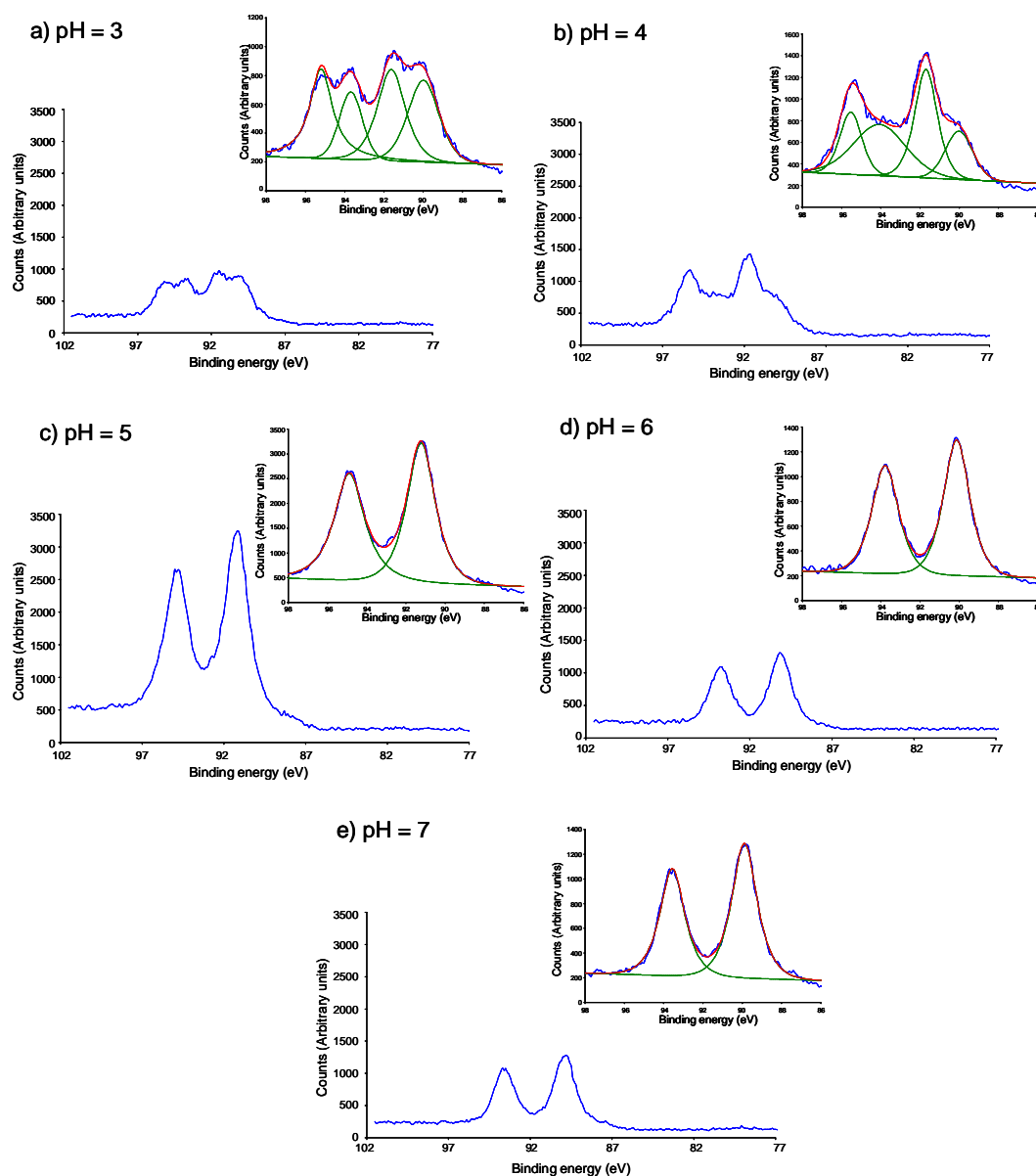
Figure 39. Au4f XPS spectra of APTMS modified Si₃N₄ substrates with citrate passivated Au nanoparticles adsorbed at a) pH 3, b) pH 4, c) pH 5, d) pH 6 and e) pH 7. Insets in each image shows the peak fitting.

Table 3. Binding energies of $Au4f_{5/2}$ and $Au4f_{7/2}$ peaks for the adsorption of citrate passivated Au nanoparticles on APTMS SAMs at 5 different values of pH. (Also shown is the average binding energy for the $Au4f_{5/2}$ and $Au4f_{7/2}$ peaks of bulk Au from the NIST database[27])

pH	Binding energy (eV)			
	$Au4f_{5/2}$		$Au4f_{7/2}$	
3	93.7	95.1	90.2	91.5
4	93.8	95.6	90.4	91.6
5	94.8		91.1	
6	93.7		90.1	
7	93.6		89.8	
Bulk Au[27]	84.0		87.7	

Figure 39 shows the Au4f spectra at each value of pH at which nanoparticle adsorption was carried out and shows a maximum Au intensity at pH 5 (**Figure 39c**). A splitting of the $Au4f_{5/2}$ and $Au4f_{7/2}$ peaks can be seen at pH values of 3 and 4 (**Figure 39a** and **Figure 39b,** respectively). However, this peak splitting is not evident at higher values of pH. **Table 3** shows that both the $Au4f_{5/2}$ and $Au4f_{7/2}$ peaks show an increased binding energy compared to that of bulk Au which can be explained by surface charging during the XPS measurement due to the substrate, Si_3N_4, being a poor conductor. During the XPS measurements photoelectrons are ejected from the sample resulting in the sample becoming slightly positively charged. As the substrate is a poor conductor the surface charge cannot dissipate. Therefore, the surface becomes positively charged and leads to a shift in the binding energy towards higher values, as greater energy is required for a photoelectron to leave the surface.[28]

Peak splitting has been shown to occur due to charging of the surface.[29] Therefore, the extra positive charge of the surfaces immersed in low pH solutions (pH 3 and 4) will have a more positively charged surface than those immersed in solutions of higher values of pH (i.e. 5, 6 and 7). Therefore, this extra charging may induce peak splitting. Another factor that could induce peak splitting is the presence of nanoparticulate aggregates. These aggregates can be seen adsorbed to the APTMS SAMs after the immersion was performed at pH 3 and 4 (**Figure 37a** and **b**) and concur with the splitting of the Au4f peaks in the XPS spectra (**Figure 39a** and **b**). A possible explanation for the formation of such aggregates is that at pH values below 5 the citrate passivants could become protonated, hence negating the repulsive force between the nanoparticles. The binding energy of discrete Au nanoparticles has been shown to be slightly higher (a few eV) than bulk Au.[30] The formation of nanoparticulate aggregates may result in the presence of 'bulk' Au in the system. Thus, the splitting of the Au4f peaks reflects the presence of 'bulk' Au (aggregates) and nanoparticulate Au (discrete nanoparticles).

Figure 40 shows that the maximum Au/Si ratio occurs at pH ~ 5 which shows that the maximum nanoparticle adsorption occurs at pH ~ 5. This result concurs with the AFM data (**Figure 38**).
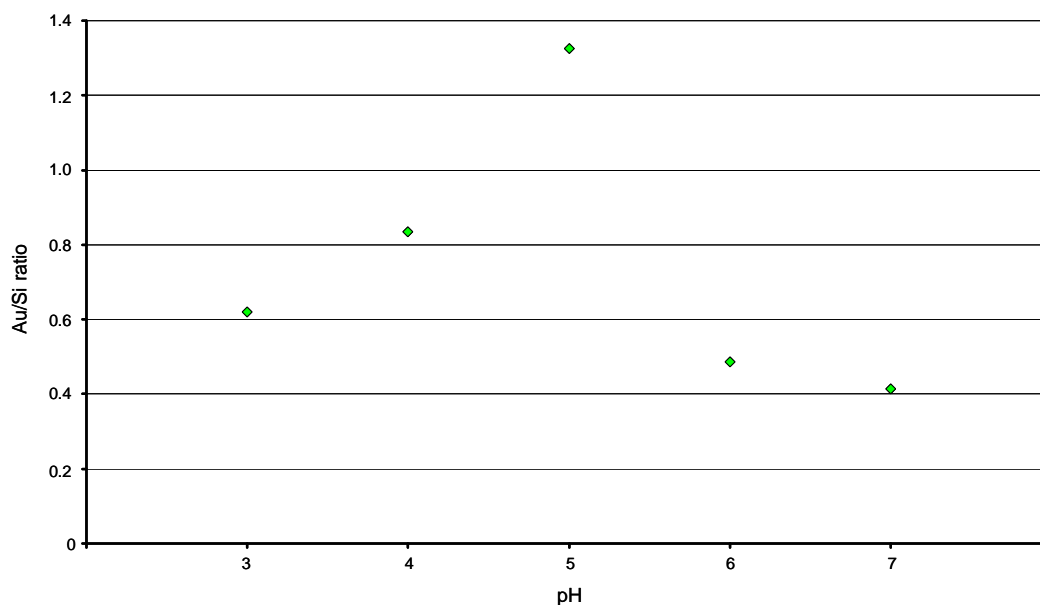
Figure 40. Graph showing the Au/Si ratio vs pH of citrate passivated Au nanoparticles adsorbed onto APTMS modified Si_3N_4 substrates

4.3.2.3. Mass adsorption measurements

Initial mass adsorption measurements were made by measuring the frequency shift of simple 'flap' type resonators (**Figure 41**) at three different pH values. These devices were excited by mounting the device to a piezoelectric chip in an SEM which was connected to a vibrometer. Careful tuning of the drive frequency, coupled with real time observation under the SEM, of the piezoelectric crystal allowed the resonant frequency to be found once the edge of the flap became blurred.
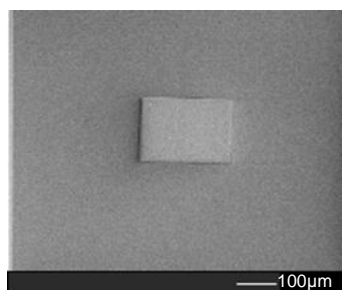
a) SEM image of flap resonator

b) Bare resonator

Resonant frequency = F_{R1}

c) SAM formed on resonator

Resonant frequency = F_{R2}

d) Nanoparticles adsorbed on resonator

Resonant frequency = F_{R3}
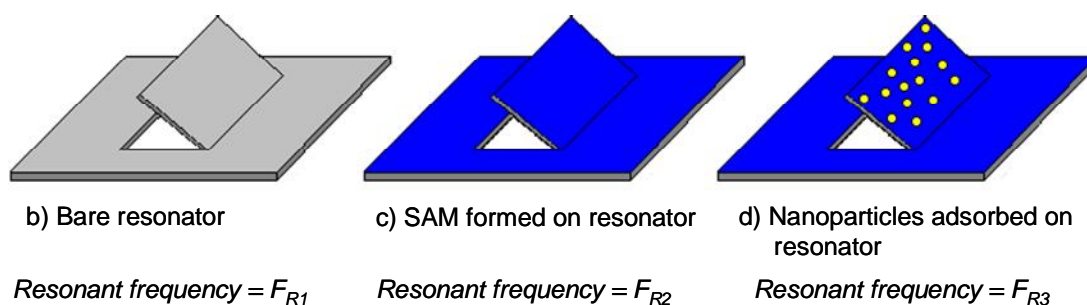
Figure 41. a) An SEM image of the 'flap' type resonator and b) - d) the frequencies measured in order to calculate mass adsorption

The devices were calculated to have a frequency shift of 590 Hz/10^{-8}g. Therefore, this value was used to calculate the masses adsorbed on the resonators once the frequency shift was determined. **Figure 42** indicates maximum nanoparticle adsorption at pH 5, in agreement with the AFM and XPS data (**Figure 38** and **Figure 40** respectively) though the difference in absorbance between pH 5 and 6 is not as pronounced as shown in **Figure 38** and **Figure 40**.
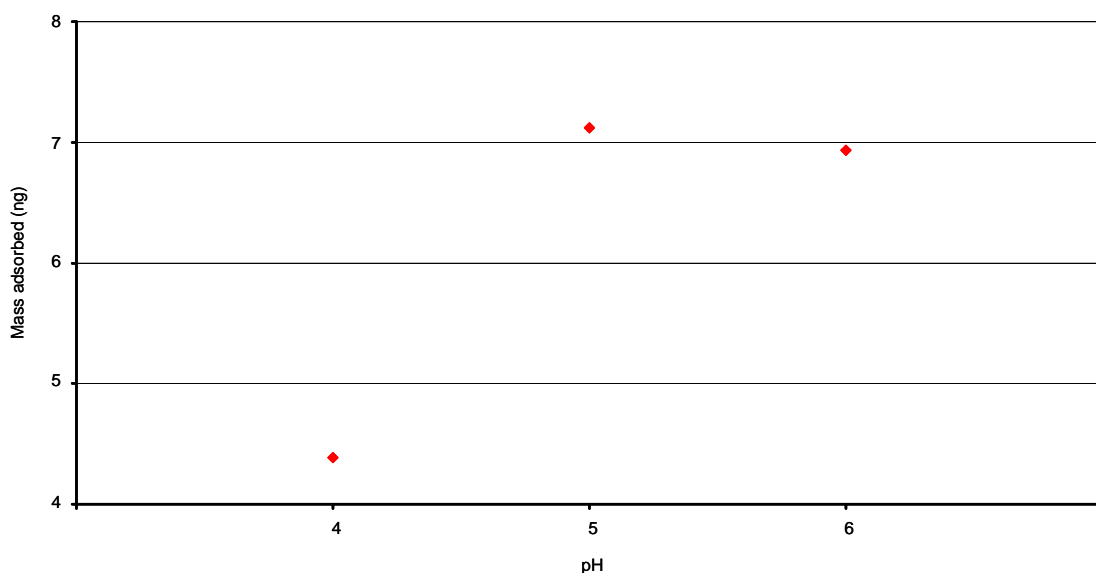
Figure 42. Graph showing the mass of citrate passivated Au nanoparticles adsorbed on APTMS modified Si_3N_4 'flap' resonators vs pH.

4.4. Conclusions

The aim of this chapter was to show that the pH dependent adsorption of citrate passivated Au nanoparticles can be used as a model system for the development of MEMS nanoparticulate mass sensors. The work presented in this chapter shows that the degree of adsorption of citrate passivated Au nanoparticles to APTMS SAMs, formed on Si_3N_4 substrates, changes as a function of pH. AFM investigations shows that maximum adsorption of nanoparticles occurs at pH 5 with nanoparticle aggregation common at pH 3 and 4 (**Figure 37** and **Figure 38**). XPS investigations show that the Au 4f spectrum follows the aggregation of Au nanoparticles by the presence of two distinct peaks

(pH 5, 6 and 7) which then split upon aggregation of Au nanoparticles at pH 3 and 4 (**Figure 39**). XPS analysis was also used to obtain a graph of the Au/Si ratio as a function of pH (**Figure 40**) which shows that maximum Au nanoparticle coverage of an APTMS SAM occurs at pH 5. This result is in agreement with the AFM data and provides a model with which to compare the results of mass adsorption experiments. The mass adsorption experiments (**Figure 41**) were carried out on chemically modified Si_3N_4 cantilevers by measuring the resonant frequencies of the devices before and after immersion in aqueous solutions of citrate passivated Au nanoparticles at different values of pH. The results of the mass adsorption experiments (**Figure 42**) confirmed maximum adsorption of the Au nanoparticles at pH 5 which is in good agreement with both the AFM and XPS data. Therefore, the nanoparticle / SAM system, studied in this chapter, shows potential for use as a proof-of-principle system for the development of a MEMS nanoparticle mass sensing device.

4.5. Future Work

The work presented in this chapter has shown that simple resonators (**Figure 41**), with a 'flap' type architecture, can be successfully functionalised with APTMS SAMs and shown to act as mass-sensing devices. However, the next stage of this project will be to use a similar methodology in order to modify resonators with a high Q-factor, in order to fabricate highly sensitive mass-detecting MEMS devices. The Q-factor is a measure of the damping of the

oscillation of a MEMS device and relates to energy loss due to friction, from both internal and external influences, upon resonance. Resonators with high Q-factors exhibit a clear resonance signal that is easily recognisable from the background noise.[31] A paddle resonator (**Figure 43a**), fabricated using a FIB and comprising of a Si_3N_4 paddle resonator with a platinum wire around its periphery (**Figure 43b**), has been shown to exhibit a high Q-factor.[32, 33] Therefore, such a device will be chemically modified with APTMS SAMs and used to detect citrate passivated Au nanoparticles and the results compared to those presented in this chapter.
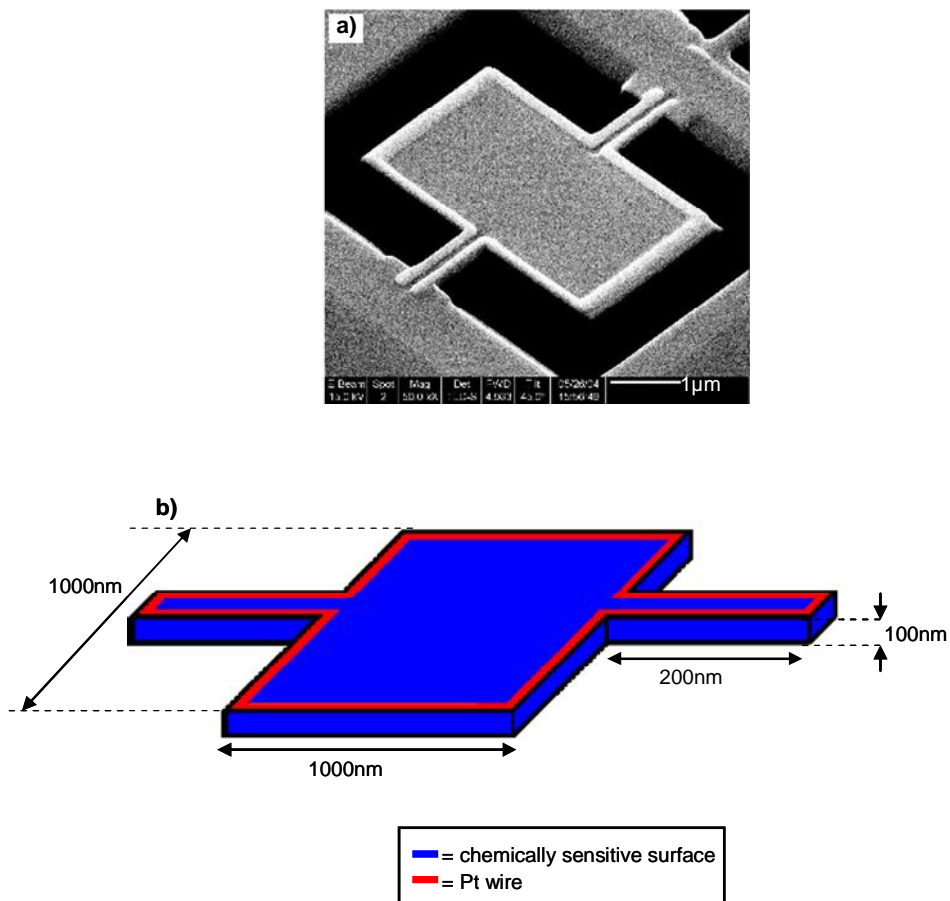
Figure 43. a) an SEM image of the proposed device for mass detection and b) a cartoon representation of the architecture and dimensions of the proposed device

The use of the paddle resonators to detect gaseous species could be performed by modifying the resonators with SAMs other than APTMS. For example SAMs of phthalocyanines (Pc) derivatives could be investigated for the detection of gaseous NO_2, a common pollutant. Previous work by Simpson *et al.*[34, 35] has shown that Pc derivatives can be used to detect NO_2 by either surface plasmon resonance[34] or evanescent wave excited fluorescence.[35] Therefore, Pc derivatives could be attached to the paddle resonators in order to detect NO_2 by mass detection.

4.6. Experimental

All chemicals were obtained from Aldrich unless stated.

4.6.1. Preparation of citrate passivated Au nanoparticles

An aqueous solution of citrate passivated Au nanoparticles was prepared by the method described by Frens[36] to yield particles with a diameter of 16 nm.[36] Chloroauric acid (0.01 g, 2.5 mmol) was dissolved in UHQ water (100 ml) and heated to reflux. Sodium citrate tribasic dihydrate (0.023 g, 0.15 mol) was added to the chloroauric acid solution at reflux. The system was left at reflux until there was no further colour change. The solution was allowed to cool to room temperature, centrifuged (at 3500 rpm) and the supernatant retained.

4.6.2. Adsorption studies

4.6.2.1. Changing the pH of the solutions

Aqueous solutions of NaOH (1 mM) (Fisher Scientific) and HCl (1 mM) (37 %, Fisher Scientific) were prepared and used as stock solutions for the pH adjustment of the citrate passivated Au nanoparticle solutions. The pH values of the solutions were adjusted by adding minimal amounts of the stock solutions to citrate passivated Au nanoparticle solution (4 ml) with the use of a micropipette. The pH values of the solutions were monitored using a digital pH meter (IQ Scientific Instruments).

4.6.2.2. Adsorption of Au nanoparticles

The APTMS modified silicon nitride surfaces were immersed in one of the pH altered citrate passivated Au nanoparticle solutions for 2 hr and rinsed well with UHQ water and dried under a stream of $N_{2(g)}$.

4.6.3. Characterisation

4.6.3.1. AFM

AFM images were obtained using a MultiMode Scanning Probe Microscope (Veeco) and the images analysed using Nanoscope III v5.12r software. All AFM images were obtained by operating the AFM in non contact

mode with the use of RTESP – Tap300 Metrology Probes (Veeco) (nominal spring constant = 20 - 80 Nm^{-1}, nominal resonant frequency = 288 - 328 kHz).

4.6.3.2. XPS

XPS measurements were performed using a VG ESCALab 250 equipped with an Al K$_\alpha$ x-ray source (1486.68 eV) which was operated at 15 kV. Peak fitting and analysis of the data was carried out using Avantage software.

4.7. References

1. Maboudian R., Surface processes in MEMS technology. *Surf. Sci. Rep.* **1998,** 30, 207-269.

2. Liew L.-A.; Saravanan R. A.; Bright V. M.; Dunn M. L.; Daily J. W.; Raj R., Processing and characterization of silicon carbon-nitride ceramics: application of electrical properties towards MEMS thermal actuators. *Sensor. Actuat. A-Phys* **2003,** 103, 171-181.

3. Srika, V. T.; Spearing S. M., Materials selection for microfabricated electrostatic actuators. *Sensor. Actuat. A-Phys* **2003,** 102, 279-285.

4. Tuller H. L.; Mlcak R., Photo-assisted silicon micromachining: Opportunities for chemical sensing. *Sensor. Actuat. B-Chem.* **1996,** 35, 255-261.

5. Weetall H. H., Chemical sensors and biosensors, update, what, where, when and how. *Biosens. Bioelectron.* **1999,** 14, 237-242.

6. Varadan V. K.; Varadan V. V., Microsensors, microelectromechanical systems (MEMS), and electronics for smart structures and systems. *Smart Mater. Struct.* **2000,** 9, 953-972.

7. Datskos P. G.; Sepaniak M. J.; Tipple C. A.; Lavrik N., Photomechanical chemical microsensors. *Sensor. Actuat. B-Chem.* **2001,** 76, 393-402.

8.   Zee F.; Judy J. W., Micromachined polymer-based chemical gas sensor array. *Sensor. Actuat. B-Chem.* **2001,** 72, 120-128.

9.   Gong J. W.; Chen Q. F.; Fei W. F.; Seal S., Micromachined nanocrystalline SnO_2 chemical gas sensors for electronic nose. *Sensor. Actuat. B-Chem.* **2004,** 102, 117-125.

10. Lavrik N. V.; Sepaniak M. J.; Datskos P. G., Cantilever transducers as a platform for chemical and biological sensors. *Rev. Sci. Instrum.* **2004,** 75, 2229-2253.

11. Choi N. J.; Lee Y. S.; Kwak J. H.; Park J. S.; Park K. B.; Shin K. S.; Park H. D.; Kim J. C.; Huh J. S.; Lee D. D., Chemical warfare agent sensor using MEMS structure and thick film fabrication method. *Sensor. Actuat. B-Chem.* **2005,** 108, 177-183.

12. Meier D. C.; Taylor C. J.; Cavicchi R. E.; White V. E.; Ellzy M. W.; Sumpter K. B.; Semancik S., Chemical warfare agent detection using MEMS-compatible microsensor arrays. *IEEE Sens. J.* **2005,** 5, 712-725.

13. Zhou W.; Khaliq A.; Tang Y. J.; Ji H. F.; Selmic R. R., Simulation and design of piezoelectric microcantilever chemical sensors. *Sensor. Actuat. A-Phys* **2005,** 125, 69-75.

14. Hauptmann P. R., Selected examples of intelligent (micro) sensor systems: state-of-the-art and tendencies. *Meas. Sci. Technol.* **2006,** 17, 459-466.

15. Li P.; Li X. X., A single-sided micromachined piezoresistive SiO_2 cantilever sensor for ultra-sensitive detection of gaseous chemicals. *J. Micromech. Microeng.* **2006,** 16, 2539-2546.

16. Mlsna T. E.; Cemalovic S.; Warburton M.; Hobson S. T.; Mlsna D. A.; Patel S. V., Chemicapacitive microsensors for chemical warfare agent and toxic industrial chemical detection. *Sensor. Actuat. B-Chem.* **2006,** 116, 192-201.

17. Handel P. H.; Tournier A.; Henning B., Quantum 1/f effect in resonant biochemical piezoelectric and MEMS sensors. *IEEE T. Ultrason. Ferr.* **2005,** 52, 1461-1467.

18. Britton C. L.; Jones R. L.; Oden P. I.; Hu Z.; Warmack R. J.; Smith S. F.; Bryan W. L.; Rochelle J. M., Multiple-input microcantilever sensors. *Ultramicroscopy* **2000,** 82, 17-21.

19. Lazcka O.; Campo F. J. D.; Munoz F. X., Pathogen detection: A perspective of traditional methods and biosensors. *Biosensors and Bioelectronics* **2007,** 22, 1205-1217.

20.   O'Sullivan C. K.; Guilbault G. G., Commercial quartz crystal microbalances - theory and applications. *Biosens. Bioelectron.* **1999,** 14, 663-670.

21.   Dorozhkin L. M.; Rozanov I. A., Acoustic wave chemical sensors for gases. *J. Anal. Chem.* **2001,** 56, 399-416.

22.   Smith J. P.; Hinson-Smith V., The new era of SAW devices. *Anal. Chem.* **2006,** 78, 3505-3507.

23.   Zhu T.; Fu X.; Mu T.; Wang J.; Liu Z., pH-dependent adsorption of gold nanoparticles on p-aminothiophenol-modified gold substrates. *Langmuir* **1999,** 15, 5197-5199.

24.   Patai S., *The chemistry of the amino group.* Interscience Publishers: London, 1968.

25.   Wang B.; Oleschuk R. D.; Horton J. H., Chemical force titrations of amine- and sulfonic acid-modified poly(dimethylsiloxane). *Langmuir* **2005,** 21, 1290-1298.

26.   Atkins P. W., *Physical chemistry (6th edition).* Oxford University Press: Oxford, 1998.

27.   NIST X-ray Photoelectron Spectroscopy Database. *http://srdata.nist.gov/xps/Bind_e_spec_query.asp.*

28.   Briggs D.; Seah M. P., *Practical surface analysis Volume 1- Auger and X-ray photoelectron spectroscopy.* John Wiley & Sons: Chichester (UK), 1996.

29.   Ertas G.; Korcan D. U.; Suzer S., Enhanced peak separation in XPS with external biasing. *Appl. Surf. Sci.* **2005,** 249, 12-15.

30.   Guczi L.; Pászti Z.; Frey K.; Beck A.; Pető G.; Daróczy Cs. S., Modeling gold/iron oxide interface system. *Top. Catal.* **2006,** 39, 137-143.

31.   Beeby S., *MEMS Mechanical Sensors.* Artech House Incorporated: 2004.

32.   Huang J. M.; Liew K. M.; Wong C. H.; Rajendran S.; Tan M. J.; Liu A. Q., Mechanical design and optimization of capacitive micromachined switch. *Sensor. Actuat. A-Phys* **2001,** 93, 273-285.

33.   Boonliang B. Micro-nano paddle resonator for mass detection by focused ion beam fabrication. University of Birmingham, Birmingham, 2006.

34.   Simpson T. R. E.; Cook M. J.; Petty M. C.; Thorpe S. C.; Russell D. A., Surface plasmon resonance of self-assembled phthalocyanine

monolayers: Possibilities for optical gas sensing. *Analyst* **1996,** 121, 1501-1505.

35.   Simpson T. R. E.; Revell D. J.; Cook M. J.; Russell D. A., Evanescent wave excited fluorescence from self-assembled phthalocyanine monolayers. **1997**, 13, 460-464.

36.   Frens G., Controlled nucleation for the regulation of the particle size in monodisperse gold suspensions. *Nat. Phys. Sci.* **1973,** 241, 20-22.

4.8. Acknowledgments

CHAPTER 5

Sticky SAMs for sperm arrays

CHAPTER 5

Sticky SAMs for sperm arrays

The microcontact printing section **Chapter 5** (section 5.1) has been published as part of a book chapter entitled *'Integrating nanolithography with nanoassembly using soft lithographic methods'* in the book entitled *'Bottom-up nanofabrication: Supramolecules, Self-Assemblies and Organized Films'* (2007) edited by K. Ariga and H. S. Nalwa[1] and has also been published as part of the review: Diegoli et al *Proc. IMechE.* **221** 589-629 (2007)[2]

ABSTRACT: Bioarrays are an approach to high throughput screening of various biological species and can be used to investigate the behaviour of a large number of individual cells in a parallel fashion.[3-5] This work utilises microcontact printing for the fabrication of a bioarray in order to immobilize human spermatozoa cells allowing specific sperm cells to be individually addressed. Such an array could have an impact in the field of artificial insemination.

5.1. Introduction

Nanotechnology promises great advances in medicine, as outlined in **Chapter 1 (section 1.2.2.)**. Bioarrays are one of the methods in which much research has been carried out to advance the understanding of biomolecular interactions. Bioarrays, often referred to as 'microarrays', are patterns of specific chemical functionality that allow the specific adsorption of biological species, such as proteins[6, 7] or cells,[8, 9] in order to analyse biological interactions. The patterned adsorption of cells also enables specific cells to be addressed and

investigated. A variety of patterning methodologies have been employed for the fabrication of bioarrays such as photolithography[10] and patterning using electron beams.[11] Soft lithographic methods,[12] for example microcontact printing, have also been utilized for bioarray fabrication.[7, 13] Microcontact printing, introduced in **Chapter 1 (section 1.3.2.1.ii)**, will now be discussed in greater detail because it is utilised in this chapter for the fabrication of a bioarray.

5.1.1. Microcontact printing (µcp)

Microcontact printing is the formation of chemical patterns from a pre-fabricated master on a substrate *via* an inked stamp. There are many factors that influence the definition and feature size of patterns created by microcontact printing and these will be discussed in this section. There are several ways in which the stamp itself can distort (**Figure 44**) all of which significantly affect the transferred pattern. Roof collapse (**Figure 44b**) occurs when the distance between features (r) is too large and the height of the features (h) is relatively small. This can result in the roof of the stamp collapsing and making conformal contact with the substrate that can result in masking of the desired pattern.

Figure 44c shows the pairing of features that can occur due to mechanical instabilities of adjacent features with high aspect ratios (h/w), and relatively narrow roofs (r) resulting in interfacial adhesion, due to capillary forces, between such features. This feature pairing results in inaccurate replication of the

desired pattern upon printing. PDMS has been shown to trap solvent molecules[14] within the polymeric network which results in swelling of the stamp (**Figure 44d**). Therefore, the swelling of the stamp results in inaccurate replication of the desired pattern.
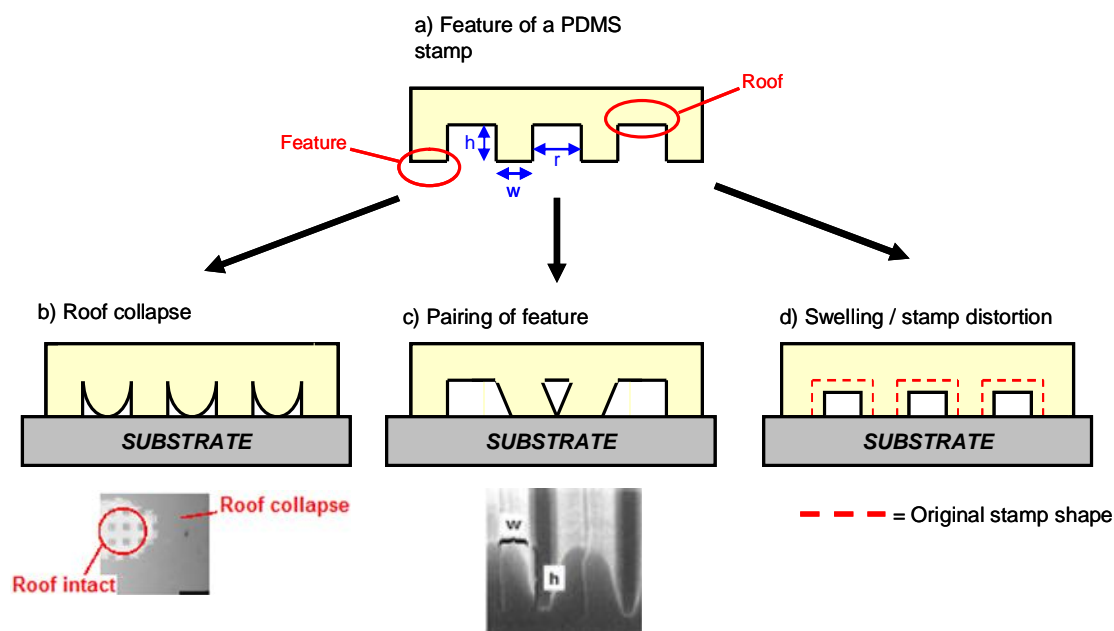
Figure 44. Cartoon representations of stamp distortions in microcontact printing, a) the dimensions of the original, undistorted stamp, b) roof collapse (inset: optical microscope image from[15]), c) the pairing of features (inset from[16]), and d) swelling of stamp

The process of inking the stamp is a fundamental step in microcontact printing, and can also affect the lateral resolution of features formed by microcontact printing. A widely used method of inking the stamp is wet inking which is the application of the ink solution to the entire patterned surface of the stamp and subsequent drying of the stamp to remove excess ink resulting in a uniform layer of ink over the entire patterned surface[17] (**Figure 45a**). This method

results in the inking of not only the areas of the stamp that will be in contact with the substrate, but also of the surfaces of the sidewalls, raised features and roofs of the pattern on the stamp. Such indiscriminate inking of the stamp can have a deleterious effect on the printed pattern as ink molecules can be transferred from the sidewalls and roofs of the stamp to the substrate *via* vapour phase diffusion.[18]

A permanently inked stamp[19] can be obtained by either using a stamp with an inkwell on the back of the stamp (**Figure 45b**) or by immersing the entire stamp in ink solution in order for the entire stamp to be impregnated with ink,[20] and then drying it prior to stamping. Both of these methods (to achieve permanent inking) rely on ink diffusion through the bulk of the stamp. As the entire stamp is inked the roofs and sidewalls of the raised features are inked and, therefore, similar problems to wet inking apply with regard to vapour phase diffusion from roofs and sidewalls to the substrate.
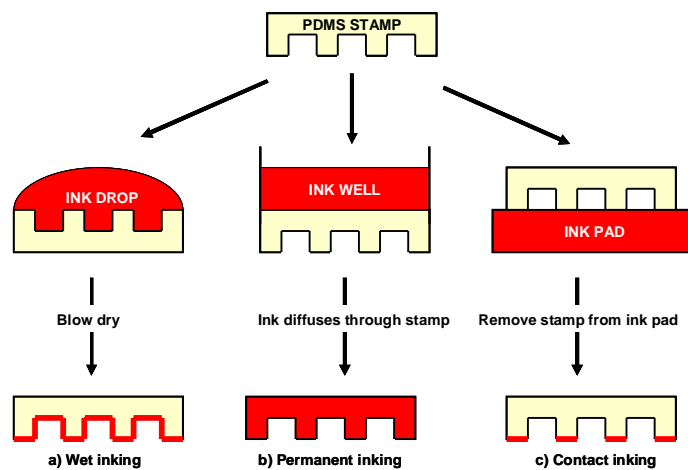
Figure 45. Cartoon representation of three different inking methods of stamps for microcontact printing, a) Wet inking, b) permanently inked stamp, and c) contact inking.

Contact inking[21] involves placing the stamp patterned side down onto an ink pad. The ink pad is a featureless block of PDMS that is immersed in ink solution then dried. This method of inking allows only the areas in contact with the pad to be inked (**Figure 45c**). As only the areas of the stamp in contact with the ink pad are inked the problems of vapour phase diffusion of ink from the side walls and roofs to the substrate are negated.

In order to minimize stamp distortions, due to mechanical instabilities associated with soft PDMS, stiff polymers and composite stamps have been the subject of much research. When stiffer materials are used they must still be soft enough to ensure conformal contact between the stamp and the substrate because, if conformal contact is not achieved, poor transfer of the ink can result.[19, 22, 23] Blends of vinyl-terminated polydimethylsiloxanes with both vinylmethylsiloxane-dimethylsiloxane and methylhydrosilane-dimethylsiloxane have been investigated by Schmidt *et al.*[23] to produce stiffer stamps. A composite stamp was made using these siloxane blends impregnated with glass beads as the materials for the patterned face of the stamp, which was supported by a layer of 'soft' PDMS attached to a glass back plate. These composite stamps were used to produce patterns with sub 100 nm lateral resolution.[23] A stiff composite PDMS, referred to in the literature as *'material C'*, is a custom synthesized PDMS which is 4 - 5 times harder than the Sylgard 184 due to a higher cross-link density. Delamarche *et al.*[22, 24] have used *material C* to print 120 nm wide lines as templates for the formation of sub-micron wires.[22]

5.2. Aims and objectives

The aim of the research described in this chapter is to create a bioarray in order to immobilize individual human spermatozoa cells in such a way as to enable the cells to be individually addressed. This could allow removal of genetic material from individual sperm cells or the removal of specific sperm cells for the use in artificial insemination techniques.

The bioarray 'spots' will consist of an -NH_2 terminated SAM which, when protonated, will present a cationic surface to the surrounding environment. The sperm head consists of fatty acids,[25] which present anionic carboxylate terminal groups. The resultant electrostatic attraction between the sperm head and the -$^+NH_3$ terminated array will result in the immobilization of the sperm cells on the bioarray (**Figure 46**).

a) Amino terminated SAM   b) Protonated SAM   c) Electrostatic attachment of sperm cell
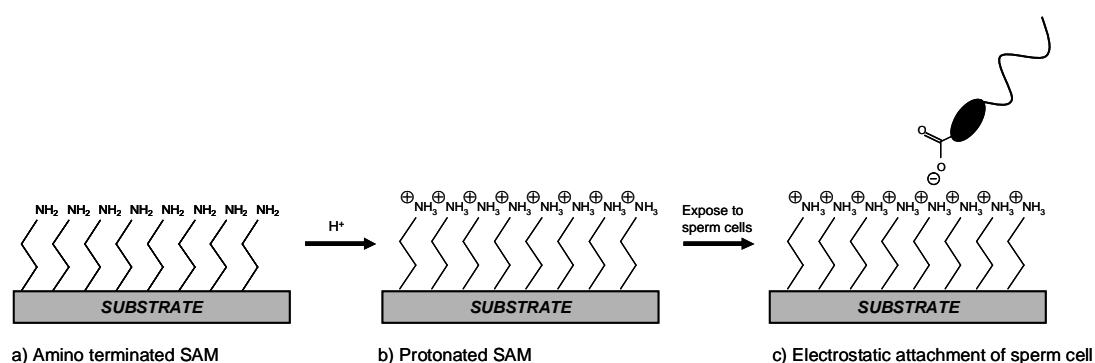
Figure 46. Interaction between a sperm cell and -NH_2 terminated SAM

The approach to forming the array is to microcontact print 2-aminoethanethiol (AET) in order to fabricate an array of -NH_2 terminated dots

(**Figure 47**). The patterned array of dots will allow the preferential adsorption of sperm cells to the dots using the electrostatic interaction described in **Figure 46**.

a) Au/glass substrate

b) Array of AET dots

μcp AET

AET dots

Expose to sperm cells

c) Sperm cells adsorbed on AET dots

Tail

Head

Sperm cells
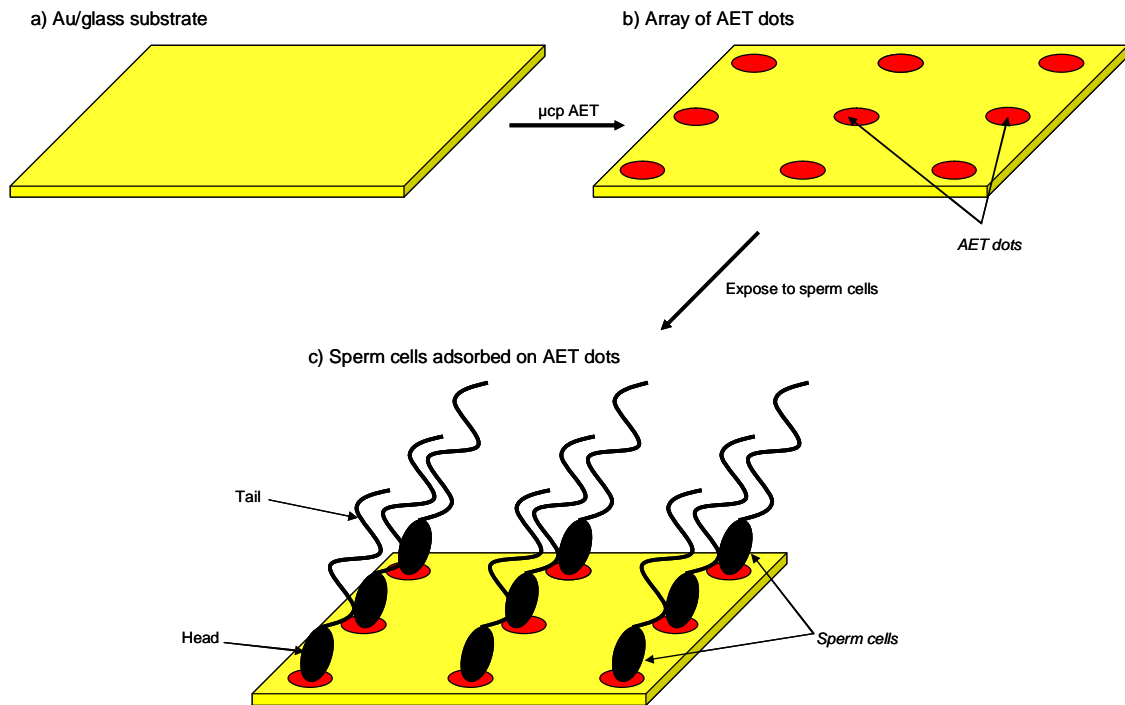
Figure 47. Approach to the formation of a bioarray

5.3. Results and discussion

5.3.1. Array design

A typical sperm consists of a head and tail. The head is roughly elliptical with dimension 2 μm x 1 μm and the tail 30 μm long. Thus, to surface immobilize individual sperm cells an array of circular dots (2 μm in diameter) separated by 55 μm on a square grid was formulated (**Figure 48**). Therefore, in principle only one head group can be attached to one dot, which negates crowding of the tails.
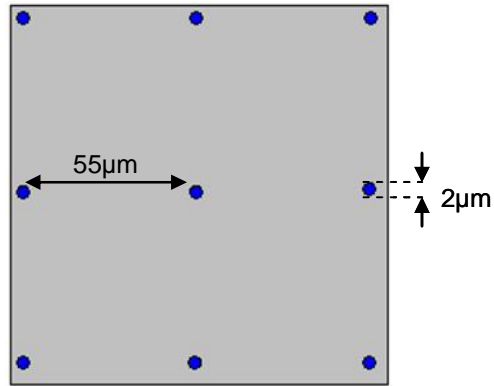
Figure 48. Design of the array pattern

5.3.2. Array formation

5.3.2.1 Pattern transfer from master to stamp

A photomask, Cr on glass (purchased from Delta Mask VOF, The Netherlands) was used in combination with standard photolithographic techniques in order to create a patterned master. The master consists of holes, etched into a resist, on a Si substrate (**Figure 49**).
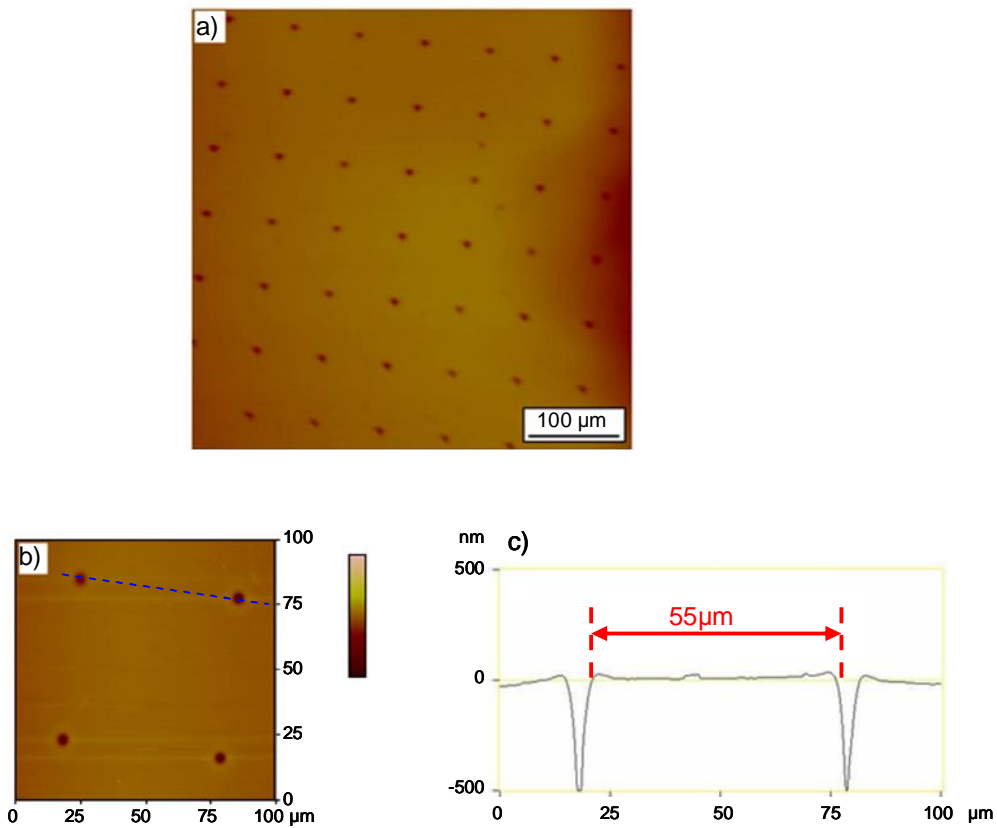
Figure 49. a) Optical micrograph of master bearing the array pattern. b) an AFM image of 4 dots of the array pattern and c) cross section of two dots (as indicated by the dotted blue line on **Figure 49b**)

PDMS was cast against the master (depicted in **Figure 49**), cured and then peeled from the master in order to fabricate the stamp. The optical system of the AFM was used to investigate the surface of the stamp and it was found that the pattern consists of a square array of circular dots 55 µm apart (**Figure 50**). Therefore, the array pattern was successfully transferred from the master to the stamp.
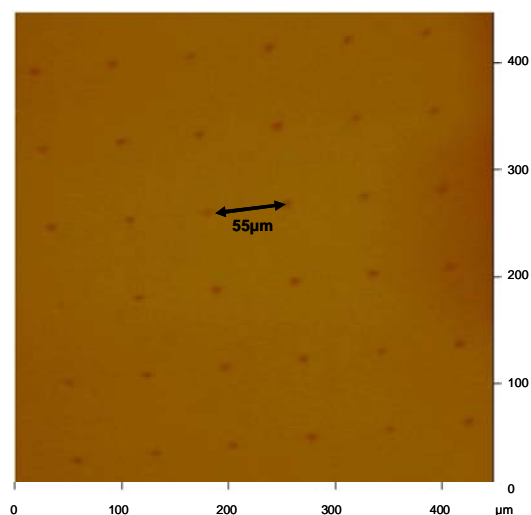
Figure 50. Optical micrograph of a PDMS stamp cast against an array patterned master

5.3.2.2. Pattern transfer from stamp to substrate

Microcontact printing of AET on Au

In order to form the desired bioarray, AET was microcontact printed onto Au substrates. However, AFM imaging (**Figure 51**) reveals no transfer of the array pattern from the PDMS stamp to the Au substrate, which may have been the result of AET not transferring well from the stamp to the substrate. Poor transfer of AET from the stamp to the substrate may be due to AET being such a small molecule which could diffuse into the stamp rather than remaining on the surface of the stamp. Thus, a system was investigated in which transfer is known and this is the microcontact printing of long chain alkanethiols on Au.[26-28]
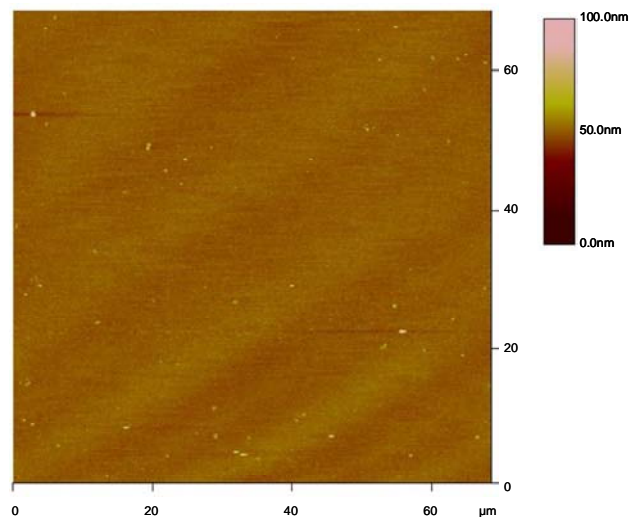
Figure 51. AFM image of AET microcontact printed onto Au

Microcontact printing of dodecanethiol (DDT) on Au

Microcontact printing of DDT followed by etching

Microcontact printing of the array pattern was carried out by applying dodecanethiol (DDT) ink (1 µM in EtOH) to a patterned PDMS stamp by wet inking using a cotton Q-tip. The inked PDMS stamp was then brought into conformal contact with the Au substrate and left for 1 min. Again, no pattern transfer was observed. However, this may have been due to the small height contrast of the patterned DDT SAM. Therefore, the printed substrate was immersed for 7 - 8 min in an etching solution in order to develop the pattern by the removal of the areas of bare Au. The etching solution used was a cyanide etchant developed by Xia *et al.*[29]

125

As can be seen in **Figure 52** the array pattern still could not be seen even after immersion in the cyanide etchant. This failure of pattern transfer could be due to roof collapse of the stamp (**Figure 44b**) upon printing[30] given the large aspect ratio of the gap in between features compared to the feature size. The feature sizes are 2 µm diameter circular dots that are 55 µm apart.
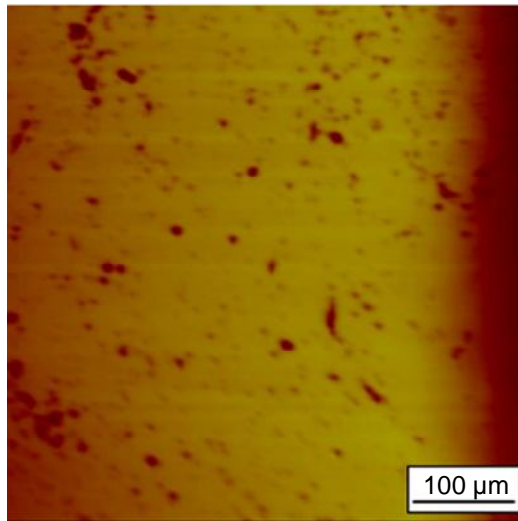
Figure 52. Optical micrograph of Au substrate after microcontact printing of the array pattern

'Submerged' microcontact printing

Bessueille *et al.*[15] have shown that the problem of roof collapse can be overcome by performing the microcontact printing operation under water. This variation of the basic microcontact printing technique is known as 'submerged' microcontact printing (sµCP)[15] and overcomes the problem of roof collapse of the PDMS stamp due to the presence of an incompressible liquid (**Figure 53**). It has been shown that PDMS stamps displaying features with aspect ratios (r/w) up to 100:1 have been successfully used for microcontact printing.[15]
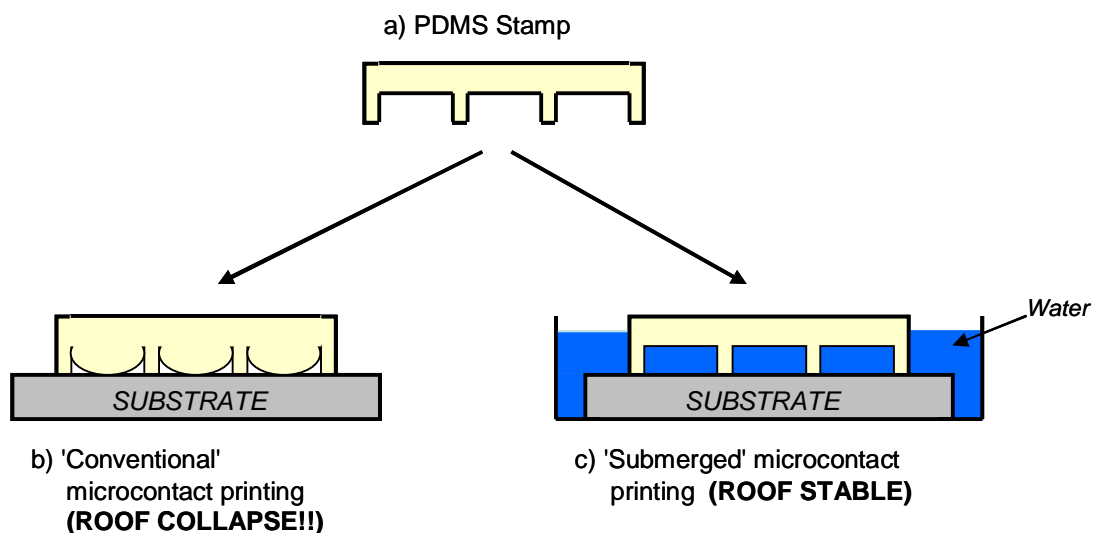
Figure 53. Cartoon of a) a PDMS stamp undergoing roof collapse during b) a 'conventional' microcontact printing process whilst being stable during c) a 'submerged' microcontact printing process

The array pattern was printed onto Au substrates, again using DDT as ink and a contact time of 1min with the printing operation performed under ~1 cm depth of UHQ H_2O. After subsequent etching, using a cyanide etch,[29] the array pattern was shown to be successfully transferred from the stamp to the Au substrate (**Figure 54**).
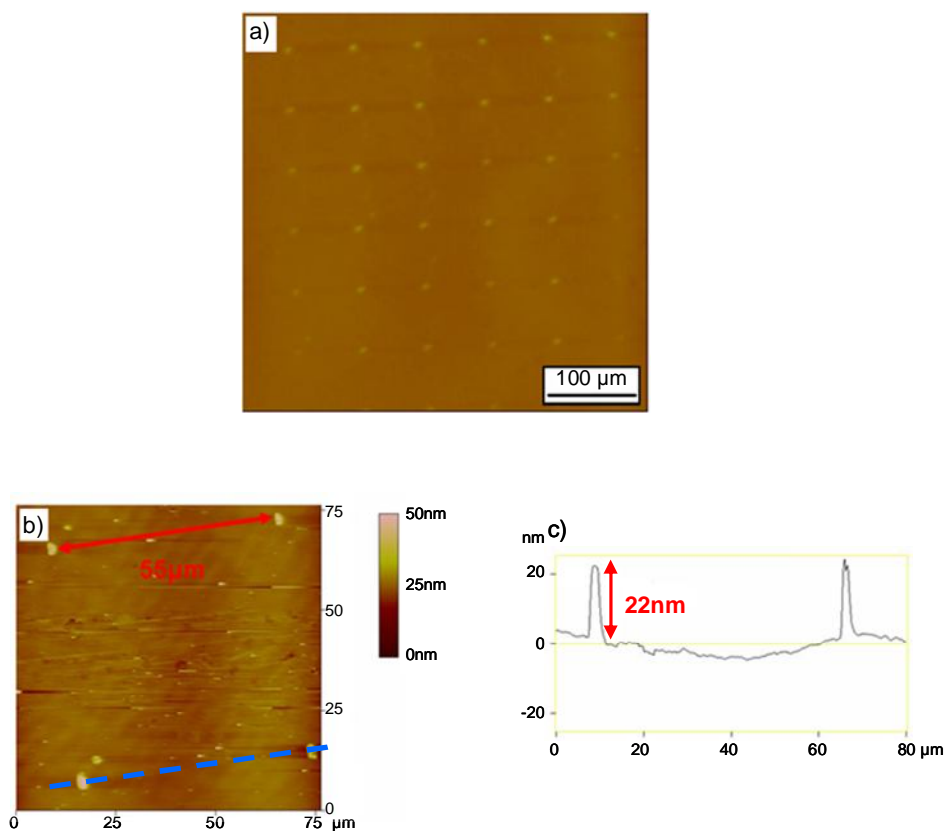
Figure 54. a) Optical micrograph of the array pattern successfully transferred using submerged microcontact printing. b) AFM image of 4 dots in the array and c) cross section of 2 dots (as indicated by dotted blue line on **Figure 54b**)

5.3.3. The functionalization of Au islands

The sequential use of submerged microcontact printing and etching has been shown to fabricate an array of Au islands passivated with DDT SAMs (**Figure 54**). The removal/exchange of the DDT SAM could allow the modification of the resultant (unpassivated) Au islands to be modified with alkanethiol SAMs by self-assembly from the solution phase. Thus, such a methodology (**Figure 55**)

was investigated in order to form the bioarray for the patterned immobilization of sperm cells.
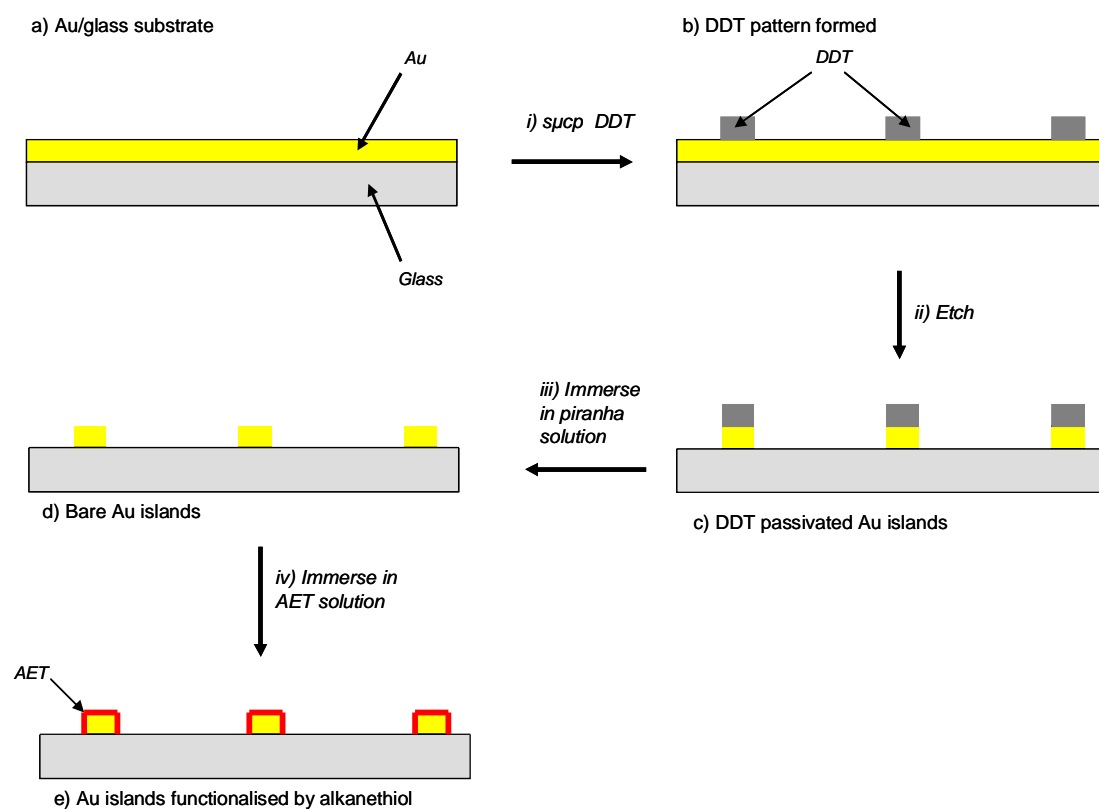
Figure 55. Schematic outline of the methodology for bioarray fabrication using Au islands.

5.3.3.1. Removal of DDT SAMs and AET functionalization of Au substrates

XPS analysis was used to investigate the removal of unpatterned DDT SAMs from Au substrates. These experiments were carried out by immersing clean Au/glass substrates into DDT solution (1 µM in EtOH) for 24 hr. After immersion the DDT SAMs were immersed in piranha solution, which was left to cool to room temperature after preparation, for 10 min. After removal from

piranha solution the substrates were rinsed well with UHQ H_2O then immersed in AET solution (1 μM in EtOH) for 24 hr.

XPS spectra indicate the removal of DDT from the Au/glass substrate upon immersion in piranha solution due to a decrease in the counts of both the doublet at ~ 159 eV and ~157 eV, in the S2p spectra (comparing **Figure 56a(i)** and **Figure 56a(ii)**), and the peak, at ~281 eV, in the C1s spectra (**Figure 56b(i)** and **Figure 56b(ii)**).

Upon immersion of substrates, from which DDT SAMs were removed, into AET solution the doublet peak at ~159 eV and ~157 eV reappears (**Figure 56a**) indicating the adsorption of a species containing S on the surface. The peak at ~280 eV in the C1s spectrum (**Figure 56b**) indicates the increase of the amount of C on the surface. The appearance of a peak at ~397 eV in the N1s spectrum (**Figure 57(ii)**) indicates the presence of a species containing N adsorbed on the surface. The presence of both groups containing S and N on the surface, coupled with an increase in the C1s peak, indicates the successful adsorption of AET on the substrate indicating successful functionalization of the Au substrate after removal of a DDT SAM using piranha solution.
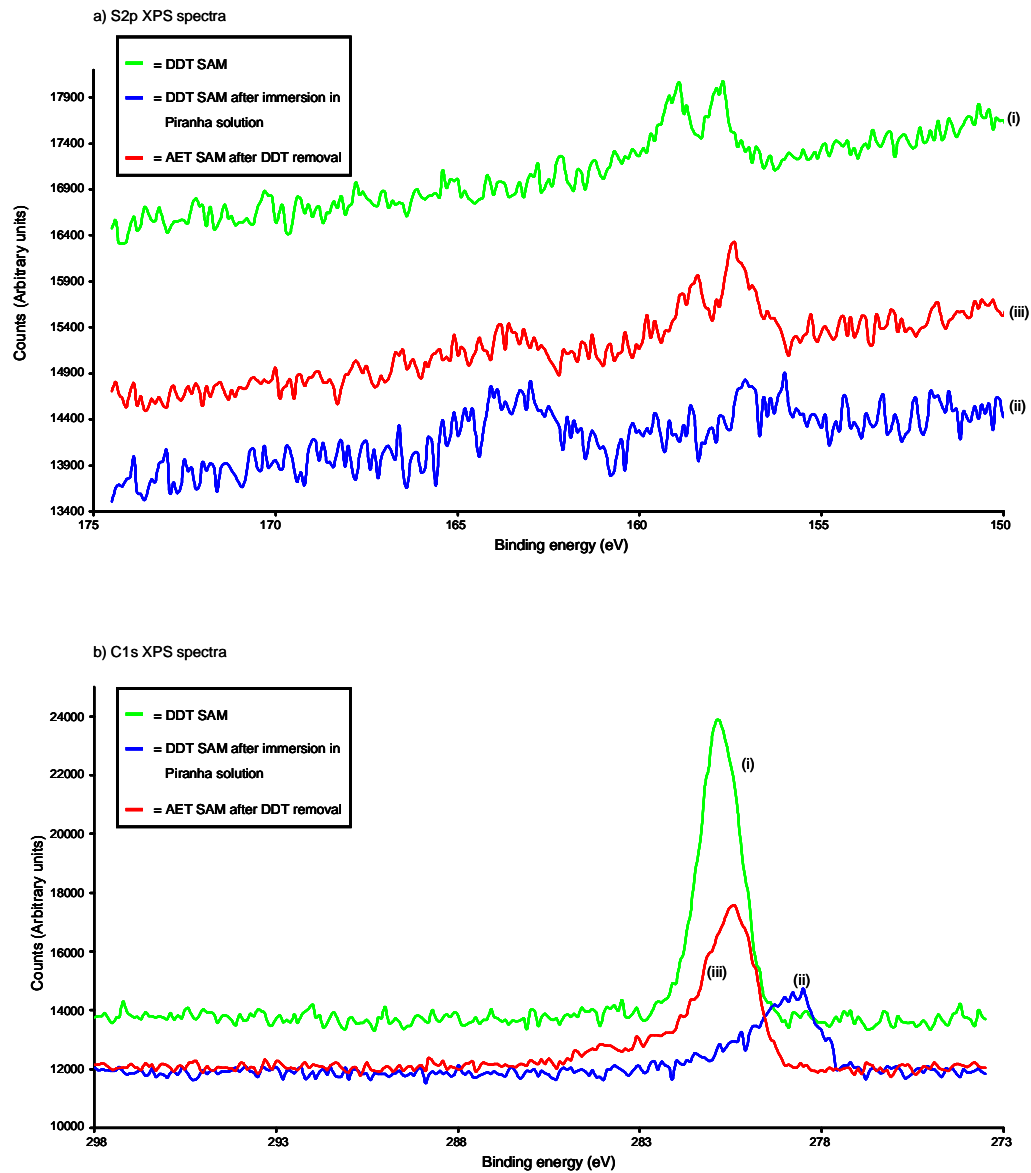
Figure 56. a) S2p XPS spectra and b) C1s XPS spectra of DDT SAM, DDT SAM after immersion in piranha solution and Au substrates (after removal of DDT SAM) in AET solution
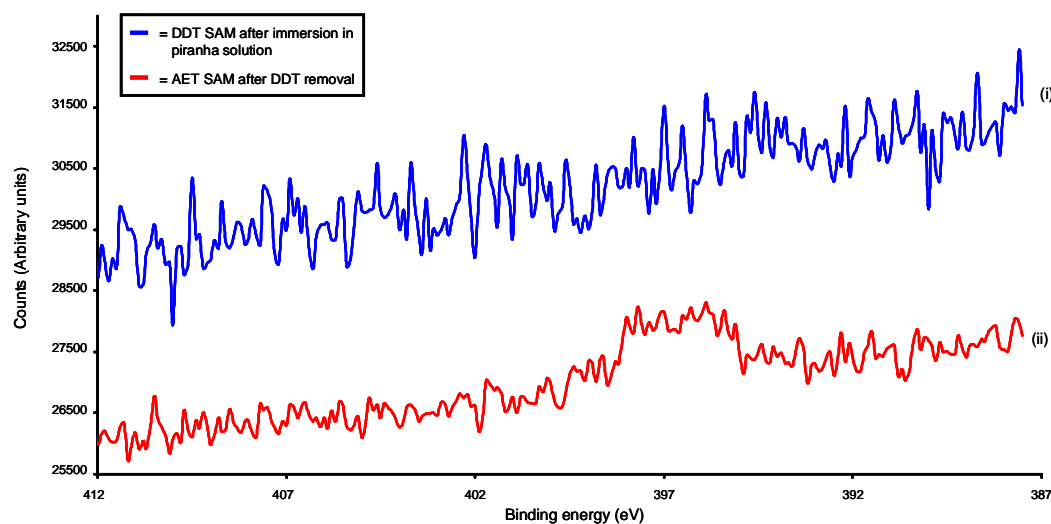
Figure 57. N1s XPS spectra of DDT SAM and that of immersion of Au substrates (after removal of DDT) in AET solution

5.3.3.2. Stability of Au islands

The submerged microcontact printing and etching process, described in **section 5.3.2.2.**, was carried out and the pattern subsequently immersed in piranha solution at room temperature for 10 min. This process was carried out in order to investigate the stability of the Au islands in piranha solution which needed to be assessed in order to facilitate the subsequent functionalization of the islands with alkanethiols. Optical microscopy and AFM images were obtained of Au islands, passivated with DDT, before and after immersion in piranha solution (**Figure 58**). It can be seen that the Au islands are present both before and after immersion in piranha solution and this shows that the Au islands are stable in piranha solution. Thus, this observation allows the possible further functionalization of the Au islands with alkanethiols.

a) DDT passivated Au islands (Optical)

b) DDT passivated Au islands (AFM)

c) Au islands after immersion in Piranha solution (Optical)

d) Au islands after immersion in Piranha solution (AFM)
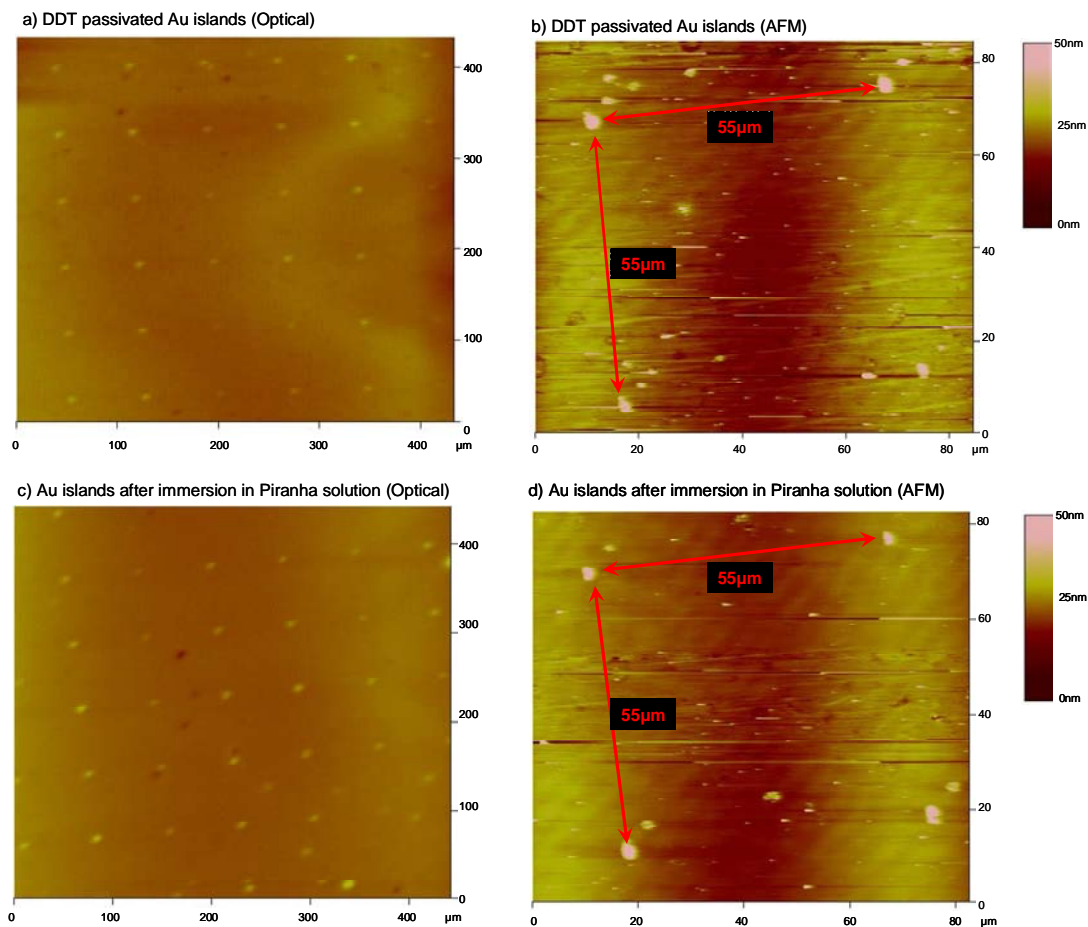
Figure 58. a) Optical and b) AFM images of DDT passivated Au islands before immersion in piranha solution. c) Optical and d) AFM images of Au islands after immersion in piranha solution

5.3.4. Characterisation of amino terminated SAMs on Au

In order to assess the stability of the sperm cells to -NH$_2$ terminated surfaces experiments were first carried out on non-patterned surfaces. Two -NH$_2$ terminated thiolated surfactants were investigated for their use as immobilization platforms for sperm adsorption. These surfactants were 2-aminoethanethiol (AET) (**Figure 59a**) and the polypeptide CL$_3$K$_4$ (**Figure 59b**).

a) Aminoethanethiol (AET)
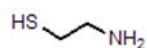
b) CL_3K_4
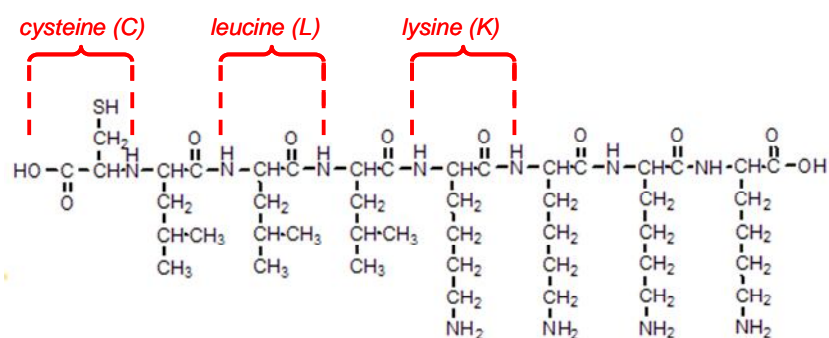
Figure 59. Structures of a) 2-aminoethanethiol (AET) and b) the polypeptide CL_3K_4 (where the cysteine, leucine and lysine residues are indicated)

The polypeptide consists of a cysteine residue, three leucine residue and four lysine residues (CL_3K_4). The rationale behind using this polypeptide was to terminate the molecule with a cysteine residue. Thus, providing a -SH group to facilitate binding to the Au substrate. The lysine residues provide -NH$_2$ groups to facilitate immobilization of the sperm cells to the modified surfaces. The leucine backbone provides a hydrocarbon chain to increase the van der Waals intermolecular interactions between adjacent polypeptide molecules on the surface,[31] thus encouraging the formation of a dense SAM.

5.3.4.1. AET

Contact angle

Contact angle data shows that Au substrates, immersed in AET solution (1 µM in EtOH), become significantly more hydrophilic after an immersion time of 1200 min (**Figure 60**). This is due to the AET molecules displacing volatile organic compounds, which adsorb to the Au upon exposure of the clean substrate to air and replace them, forming a much more hydrophilic -NH$_2$ terminated surface. By comparing the contact angle data with the literature value of AET SAMs on Au, which is of the range 20 - 40 °,[32] it can be seen that complete AET SAM formation occurs after 1200 min immersion.
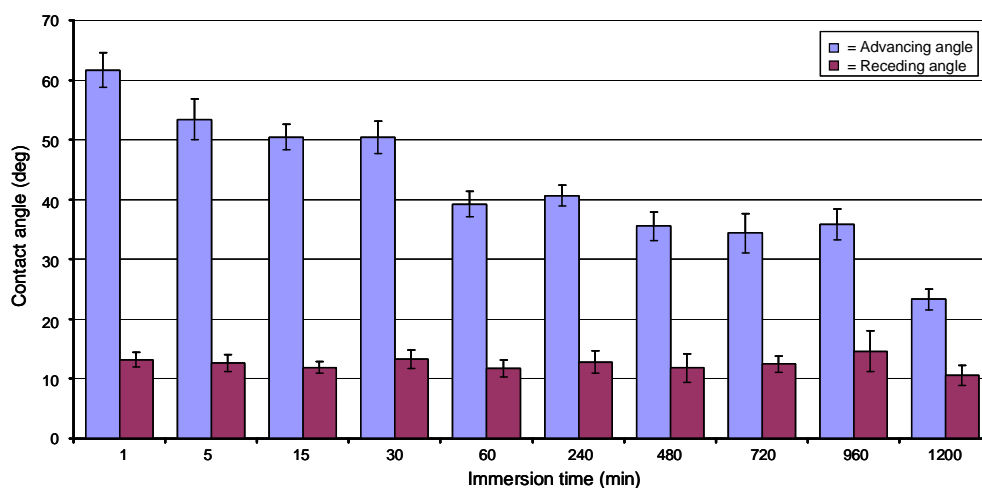
Figure 60. Contact angle analysis of immersion of Au substrates immersed in AET solution (1 µM in EtOH)

Ellipsometry

Ellipsometric data is not presented for AET because the error for each individual measurement was greater than ellipsometric thickness obtained for each reading. Therefore, the ellipsometric measurements were unreliable. The fact that unreliable ellipsometric data were obtained could be due to the fact that AET is a very short molecule (~0.4 nm) meaning that is could be 'masked' by the roughness of the underlying Au substrate (~1.8 nm).

XPS

XPS was used to track the N/Au ratio of Au surfaces immersed in AET solution (1 μM in EtOH) (**Figure 61**) and it can be seen that the N/Au ratio increases as a function of immersion time. **Figure 61** indicates that the highest density of AET coverage of the substrate occurs after 1200 min immersion of the Au substrate in AET solution, which is consistent with the contact angle data (**Figure 60**).
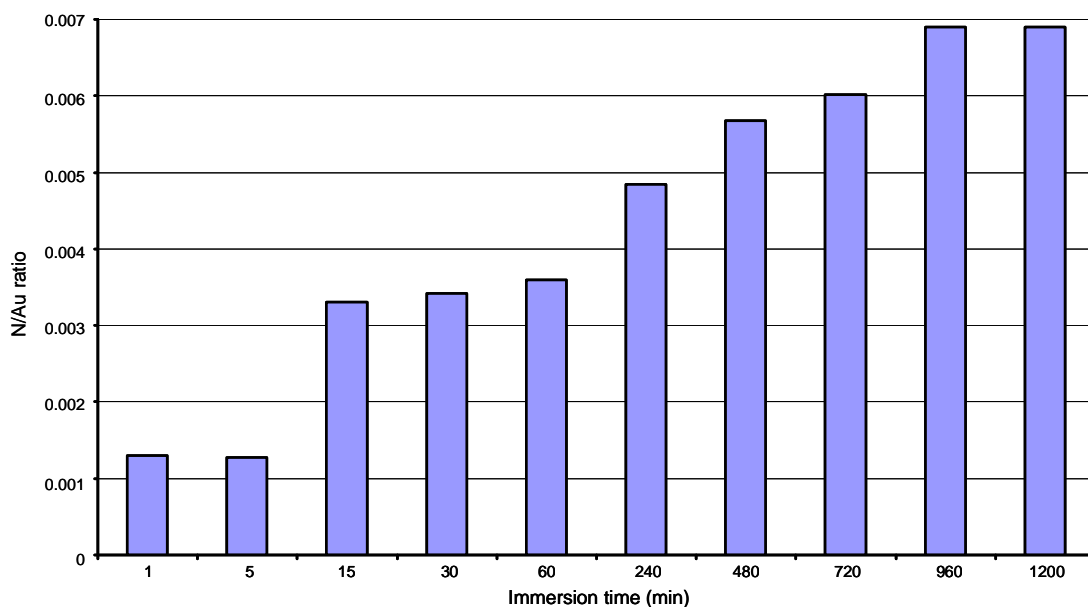
Figure 61. Ratio of N1s and Au4f XPS peaks of AET adsorbed on Au surfaces as a function of

immersion time of Au in AET solution (1 µM in EtOH)

In summary, the contact angle of Au substrates after immersion for 1200

mins (23.3 °± 1.7 °) in ethanolic AET solution (1 µM) is comparable to that in the

literature (20 - 40 °)[32] and the N/Au ratio, as determined by XPS, appears to level

out at 1200 mins. These results indicate formation of AET SAMs on Au after

1200 min immersion in ethanolic AET solution (1 µM). However, it was not

possible to obtain ellipsometric data for this system given that the AET molecule

is shorter than the RMS roughness of the underlying Au. Therefore, it is not

possible to determine whether monomolecular coverage of AET on Au sybstrates

has been obtained.

5.3.4.2. CL$_3$K$_4$

Contact angle

Contact angle data of Au substrates immersed in CL$_3$K$_4$ solutions (1 µM in EtOH) for various immersion times (**Figure 62**) shows that the contact angle increases to an advancing angle of 102.3 $\pm$ 1.1 ° after an immersion time of 1200 min. The literature value for the contact angle of poly-l-lysine, supported on a metallic substrate, varies from 51 - 72 °.[33] Therefore, a contact angle of 102.3 $\pm$ 1.1 ° of the CL$_3$K$_4$ modified Au substrate indicates a significantly higher contact angle than that reported in the literature. Such an obervation may be due to the exposure of hydrophobic leucine groups at the surface, rather than hydrophillic lysine groups.
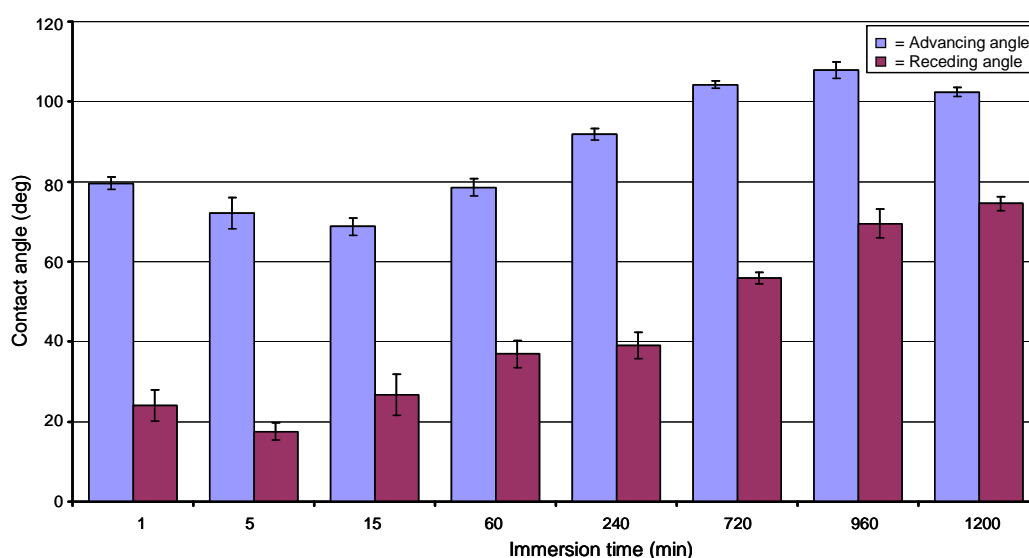
Figure 62. Contact angle analysis of Au substrates after immersion in CL$_3$K$_4$ solution (1 µM in EtOH)

Ellipsometry

The ellipsometric thicknesses of CL_3K_4 modified Au substrates was measured for different immersion times of Au substrates immersed in CL_3K_4 solution (1 μM in EtOH) as shown in **Figure 63**. It can be seen that the ellipsometric thickness increases for immersion times up to 1200 min (**Figure 63**). The length of a fully extended CL_3K_4 molecule is ~2.7 nm from the S atom to the N atom of the -NH_2 group furthest from the S atom. Therefore, after 1200 min immersion the ellipsometric thickness is significantly less than that of a fully extended CL_3K_4 molecule. Thus, this thickness measurement indicates that either i) the CL_3K_4 molecules on the Au surface are not fully elongated, ii) the Au substrate is not fully covered by CL_3K_4 molecules or iii) the immobilized CL_3K_4 molecules are tilted.
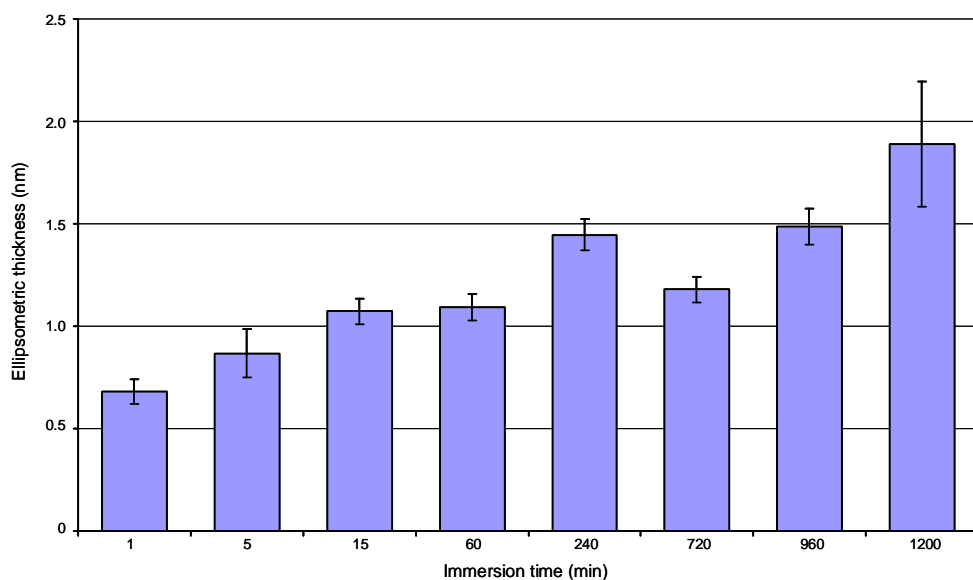
Figure 63. Graph showing the ellipsometric thickness of CL_3K_4 SAMs after immersion of Au substrates in CL_3K_4 solutions (1 μM in EtOH) for various immersion times

XPS spectra confirm that C, N, O and S are present on the Au substrate after an immersion time of 1200 min.
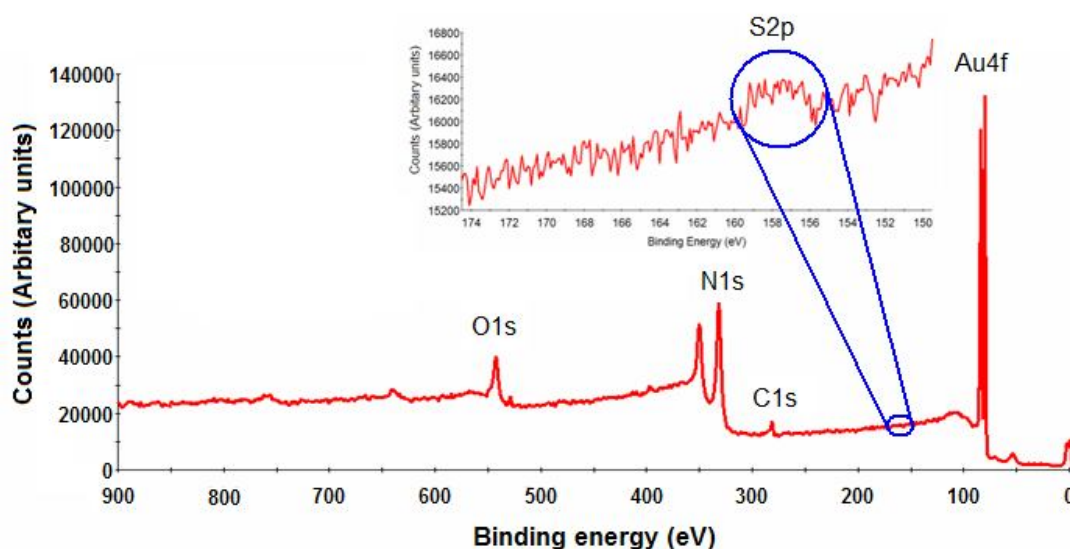
Figure 64. XPS survey spectrum of Au substrate immersed in CL_3K_4 solution (1μM in EtOH) for 1200 min

In summary, the contact angle of Au substrates immersed in ethanolic CL_3K_4 solution (1μM) for 1200 min is 102.3 $\pm$ 1.1 ° with an ellipsometric thickness of 1.9 $\pm$ 0.3 nm. XPS analysis of Au substrates immersed in ethanolic CL_3K_4 solution for 1200 min confirms the presence of sulphur which indicates the attachment of CL_3K_4 to the Au substrate. A combination of a high contact angle and a low ellipsometric thickness, in comparison to a fully extended CL_3K_4 molecule, suggests that the CL_3K_4 molecules on the surface may be bent, thus exposing hydrophobic leucine groups to the surrounding environment.

5.3.4.3. Sperm adsorption experiments on unpatterned SAMs

Sperm adsorption experiments were carried out on unpatterned SAMs of either AET or Cl_3K_4 by placing the modified Au/glass substrate in a flow cell (**Figure 65a** and **b**). Earle's balanced salt solution (EBSS), containing sperm cells, was injected into the flow cell and the flow cell was then incubated at 37 °C for 25 min under a 5 % CO_2 atmosphere (**Figure 65c**). The flow cell was then placed under an optical microscope (**Figure 65a**) and EBSS was pumped through the flow cell in order to remove unattached sperm cells from the SAM (**Figure 65d**).
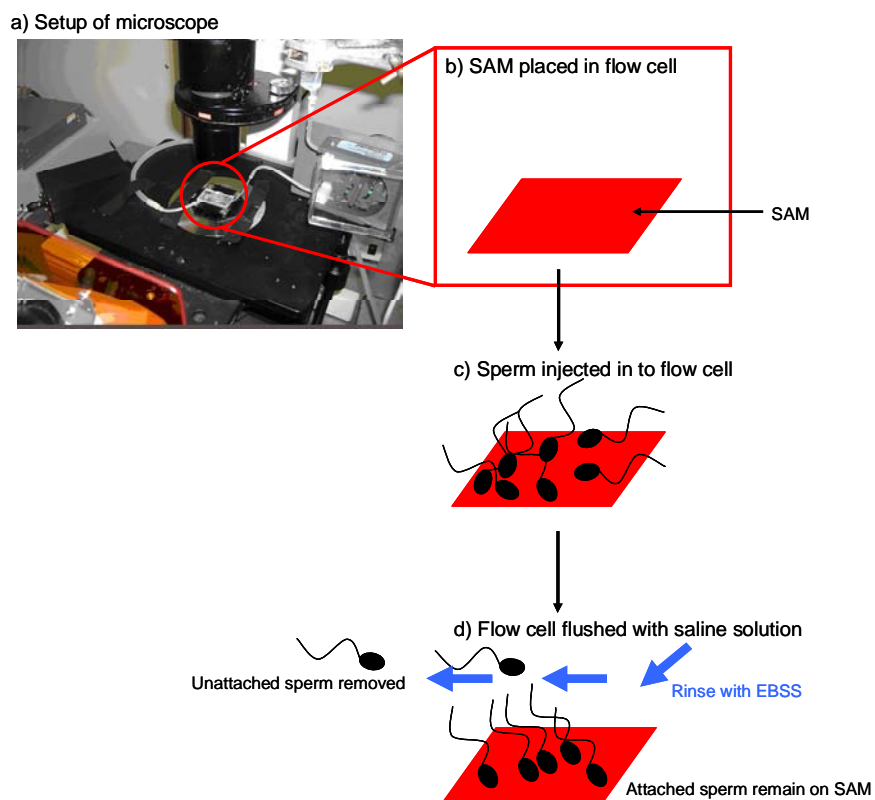
Figure 65. a) Photograph showing the setup of the flow cell and microscope and cartoon representation of sperm adsorption experiments. b) SAM placed in flow cell, c) sperm injected into flow cell and incubated, d) flow cell flushed with EBSS

Immobilization of sperm cells on Au substrates modified with either AET or CL_3K_4 was investigated by placing the substrates in a flow cell containing sperm cells. EBS solution was then passed through the flow cell in order to wash off any sperm that were unattached to the substrate. This method is described in **section 5.6.3.** and optical microscope images from these experiments are shown in **Figure 66**. Sperm adsorption experiments were also performed on bare Au substrates and optical microscope images of these can be seen in **Appendix C**.

a) AET
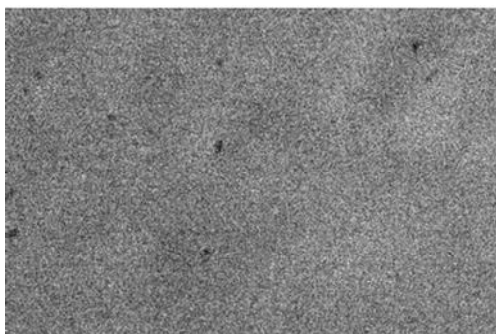
b) CL_3K_4
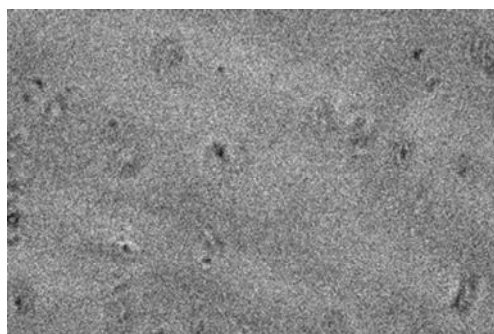
c) Bare Au
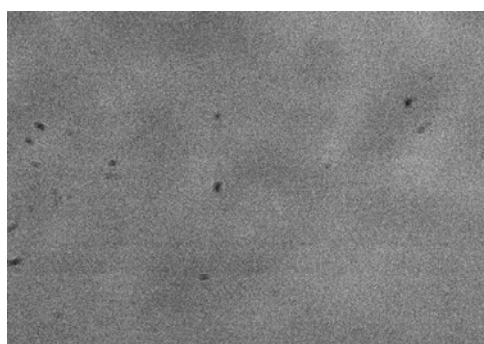
Figure 66. Optical images showing the degree of sperm adhesion on Au substrates modified by immersion in solutions of a) AET, b) CL_3K_4 and, c) bare Au after flowing EBS through the flow cell

Sperm adsorption studies (**Figure 66**) indicate that there is little, or no, sperm adsorption to either AET or CL_3K_4 SAMs. These results show that neither AET nor CL_3K_4 can be used to chemically functionalise the Au islands (see **Figure 55)** in order to create a functional bioarray for the immobilization of sperm cells. Therefore, a different methodology to forming the array was utilised by using poly-l-lysine and the results are described in the next section.

5.3.5. Pattern formation using poly-l-lysine

Poly-l-lysine has previously been used to facilitate sperm adsorption.[34] Therefore, the submerged microcontact printing of poly-l-lysine onto glass microscope slides was investigated as a method of fabricating the bioarrays in order to facilitate the sperm array (**Figure 67**). The submerged microcontact printing of poly-l-lysine was performed under heptane due to poly-l-lysine being soluble in H_2O.

a) Glass substrate
μcp poly-l-lysine
b) Array of poly-l-lysine dots
poly-l-lysine dots
Expose to sperm cells
c) Sperm cells adsorbed on poly-l-lysine dots
Sperm cells
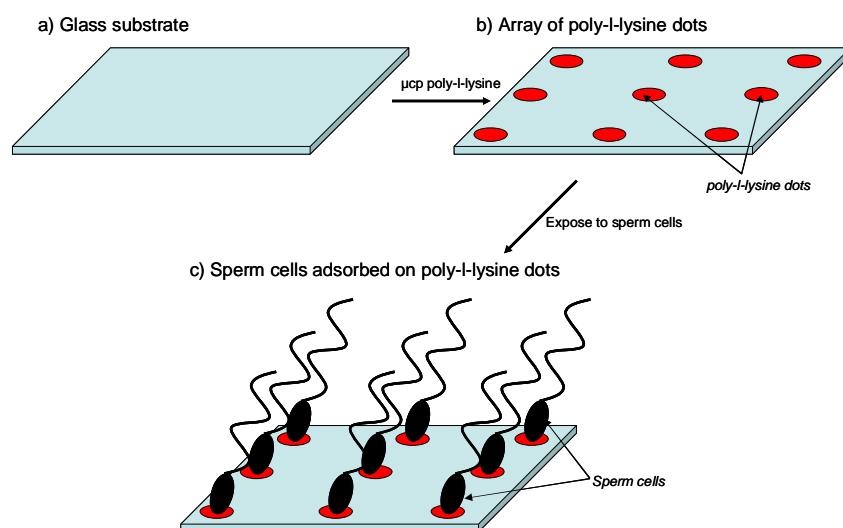
Figure 67. Microcontact printing of poly-l-lysine for formation of bioarray

143

Sperm adsorption experiments (**Figure 65**) were performed on both bare glass slides and on unpatterned poly-l-lysine modified glass slides (**Figure 68**). The experiment show that the sperm adsorption to bare glass slides (**Figure 68**a and **b**) is poor due to most of the sperm cells removed upon washing EBS through the flow cell. Sperm adsorption experiments were also performed on glass slides modified by applying drops of poly-l-lysine solution to the glass slide and allowing it to air dry. These experiments show that the glass slides modified with, poly-l-lysine, exhibit a greater capacity to immobilise sperm cells than both bare glass slides (**Figure 68a** and **b**) and the two thiols studied in this chapter (**Figure 66**). Videos taken from these experiments can be found on the CD attached to this thesis (see **Appendix C1**).
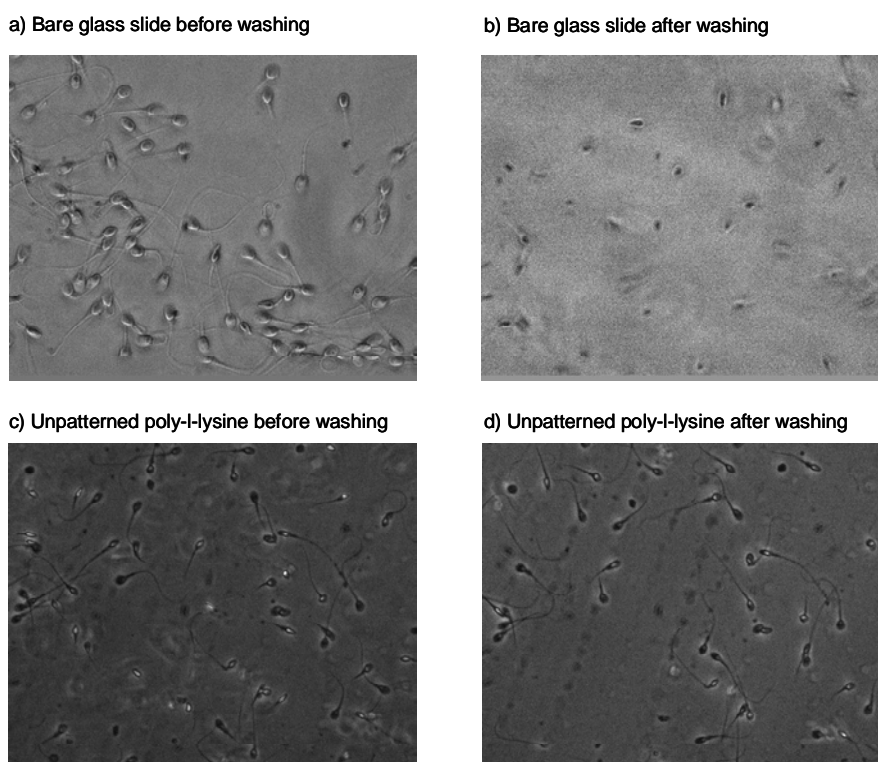
Figure 68. Optical microscope images of sperm adsorption experiments performed on bare glass substrates, a) and b), and glass substrates modified with poly-l-lysine (unpatterned), c) and d) before and after washing with EBS

Optical microscope images of sperm adsorption experiments carried out on glass slides after the submerged microcontact printing of poly-l-lysine are shown in **Figure 69**. The PDMS stamp used for the submerged microcontact printing was peeled from a silicon master exhibiting an array pattern of 2 µm diameter dots which are 55 µm apart (see **Figure 49**).

a) PLL sµcp: no wash

b) PLL sµcp: 1.5ml wash

c) PLL sµcp: 4ml wash
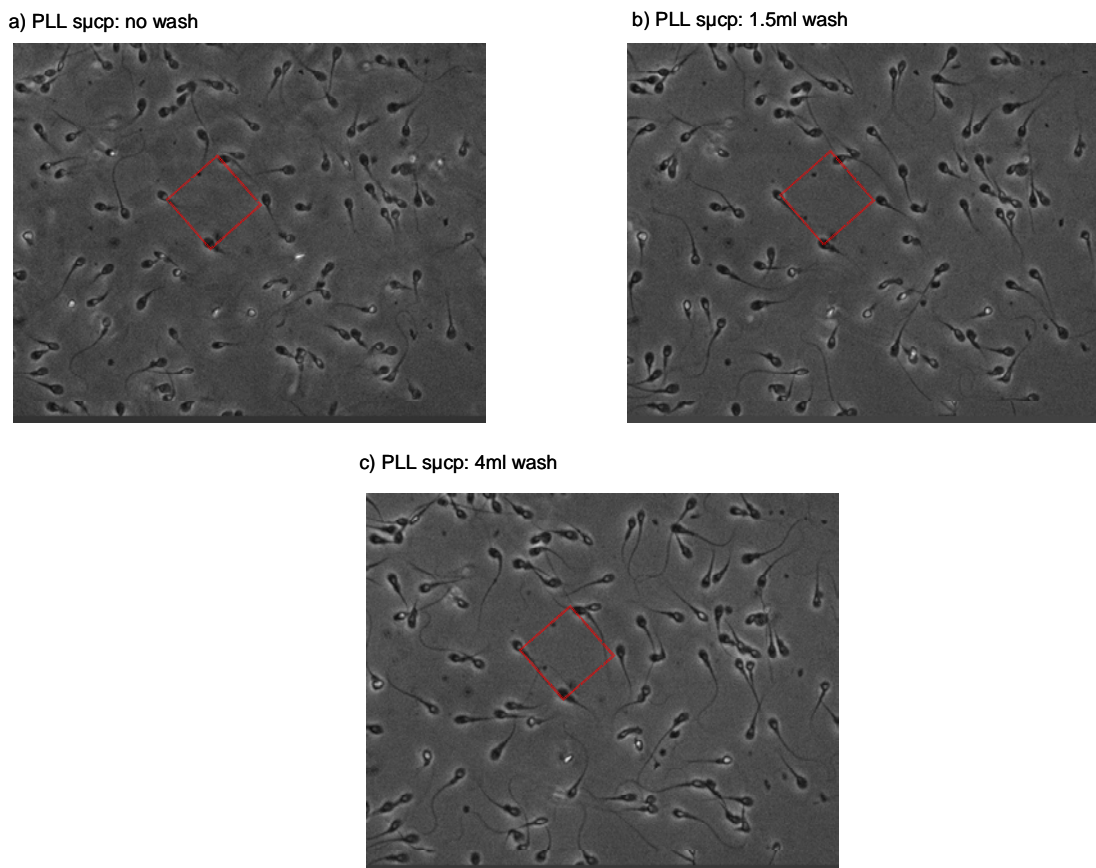
Figure 69. Optical images of sperm adsorption experiments performed on array pattern after sµcp of poly-l-lysine on a glass microscope slide (red square indicated array of sperm cells) after a) before washing and after washing b) 1.5ml and c) 4ml of EBS through the flow cell

Figure 69 suggests that the array pattern may have been successfully transferred to the glass slide given that the 'square' array of sperm cells (as indicated by the red square in **Figure 69a**) is still evident after washing the surface with either 1.5 ml (**Figure 69b**) or 4 ml (**Figure 69c**) of EBSS. Individual

sperm cells can be seen rotating around a single spot on the surface as if tethered to a single point which could be a poly-l-lysine dot. This observation can be seen in the file 'Movie 3 (PLLdots).avi' located on the CD attached to this thesis. However, the microcontact printing of poly-l-lysine does result in a surface which facilitates the non-specific binding of discrete sperm cells (**Figure 69**). This observation may be due to the sperm cells attaching to secondary species, such as antibodies, which may be present in the donated sperm sample. Such secondary species may attach to the unpatterned areas of the glass slide and mask the printed array pattern. The microcontact printing poly-l-lysine surface (**Figure 69**) also shows much better sperm immobilisation than glass slides modified with unpatterned poly-l-lysine (**Figure 68c** and **d**). This observation may indicate that the unpatterned poly-l-lysine glass slide, prepared by simply dropping poly-l-lysine onto the surface and allowing it to dry, may not be the ideal control to use for this system. A better control would have been to use a featureless PDMS stamp to print an unpatterned surface of poly-l-lysine onto the glass slide.

5.4. Conclusions

The aim of the work presented in this chapter was to form a bioarray on a Au coated microscope slide *via* the microcontact printing of an array pattern of AET onto a Au glass substrate. No AET pattern transfer of the array pattern from the PDMS stamp could be seen on the Au/glass substrate by AFM imaging (**Figure 51**). Therefore, the pattern transfer was investigated by microcontact

printing DDT onto Au/glass substrates, a well studied system. AFM indicated no pattern transfer of the array pattern using DDT. Therefore, the Au/glass substrate, on which the pattern was printed, was immersed in a cyanide etchant, in order to remove the unprotected Au, and still no pattern could be seen by AFM (**Figure 52**). This observation was shown to be due to roof collapse of the stamp due to the pattern being visible by AFM (**Figure 54**) after using submerged microcontact printing of DDT on the Au/glass substrate and subsequent etching of the substrate to develop the pattern. The formation of DDT passivated Au 'islands', formed by printing the array pattern using DDT and then subsequent etching, then opened up the possibility of an alternative methodology for fabricating the bioarray. This alternative approach was to form the DDT passivated Au islands and then remove the DDT passivating layer, from the islands, and forming AET SAMs on the exposed Au (**Figure 55**). This method was shown to be viable by XPS analysis confirming the removal of unpatterned SAMs of DDT formed on Au/glass substrates (**Figure 56**) upon immersion of DDT SAMs in piranha solution. XPS was also used to confirm the subsequent adsorption of AET on the Au surface exposed by the removal of DDT SAMs (**Figure 57**). The Au islands were also been shown to be stable upon their immersion in piranha solution (**Figure 58**). Therefore, such a methodology looked promising for the construction of a bioarray by forming AET SAMs on unpassivated Au islands.

SAMs of both AET and CL_3K_4 (a polypeptide) were characterised by contact angle, XPS and, in the case of CL_3K_4, ellipsometry. The characterisation confirmed the formation of SAMs of both AET and CL_3K_4 on Au surfaces after immersion of Au substrates in solution of the respective thiol for 20 hr. However, sperm adsorption experiments, performed on SAMs of both AET and CL_3K_4, showed that neither of these SAMs were suitable to immobilise sperm cells (**Figure 66**). Therefore, neither AET nor CL_3K_4 are suitable for the passivation of Au islands in order to form the bioarray for sperm immobilization.

Therefore, poly-l-lysine was used to modify glass substrates in order to form the bioarray. Sperm adsorption experiments showed that unpatterned poly-l-lysine modified glass substrates immobilized sperm cells (**Figure 68**). Poly-l-lysine was patterned onto glass substrates using submerged microcontact printing and subsequent sperm adsorption experiments indicated that the array pattern was successfully transferred to the glass substrate. The sperm adsorption experiments showed areas of sperm cells which replicated the array pattern (**Figure 69**). However, non-specific adsorption of the sperm cells to the glass substrate masked the pattern. the work presented in this chapter has shown that the microcontact printing of poly-l-lysine on glass microscope slides can be used to fabricate a surface to which sperm cells can be immobilised in such a way that individual sperm cells can be individually addressed which could have applications in the area of artificial insemination.

5.5. Future work

The work carried presented in this chapter has shown that Au islands, defined by the submerged microcontact printing of DDT on Au/glass substrates and subsequent etching, are stable to the removal of the DDT passivant upon immersion in piranha solution. Therefore, the immersion of these islands in a thiol solution could provide an interesting route in to fabricate Au islands of a desired functionality using thiols with specifically functionalised head groups. This approach could provide templates for further bottom-up nanofabrication methodologies.

This work has shown the ability to capture individual sperm cells with the use of a bioarray. The next step will be to successfully release the desired sperm cell from the array without damaging it. One approach might be to briefly, and locally, change the pH of the environment surrounding the desired cell which would cause the protonated $-NH_3^+$ surface, immobilising the sperm cell, to deprotonate thus, releasing the sperm cell.

5.6. Experimental

All chemicals were obtained from Aldrich unless stated.

5.6.1. SAMs

5.6.1.1. Preparation of Au substrates

Glass coverslips (22 x 50 mm, BDH - Cat. No: 406/0188/44) were cleaned by immersion in piranha solution (70 % H_2SO_4 (98 %):30 % H_2O_2 (30 %)) for 30 min at room temperature. The coverslips were then removed from the piranha solution then rinsed well with UHQ H_2O (resistivity = 18 MΩcm) and stored in UHQ H_2O until use.

A thermal evaporator (Edwards Auto 306) was used to evaporate Cr, ~ 5 nm thickness onto clean glass coverslips (22 x 50 mm, BDH - Cat. No: 406/0188/44) in order to facilitate subsequent Au adhesion to the glass. Au was subsequently evaporated onto the Cr layer. The thickness of the Au layer was either ~20 nm thick, in order to allow light to pass through the film for optical microscopy for sperm adsorption experiments, or ~100 nm, in order to fabricate films reflective to light in the wavelength range 280 - 800 nm allowing ellipsometric measurements to be performed.

5.6.1.2. Cleaning of Au substrates

Au substrates were immersed in piranha solution (70 % H_2SO_4 (98 %, Fisher Scientific):30 % H_2O_2 (30 %, Fisher Scientific) for 10 min at room

temperature. The samples were then rinsed with UHQ water and EtOH (Fisher Scientific, HPLC grade) and used 'wet', for immersion in surfactant solution, or dried under a stream of $N_{2(g)}$, for microcontact printing.

5.6.1.3. Preparation of surfactant solutions

Surfactant solutions were prepared by diluting the respective surfactant in EtOH (HPLC grade) in a 250 ml Duran flask and swirled by hand before immersion of the flask in a sonic bath for 10 min. The solutions were stored at ambient temperature in the Duran flask until use.

5.6.1.4. Preparation of SAMs

SAMs of thiols on Au were prepared by immersing a clean Au substrate in a specified surfactant solution (~25 ml) in a glass Petri dish which was then covered and left for the desired immersion time. After removal from the solution the substrate was rinsed in EtOH (~100 ml, HPLC grade) and dried under a stream of $N_{2(g)}$. 2-aminoethanethiol (AET) was used as received and CL_3K_4 (Alta Bioscience) was purified by a colleague using preparative RP-HPLC (Phenomenex), C_{18} with 250 mm $\times$ 21.2 mm ID and 10 μm pore size. Crude CL_3K_4 (20 mg) was dissolved with 700 μl water and injected onto a column using MeCN/H_2O (in a ratio of 3:7) plus 0.05% TFA as an elution solvent at a flow rate of 10 ml/min. Pure CL_3K_4 was obtained after a retention time of 4.9 min.

5.6.1.5. Removal of DDT SAMs from Au substrates

DDT SAMs were removed from Au substrates by the immersion of DDT SAMs, formed on Au/glass substrates, in piranha solution (70 % H_2SO_4 (98 %, Fisher Scientific):30 % H_2O_2 (30 %, Fisher Scientific) for 10min at room temperature. The Au/glass substrates were then rinsed with UHQ water and dried under a stream of $N_{2(g)}$.

5.6.1.6. Preparation of glass slides coated with poly-l-lysine

Glass microscope slides were cleaned by rinsing with acetone and then immersed in EtOH in a sonic bath for 10 min. The slide was then dried using $N_2(g)$ and then poly-l-lysine solution (~4 ml, 0.01 wt%)was applied to the slide in order as to just cover the surface. The slide was then allowed to dry under ambient laboratory conditions.

5.6.2. Microcontact printing

5.6.2.1. Stamp preparation

A photolithographically defined master, of a resist on a Si wafer, was cleaned by rinsing with copious amount of UHQ water then drying under a stream of $N_{2(g)}$.

Sylgard 184 silicone elastomer (Dow Corning) was prepared by vigorously stirring, by hand, Sylgard 184 parts A and B (in a 10:1 ratio) with a wooden stirring stick in a plastic cup for 10 min. The liquid polymer was poured over the clean master in a plastic Petri dish and left to stand under ambient conditions for 90 min in order for the liquid polymer to degas. The Petri dish, containing the master and liquid polymer mixture, was then put into an oven and cured at 65 °C for 90 min. The cured polymer was then peeled away from the master and trimmed, using a scalpel, to form stamps of about 1 cm x 1 cm in size. The stamp was then cleaned by rinsing with EtOH (~100 ml, HPLC grade), heptane (~100 ml, HPLC grade) then, again, with EtOH (~100 ml, HPLC grade) and dried under a stream of $N_{2(g)}$.

5.6.2.2. Printing - 'conventional' microcontact printing

A clean silicone stamp, fabricated as described in **section 3.6.2.1.**, was inked by soaking a cotton bud (or Q-tip) in a surfactant ink solution then brushed over the patterned surface of the stamp several times. The stamp was then dried under a stream of $N_{2(g)}$ and placed, inked side down, on a clean Au substrate, cleaned as described in **section 3.6.1.2.** Light hand pressure was used to ensure that the stamp made conformal contact with the substrate. After the desired printing time, the inked stamp was then removed from the Au substrate which was then rinsed with EtOH (~100 ml, HPLC grade) then dried under a stream of $N_{2(g)}$.

5.6.2.3. Printing - 'submerged' µcp

The protocol for submerged printing technique was the same as that described in **section 5.6.2.2.** for 'conventional' µcp, with the exception that the clean Au substrate was placed in a glass Petri dish containing enough UHQ water to completely submerge the stamp when on top of the substrate. The inked stamp was then placed on the submerged Au substrate using light hand pressure to ensure conformal contact between the stamp and the Au substrate. The stamp was left in contact with the substrate for the desired printing time before being removed from the substrate which was then rinsed with EtOH (~100 ml, HPLC grade) and dried under a stream of $N_{2(g)}$. For the submerged contact printing of poly-l-lysine arrays heptane, rather than UHQ H_2O, as a printing medium due to the poly-l-lysine being soluble in H_2O.

5.6.2.4. Etching of microcontact printed pattern

The cyanide etchant, as described in reference[29], consisted of KOH (5.6 g, 1.0 M, Fisher Scientific), $K_2S_2O_3$ (1.9 g, 0.1 M), $K_3Fe^{III}(CN)_6$ (0.34 g, 10 mM) and $K_4Fe^{IV}(CN)_6$ (0.038 g, 1 mM) which were weighed out into glass vials and transferred to a 400 ml glass crystallization basin and the vials rinsed with 100 ml UHQ H_2O (resistivity = 18 MΩcm) and the washing placed in the crystallization basin. The solution was then placed in a sonic bath and sonicated for 20 min to ensure complete mixing of the components. The Au substrates were then placed

in the etchant about 8 min with the basin being swirled by hand approximately every 2 min. The substrates were then rinsed with UHQ H_2O and blown dry under a stream of $N_{2(g)}$.

5.6.3. Sperm adhesion experiments

Au substrates, modified with a given surfactant solution, were placed in a flow cell and incubated in a suspension of sperm cells in Earle's balanced salt (EBS) solution at 37 °C for 20 - 25 min in a 5% CO_2 atmosphere. Earle's balanced salt solution is made up of NaCl (116.4 mM), KCl (5.4 mM), $CaCl_2$ (1.8 mM), $MgCl_2$ (1 mM), glucose (5.5 mM), $NaHCO_3$ (25 mm), Na pyruvate (2.5 mM), Na lactate (19 mm), $MgSO_4$ (0.81 mM); also BSA at 0.3 % w/v. pH: 7.4. Each flow cell was connected to syringe filled with EBS soltuion, and EBS solution was then pumped through the cell at about 0.5 ml.min^{-1}. This was used to move the sperm cells which were not bound to the surface of the slides. The flow cell experiments were conducted at a temperature of 26 - 27 °C and at a relative humidity at 44 - 46 %.

5.7. References

1.   Hamlett, C. A. E.; Preece, J. A., Book chapter entitled 'Integrating nanolithography with nanoassembly using soft lithographic methods' published in Ariga, K.; Nalwa, H. S., (Eds) Bottom-up nanofabrication (Supramolecules, Self-   Assemblies and Organized Films), American Scientific Publishers, California   (2007)

2   Diegoli, S.; Hamlett, C. A. E.; Leigh, S. J.; Mendes, P. M.; Preece, J. A., Engineering nanostructures at surfaces using nanolithography. *J. Aerospace Eng.* **2007,** 221, 589-629.

3.   Jaluria P.; Konstantopoulos K.; Betenbaugh M.; Shiloach J., A perspective on microarrays: current applications, pitfalls, and potential uses. *Microb. Cell Fact.* **2007,** 6, 4-18.

4.   Kumar A.; Goel G.; Fehrenbach E.; Puniya A. K.; Singh K., Microarrays: the technology, analysis and application. *Eng. Life Sci.* **2005,** 5, 215-222.

5.   Lam K. S.; Renil M., From combinatorial chemistry to chemical microarray. *Curr. Opin. Chem. Bio.* **2002,** 6, 353-358.

6.   Petrou P. S.; Chatzichristidi M.; Douvas A. A.; Argitis P.; Misiakos K.; Kakabakos S. E., A biomolecule friendly photolithographic process for fabrication of protein microarrays on polymeric films coated on silicon chips. *Biosens. Bioelectron.* **2007,** 22, 1994-2002.

7.   Inerowicz H. D.; Howell S.; Regnier F. E.; Reifenberger R., Multiprotein immunoassay arrays fabricated by microcontact printing. *Langmuir* **2002,** 18, 5263-5268.

8.   Chechetkin V. R., Kinetics of binding and geometry of cells on molecular biochips. *Phys. Lett. A* **2007,** 366, 460-465.

9.   Castel D.; Pitaval A.; Debily M.-A.; Gidrol X., Cell microarrays in drug discovery. *Drug Discov. Today* **2006,** 11, 616-622.

10.   Singh-Gasson S.; Green R. D.; Yue Y.; Nelson C.; Blattner F.; Sussman M. R.; Cerrina F., Maskless fabrication of light-directed oligonucleotide microarrays using a digital micromirror array. *Nat. Biotechnol.* **1999,** 17, 974-978.

11.   Cherniavskaya O. ; Chen C. J.; Heller E.; Sun E.; Provezano J.; Kam L.; Hone J.; Sheetz M. P.; Wind S. J., Fabrication and surface chemistry of nanoscale bioarrays designed for the study of cytoskeletal protein binding

interactions and their effect on cell motility. *J. Vac. Sci. Technol. B* **2005,** 23, 2972-2978.

12. Truskett V. N.; Watts M. P. C., Trends in imprint lithography for biological applications. *Trends Biotechnol.* **2006,** 24, 312-317.

13. Feng C. L.; Vancso G. J.; Schönherr H., Fabrication of robust biomolecular patterns by reactive microcontact printing on *N*-hydroxysuccinimide ester-containing polymer films. *Adv. Funct. Mater.* **2006,** 16, 1306-1312.

14. Lee J. N.; Park C.; Whitesides G. M., Solvent compatibility of poly(dimethylsiloxane)-based microfluidic devices. *Anal. Chem.***2003,** 75, 6544-6554.

15. Bessueille F.; Pla-Roca M.; Mills C. A.; Martinez E.; Samitier J.; Errachid A., Submerged microcontact mrinting (sμcp): An unconventional printing technique of thiols using high aspect ratio, elastomeric stamps. *Langmuir* **2005,** 21, 12060-12063.

16. Delamarche E.; Schmid H.; Michel B.; Biebuyck H., Stability of molded polydimethylsiloxane microstructures. *Adv. Mater.* **1997,** 9, 741-746.

17. Kumar A.; Biebuyck H. A.; Whitesides G. M., Patterning self-assembled monolayers: Applications in materials science. *Langmuir* **1994,** 10, 1498-1511.

18. Delamarche E.; Schmid H.; Bietsch A.; Larsen N. B.; Rothuizen H.; Michel B.; Biebuyck H., Transport mechanisms of alkanethiols during microcontact printing on gold. *J. Phys. Chem. B* **1998,** 102, 3324-3334.

19. Balmer T. E.; Schmid H.; Stutz R.; Delamarche E.; Michel B.; Spencer N. D.; Wolf H., Diffusion of alkanethiols in PDMS and its implications on microcontact printing (μcp). *Langmuir* **2005,** 21, 622-632.

20. Sharpe R. B. A.; Burdinski D.; Huskens J.; Zandvleit H. J. W.; Reinhoudt D. N.; Poelsema B., Spreading of 16-mercaptohexadecanoic acid in microcontact printing. *Langmuir* **2004,** 20, 8646-8651.

21. Libioulle L.; Bieysch A.; Schmid H.; Michel B.; Delamarche E., Contact-inking stamps for microcontact printing of alkanethiols on gold. *Langmuir* **1999,** 15, 300-304.

22. Geissler M.; Wolf H.; Stutz R.; Delamarche E.; Grummt U.-W.; Michel B.; Bietsch A., Fabrication of metal nanowires using microcontact printing. *Langmuir* **2003,** 19, 6301-6311.

23. Schmid H.; Michel B., Siloxane polymers for high-resolution, high-accuracy soft lithography. *Macromolecules* **2000,** 33, 3042-3049.

24. Balmer T. E.; Schmid H.; Stutz R.; Delamarche E.; Michel B.; Spencer N. D.; Wolf H., Diffusion of alkanethiols in PDMS and its implications on microcontact printing (μcp). *Langmuir* **2005,** 21, 622-632.

25. Furland N. E.; Oresti G. M.; Antollini S. S.; Venturino A.; Maldonado E. N.; Aveldano M. I., Very long-chain polyunsaturated fatty acids are the major acyl groups of sphingomyelins and ceramides in the head of mammalian spermatozoa. *J. Biol. Chem.* **2007,** 282, 18151-18161.

26. Wilbur J. L.; Kumar A.; Biebuyck H. A.; Kim E.; Whitesides G. M., Microcontact printing of self-assembled monolayers: applications in microfabrication. *Nanotechnology* **1996,** 7, 452-457.

27. Xia Y.; Zhao X.-M.; Whitesides G. M., Pattern transfer: Self-assembled monolayers as ultrathin resists. *Microelectron. Eng.* **1996,** 32, 255-268.

28. Miksich M.; Chen C. S.; Xia Y.; Dike L. E.; Ingber D. E.; Whiesides G. M., Controlling cell attachment on contoured surfaces with self-assembled monolayers of alkanethiolates on gold. *P. Natl. Acad. Sci. USA* **1996,** 93, 10775-10778.

29. Xia Y.; Zhao X.-M.; Kim E.; Whitesides G. M., A selective etching solution for use with patterned self-assembled monolayers of alkanethiolates on gold. *Chem. Mater.* **1995,** 7 2332-2337

30. Huang Y. Y.; Zhou W.; Hsia K. J.; Menard E.; Park J.-U.; Rogers J. A.; Alleyne A. G., Stamp collapse in soft lithography. *Langmuir* **2005,** 21, 8058-8068.

31. Ulman A., *An Introduction to Ultrathin Organic Films from Langmuir-Blodgett to Self-Assembly*. Adademic Press Limited: London, 1991.

32. Notsu H.; Kubo W.; Shitanda I.; Tatsuma T., Super-hydrophobic/super-hydrophilic patterning of gold surfaces by photocatalytic lithography. *J. Mater. Chem.* **2005,** 15, 1523-1527.

33. Yamamoto, H.; Ogawa, T.; Nishida, A., Molecular weight dependence of wettability and molecular adsorption of poly-l-lysine at the air-water interface. *J. Colloid Interf. Sci.* **1995**, 105-110.

34. Reeve L.; Ledger W. L.; Pacey A. A., Does the Arg-Gly-Asp (RGD) adhesion sequence play a role in mediating sperm interaction with the human endosalpinx? *Hum. Reprod.* **2003,** 18, 1461-1468.

5.8. Acknowledgments

CHAPTER 6

Formation of fibres from aqueous PEO/Au nanoparticle composite solutions via electrospinning

CHAPTER 6

Formation of sub-micron fibres from aqueous PEO/Au nanoparticle composite solutions via electrospinning

The work presented in **Chapter 6** has been published in the following research article: Hamlett et al. *Tetrahedron* **64** 8476-8483 (2008).[1]

ABSTRACT: Electrospinning is a method used for the formation of polymeric fibres and relies on repulsive electrostatic forces on the surfaces of a polymeric solution held in a metallic syringe (spinneret). The use of polymeric solutions containing nanoparticles is an interesting route to the fabrication of composite nanofibres. This work investigates the electrospinning of composite sub-micron fibres from aqueous solutions of polyethylene oxide (PEO) containing citrate passivated Au nanoparticles. The organisation of such composite nanofibres could provide templates for subsequent self-assembled nanostructures.

6.1. Introduction

Electrospinning is a method of fabricating fibres from a wide range of polymeric solutions[2-5] and relies on the electrostatic repulsion of charges on the surface of the electrospinning solution. The first patent concerning electrospinning was filed in 1934 by Anton Formhals.[6] **Figure 70a** represents the basic setup of an electrospinning procedure and shows a metallic syringe (spinneret) in electrical contact with a collecting plate. The spinneret is filled with

a solution of the desired polymer, from which the fibres will be fabricated. Upon application of a direct electrical current (**Figure 70b**) the surface of the polymeric solution, exposed to the atmosphere, becomes positively charged. It is the repulsion of the positive charges that imposes a stretching force on the polymeric solution and results in an increase of the area of the interface between the exposed polymeric solution and the atmosphere (**Figure 70c**). When the repulsive electrostatic forces overcome the surface tension of the polymeric solution, jetting of the polymeric solution occurs (**Figure 70d**). Instabilities cause the jet (**Figure 70e**) to whip and 'spin'[7-9] which further expands the interface between the polymeric solution and the atmosphere. Stretching of the polymer solution results in both the thinning of the fibres and evaporation of the solvent from the polymeric solution. The polymer fibres are then deposited onto a collecting plate (**Figure 70d**).
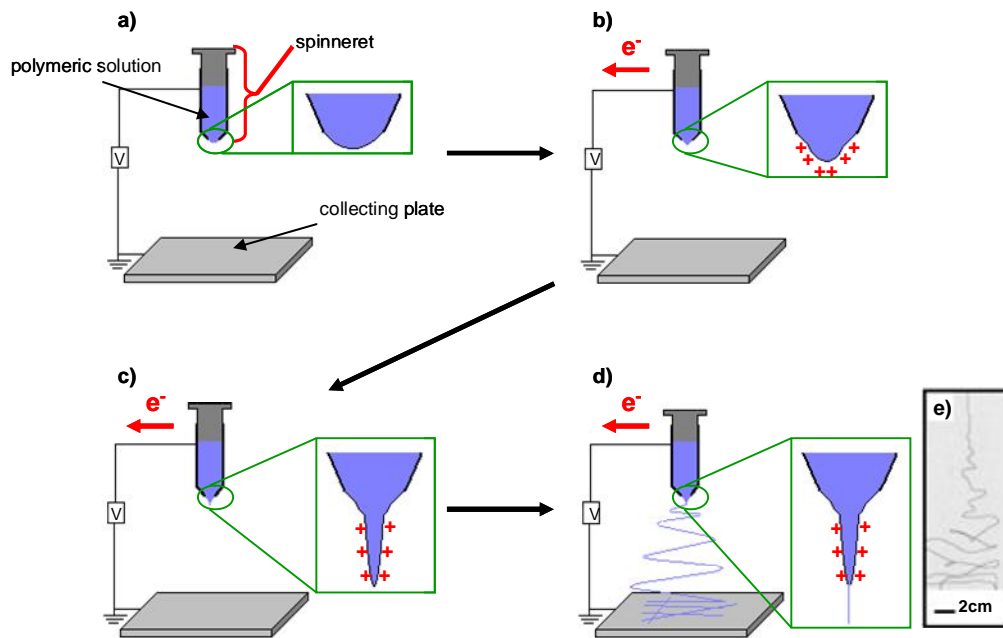
Figure 70. Schematic representation of the electrospinning process showing a) the basic setup of an electrospinning process, b) application of an electric current and resultant charging of solution/air interface, c) increase of surface area of solution/air interface and d) jetting of the polymeric solution. Figure e) shows a high-speed camera image of the jet formed during an electrospinning process.[8]

Electrospinning is not exclusively used to form fibres from polymeric solutions. Composites[10-13] and melts[14] have also been used for electrospinning. Polymeric composite fibres have been fabricated by the electrospinning of polymeric solutions containing a wide variety of inclusions such as nanoparticles[12] and nanotubes.[10, 11, 13] The formation of composite nanofibres has been studied with a view for applications such as catalysis,[15, 16] electronics[17, 18] and scaffolds for tissue engineering.[19-21]

One of the most important properties of the electrospinning solution affecting the morphology of the electrospun fibres is its viscosity. Viscosity affects the manner by which the jet is stretched by the repulsive forces induced by the applied current. Lower viscosities provide less resistance to stretching forces than solutions exhibiting higher viscosity, with solutions of lower viscosity allowing finer fibres to be electrospun.[22] Entanglement of the polymeric chains is the major influence on the viscosity of polymeric solutions. Chain entanglement is primarily determined by molecular weight, branching and the concentration of the polymeric solution. Temperature is another factor that affects the viscosity of the solution with high temperatures acting as to lower the viscosity of polymeric solutions.[23]

The conductivity of the solution influences the amount of charge that can be sustained on the surface. Solutions of higher conductivity result in more charges on the surface of the solution, and therefore increases the repulsive forces which, upon jetting, leads to the formation of smoother, finer fibres.[24] The applied voltage dictates the charging of the surface of the electrospinning solution with higher applied voltages resulting in greater charging, hence greater repulsive forces.[25, 26] Thus, finer, straighter wires result upon increasing the applied voltage.[25, 26] The feed rate of the polymer solution through the spinneret also influences the final fibres, with higher feed rates resulting in thicker fibres simply due to more material being drawn through the tip of the spinneret.[24]

The distance between the tip and collector affects both the length of time between the jet leaving the tip and contacting the collecting plate and the electric field strength. By decreasing the distance between the tip and collecting plate the time available for the solvent to evaporate from the solution decreases, thus thicker fibres, or even meshes, result due to more solvent being retained by the polymeric solution.[26] The electric field strength decreases upon increasing the distance between the tip and collecting plate which leads to less of a stretching force upon the polymeric solution, thus thicker fibres can occur as a result of increasing this distance.[25] Therefore, increasing the tip and collecting plate distance either results in finer fibres, due to more time being available for evaporation of the solvent, or thicker fibres, due to lower electric field strength. Therefore, the optimal distance between the tip and collecting plate differs from system to system.

6.2. Aims and objectives

The aim of the research described in this chapter is to characterise the morphology of fibres electrospun from aqueous solutions of PEO at different concentrations, both with and without the inclusion of citrate passivated Au nanoparticles. Optical micrographs and AFM will be used to characterise the morphology of the fibres, and TEM will be used to determine the arrangement of Au nanoparticles within the electrospun fibres. DSC will also be used to investigate the crystallinity of the fibres. The inclusion of Au nanoparticles within

the fibres, coupled with the subsequent removal of the PEO matrix after electrospinning, could allow the formation of Au patterns. Such Au patterns could then be used as templates for the formation of alkanethiol SAMs.

6.3. Results and Discussion

6.3.1. Characterization of citrate passivated Au nanoparticles

Citrate passivated Au nanoparticles were synthesised using the Frens method,[27] described in **section 6.6.1.1.**, and were characterised by UV-vis spectroscopy and TEM. In order to obtain a sufficient volume of Au nanoparticle solution, from which to make four separate batches of PEO solutions, 100 ml of nanoparticle solution was required. However, when 100 ml of solution was made in a single synthesis the resultant nanoparticle solution was blue in colour, an indication of aggregation of Au nanoparticles.[28] Therefore, in order to obtain 100 ml of Au nanoparticle solution, the nanoparticles were synthesized in two batches of 50 ml and then subsequently combined. This method allowed the use of identical solutions of Au nanoparticles for all batches of PEO/Au nanoparticle solution. The UV-vis spectra of the citrate passivated Au nanoparticles before and after mixing the two batches of solution is shown in **Figure 71**. The maximum absorbance of the nanoparticle solution, at 524 nm wavelength, is consistent with that in the literature for a solution of discrete citrate passivated Au nanoparticles.[29]
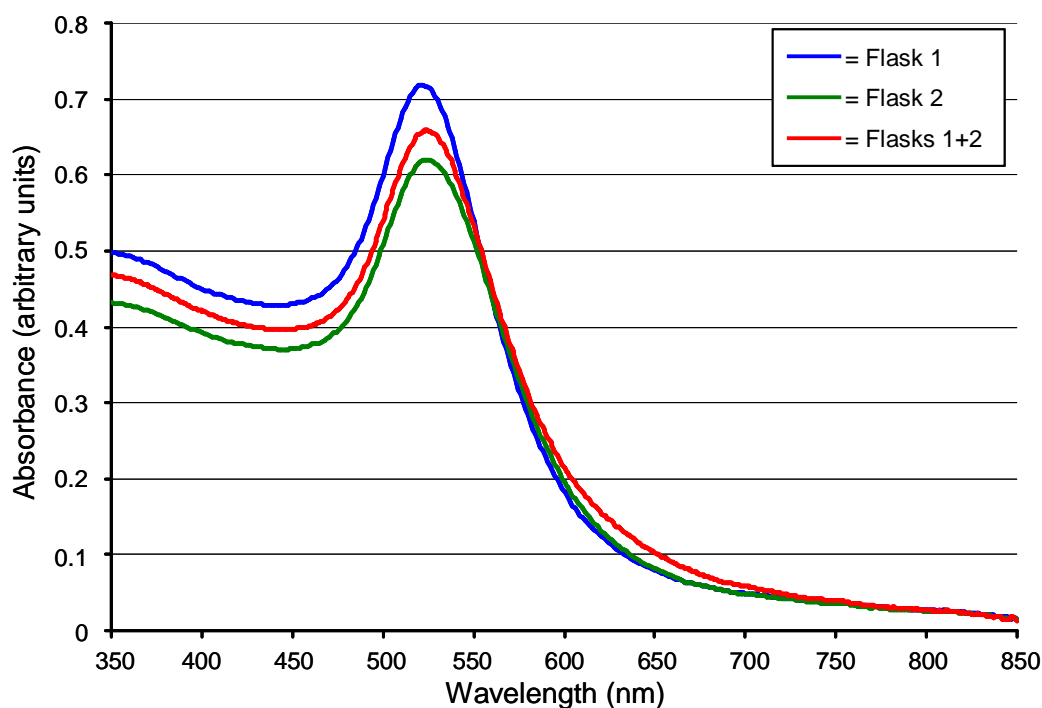
Figure 71. UV-vis spectra of the two separate batches of citrate passivated Au nanoparticles and of a sample when the two batches are mixed

TEM images were obtained of citrate passivated Au nanoparticles by placing a drop of the aqueous nanoparticle solution on TEM grids and allowing them to air dry under ambient conditions. A histogram showing the size distribution of the citrate passivated Au nanoparticles (**Figure 72a**) was obtained from the TEM images (an example of which is shown in **Figure 72b**).
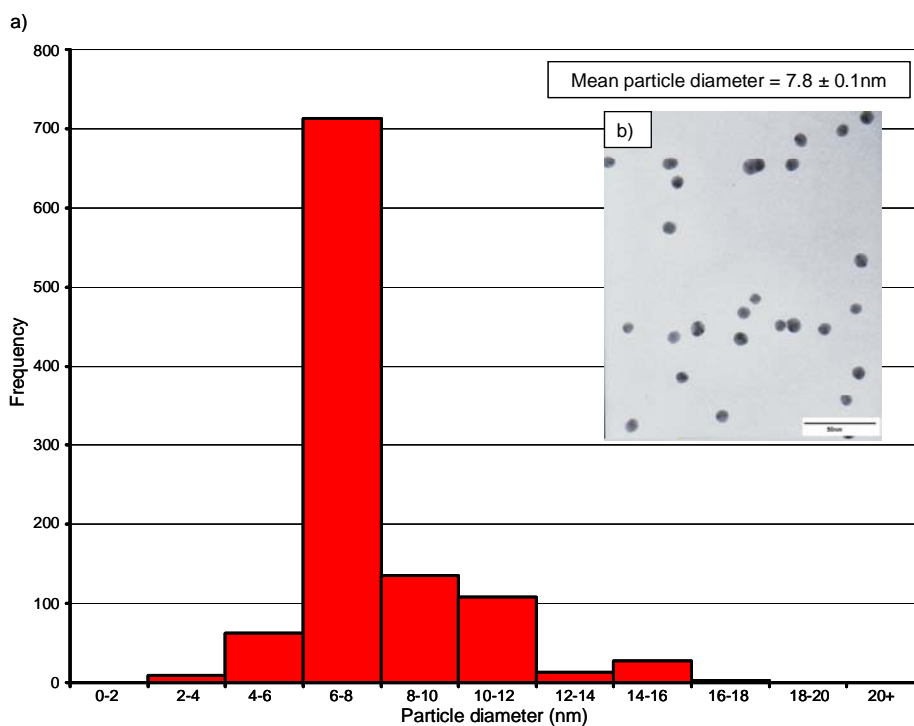
Figure 72. a) Histogram showing the size distribution of citrate passivated Au nanoparticles and

b) TEM image of citrate passivated Au nanoparticles

The citrate passivated Au nanoparticle solution contains nanoparticles of 7.8 nm $\pm$ 0.1 nm in diameter (**Figure 72a** and **b**). Knowledge of the volume of the nanoparticle solution, and the size of both the TEM images and the TEM grid, allow a nanoparticle concentration of 1.2×10^9 particles.ml^{-1} to be calculated. The calculation for this approximate nanoparticle concentration is shown in **Appendix D1**.

6.3.2. Characterization of fibres electrospun from PEO solutions

PEO solutions, of varying concentrations, were prepared by the vigorous stirring of PEO with either UHQ H_2O or aqueous dispersions of citrate passivated Au nanoparticles (see **section 6.6.1.2.**). The viscosities of the solutions (**Table 4**) were measured using a rotary viscosity meter. The viscosity, as expected, increases as the PEO concentration of the solutions is increased. The PEO solutions were then electrospun onto glass collecting plates. The resultant fibres were then characterised by optical microscopy, AFM, TEM and DSC.

Table 4. Viscosity data for the electrospinning solution

wt% PEO	Viscosity (mPa.s)	
	Aqueous PEO solution	*Aqueous PEO/Au nanoparticle solution*
2	1921	1894
3	5132	4966
4	7328	7210
5	10230	9534

6.3.2.1. Fibre morphology

Fibres were electrospun from aqueous PEO solutions onto glass collecting plates. The fibres consisted of three predominant structures, straight fibres and fibres with either beaded (**Figure 73a** and **b**) or branched (**Figure 73c** and **d**) morphologies were observed.
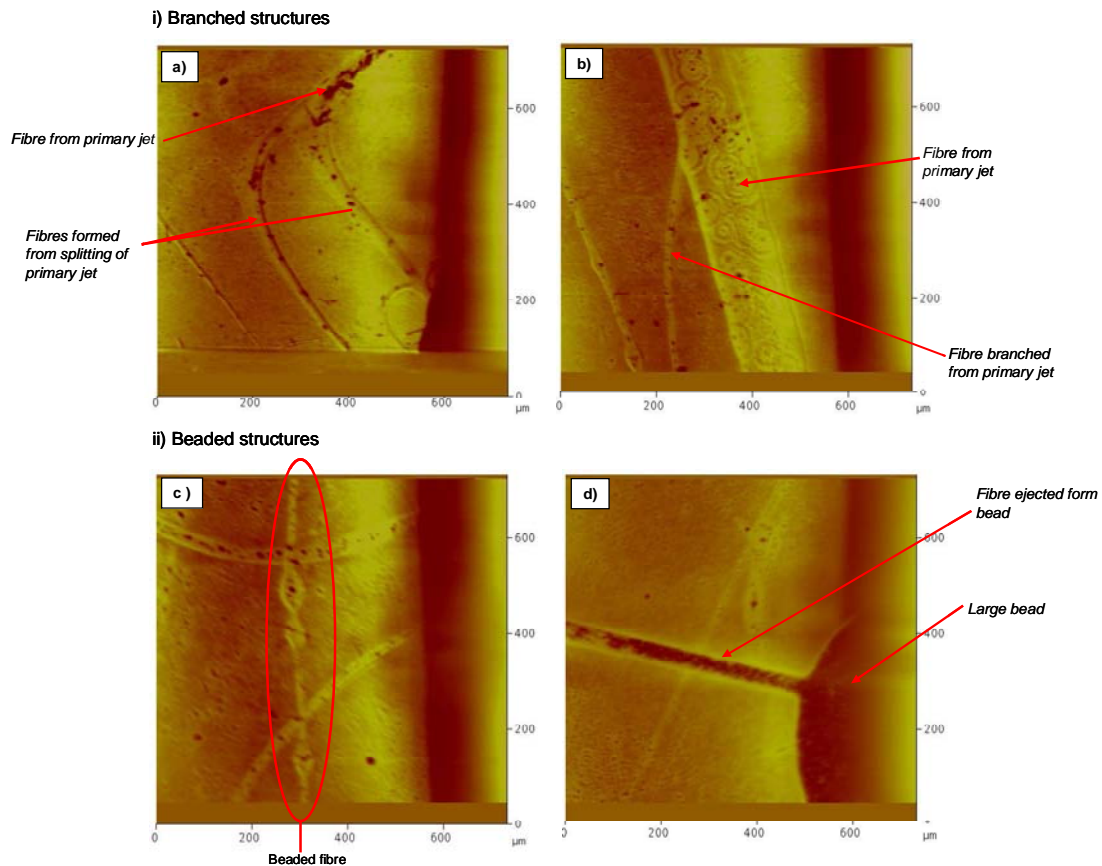
Figure 73. Optical micrographs showing a) and b) branched and c) and d) beaded structures of fibres electrospun from aqueous PEO solutions

Branched fibres (**Figure 73a** and **b** and **Figure 74a-d**) form when localised fluctuations of charge density (**Figure 74b**), on a primary jet, result in the repulsive forces of the surface charges overcoming the surface tension of the jet.[23] As a result of the localised repulsive force of the surface charges (**Figure 74b**) overcoming the local surface tension of the solution, the primary jet can either split (**Figure 74c**) or emit a smaller, secondary jet (**Figure 74d**) resulting in fibre morphologies depicted in **Figure 73a** and **Figure 73b** respectively.

Beaded fibres (**Figure 73c** and **Figure 74e-g**) form as a result of the surface tension (**Figure 74f**) of the electrospinning jet causing beads favouring the formation of spherical structures (**Figure 74g**) in order to reduce the surface area of the polymer solution. However, unlike fibres which consist of many beads (straight) fibres were found protruding from a single, large bead (**Figure 73d** and **Figure 74h-k**). Such structures are due to the surface tension forces causing large spherical beads to form at the tip of the spinneret, (**Figure 74i**) which subsequently detach from the needle tip and deposit on the collecting plate. When the repulsive force, of the surface charges on the surface of the bead, overcome the surface tension forces jetting occurs from the large beads. This jetting either occurs during the dwell time for the bead on the needle tip (**Figure 74j**) or during its travel from the needle tip to the collecting plate (**Figure 74k**) after its detachment from the spinneret.
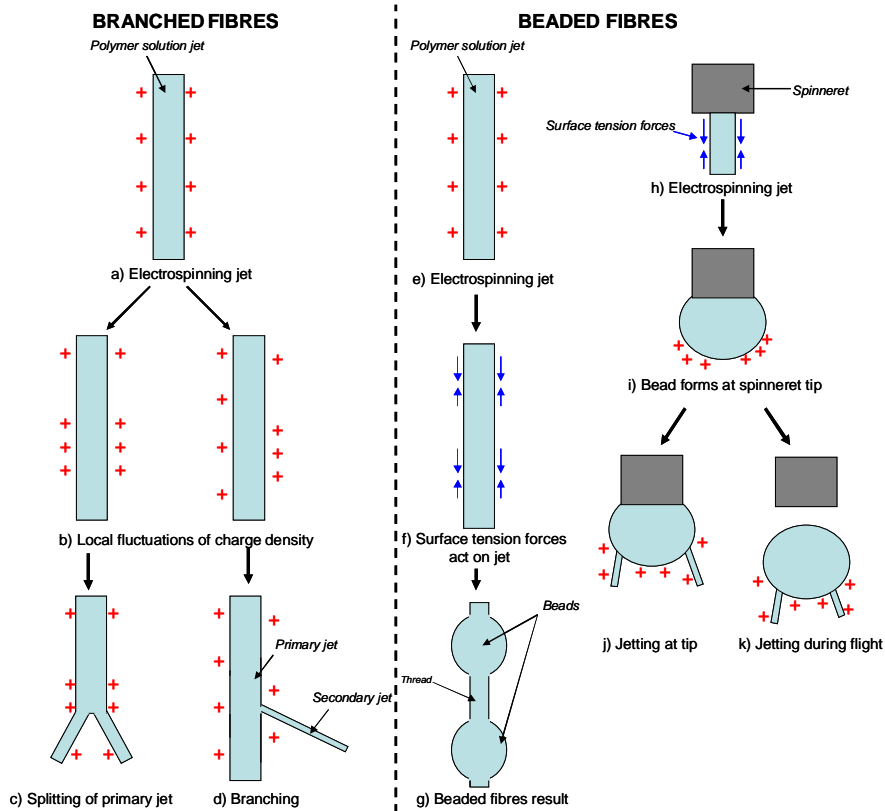
Figure 74. Cartoon representation of the formation of branched (a-d) and beaded (e-g) fibres during the electrospinning process.

6.3.2.2. Fibre dimensions

Optical microscopy and AFM were used to measure the widths of fibres electrospun from 2 wt%, 3 wt%, 4 wt% and 5 wt% aqueous solutions of PEO and PEO/Au nanoparticle composite. Histograms of the distribution of fibre widths are shown separately for fibre widths determined by either optical microscopy or AFM in **Figure 75** (2 wt% PEO), **Figure 76** (3 wt% PEO), **Figure 77** (4 wt% PEO) and **Figure 78** (5 wt% PEO). The optical micrographs and AFM images, recorded for the histograms concerning the width ranges 0 - 200+ µm and 0 - 2 µm respectively, are shown in **appendix D2**.
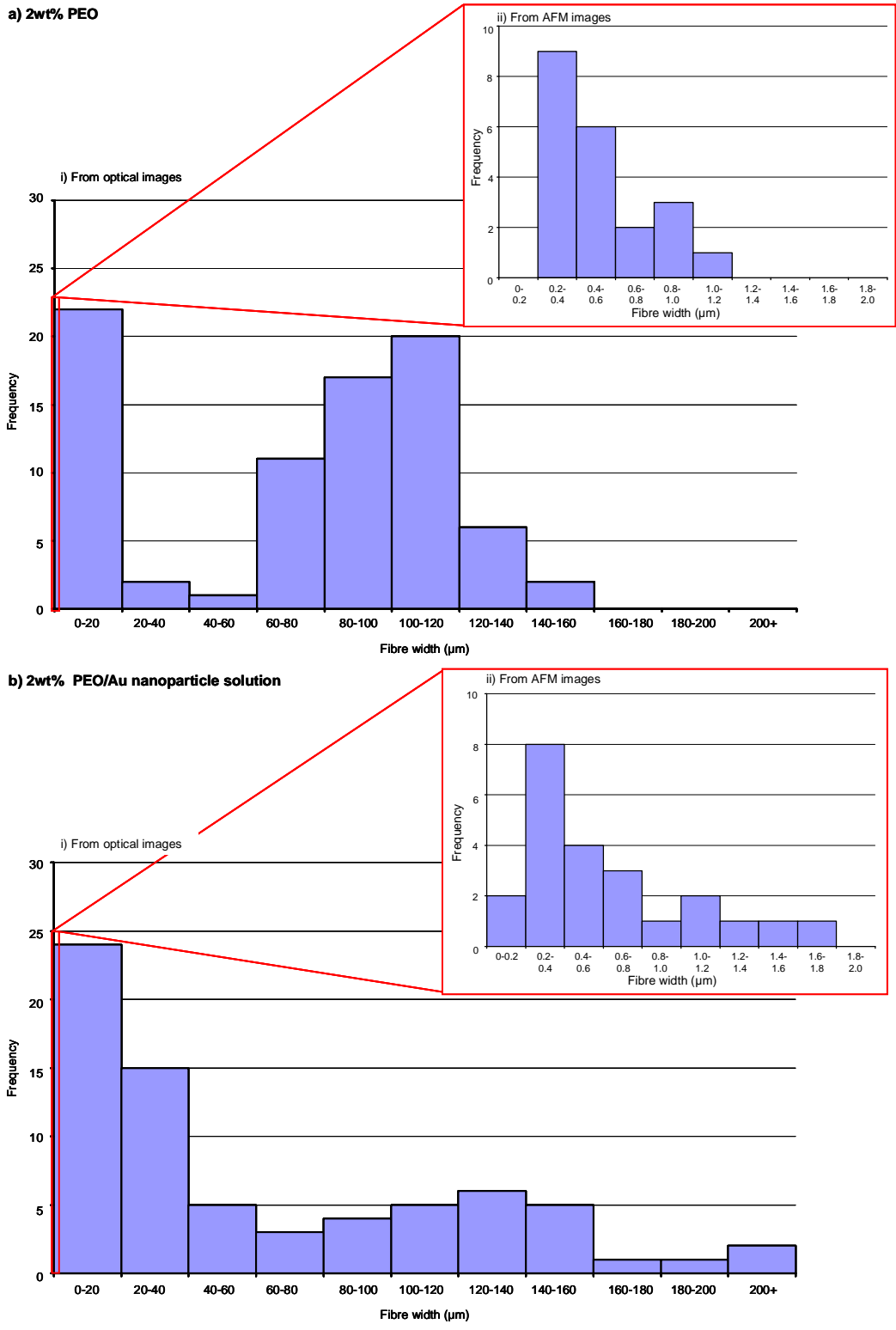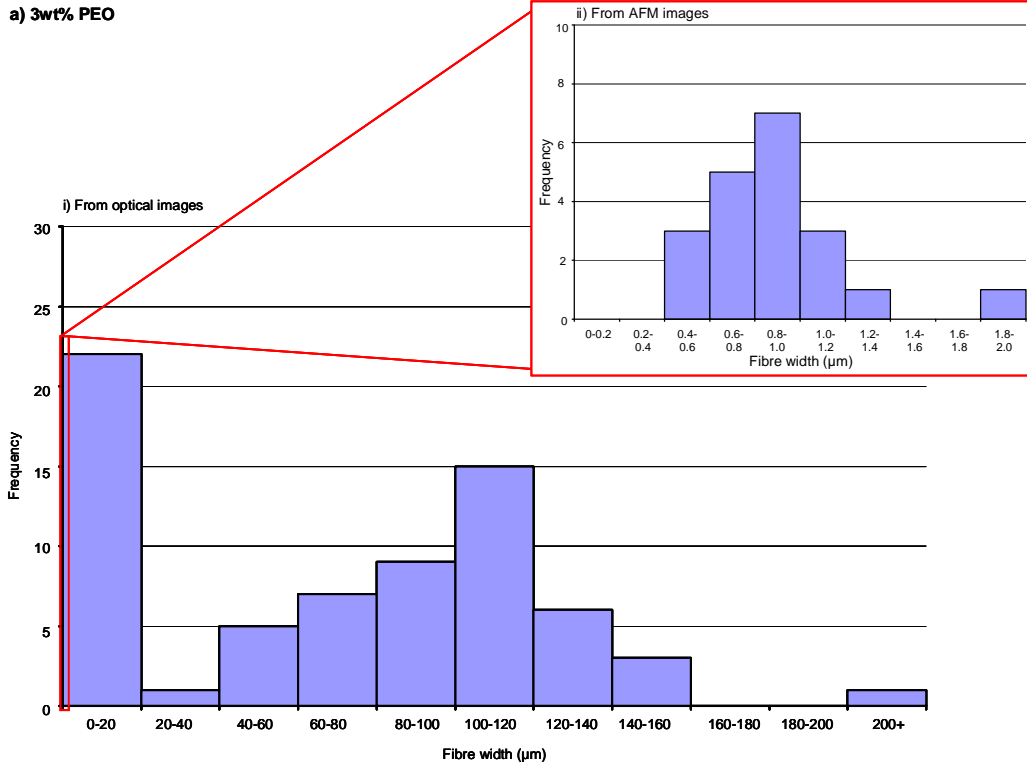
Figure 75. Histograms showing the widths of fibres electrospun from aqueous solutions of a) 2 wt% PEO and b) 2 wt% PEO/Au nanoparticle solutions (Inserts in both histograms show the fibre width distribution of sub 2 μm fibres).
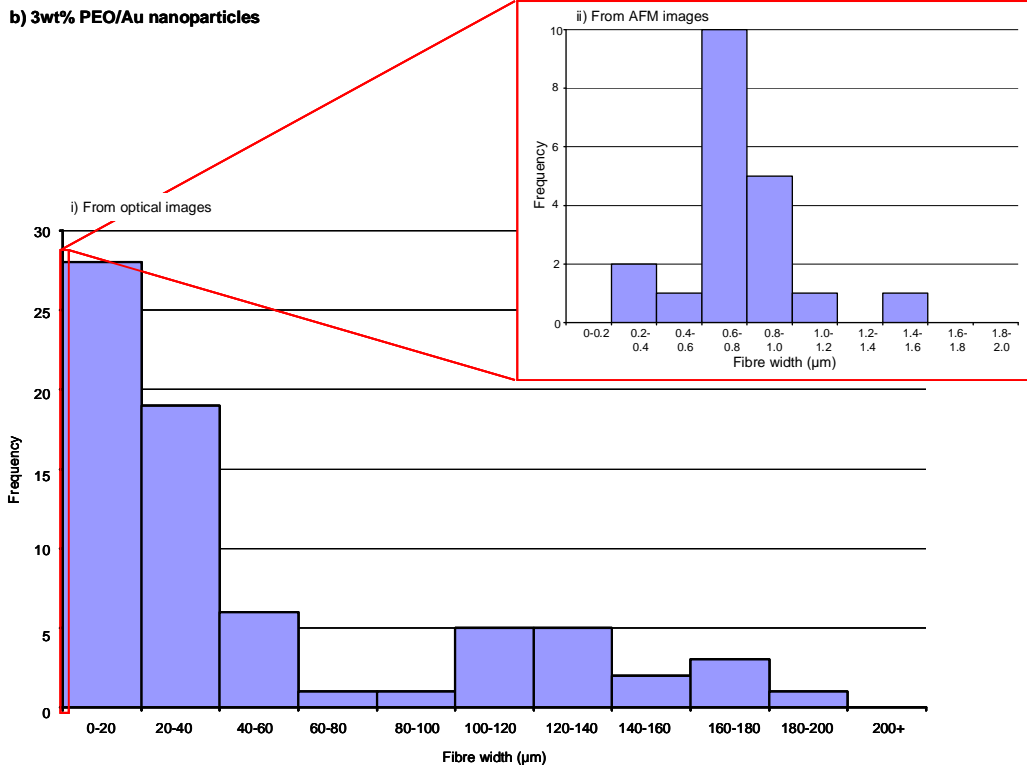
Figure 76. Histograms showing the widths of fibres electrospun from aqueous solutions of a) 3 wt% PEO and b) 3 wt% PEO/Au nanoparticle solutions (Inserts in both histograms show the fibre width distribution of sub 2 µm fibres).
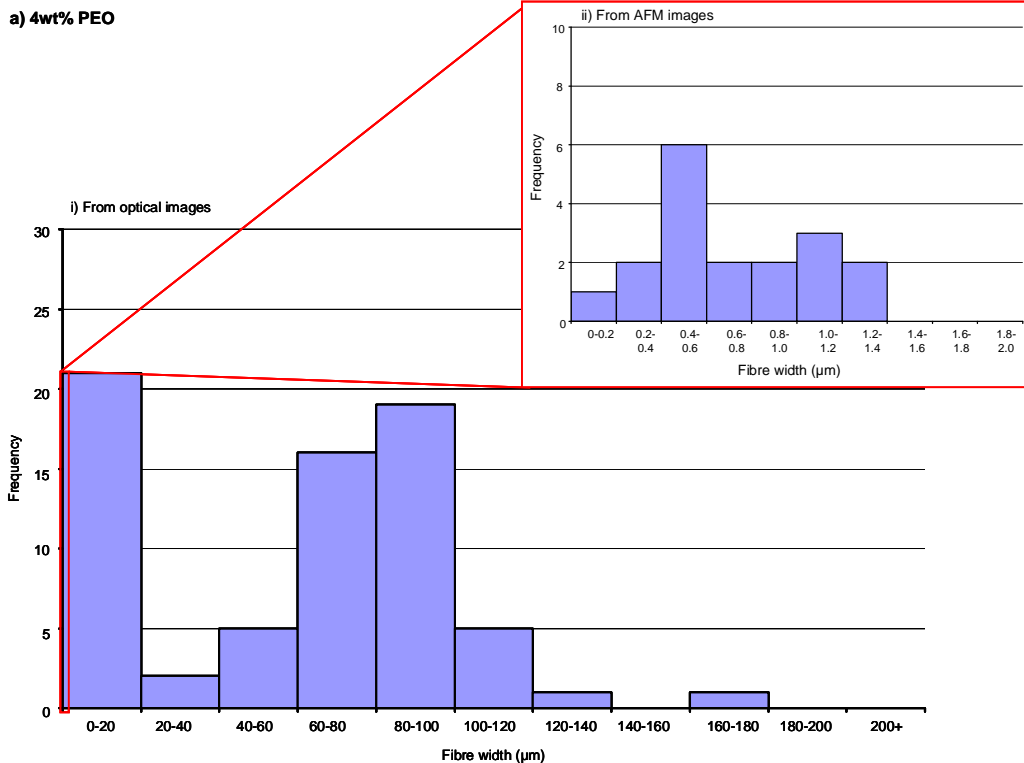
Figure 77. Histograms showing the widths of fibres electrospun from aqueous solutions of a) 4 wt% PEO and b) 4 wt% PEO/Au nanoparticle solutions (Inserts in both histograms show the fibre width distribution of sub 2 μm fibres).
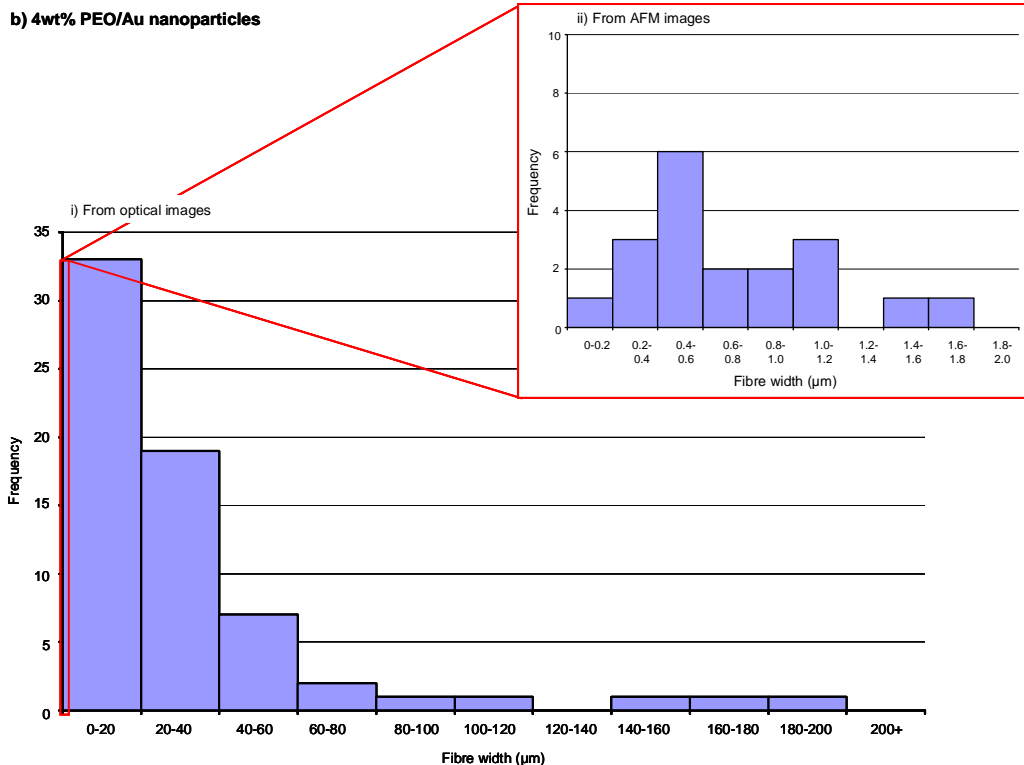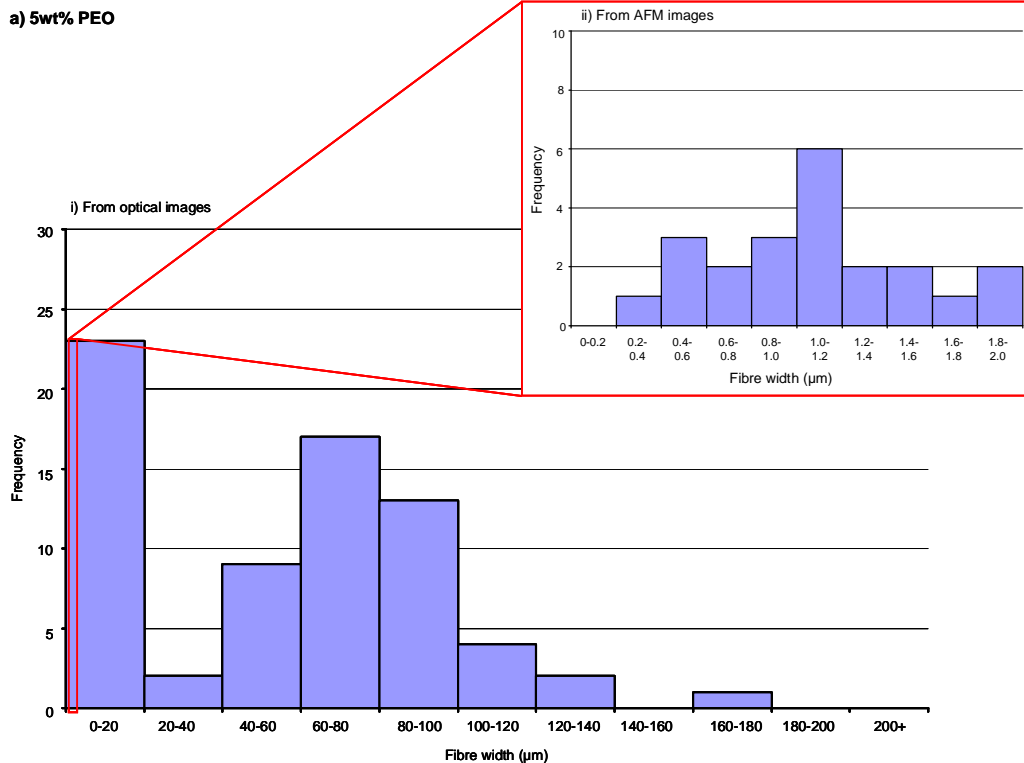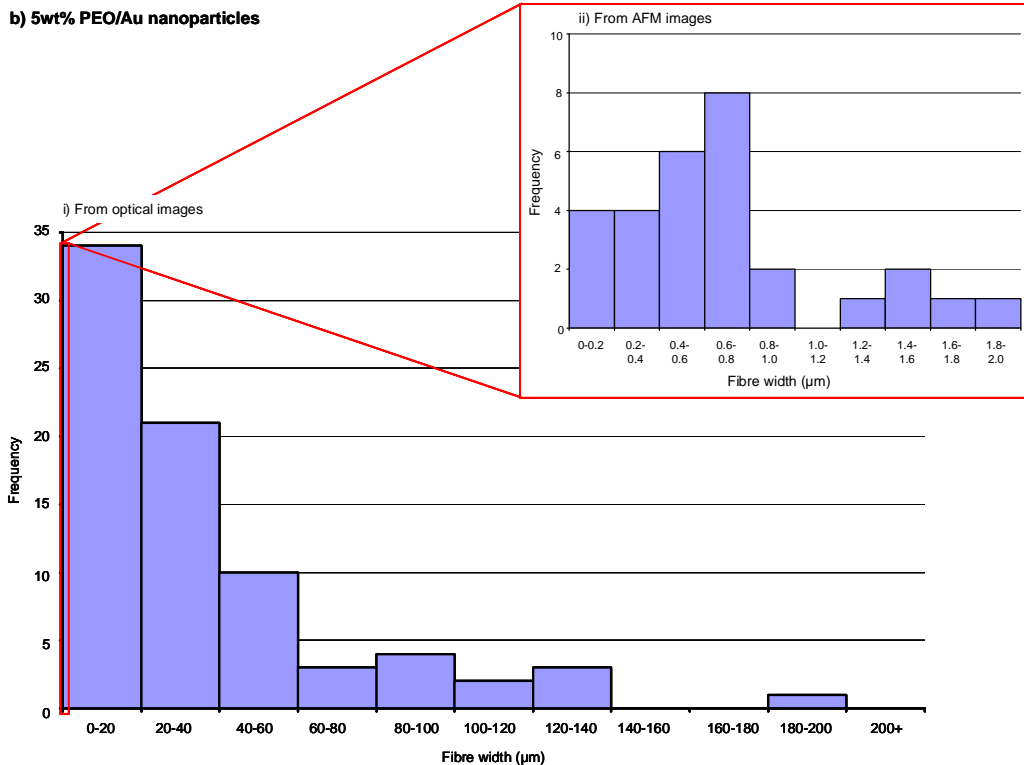
Figure 78. Histograms showing the widths of fibres electrospun from aqueous solutions of a) 5 wt% PEO and b) 5 wt% PEO/Au nanoparticle solutions (Inserts in both histograms show the fibre width distribution of sub 2 μm fibres).

The histograms obtained from optical micrographs (**Figure 75a**, **Figure 76a, Figure 77a** and **Figure 78a**) exhibit a bimodal distribution for fibres electrospun from aqueous PEO solutions. Upon the inclusion of citrate passivated Au nanoparticles in the PEO solution the distribution changes from bimodal to a unimodal distribution (**Figure 75b**, **Figure 76b, Figure 77b** and **Figure 78b**). The histograms obtained from AFM images for both aqueous solutions of PEO (insets in **Figure 75a**, **Figure 76a, Figure 77a** and **Figure 78a**) and PEO/Au nanoparticles (insets in **Figure 75b**, **Figure 76b, Figure 77b** and **Figure 78b**) show a unimodal distribution.

Upon plotting the fibre widths, obtained from both optical micrographs and AFM images, against wt% PEO of the solutions it can be seen that the standard error bars are too large to determine a conclusive trend of fibre widths as a function of wt% PEO of the electrospinning solutions (**Figure 79a** and **b**). Therefore, further fibre diameter measurements are required in order to reduce the error bars and provide a conclusive trend of the fibre widths of fibres electrospun from PEO solutions.

a) Fibre widths (optical microscopy)

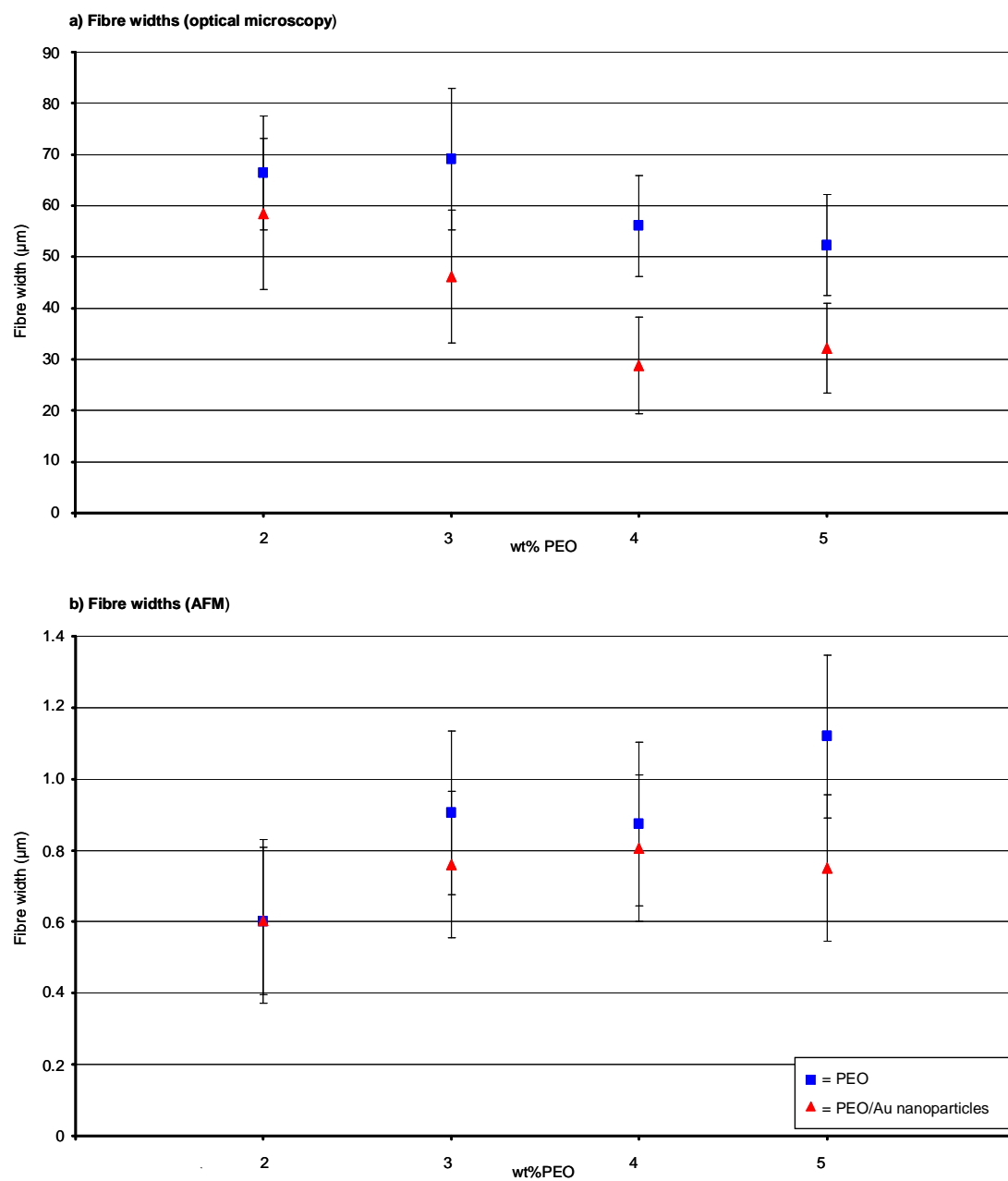**b) Fibre widths (AFM)**

Figure 79. Graphs showing average width of fibres electrospun from all wt% PEO solutions studied both with and without nanoparticles a) represents fibre widths from all fibre widths and b) represents fibre widths in the sub 2 μm regime (at 2 wt% PEO the average fibre widths for fibres electrospun from PEO and PEO/Au solutions are 0.601 μm and 0.603 μm, respectively)

6.3.2.3. Nanoparticles within fibres

In order to investigate the organisation of Au nanoparticles within the electrospun fibres TEM images (**Figure 80**) were obtained of fibres electrospun directly onto TEM Cu slot grids.
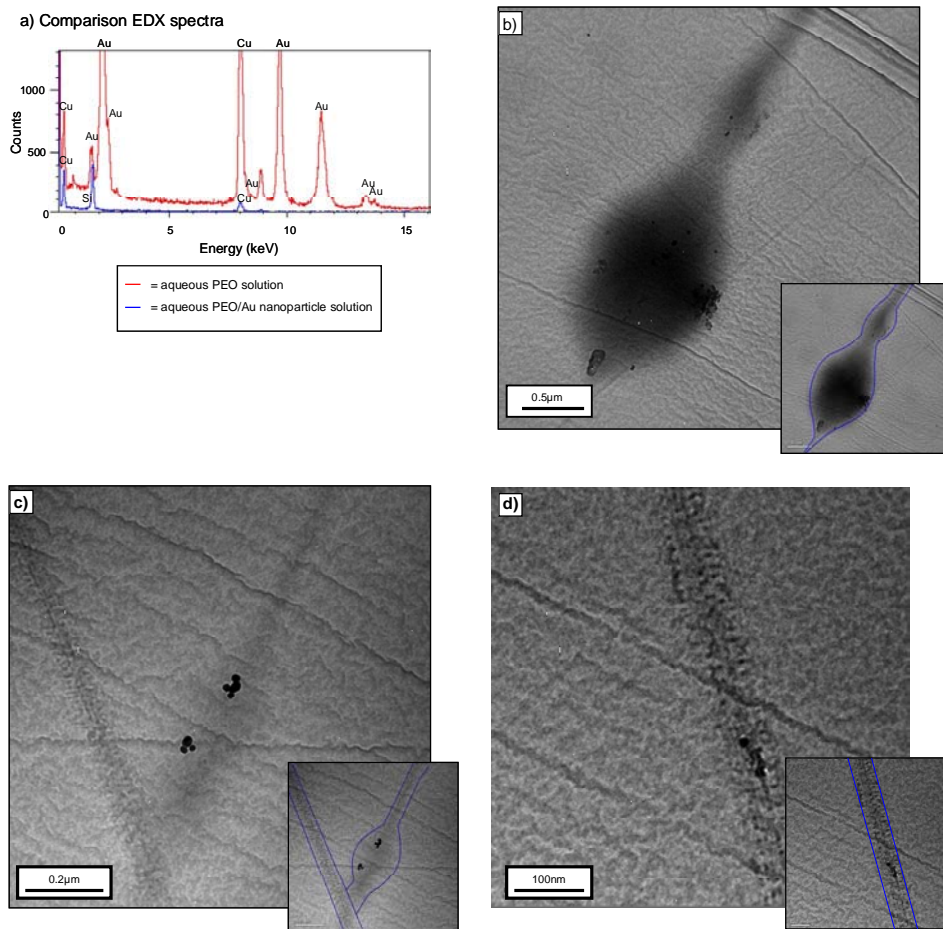

Figure 80. TEM images of fibres electrospun from 5 wt% PEO solutions containing Au nanoparticles. a) and b) show the presence of Au nanoparticles in 'beads' and c) the presence of Au nanoparticles within 'threads'. d) shows the EDX spectra of both fibres electrospun from solutions of PEO either with or without the presence of Au nanoparticles

EDX spectra (**Figure 80a**) confirmed both the presence and absence of Au within fibres electrospun from PEO solutions in which the PEO is dissolved in Au nanoparticle solution and UHQ H_2O, respectively. TEM images (**Figure 80b-d**) show that nanoparticles can be found in both the beads and threads of the electrospun fibres. However, the nanoparticles are more concentrated in the beads ($\sim 4.3 \times 10^{13}$ particles.ml^{-1}) than in the threads ($\sim 3.5 \times 10^{12}$ particles.ml^{-1}) and the concentration calculations can be found in **Appendix D3**. This observation may be due to turbulence within the PEO solution during bead formation with PEO solution flowing faster in the areas while the solution is thinning (i.e. at the threads). Therefore, the flow of PEO solution will be slower in the beads. Thus, allowing for the build up of nanoparticles within the beads. However, the difference in nanoparticle concentration within the threads, compared to within the beads, may also be due to a possible inhomogeneous distribution of Au nanoparticles within the polymeric solution.

6.3.2.4. Crystallization of electrospun fibres

The electrospinning process has been shown to have an effect on the crystallinity of electrospun fibres with areas of crystallinity being visible in the AFM phase images as lamellar structures.[12] Such lamellar structures cannot be seen in AFM height images but are clearly visible in the phase images (**Figure 81)**.
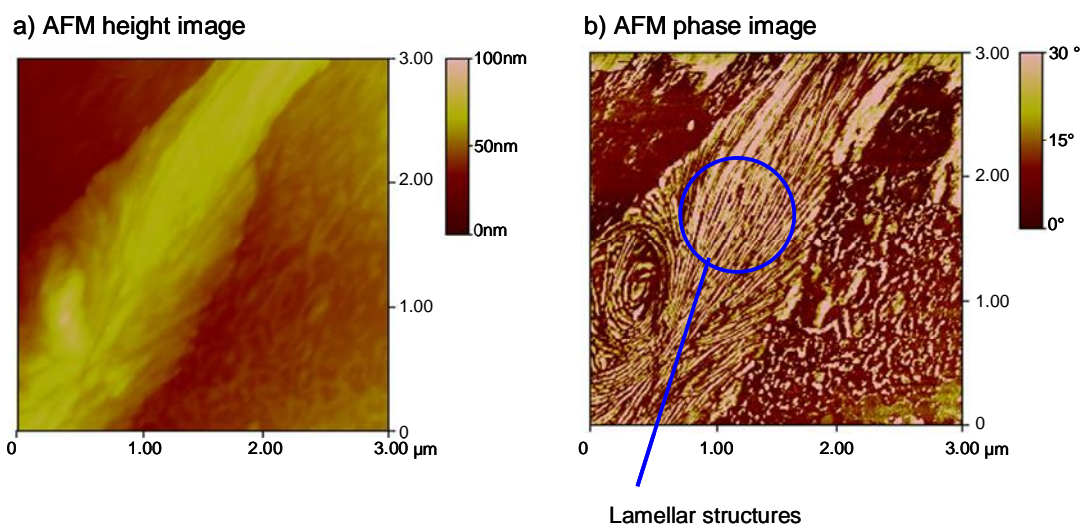
a) AFM height image   b) AFM phase image

Lamellar structures

Figure 81. AFM height a) and phase b) images of a fibre electrospun from 4 wt% PEO solution in UHQ H_2O.

AFM phase imaging gives only a local view of the degree of crystallinity of the fibres, therefore differential scanning calorimetry (DSC) was used to determine the enthalpy of fusion of fibres spun from each solution. The DSC curves can be found in **Appendix D4**. The enthalpy of fusion for each wt% PEO solution (**Table 5**) was compared to the enthalpy of fusion of 100 % crystalline PEO, which is 205 $J.g^{-1}$,[30] in order to determine the degree of crystallinity of the fibres (**Table 5** and **Figure 82**).

Table 5. Enthalpy of fusion (ΔH_f) and % crystallinity of fibres electrospun from PEO solutions either with or without the presence of Au nanoparticles

wt% PEO	Without nanoparticles		With nanoparticles	
	ΔH_f (J.g^{-1})	% crystallinity	ΔH_f (J.g^{-1})	% crystallinity[a]
2	33.51	16.35	55.88	27.26
3	70.66	34.47	91.20	44.49
4	86.02	41.96	111.29	54.29
5	89.23	43.53	111.37	54.32

[a] % crystallinity is calculated by dividing ΔH_f (measured) by ΔH_f (from literature for 100 % crystalline PEO then multiplying by 100. The literature value for 100% crystalline PEO is 205 J.g^{-1}.[30]
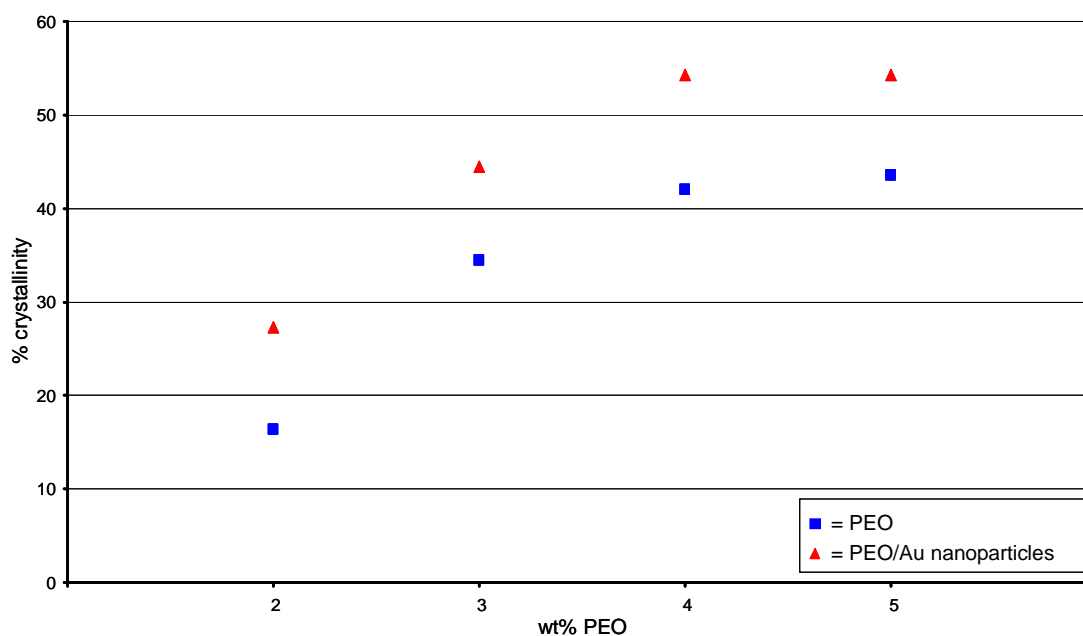

Figure 82. Graph showing the %crystallinity of fibres electrospun from aqueous PEO solutions either with or without the presence of citrate passivated Au nanoparticles

Table 5 shows that both the enthalpy of fusion and the %crystallinity, increase as the wt% PEO of the solutions is increased. The %crystallinity also appears to increase upon the introduction of Au nanoparticles into the solution (**Figure 82**). The increase of crystallinity, upon the inclusion of Au nanoparticles,

could be due to the nanoparticles acting as heterogeneous nucleation sites for polymer crystallisation.[31, 32]

6.4. Conclusions

The aim of this chapter was to characterise aqueous solutions of different concentrations of both PEO and PEO/citrate passivated Au nanoparticles in order to investigate the effect of the inclusion of citrate passivated Au nanoparticles on the electrospun fibres. The work presented in this chapter shows that aqueous solutions of citrate passivated Au nanoparticles were prepared by using the Frens method[27] and characterised using both UV-vis spectroscopy and TEM. UV-vis spectroscopy was used to show that the nanoparticle solution consisted of discrete Au nanoparticles (**Figure 71**) and TEM was used to evaluate both the size of the nanoparticles (**Figure 72**) and the approximate concentration of nanoparticles in the solution.

AFM was used to investigate the morphology of the fibres and it could be seen that the fibres were present in three different morphologies, these being straight fibres and fibres with both beaded and branched structures (**Figure 73**). The fibre width distribution of the fibres showed that, upon the inclusion of Au nanoparticles in the solution, the fibre width distribution changes from a bimodal distribution to one displaying a unimodal distribution at all concentrations of PEO (**Figure 75, Figure 76, Figure 77** and **Figure 78**). The distribution of citrate

passivated Au nanoparticles, within the fibres, was studied by TEM (**Figure 80**) and if could be seen that, in beaded fibres, the concentration of nanoparticles was greater in the beads compared to the threads. The presence of Au nanoparticles was also found to affect the crystallinity of the fibres electrospun from PEO solutions as shown by DSC analysis (**Figure 82**). This observation could be due to the Au nanoparticles acting as nucleation sites for PEO crystallization.

6.5. Future work

The work presented in this chapter shows that Au nanoparticles can be successfully incorporated into PEO fibres. The next stage of this project will be to form Au structures using the methodology outlined in **Figure 83.** Patterned arrays of electrospun fibres (**Figure 83b**) could be produced by electrospinning onto a rotating collection plate in order to obtain aligned fibres, which has previously been shown.[33-35] The PEO matrix could be removed using selective etching methods which will result in an Au pattern. This Au pattern could be used as a template on which to assemble nanostructures using alkanethiol self assembly techniques.
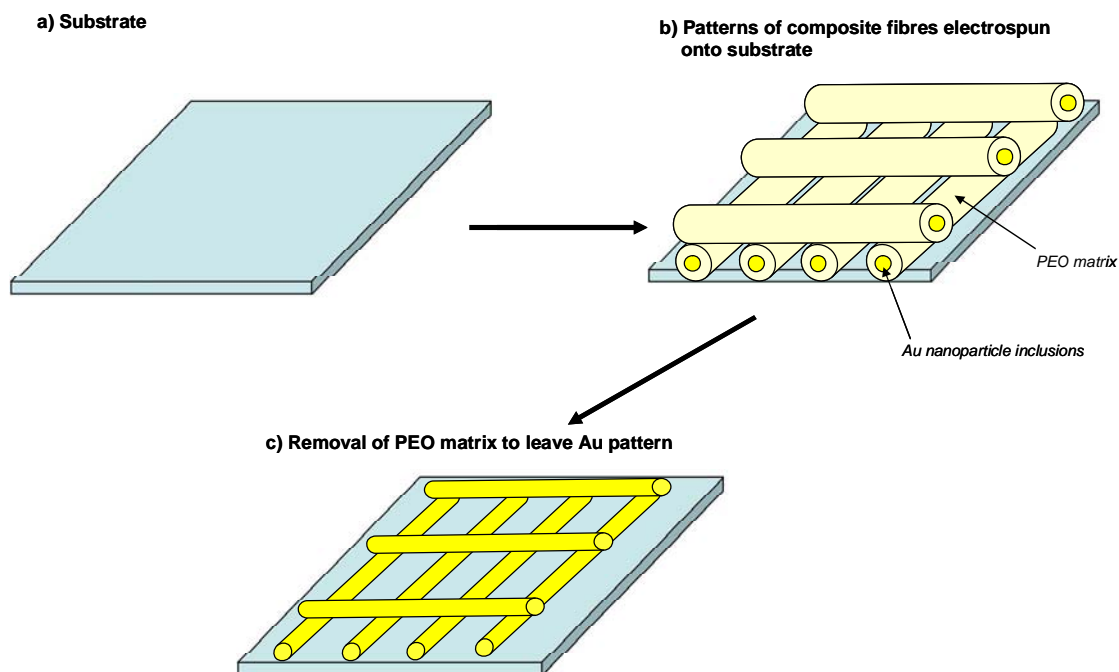
Figure 83. Formation of Au patterns from electrospun fibres. a) bare substrate b) PEO/Au fibres electrospun on substrate in a patterned manner. c) bare Au patterns remaining after removal of PEO

6.6. Experimental

All chemicals were obtained from Aldrich unless stated.

6.6.1. Fabrication of fibres

6.6.1.1. Preparation of citrate passivated Au nanoparticles

An aqueous solution of citrate passivated Au nanoparticles were prepared by the method described by Frens.[27] Chloroauric acid (0.01 g, 2.5 mmol) was dissolved in UHQ water (100 ml) and heated to reflux. Sodium citrate tribasic

dihydrate (0.023 g, 0.15 mol) was added to the refluxing chloroauric acid solution and heated under reflux continued until there was no further colour change. The solution was allowed to cool to room temperature and centrifuged (at 3500 rpm) and the supernatant retained.

6.6.1.2. Preparation of PEO solutions

Polyethylene oxide (PEO) solutions were prepared by adding PEO (2 000 000 MWt) to either UHQ H_2O (resistivity = 18 MΩ.cm) or a solution of citrate passivated Au nanoparticles. The PEO was added slowly to either the UHQ H_2O or nanoparticle solution under vigorous stirring in a 100 ml glass Duran flask and continuously stirred for 24 hr. The mass of PEO and the volume of either UHQ H_2O or Au nanoparticle solution used for each wt% solution is shown in **Table 6**.

Table 6. The composition of each aqueous PEO (2 000 000 MWt) solution

wt% PEO solution	Mass of PEO added (g)	Volume of UHQ H_2O *OR* citrate passivated Au nanoparticle solution (ml)
2	0.80	39.2
3	1.20	38.8
4	1.44	34.6
5	1.80	34.2

6.6.1.3. Electrospinning of fibres

The fibres were electrospun at a voltage of 12 kV between the tip of a metallic syringe and a glass collecting plate which was at a distance of 10 cm from the tip of the syringe at a flow rate of 10^{-9} m^3s^{-1}. The electrospinning process was performed for 10 min per sample.

6.6.2. Characterisation

UV-vis spectroscopy and TEM was used for the characterisation of the citrate passivated Au nanoparticles whilst AFM, DSC and TEM were used to characterise the electrospun fibres and the parameters used for each technique are described in this section.

6.6.2.1. UV-visible absorption spectroscopy

UV-vis spectra were obtained using a Hewlett-Packard 8452A spectrometer operated at wavelengths between 350 nm and 850 nm with a 2 nm band width at 240 $nm.min^{-1}$.

6.6.2.2. Atomic Force Microscopy

AFM images were obtained by using either a Nanoscope 3100 Dimension AFM (Veeco) or a PicoScan AFM (Molecular Imaging) and these images were analysed using either Nanoscope III software (version 5.12r3) or PicoScan 5 software, respectively. AFM images were obtained in tapping mode with the use of an etched Si tip (Veeco model: RTESP). Before engaging the AFM tip the surface of the sample was observed using the optical system of the microscope in order to find areas on the surface where PEO had been deposited. The AFM tip was engaged with the surface and the images were obtained in tapping mode at a frequency of 1 Hz and the images were made up of 512 lines with 512 samples per line.

6.6.2.3. Differential Scanning Calorimetry

DSC measurements were recorded by placing ~1 mg of PEO fibres into an Al pan onto which a lid was placed, crimped closed and placed into a differential scanning calorimeter (Perkins Elmer Pyris with Pyris control software) along with an empty pan which was used as a reference. The pan was held at 25 °C for 1 min then heated to 120 °C at 5 °C.min^{-1} then held at 120 °C for 1 min before being cooled to 25 °C at -5 °C.min^{-1}.

6.6.2.4. TEM and EDX

TEM specimens of citrate passivated Au nanoparticles were prepared by placing a drop of aqueous citrate passivated Au nanoparticle solution (~3 ml) on a Formvar coated Cu TEM grid (Agar) and allowed to air-dry. TEM characterisation of citrate passivated Au nanoparticles was performed using a JEOL 1200ex TEM operated at 80 kV.

Electrospun fibres were prepared for characterisation by TEM by electrospinning the fibres directly onto copper slot TEM grids (Agar Scientific). TEM characterisation of the electrospun fibres was carried out using a Technai F20 FEG TEM (Philips) operated at 200 kV. EDX spectra were obtained in situ in the Technai F20 FEG TEM and analysed by using ISIS 300 EDX software (Oxford Instruments).

6.7. References

1. Hamlett, C. A. E.; Jayasinghe, S. N.; Preece, J. A., Electrospinning nanosuspensions loaded with passivated Au nanoparticles. *Tetrahedron* **2008**, 64, 8476-8483.

2. Li D.; Xia Y., Electrospinning of nanofibers: Reinventing the wheel? *Adv. Mater.* **2004,** 16, 1151-1170.

3. Huang Z.-M.; Zhang Y.-Z.; Kotaki M.; Ramakrishna S., A review on polymer nanofibers by electrospinning and their applications in nanocomposites. *Compos. Sci. Technol.* **2003,** 63, 2223-2253.

4. Dersch R.; Steinhart M.; Boudriot U.; Greiner A.; Wendorff J. H., Nanoprocessing of polymers: applications in medicine, sensors, catalysis, photonics. *Polym. Advan. Technol.* **2005,** 16, 276-282.

5. Subbiah T.; Bhat G. S.; Tock R. W.; Parameswaran S.; Ramkumar S. S., Electrospinning of nanofibers. *J. Appl. Polym. Sci.* **2005,** 96, 557-569.

6. Formhals, A. Process and Apparatus of Preparing Artificial Threads. US Patent number: 1 975 504, **1934**.

7. Reneker D. H.; Yarin A. L.; Fong H.; Koombhongse S., Bending instability of electrically charged liquid jets of polymer solutions in electrospinning. *J. Appl. Phys.* **2000,** 87, 4531-4547.

8. Shin Y. M.; Hohmann M. M.; Brenner M. P.; Rutledge G. C., Experimental characterization of electrospinning: the electrically forced jet and instabilities. *Polymer* **2001,** 42, 9955-9967.

9. Yarin A. L.; Koombhongse S.; Reneker D. H., Taylor cone and jetting from liquid droplets in electrospinning of nanofibers. *J. Appl. Phys.* **2001,** 90, 4836-4846.

10. Salalha W.; Dror Y.; Khalfin R. L.; Cohen Y.; Yarin A. L.; Zussman E., Single-walled carbon nanotubes embedded in orientated polymeric nanofibers by electrospinning. *Langmuir* **2004,** 20, 9852-9855.

11. Mathew G.; Hong J. P.; Rhee J. M.; Lee H. S.; Nah C., Preparation and characterization of properties of electrospun poly(butylene terephthalate) nanofibers filled with carbon nanotubes. *Polym. Test.* **2005,** 24, 712-717.

12. Kim G.-M.; Wutzler A.; Radusch H.-J.; Michler G. H.; Simon P.; Sperling R. A.; Parak W. J., One-dimensional arrangement of gold nanoparticles by electrospinning. *Chem. Mater.* **2005,** 17, 4949-4957.

13. Yang B.-X.; Shi J.-H.; Pramoda K. P.; Goh S. H., Enhancement of stiffness, strength, ductility and toughness of poly(ethylene oxide) using phenoxy-grafted multiwalled carbon nanotubes. *Nanotechnology* **2007,** 18, 125606 (7pp).

14. Lyons J.; Li C.; Ko F., Melt-electrospinning part I: processing parameters and geometric properties. *Polymer* **2004,** 45, 7597.

15. Stasiak M.; Studer A.; Greiner A.; Wendorff J. H., Polymer fibers as carriers for homogeneous catalysts. *Chem. Euro. J.* **2007,** 13, 150-156.

16. Wang Z.-G.; Ke B.-B.; Xu Z.-K., Covalent immobilization of redox enzyme on electrospun nonwoven poly(acrylonitrile-co-acrylic acid) nanofiber

mesh filled with carbon nanotubes: A comprehensive study. *Biotechnol. Bioeng.* **2007,** 97, 708-720.

17.   Mieszawska A. J.; Jalilian R.; Sumanasekera G. U.; Zamborini F. P., The synthesis and fabrication of one-dimensional nanoscale heterojunctions. *Small* **2007,** 3, 722-756.

18.   Jin M.; Zhang X.; Nishimoto S.; Liu Z.; Tryk D. A.; Murakami T.; Fujishima A., Large-scale fabrication of Ag nanoparticles in PVP nanofibres and net-like silver nanofibre films by electrospinning. *Nanotechnology* **2007,** 18, 075605 (7pp).

19.   Li W.-J.; Mauck R. L.; Cooper J. A.; Yuan X.; Tuan R. S., Engineering controllable anisotropy in electrospun biodegradable nanofibrous scaffolds for musculoskeletal tissue engineering. *J. Biomech.* **2007,** 40, 1686-1693.

20.   Jiang H.; Zhao P.; Zhu K., Fabrication and characterization of zein-based nanofibrous scaffolds by an electrospinning method. *Macromol. Biosci.* **2007,** 7, 517-525.

21.   Lannutti J.; Reneker D.; Ma T.; Tomasko D.; Farson D., Electrospinning for tissue engineering scaffolds. *Mat. Sci. Eng. C* **2007,** 27, 504-509.

22.   Demir M. M.; Yilgor I.; Yilgor E.; Erman B., Electrospinning of polyurethane fibers. *Polymer* **2002,** 43, 3303-3309.

23.   Ramakrishna S.; Fujihara K.; Teo W.-E.; Lim T.-C.; Ma Z., *An Introduction to Electrospinning and Nanofibers*. World Scientific Publishing Co.: London, 2005.

24.   Zong X.; Kim K.; Fang D.; Ran S.; Hsiao B. S.; Chu B., Structure and process relationship of electrospun bioabsorbable nanofiber membranes. *Polymer* **2002,** 43, 4403-4412.

25.   Lee J. S.; Choi K. H.; Ghim H. D.; Kim S. S.; Chun D. H.; Kim H. Y.; Lyoo W. S., Role of molecular weight of atactic poly(vinyl alcohol) (PVA) in the structure and properties of PVA nanofabric prepared by electrospinning. *J. Appl. Polym. Sci.* **2004,** 93, 1638-1646.

26.   Buchko C. J.; Chen L. C.; Shen Y.; Martin D. C., Processing and microstructural characterization of porous biocompatible protein polymer thin films. *Polymer* **1999,** 40, 7397-7407.

27.   Frens G., Controlled nucleation for the regulation of the particle size in monodisperse gold suspensions. *Nat. Phys. Sci.* **1973,** 241, 20-22.

28. Doria G.; Franco R.; Baptista P., Nanodiagnostics: fast colorimetric method for single nucleotide polymorphism/mutation detection. *IET Bionanotechnology* **2007,** 1, 53-57.

29. Diegoli S.; Mendes P. M.; Baguley E. R.; Leigh S. J.; Iqbal P.; Garcia Diaz Y. R.; Begum S.; Critchley K.; Hammond G. D.; Evans S. D.; Attwood D.; Jones I. P.; Preece J. A., pH-dependant gold nanoparticle self-organization on funtionalised Si/SiO$_2$ surfaces. *J. Exp. Nanosci.* **2006,** 1, 333-353.

30. Yang Y.; Jia Z.; Li Q.; Guan Z., Experimental investigation of the governing parameters in the electrospinning of polyethylene oxide solution. *IEEE T. Dielect. El. In.* **2006,** 13, 580-585.

31. Saujanya C.; Radhakrishnan S., Structure development and crystallization behaviour of PP/nanoparticulate composite. *Polymer* **2001,** 42, 6723-6731.

32. Elias H.-G., *An Introduction to Polymer Science*. VCH: Weinheim, 1997.

33. Dror Y.; Salalha W.; Khalfin R. L.; Cohen Y.; Yarin A. L.; Zussman E., Carbon nanotubes embedded in oriented polymer nanofibers by electrospinning. *Langmuir* **2003,** 19, 7012-7020.

34. Fennessey S. F.; Farris R. J., Fabrication of aligned and molecularly oriented electrospun polyacrylonitrile nanofibers and the mechanical behavior of their twisted yarns. *Polymer* **2004,** 45, 4217-4225.

35. Zhang Q.; Chang Z.; Zhu M.; Mo Xi.; Chen D., Electrospun carbon nanotube composite nanofibres with uniaxially aligned arrays. *Nanotechnology* **2007,** 18, 115611 (6pp).

6.8. Acknowledgements

APPENDICIES

Appendix

Appendix A: *Formation of amino terminated self-assembled monolayers on silicon nitride from the vapour phase*

Appendix A1 - Reduced boiling point of APTMS

The boiling point of APTMS is 91-92 °C at 15 mmHg.[1] At reduced pressure the boiling point decreases and an online conversion program was used to calculate the boiling point of APTMS at the pressures used for SAM formation.[2] The reduced boiling points at each pressure are as follows (by taking the boiling point as 91.5 °C at 15 mmHg):

Table 7. Reduced boiling points of 3-aminopropyltrimethoxysilane (APTMS)

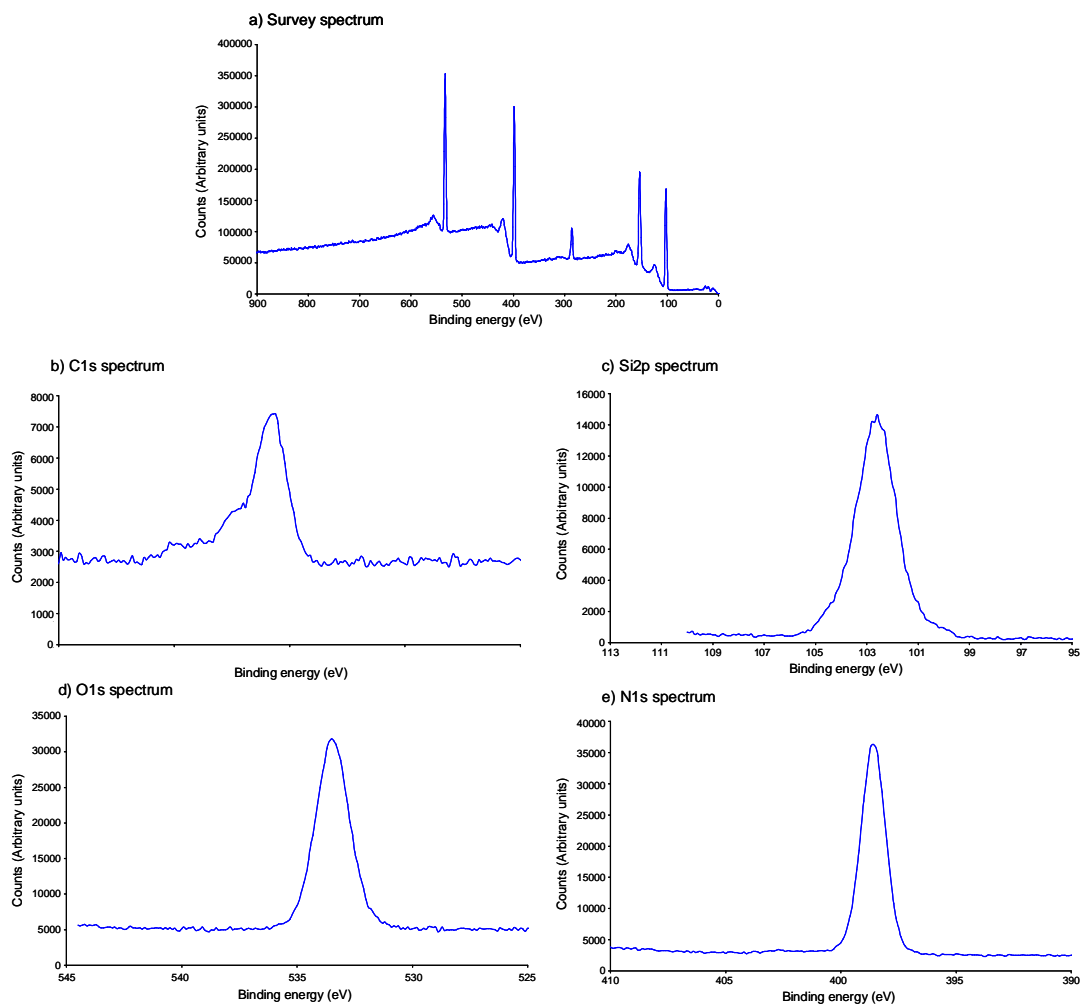| P_{dep} / mbar	Boiling point / °C
0.1	14.3
1.15	43.3
30	99.3
168	141.7
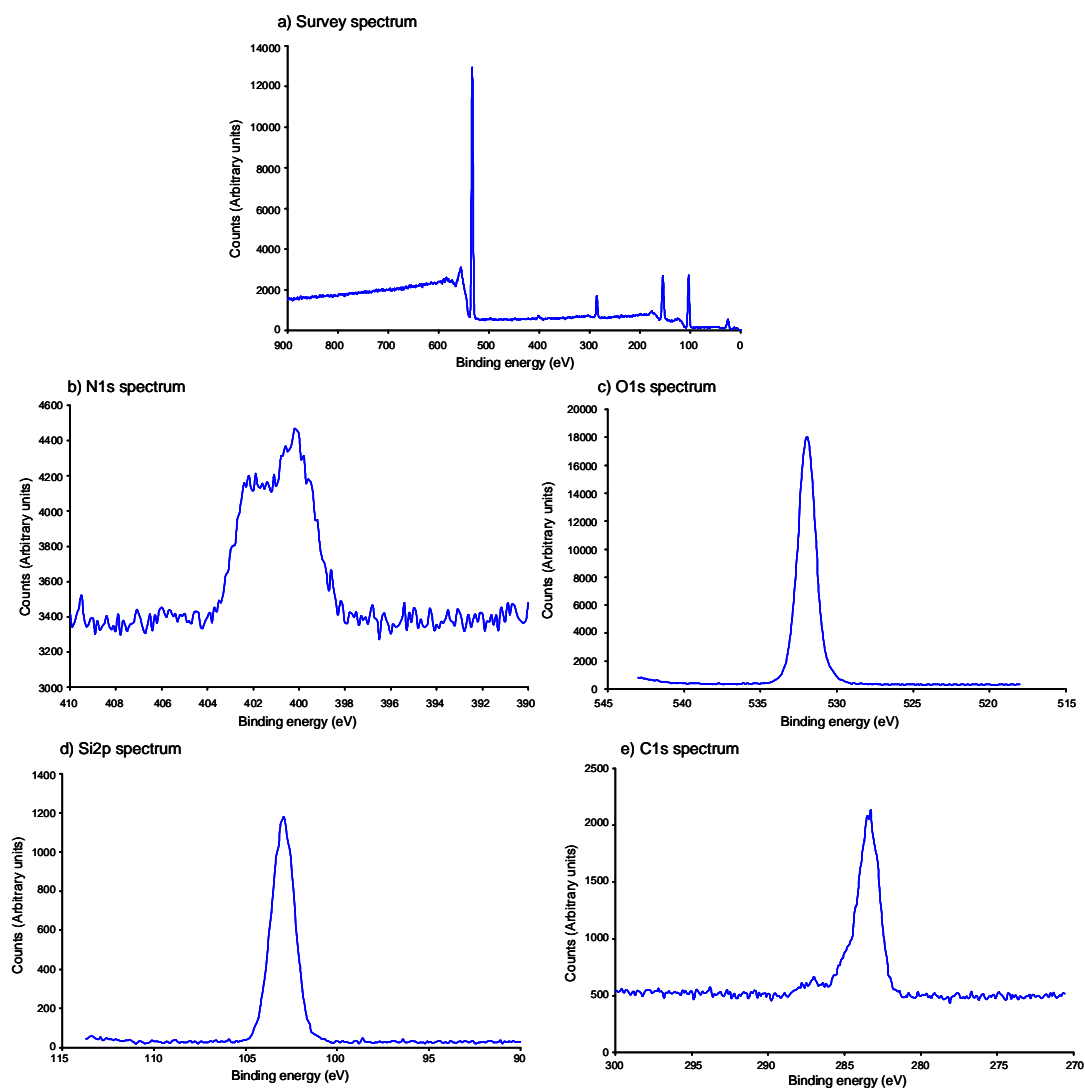
Figure 84. a) survey spectrum and b-e) high resolution spectra XPS spectra of Si/SiO$_2$ substrates immersed in APTMS solution (0.5 mmol in EtOH) for 1 hr.
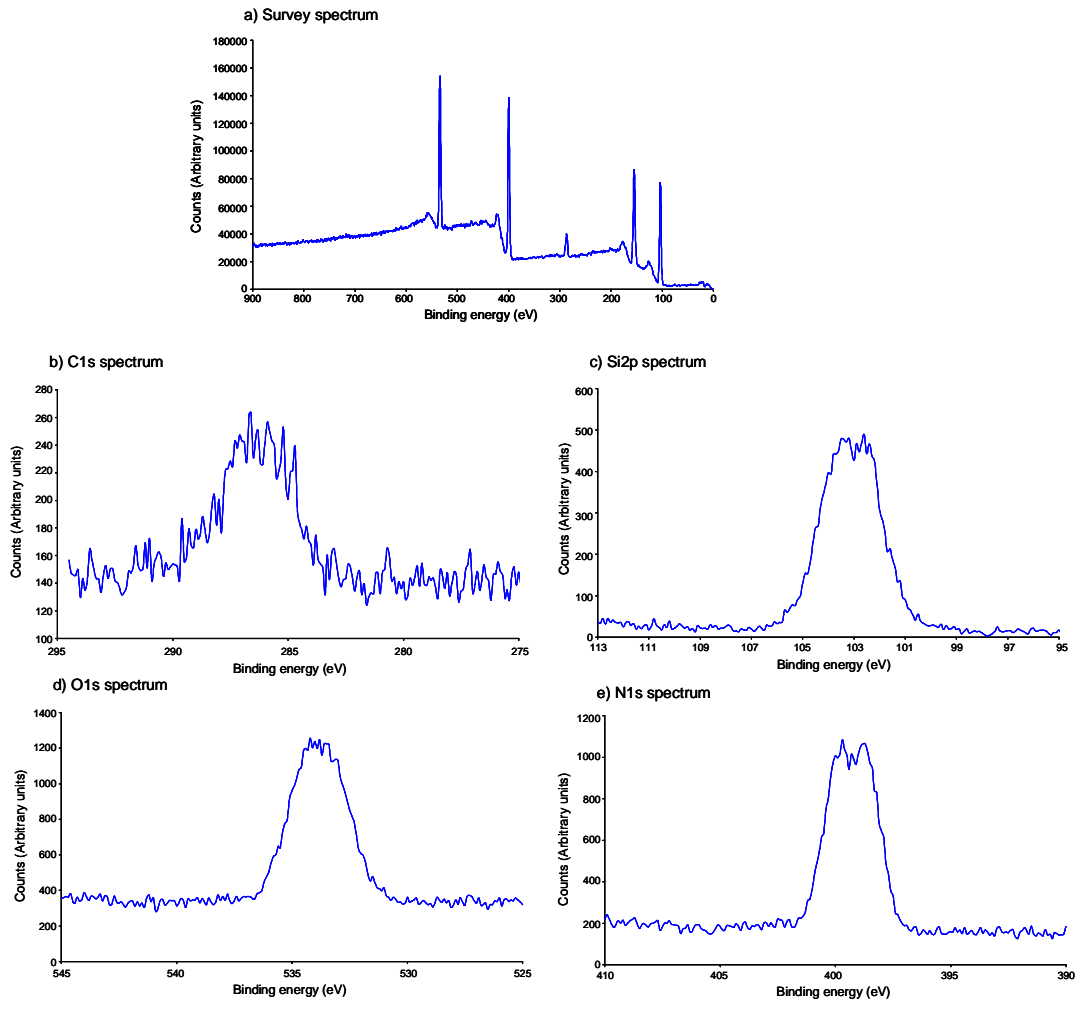
Appendix A3 - SAMs of APTMS on Si_3N_4 by solution deposition (XPS)

XPS spectra were recorded after immersion of Si_3N_4 substrates in APTMS solution (0.5 mM in EtOH) for three different immersion times:
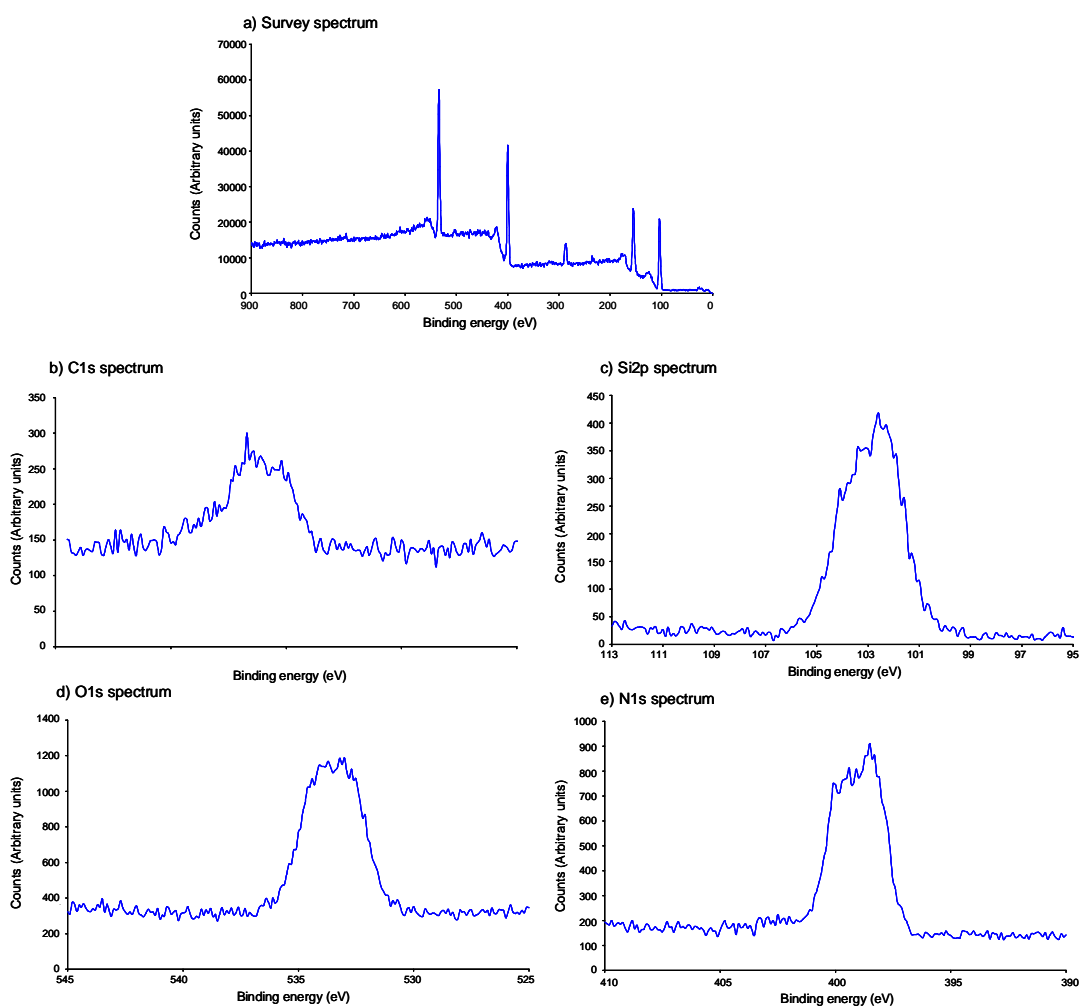
Figure 85. a) survey spectrum and b-e) high resolution spectra XPS spectra of Si_3N_4 substrates immersed in APTMS solution (0.5 mmol in EtOH) for 30 min.

Figure 86. a) survey spectrum and b-e) high resolution spectra XPS spectra of Si_3N_4 substrates immersed in APTMS solution (0.5 mmol in EtOH) for 1 hr.

Figure 87. a) survey spectrum and b-e) high resolution spectra XPS spectra of Si_3N_4 substrates immersed in APTMS solution (0.5 mmol in EtOH) for 2 hr.

XPS spectra (both a survey spectrum and C1s, Si2p, O1s and N1s high resolution spectra) are shown of APTMS SAMs formed on Si$_3$N$_4$ substrates *via* vapour deposition at four different deposition pressures (P$_{dep}$).
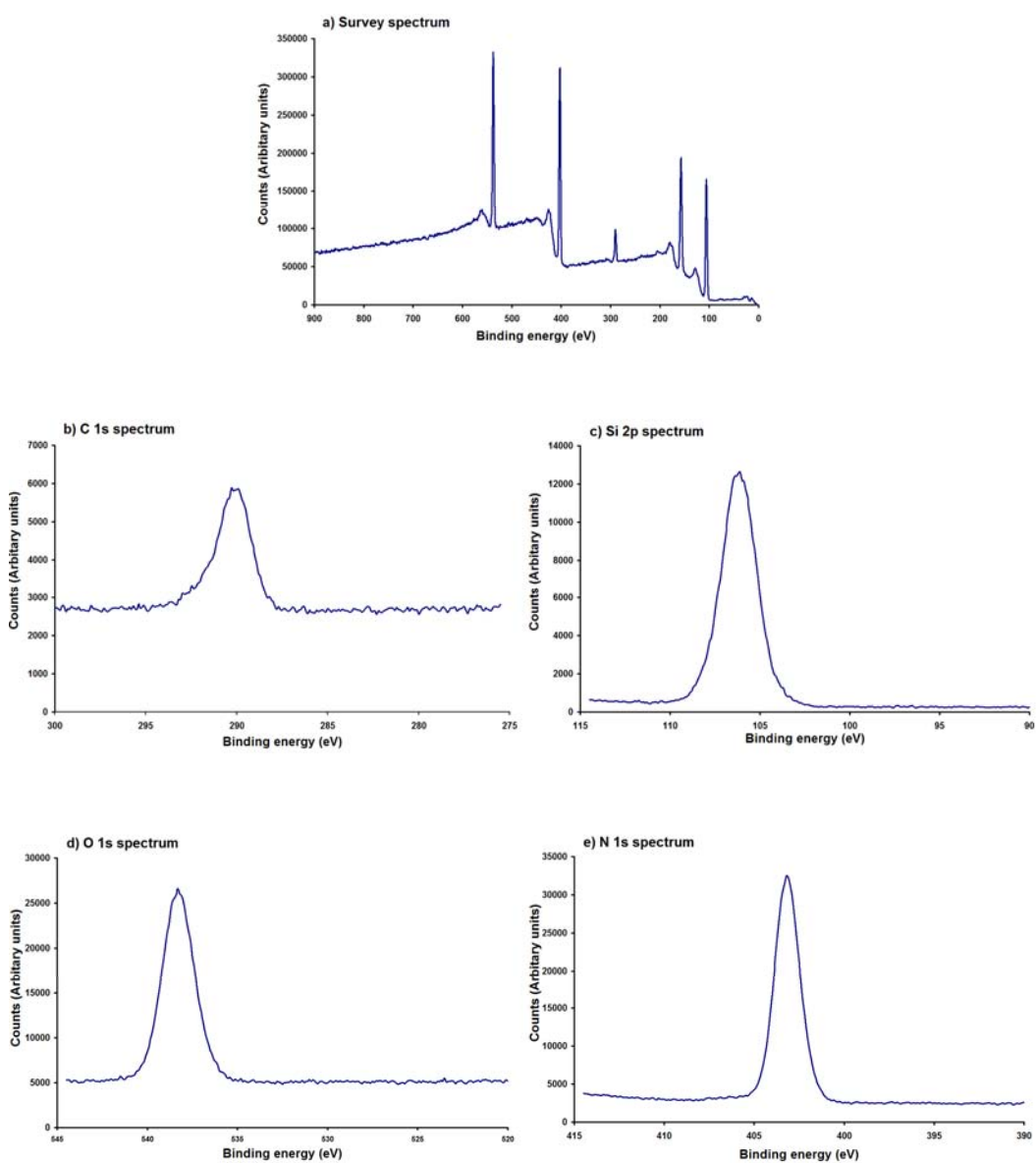
Figure 88. XPS spectra of Si$_3$N$_4$ substrates exposed to APTMS vapour at 0.1 mbar. a) survey spectrum and b-e) high resolution spectra
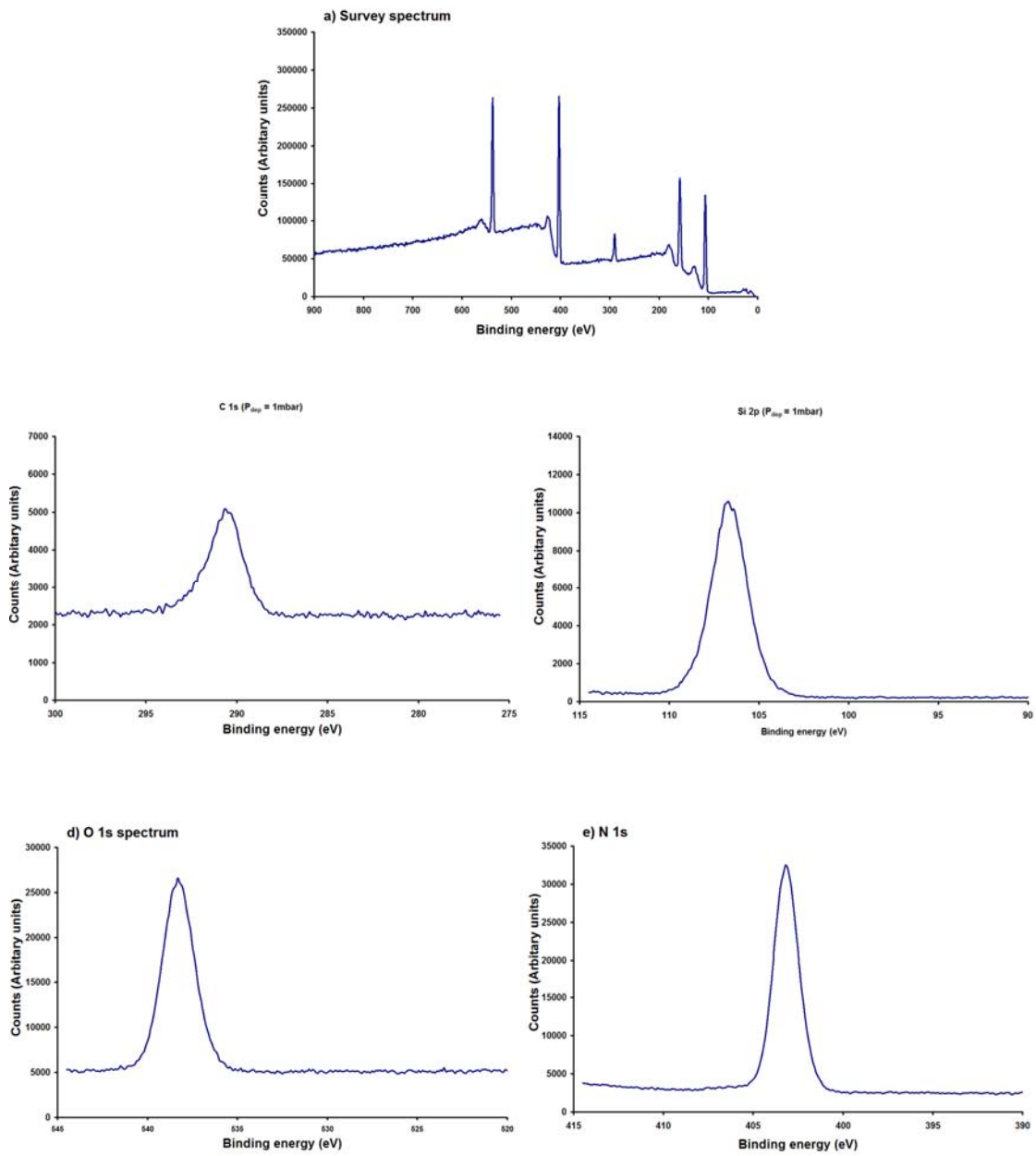
Figure 89. XPS spectra of Si₃N₄ substrates exposed to APTMS vapour at 1.15 mbar. a) survey

spectrum and b-e) high resolution spectra
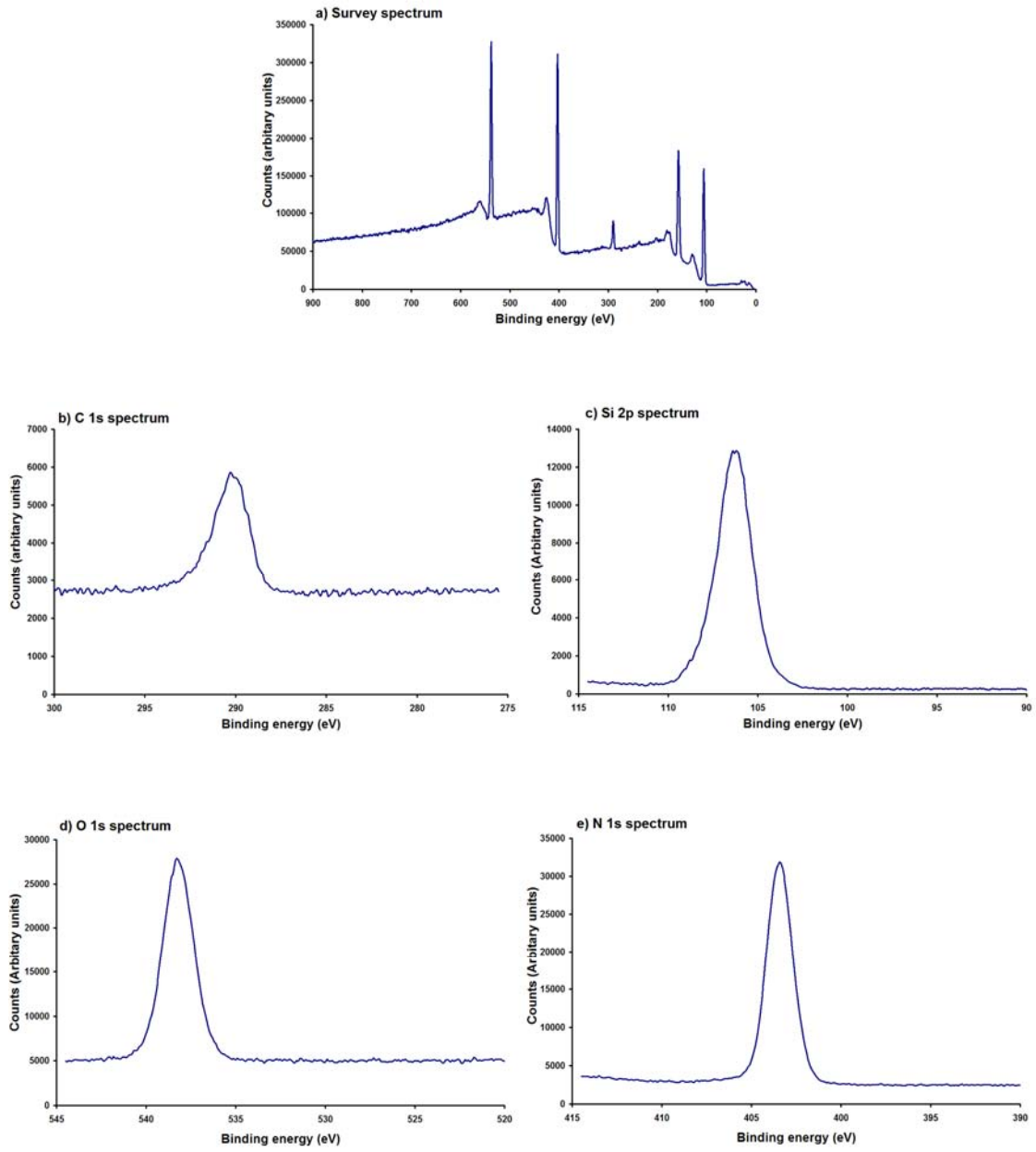
Figure 90. XPS spectra of Si_3N_4 substrates exposed to APTMS vapour at 30 mbar. a) survey
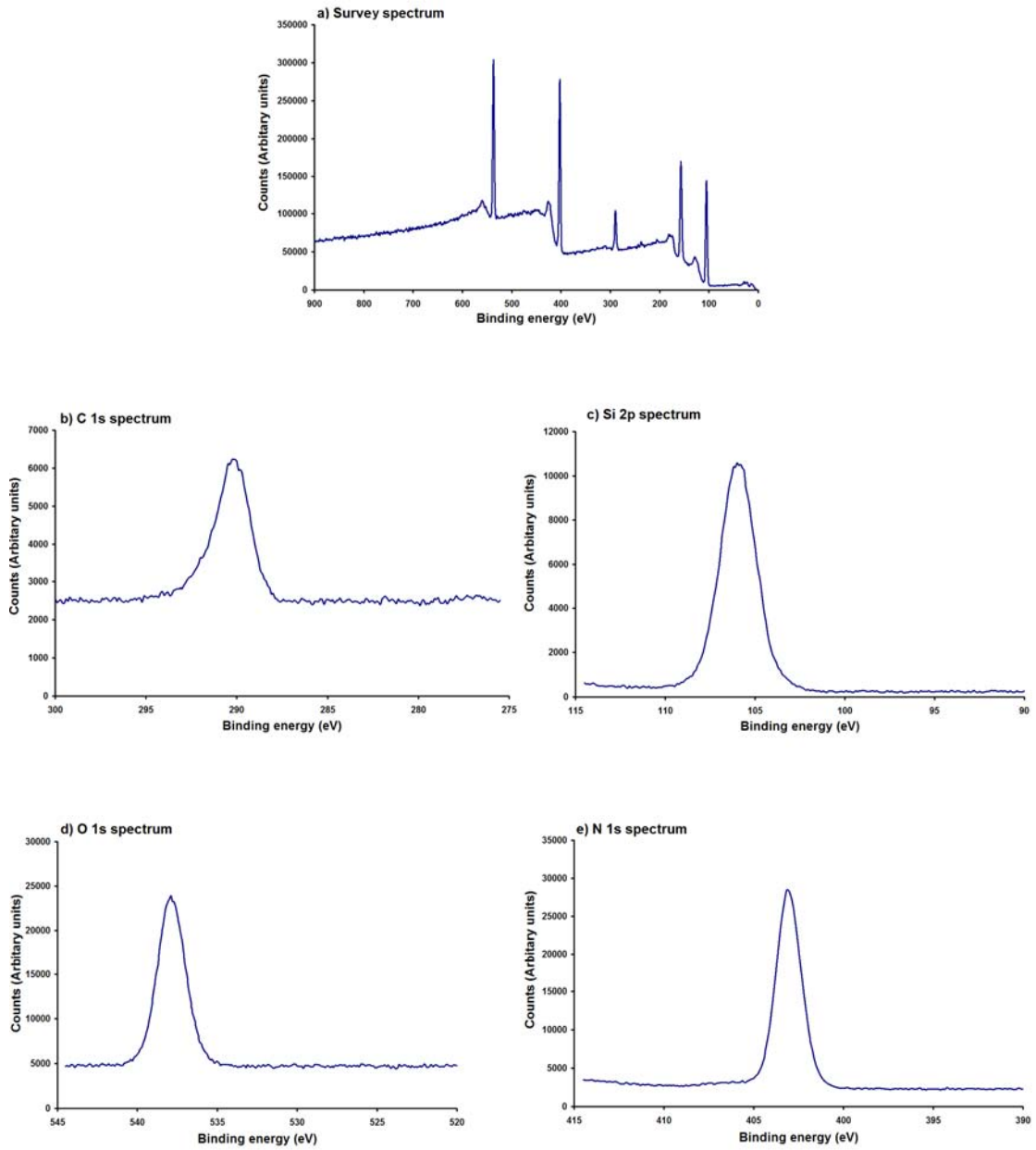
spectrum and b-e) high resolution spectra

Figure 91. XPS spectra of Si_3N_4 substrates exposed to APTMS vapour at 168 mbar. a) survey spectrum and b-e) high resolution spectra

Appendix B - *Mass sensing using a chemically modified microresonator: SAMs meets MEMS*

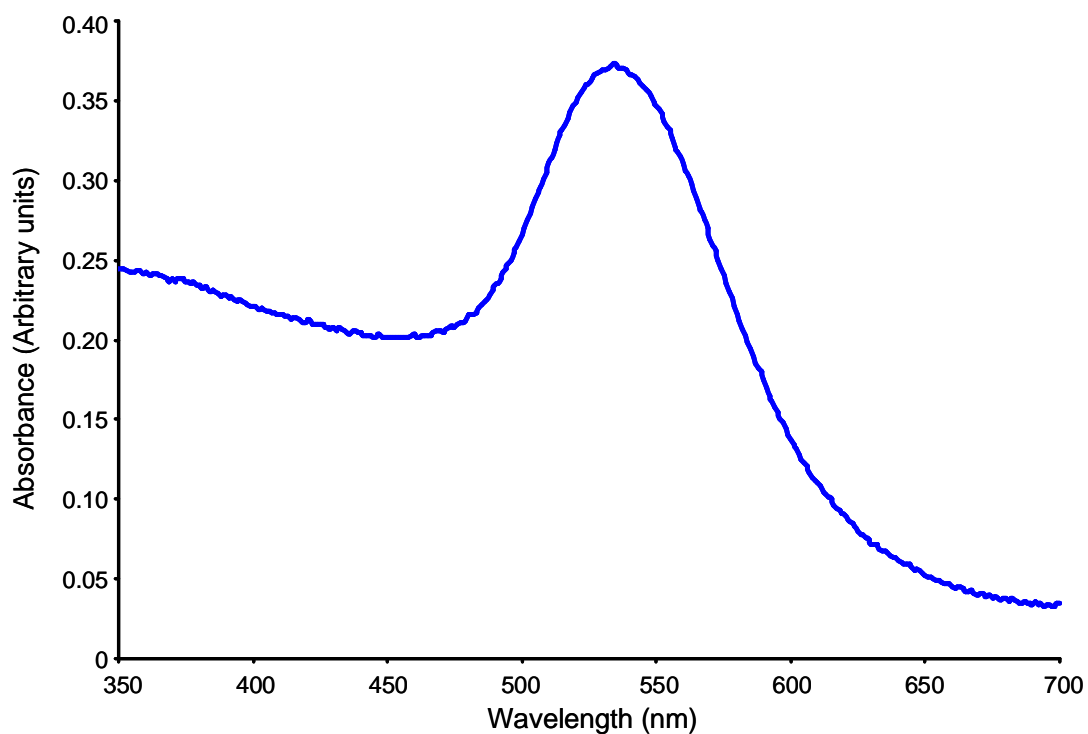*Appendix B1: UV-vis spectrum of citrate passivated Au nanoparticles used for adsorption studies*

Figure 92. UV-vis spectrum of citrate passivated Au nanoparticles used for pH dependent

adsorption experiments

The survey and Si2p spectra for APTMS SAMs formed on Si_3N_4 and subsequently immersed in citrate passivated Au nanoparticle solutions at five different values of pH (3, 4, 5, 6 and 7) are shown in **Figure 93** and **Figure 94**.
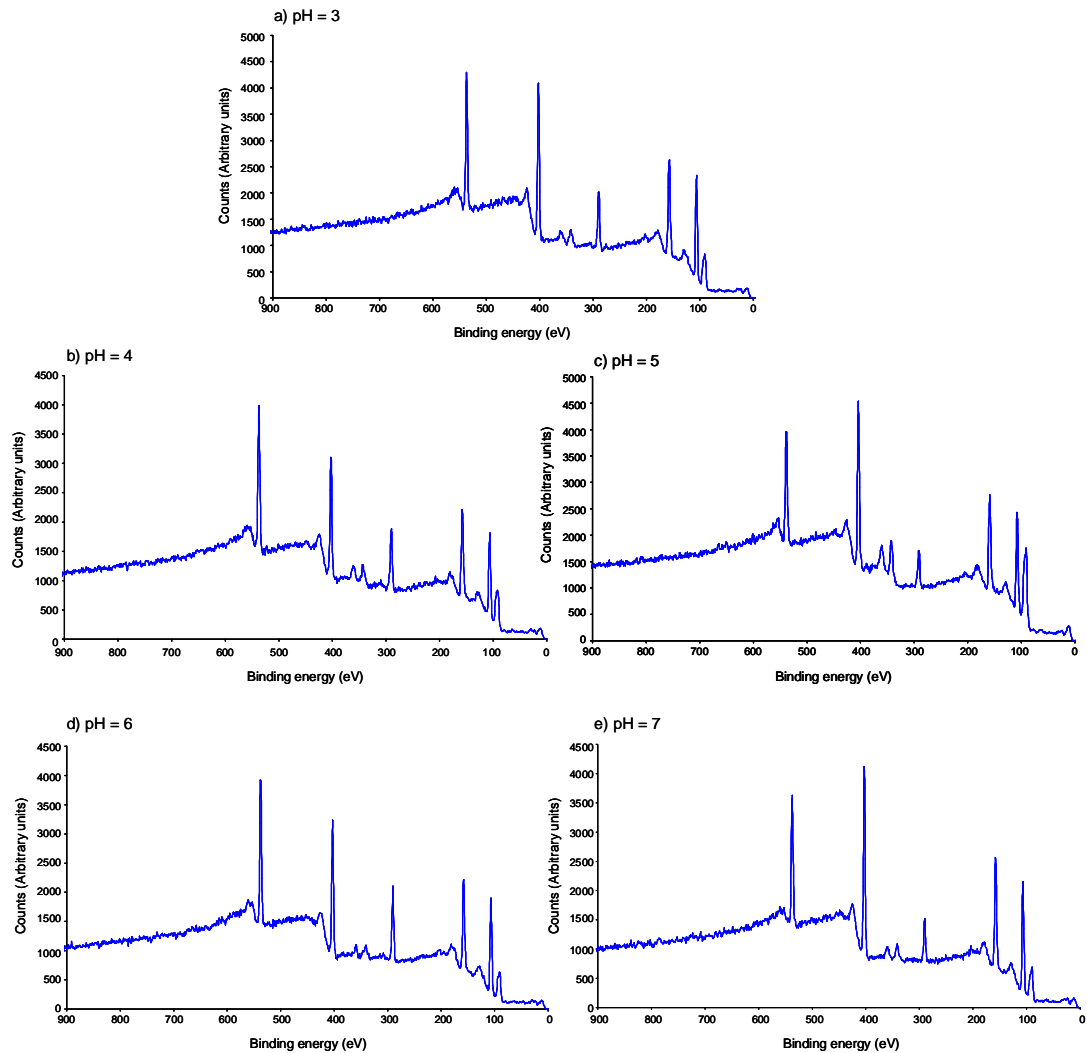

Figure 93. XPS survey spectra of APTMS SAMs on Si_3N_4 substrates after immersion in citrate passivated Au nanoparticles at five different values of pH
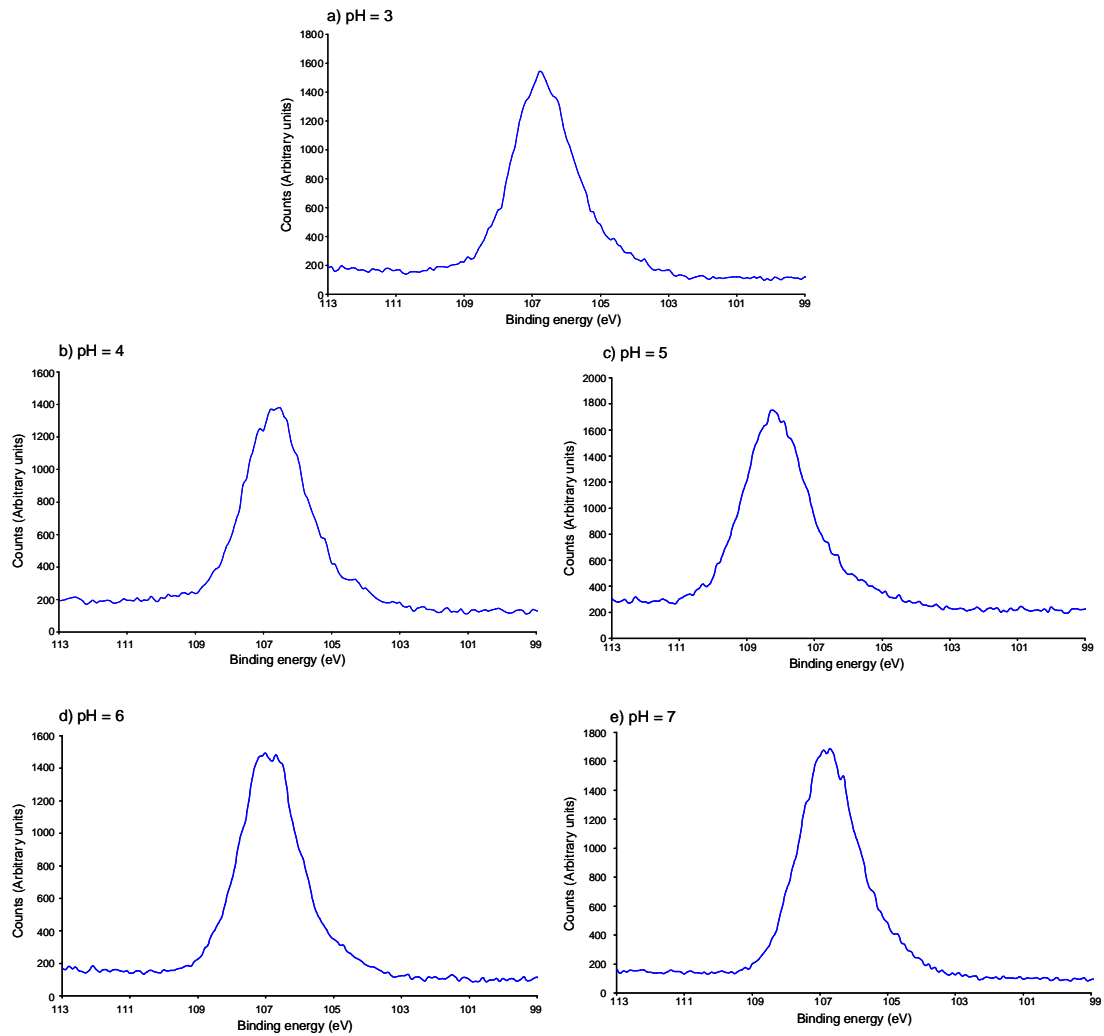
Figure 94. High resolution XPS spectra of Si2p peaks of APTMS SAMs on Si_3N_4 substrates after immersion in citrate passivated Au nanoparticles at five different values of pH

Appendix C1 - Sperm adsorption to glass and poly-l-lysine

The videos of sperm adsorption to glass, unpatterned poly-l-lysine and the poly-l-lysine dot array pattern can be found on the CD attached to this thesis. The videos can be found in the files as outlined in **Table 8**.

Table 8. Video file names of videos showing sperm adsorption to three different surfaces. Files can be found in the folder named 'Appendix C - videos' on the CD attached to this thesis

Video file name	Surface
Movie1(Glass).avi	Bare glass
Movie2(UnpatternedPLL).avi	Unpatterned poly-l-lysine
Movie3(PLLdots).avi	Poly-l-lysine dot array

Appendix D - Formation of sub-micron fibres from PEO/Au nanoparticle composite solutions via electrospinning

Appendix D1 - TEM characterisation of citrate passivated Au nanoparticles

TEM images were obtained of the citrate passivated Au nanoparticles prepared using the Frens method[3] by placing a drop of solution onto a TEM grid. The TEM images shown were used to calculate both the mean nanoparticle diameter and the concentration of Au nanoparticles.
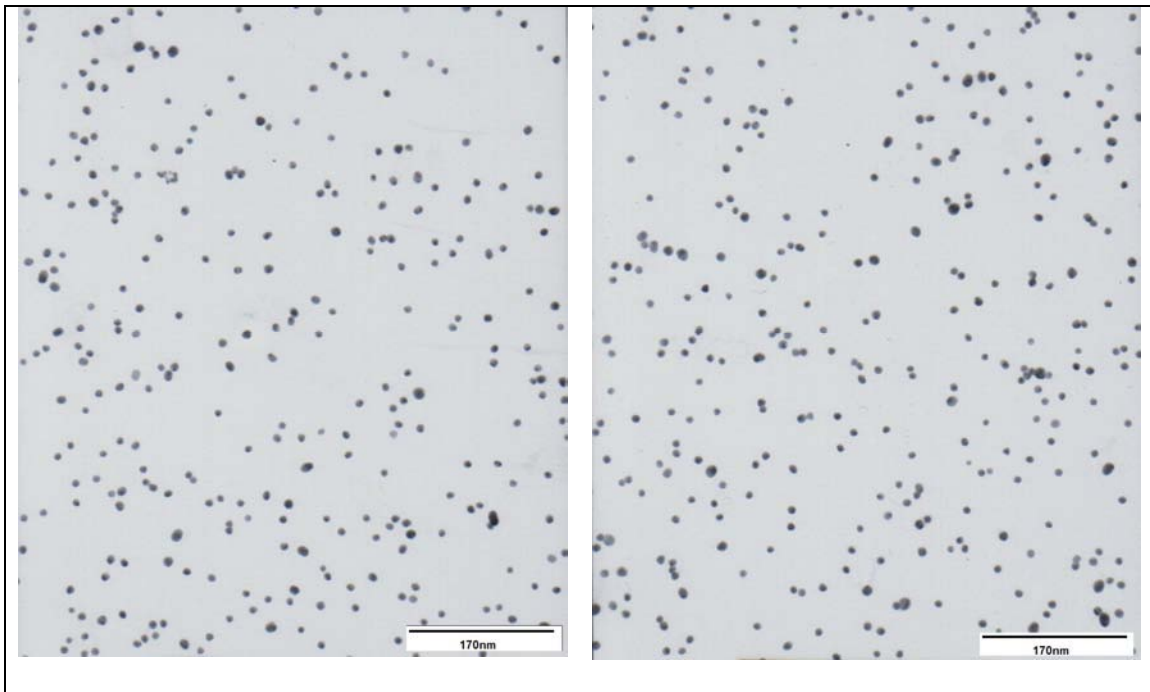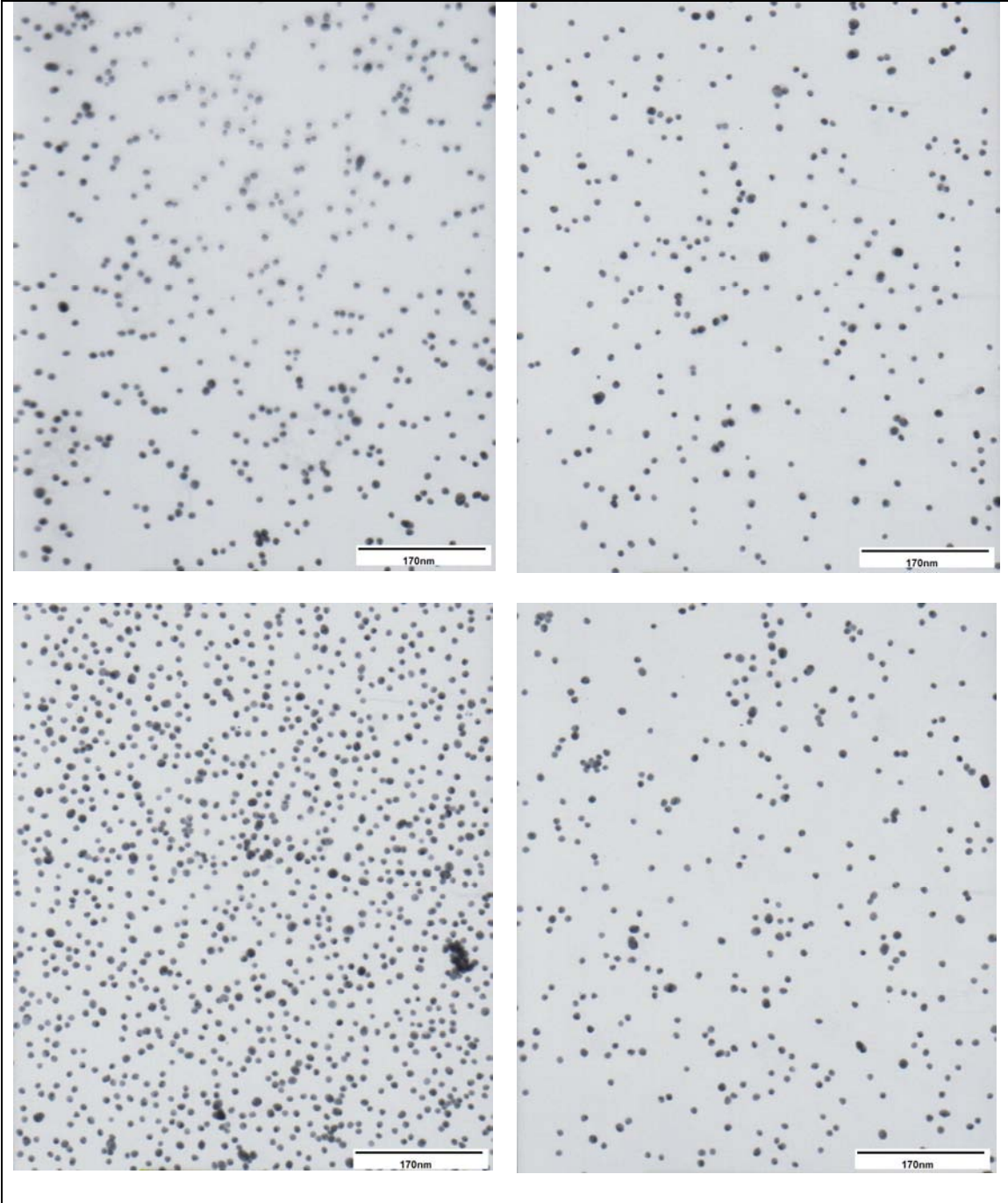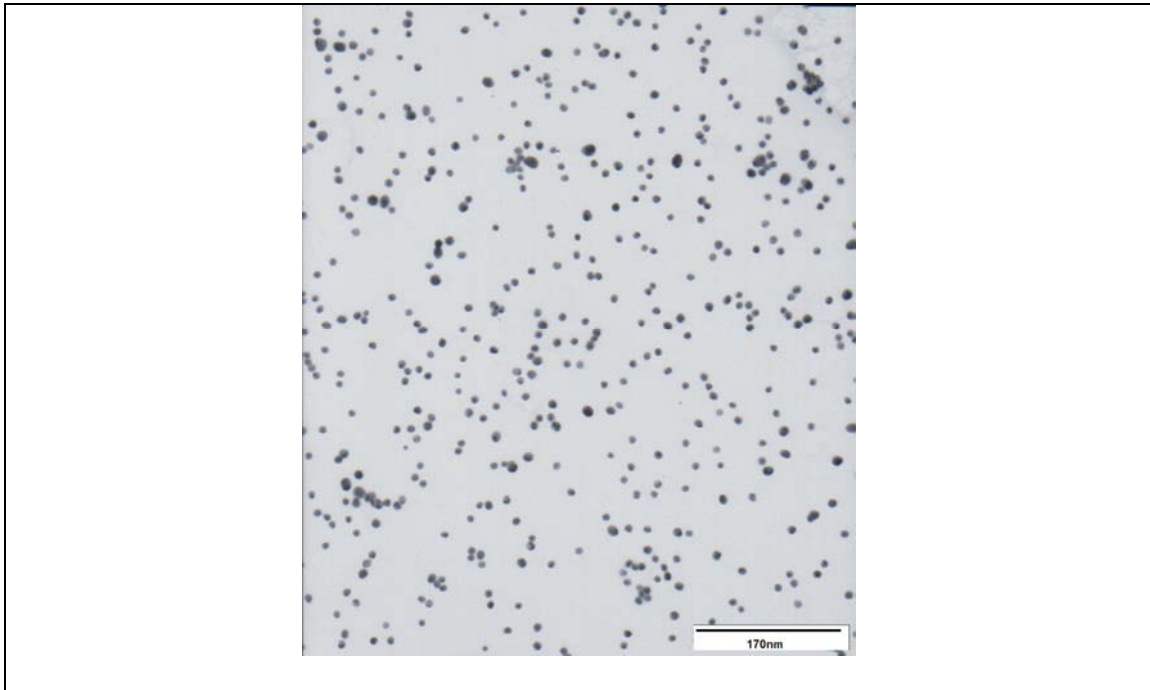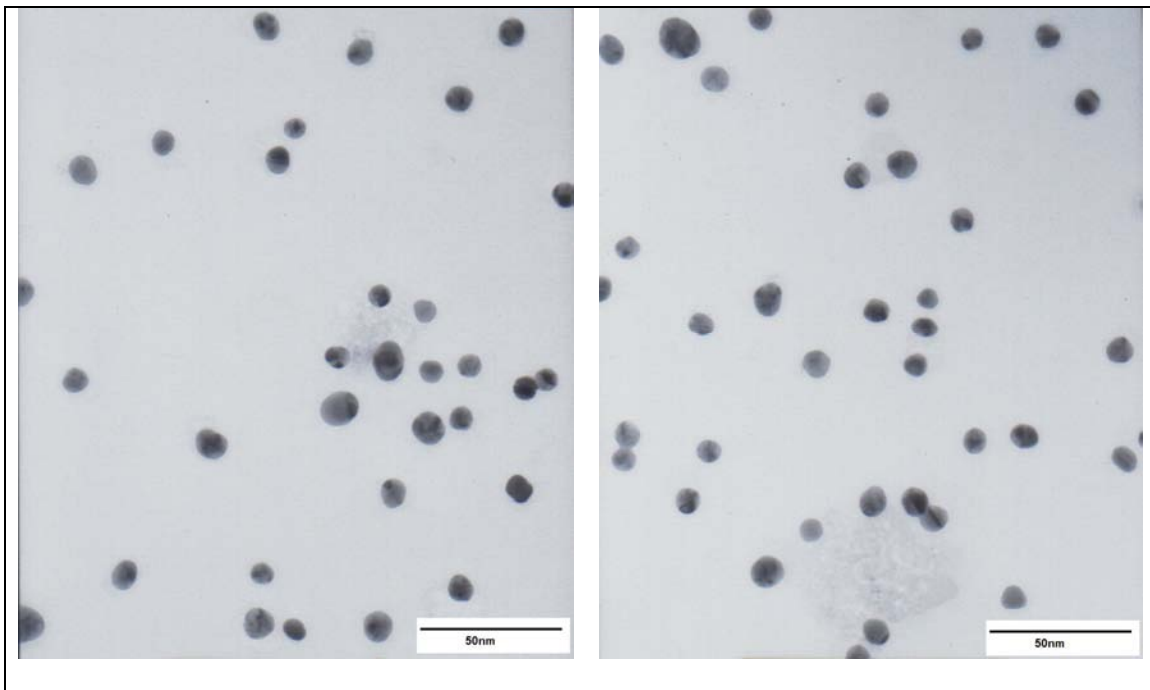
Figure 95. TEM images of citrate passivated Au nanoparticles (Lower of the two magnifications used)
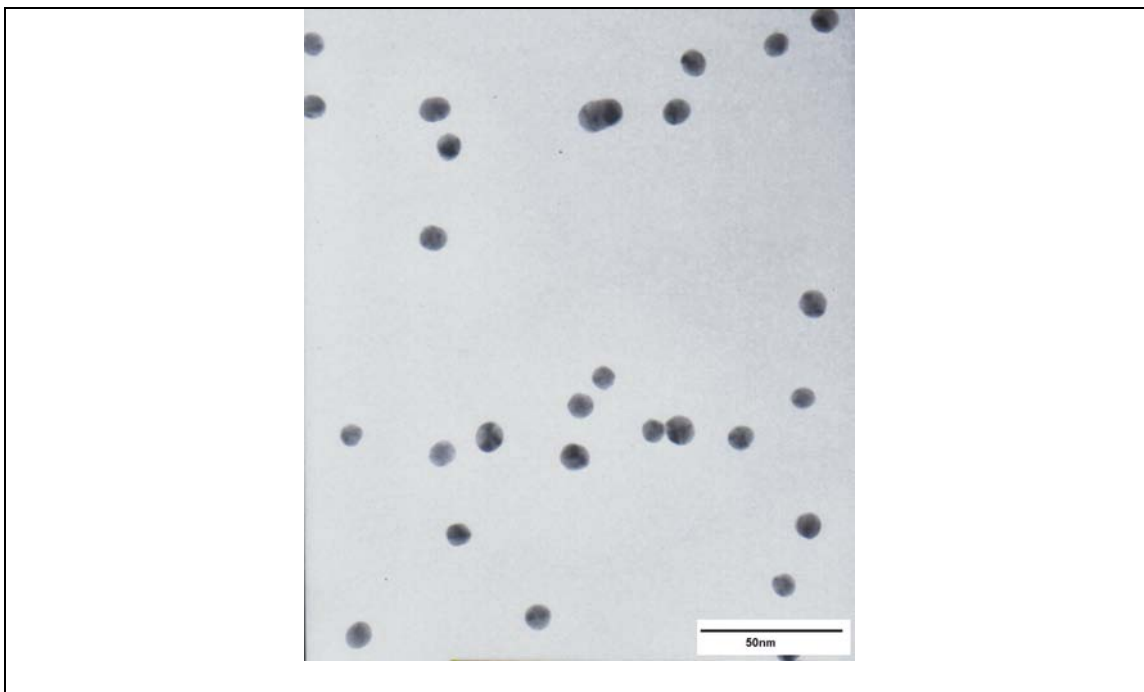
Figure 96. TEM images of citrate passivated Au nanoparticles (Higher of the two magnifications used)

Table 9 summarises the diameters of the citrate passivated Au nanoparticles shown in **Figure 95** and **Figure 96**.

Table 9. Citrate passivated Au nanoparticle diameters extrapolated from TEM images

Particle diameter (nm)	Number of particles
0-2	0
2-4	9
4-6	62
6-8	713
8-10	135
10-12	108
12-14	13
14-16	27
16-18	2
18-20	0
20+	0

Calculation of nanoparticle concentration:

The concentration of citrate passivated Au nanoparticles were calculated from the above TEM images as follows:

Area of TEM image: Low mag: $5.69 \times 10^{-13}\, m^2$

High mag: $4.97 \times 10^{-14}\, m^2$

Area of TEM grid: $1.41 \times 10^{-5}\, m^2$

Total area of TEM images: **$4.13 \times 10^{-12}\, m^2$**

Number of particles in TEM images: 1069

Estimated number of particles on grid: **3.66×10^{9}**

Volume of citrate passivated Au nanoparticle solution on grid: 3 ml

Approximate concentration or particles: **1.22×10^{9} particles.ml^{-1}**

Appendix D2: - Fibre widths

All optical and AFM images recorded of fibres electrospun from 2 wt%, 3 wt%, 4 wt% and 5 wt% of aqueous solutions of both PEO and PEO/Au nanoparticle solutions can be found in the folder entitled '**Appendix D2**' on the CD attached to this thesis.

*Appendix D3: - Nanoparticle concentration within electrospun fibres*

The average nanoparticle concentration within fibres electrospun from 5 wt% PEO/Au nanoparticle solutions were calculated by modelling the threads as cylinders and the beads as spheres.
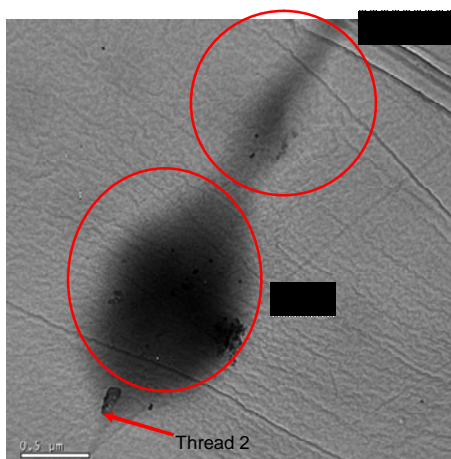
	Thread 1	Thread 2	Bead
Diameter (nm)	440	100	1040
Length (nm)	1360	500	-
Volume (ml)	2.0×10^{-13}	3.9×10^{-15}	5.9×10^{-13}
Number of particles	2	0	23
Conc. of particles (particles.ml^{-1})	9.7×10^{12}	0	3.9×10^{13}
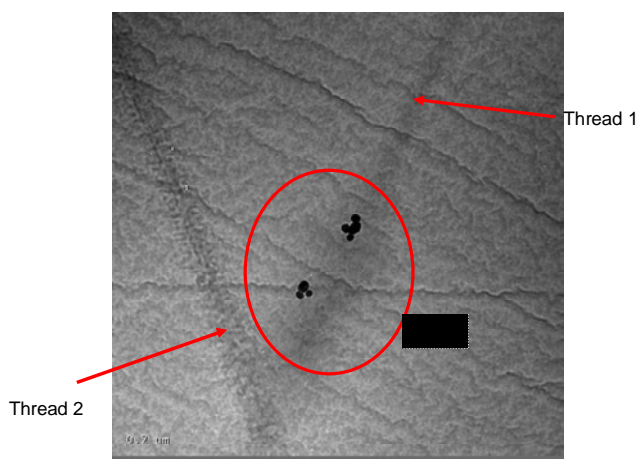
	Thread 1	Thread 2	Bead
Diameter (nm)	220	260	660
Length (nm)	1280	460	-
Volume (ml)	4.9×10^{-14}	2.4×10^{-14}	1.5×10^{-13}
Number of particles	0	0	7
Conc. of particles (particles.ml^{-1})	0	0	4.7×10^{13}
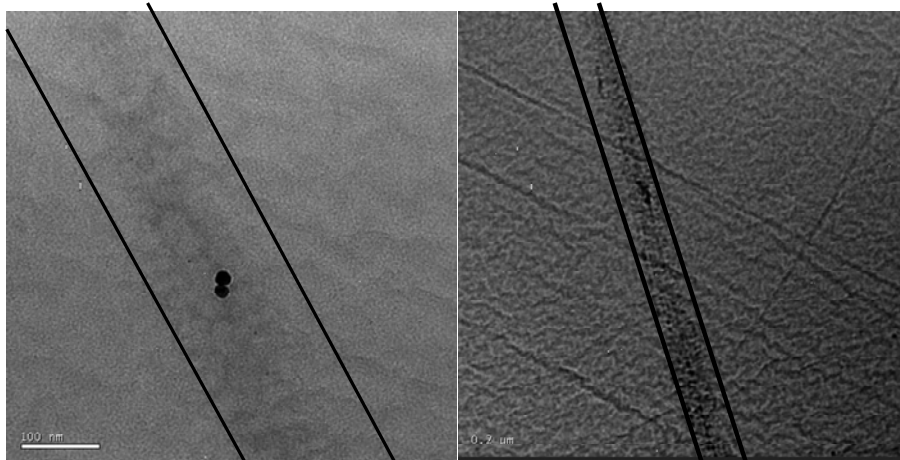
	Thread
Diameter (nm)	600
Length (nm)	3440
Volume (ml)	9.7×10^{-13}
Number of particles	2
Conc. of particles (particles.ml^{-1})	2.1×10^{12}

	Thread
Diameter (nm)	300
Length (nm)	3300
Volume (ml)	2.3×10^{-13}
Number of particles	3
Conc. of particles (particles.ml^{-1})	1.3×10^{13}
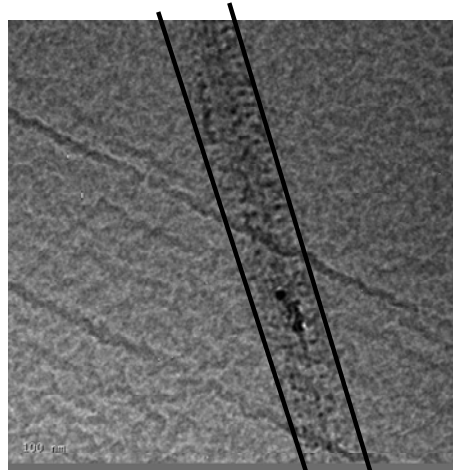
	Thread
Diameter (nm)	380
Length (nm)	3320
Volume (ml)	3.8×10^{-13}
Number of particles	1
Conc. of particles (particles.ml^{-1})	2.7×10^{12}

The concentrations within individual fibres are outlined above and the overall concentrations (4.3×10^{13} particles.ml^{-1} in beads; 3.5×10^{12} particles.ml^{-1} for threads) were calculated by taking an average of the concentrations outlined above.
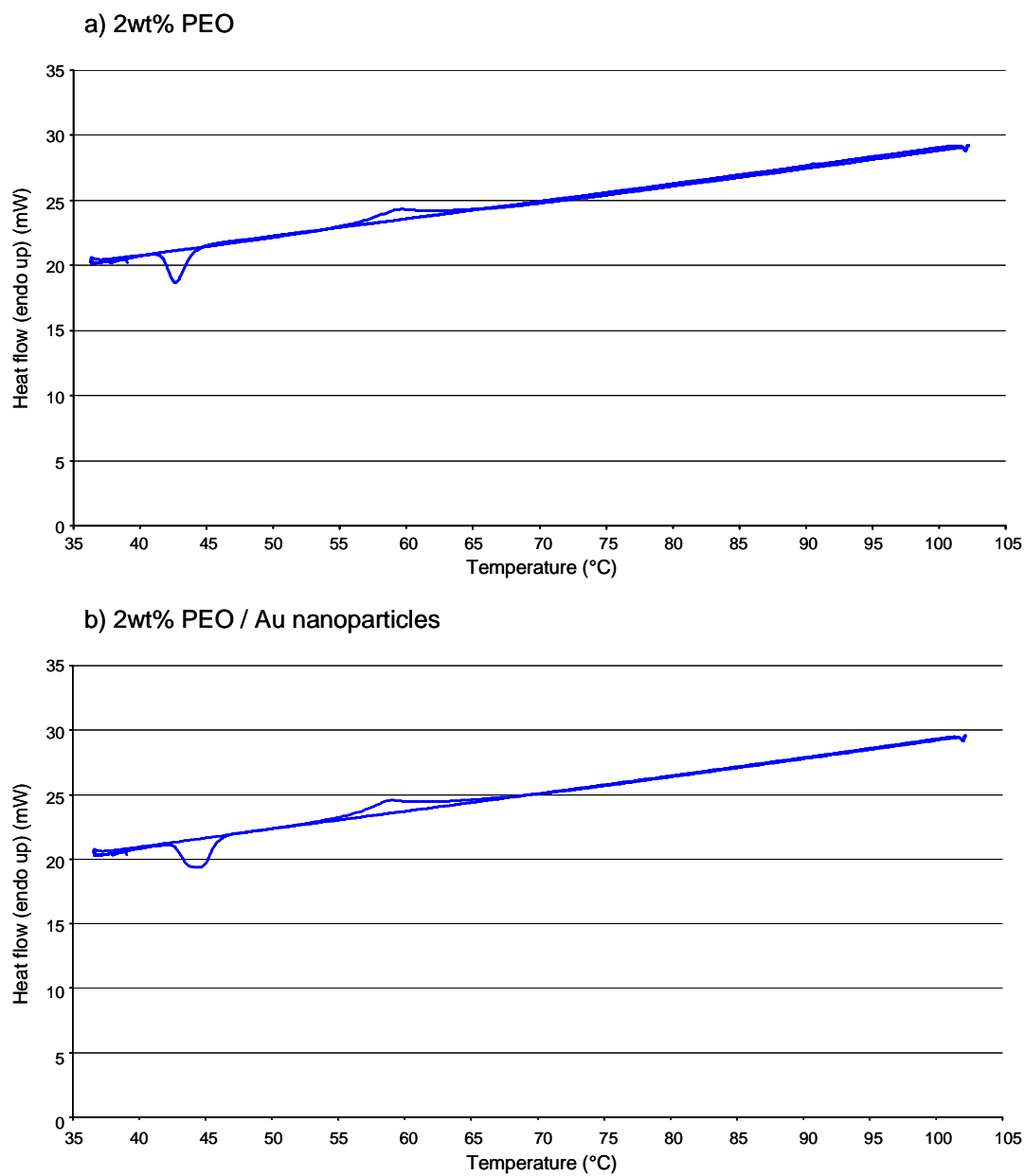
Appendix D4: - DSC curves of PEO fibres:

a) 2wt% PEO

b) 2wt% PEO / Au nanoparticles

Figure 97. DSC curves of fibres electrospun from aqueous solutions of a) 2 wt% PEO and

b) 2 wt% PEO/Au nanoparticles

a) 3 wt% PEO

b) 3 wt% PEO / Au nanoparticles

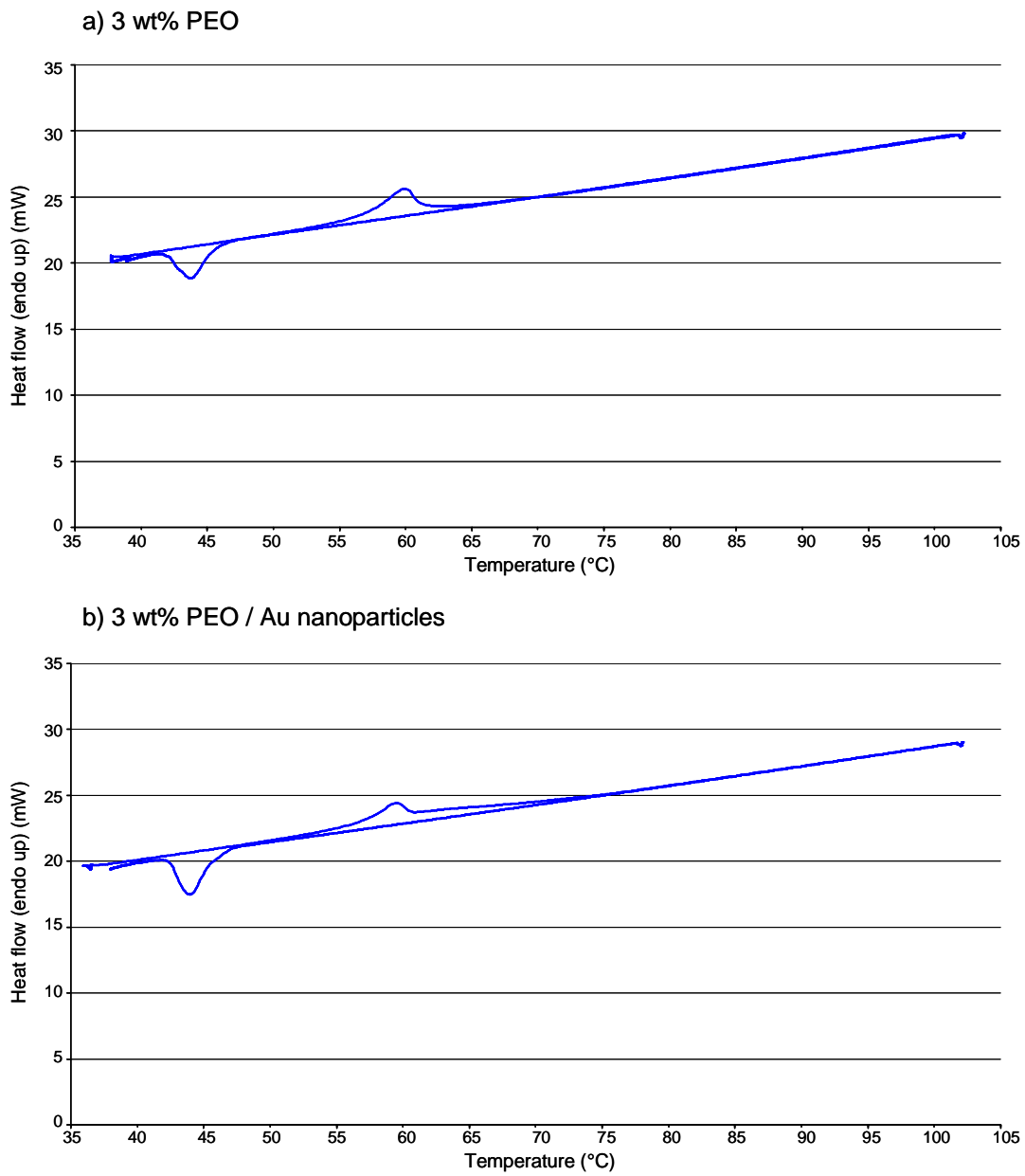**Figure 98.** DSC curves of fibres electrospun from aqueous solutions of a) 3 wt% PEO and

b) 3 wt% PEO/Au nanoparticles

a) 4 wt% PEO

b) 4 wt% PEO / Au nanoparticles

Figure 99. DSC curves of fibres electrospun from aqueous solutions of a) 4 wt% PEO and

b) 4 wt% PEO/Au nanoparticles
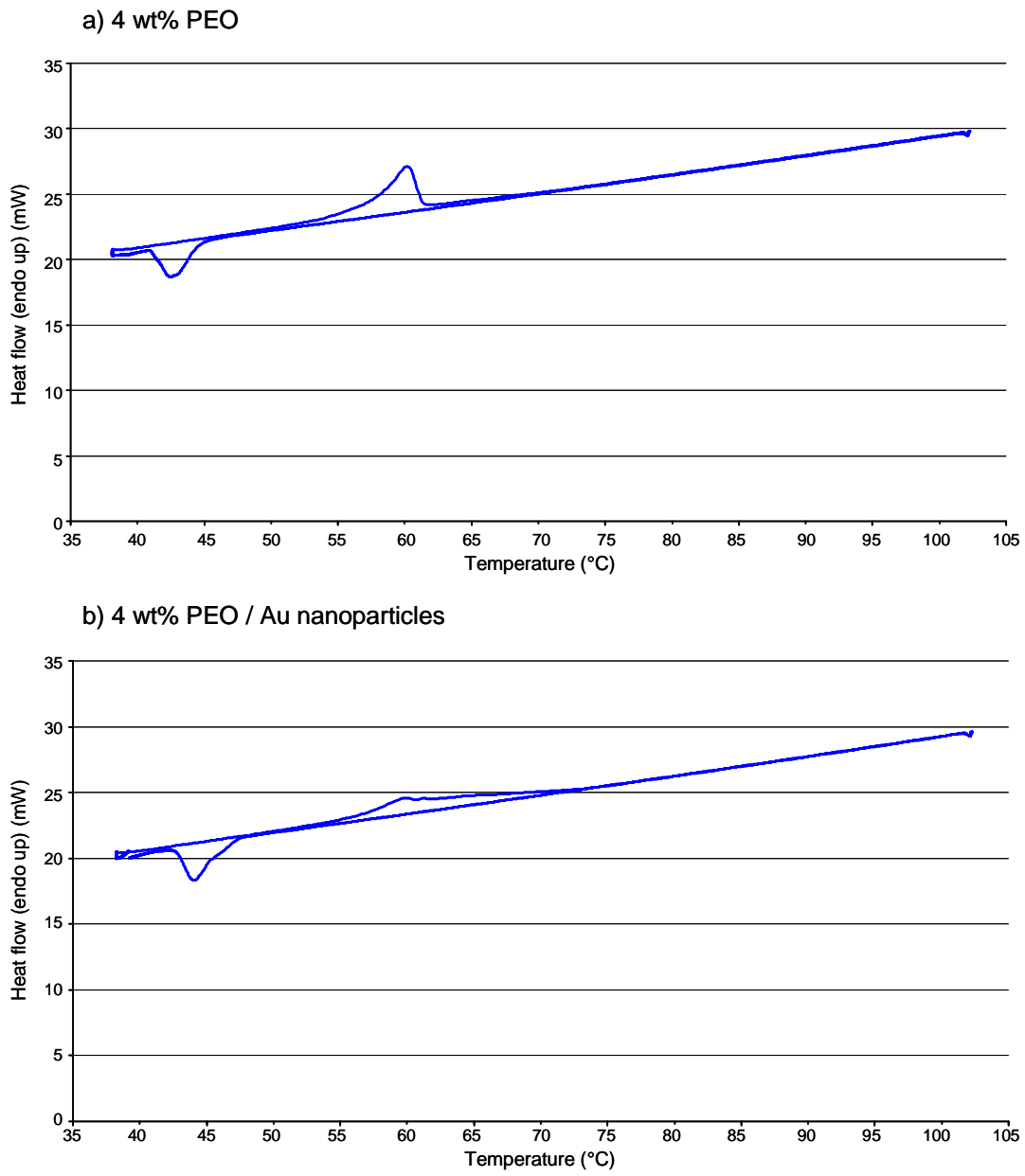
a) 5 wt% PEO

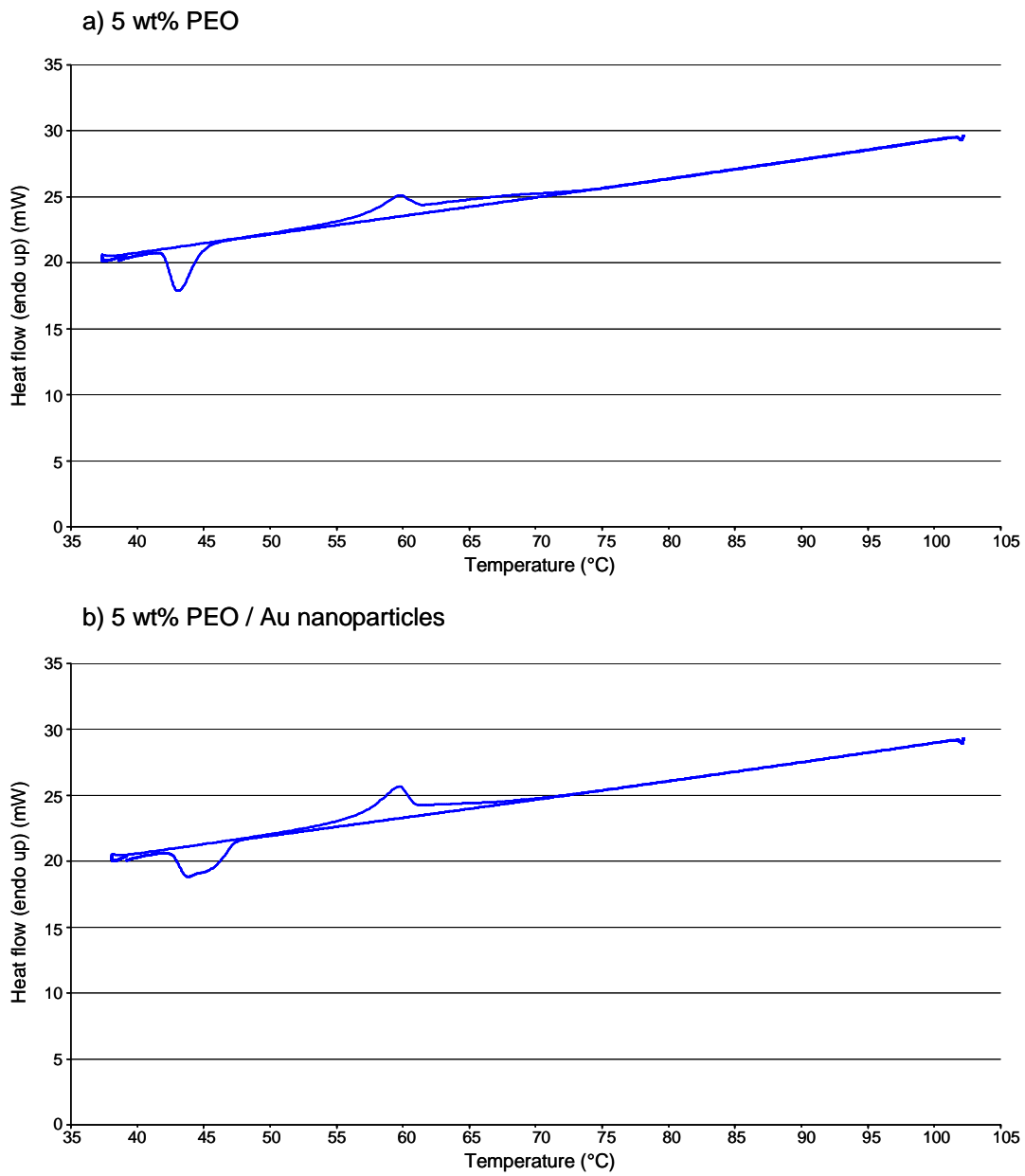
b) 5 wt% PEO / Au nanoparticles

Figure 100. DSC curves of fibres electrospun from aqueous solutions of a) 5 wt% PEO and

b) 5wt% PEO/Au nanoparticles

Table 10. Data obtained from DSC curves

		ENDOTHERMIC PEAK			EXOTHERMIC PEAK		
wt%	Particles?	Temp (°C)	Area of peak (mJ)	ΔH (J/g)	Temp (°C)	Area of peak (mJ)	ΔH (J/g)
2	no	59.436	33.514	33.514	44.255	0.007	0.007
2	yes	58.967	50.288	55.876	44.594	-0.055	-0.061
3	no	59.825	77.722	70.656	44.502	-0.262	-0.238
3	yes	59.444	82.082	91.202	44.748	-0.175	-0.195
4	no	60.164	103.222	86.019	43.248	-0.202	-0.168
4	yes	59.691	100.158	111.287	45.175	-0.222	-0.247
5	no	59.649	89.229	89.229	43.999	-0.086	-0.086
5	yes	59.685	111.365	111.365	45.651	-0.503	-0.503

References

1.   www.sigmaaldrich.com.

2.   http//www.pirika.com/chem./TCPEE/BP/RPBP.htm.

3.   Frens G., Controlled nucleation for the regulation of the particle size in monodisperse gold suspensions. *Nat. Phys. Sci.* **1973,** 241, 20-22.